Dissertation
submitted to the
Combined Faculties of the Natural Sciences and Mathematics
of Heidelberg University, Germany
for the degree of
Doctor of Natural Sciences

Put forward by
Ralf Arne Klemt
Born in: Heidelberg
Oral examination: 16.06.2021

Correlations from Microscopic to Macroscopic Quantum Systems: Interactions vs Indistinguishability

Referees: **Prof. Dr. Selim Jochim**
Priv.-Doz. Dr. Martin Gärttner

Abstract:

In this thesis, I present and discuss correlation measurements of fermionic quantum systems engineered out of ultracold ^{6}Li atoms in optical potentials. A strong emphasis is placed on the complex interplay between interactions and pairing on the one hand and the effects of indistinguishability and the need for symmetrization on the other hand. The starting point will be a strongly correlated two-dimensional quantum fluid, where fermionic pairing significantly above the critical temperature for superfluidity is observed, closely related to a pseudogap regime. It is concluded that additionally measuring higher order correlation functions with full single-particle resolution will be needed to truly unravel the microscopic correlations responsible for the intricate behaviour of such a many-body quantum system.

In pursuit of this ultimate goal, I work out and follow a roadmap composed of both conceptual and technical milestones. As a first step, a novel high fidelity single-particle and hyperfine state resolved imaging system is developed, which is custom-tailored for density correlation measurements in real and momentum space. This imaging scheme is subsequently utilized to identify and quantify strong correlations and entanglement in microscopic systems of two or three atoms in different hyperfine states, deterministically prepared in tunnel-coupled optical tweezer arrays. Effects from strong interactions and Pauli symmetrization are studied both in isolation and in conjunction.

In a further step towards the many-body regime, the preparation of deterministic mesoscopic quantum systems, given by up to twelve particles in a two-dimensional harmonic oscillator potential, is presented. In this system the emergence of many-body behaviour, in the form of the precursor of a Higgs mode, is experimentally observed. This is the basis for measuring single-particle resolved pairing correlations in mesoscopic and ultimately also in macroscopic systems.

Zusammenfassung:

In dieser Arbeit präsentiere ich Korrelationsmessungen in fermionischen Quantensystemen, die aus ultrakalten ^{6}Li Atomen in optischen Potentialen aufgebaut werden. Der Schwerpunkt liegt hierbei vor allem auf dem Zusammenspiel zwischen Wechselwirkung und Paarbildung auf der einen Seite und dem Effekt der Ununterscheidbarkeit und den daraus resultierenden Symmetrisierungsbedingungen auf der anderen Seite. Als Startpunkt wähle ich ein stark korreliertes zweidimensionales Quantengas, in welchem, eng mit der Existenz einer sogenannten Pseudogap verwandt, fermionische Paarbildung deutlich über der kritischen Temperatur für Supraleitung beobachtet wird. Ich lege dar, dass jedoch zusätzlich Korrelationsmessungen höherer Ordnung mit Einteilchenauflösung benötigt werden, um die verantwortlichen mikroskopischen Mechanismen vollständig zu entschlüsseln.
Mit diesem Ziel im Blick, entwickele und folge ich einem Plan, welcher sowohl aus konzeptionellen als auch technischen Schritten besteht. Im ersten Schritt beschreibe ich die Entwicklung eines Bildgebungsverfahrens mit Einteilchen- und Hyperfeinzustandsauflösung, welches spezifisch auf die Messung von Dichtekorrelationen in Ort und Impuls zugeschnitten ist. Mit Hilfe dieser Neuentwicklung charakterisiere ich im Folgenden starke Korrelationen und Verschränkung in mikroskopischen Systemen, welche aus zwei oder drei deterministisch präparierten Atomen in tunnelgekoppelten Anordnungen optischer Pinzetten aufgebaut werden. Der Einfluss starker Wechselwirkung sowie Pauli-Symmetrisierung wird sowohl isoliert als auch im Zusammenspiel untersucht.
Als weiteren Schritt in Richtung des Vielteilchenlimes beschreibe ich anschließend die deterministische Präparation von mesoskopischen Quantensystemen aus bis zu zwölf Teilchen in einem zweidimensionalen harmonischen Oszillatorpotential. In Form eines Vorläufers einer Higgs-Anregung werden in diesem System erste Anzeichen von Vielteilchenverhalten experimentell beobachtet. Dies legt die Grundlage für die Messung von Paarkorrelationen in mesoskopischen und schlussendlich auch makroskopischen Quantensystemen.

Contents

Part I.

Introduction: Studying quantum correlations with ultracold Fermi gases

1. Introduction

The quantum world is a very intriguing one. Only due to the rather abstract concept of quantum statistics, a certain class of particles - the bosons - seem to enjoy each other's company such that they *bunch* together and might even show fascinating collective behaviour in the form of a Bose-Einstein condensate (BEC) [1, 2]. On the other hand, another class of particles - the fermions - strictly avoid each other by *antibunching*. Therefore, instead of a BEC, they form an incompressible sea of particles, the so-called Fermi sea. Now, simply add interactions on top of this and things get truly fascinating. Introducing attractive interactions can allow the fermions to develop bound states. Only through such a pairing mechanism, the half-integer spin fermions find a way to emulate bosonic behaviour, such that they will also be able to macroscopically occupy a single energy level and show similar collective behaviour as their integer spin bosonic counterparts. This is the fundamental idea behind fermionic superfluidity. However, this is not the full story. It turns out that in three dimensions (and in free space), there is actually no two-body bound state for weak attractive point-like interactions [3]. The crucial additional ingredient, as formulated in the famous Bardeen-Cooper-Schrieffer (BCS) theory for weakly interacting systems [4], is the presence of the Fermi sea that strongly restricts the accessible phase-space of the fermions. Particles can only explore states at the top of the Fermi sea, the so-called Fermi surface, with all other states blocked due to the antibunching of indistinguishable fermions. Therefore, the effective phase-space becomes two-dimensional, which turns out to be enough to allow for paired states at any attraction, such that Cooper pairs [5] form and build up a BCS superfluid. BCS theory is a prime example of interactions and indistinguishability joining forces. On the other hand, the effects still mostly separate: First, the Fermi surface is constructed, and then there is additional pairing as a perturbation on top of it. In this thesis, I am instead interested in the different regime of strongly interacting systems where the energy scales set by the interaction and the Fermi sea are comparable. This gives rise to strongly correlated system with an intriguing interplay and competition between interactions and quantum statistics.
There are many systems where such behaviour can be seen (see also [6]): A

very prominent example in the field of condensed matter physics are the high-T_C superconductors [7]. Other important examples include neutron stars and also strongly correlated quantum fluids governed by quantum chromodynamics (QCD), such as colour superfluids and the quark-gluon plasma [8, 9], which describe early phases of our universe. In addition to these true many-body systems, there are also very important microscopic and mesoscopic systems, such as heavy atoms and nuclei, possibly even brought to a state which resembles a QCD-fluid by means of a particle accelerator experiment such as ALICE [10].

In this thesis, I will investigate similar physics by studying a completely different (physical) system: Ultracold fermionic ^{6}Li atoms in two different hyperfine states, which represent an $S = 1/2$ isospin and are trapped in optical potentials. These atomic ensembles can be brought into the strongly correlated regime by resonantly enhancing the scattering between the atoms. Compared to the above examples, ultracold atomic systems offer a few key advantages [11]:[1] Atomic systems in an ultra-high vacuum can be extremely well isolated from the environment, in stark contrast to for example condensed matter systems, such that they can be described as closed quantum systems. In addition, the great control over the optical potentials allows for a very clean (that is defect-free) implementation of tailored potential landscapes. Together with the possibility of engineering specific interactions, a wide range of different Hamiltonians can be implemented offering extensive control over the individual contributing terms [13, 14]. Finally, due to the larger mass of atoms compared to electrons, typical time and length scales are brought into an experimentally more accessible regime for studying microscopic entities. In this thesis we will encounter typical length scales of $\mathcal{O}(1\,\mu\text{m})$ and typical timescales of $\mathcal{O}(10\,\text{ms})$, which will allow for great control over individual constituents of the system and to investigate dynamics. All this comes at the expense of reduced energy scales. While the absolute temperatures of these ultracold systems, at a few 10 nK, are among the coldest in the entire universe, the relative temperature compared to typical energy scales of the system (such as the Fermi temperature or the critical temperature for superfluidity) can be significantly larger than in a corresponding condensed matter system. Therefore, the quest for optimizing schemes to prepare systems with a very low entropy or temperature has been one major driving force in the field of quantum gases [11, 14].

A very interesting platform, where both quantum statistics and strong attractive

[1] There is of-course also a broad range of other *artificial* quantum platforms such as ions, molecules, superconducting circuits and many more; each with their own specific set of advantages and disadvantages [12].

interactions play a key role, is a two-component atomic Fermi gas confined to two spatial dimensions. In a previous series of experiments in our group we have already characterized the low energy phases of a strongly correlated quasi-2D Fermi gas including measurements of the critical temperature for superfluidity [15], the topological nature of the phase transition [16], and the equation of state [17]. In this thesis, we will in addition study the normal phase above the critical temperature [18]. In the strongly interacting regime, high-temperature pairing far above the critical temperature is observed. Based on a strong density dependence of the pairing energy, this effect can be identified as a genuine many-body effect closely related to a pseudogap regime.

In all these measurements, the effective behaviour of the quantum systems is discussed based on either of two methods: Macroscopic observables such as the phase coherence [15, 16], the density of states [17] or the excitation spectrum [19–22] probe the collective behaviour of the system. Using coarse-grained densities, on the other hand, for example in measurements on noise corrections [23] or EPR steering [24–26], correlations between (spatial) regions of the system can be detected. Direct access to the responsible fundamental microscopic mechanisms is not achieved in general, however.[2]

Combining the collective or coarse-grained measurements with microscopic local readout is a very desirable goal. In order to truly unravel the microscopic correlations responsible for all the intricate behaviour observed, it is required to measure higher order correlations, ideally with full single-particle resolution. Take for example the BCS superfluid again, where local (in momentum space) Cooper pairing correlations allow for the collective global phase coherence of the system. The fact that measuring such correlations might at least in principle be possible in cold atomic systems [27] is, in my opinion, the most important reason for choosing this platform.

In the main part of this thesis, I report on my contribution towards this goal of connecting microscopic observables to macroscopic phenomena. To this end, I develop and present a roadmap consisting of both conceptual and technical milestones: First, I will describe the development of a high fidelity single particle and hyperfine state resolved imaging method [28]. As this scheme does not require any confining potentials during imaging, it can be conveniently used to measure density correlations in real and momentum space. This imaging method is subsequently used to identify and quantify strong correlations in microscopic systems of two or three atoms in different hyperfine states deterministically prepared in tunnel-coupled optical tweezer arrays [29, 30]. These microscopic systems are

[2] With the exception of certain lattice models, see chapter 5.

an ideal testbed for correlation measurements, as effects from strong interactions and Pauli antisymmetrization can be studied both in isolation and in conjunction. In addition, different classes of entanglement are certified in these systems. In particular, a new measure is introduced which allows us to isolate the effects due to quantum statistics from the measured entanglement features [31]. Together, this constitutes a toolbox to fully characterize almost arbitrary microscopic correlation features. It is crucial to appreciate this: It is rather straightforward to measure *some* correlations in a many-body system. However, most of these arise from a plethora of constraints and boundary conditions by interactions, the trap potential or even the Pauli principle alone. Even for a conceptually very simple state it can be sufficient to study an unfortunate observable to measure strong correlations. Therefore it is an outstandingly important task to learn how to measure the *relevant* correlations.
Finally, as the next major step towards the many-body regime, I will present the preparation of deterministic mesoscopic quantum systems, given by up to twelve particles in a two-dimensional harmonic oscillator potential [32]. This system, in its close resemblance to the quasi-2D many-body system studied before, but also atomic or nuclear systems, will be used to search for first indications of the emergence of many-body behaviour, given by a precursor of a Higgs mode which is experimentally observed. This is the foundation for measuring single-particle resolved pairing correlations also in mesoscopic systems. In this context, and in order to fully close the circle to the quantum gas discussed in the beginning, I will also elaborate on the possibilities to extend these methods to the true many-body limit.

Structure of the thesis

This thesis is structured into three parts. In this first part, specifically in the following chapter 2, I will discuss the basic concepts needed for this thesis. This will include theoretical ideas, such as quantum correlations and entanglement, an overview of correlation functions as the basic observable used in this thesis, and the fundamental experimental schemes used. In the second part of this thesis, I will present the measurement of high temperature pairing in a macroscopic system in chapter 3, based on [18]. I will use this measurement campaign to motivate why the development of a scheme to access microscopic correlations is of such great importance. In the third and main part of this thesis, I will start by outlining my strategy and roadmap towards achieving this goal in chapter 4. In the chapters to follow, I will discuss our progress on this path. Based on [28],

I will present a new imaging scheme developed during the course of my doctoral studies in chapter 5. Subsequently, in chapter 6, we will use this scheme to study correlations and entanglement as well as the interplay between interactions and indistinguishability in microscopic systems, based on [29–31, 33]. In chapter 7, I will present the emergence of collective behaviour in mesoscopic systems, based on [32], before concluding in chapter 8.

2. Fundamental concepts in theory and experiment

In this chapter I will discuss a range of basic notions and concepts which will be needed for the discussion of the experiments performed in this thesis. I will focus on general aspects and discuss specific details in the corresponding chapters when needed. I will start by introducing the concepts of quantum entanglement. Afterwards, I will discuss the main observables used in this thesis, which are density correlation functions. Finally, I will outline how we experimentally prepare a broad range of relevant quantum states.
This section is not aiming at providing a full introduction into the basics of quantum mechanics needed for this thesis. For this, the reader is referred to for example [3, 34].

2.1. Quantum entanglement

Quantum entanglement is the feature of quantum mechanics which is probably surrounded by the most mysterious aura. This is mostly due to the fact that entanglement (a term introduced by Schrödinger [35]) lies at the heart of what was considered 'spooky action at a distance' [36] in the early days of quantum mechanics. However, also up to this day, there are still experiments ongoing trying to close certain very subtle *loopholes* which would hypothetically allow a description of nature without this spookyness. In addition, the mathematical foundation and the computational concepts of entanglement are still debated and not yet fully sorted out (see for example [37, 38] for an overview). In more recent years, entanglement as a research field gained even more momentum with the advent of quantum information and computation [39]. In addition, new experimental and technological developments enable unprecedented control over microscopic quantities in atomic, molecular and condensed matter systems, such that entanglement can be used to study the structure of quantum states as well as information spreading in these systems [40–46].
In this thesis we will mostly use the fact that 'entanglement is that feature of

quantum formalism which makes it impossible to simulate quantum correlations within any classical theory', as Horodecki et al. write in their seminal review paper [37]. This means, we are interested in the question whether correlation features, which are experimentally measured, necessarily have to be explained within a full quantum theory.

In the following section, I will introduce a few central fundamentals of entanglement. The chapter is mostly based on [37, 38], where the reader is also referred to for a more in-depth overview on quantum entanglement, as well as a presentation of the most important original literature. Here, I will restrict myself to finite dimensional systems for simplicity and also not touch on the subtleties regarding non-local but otherwise classical theories [47].

In its most basic form, entanglement describes the attribute of a compound quantum system that the individual subsystems, even if they are spacelike separated, cannot be seen as independent constituents of the whole system. This means that an operation on one of the subsystems can immediately (but to clarify, non-signaling) affect the state of the other subsystems. More formally: Assume that we have n different subsystems such that the Hilbert space of the full system is given by $\mathcal{H} = \otimes_{l=1}^{n} \mathcal{H}_l$. Based on the superposition principle we can write down a generic state as

$$|\Phi\rangle = \sum_{i_1,\cdots,i_n} c_{i_1,\cdots,i_n} |i_1\rangle \otimes |i_2\rangle \otimes \cdots \otimes |i_n\rangle \,, \tag{2.1}$$

where $c_{i_1,\cdots,i_n}$ is the complex component matrix and $|i_j\rangle$ is a basis set of $\mathcal{H}_j$. States are defined to be entangled if they cannot be expressed as a product state of individual states $|\phi_j\rangle \in \mathcal{H}_j$, such that $|\Phi\rangle \neq |\phi_1\rangle \otimes |\phi_2\rangle \otimes \cdots \otimes |\phi_n\rangle$. The most prominent example of an entangled state for a two-qubit bipartite system is the so-called Bell state [48]

$$|\phi^+\rangle = \sqrt{\frac{1}{2}} \left(|0\rangle \otimes |0\rangle + |1\rangle \otimes |1\rangle\right) , \tag{2.2}$$

which obviously cannot be written down as a product state.[1] Entangled states show up quite naturally within quantum mechanics due to coherent (as opposed to classical) superpositions, and thus are closely related to the study of coherence properties of quantum states. The *spooky* nature is thus only due to the fact that entanglement is inconsistent with a set of assumptions that a classical physical

[1] There are four equivalent incarnations of the Bell state, typically denoted by $|\phi^+\rangle$, $|\phi^-\rangle$, $|\psi^+\rangle$, $|\psi^-\rangle$, which can be transformed into each other by local (in the subsystems) unitary operations.

world should obey [36, 48]:

- **Realism:** Measurement results are solely determined by properties of the system and are never intrinsically stochastic.
- **Locality:** Measurement results are independent of any operations performed at spacelike distances.
- **Free will:** The measurement settings chosen are not influenced or predetermined by any (hidden) local theory.

This is known as the Einstein-Podolsky-Rosen (EPR) paradox [36], formalized in terms of a local hidden variable model (LHVM) assumption by Bell [48]. In addition, Schrödinger noticed that entanglement allows for the situation where the entropy of a full system might be larger than the entropy of its constituents and proclaimed that 'the best possible knowledge of a whole does not include the best possible knowledge of its parts - and this is what keeps coming back to haunt us' [35]. This feature can already been seen in the simple Bell state $|\phi^+\rangle$ where the total state is pure while each subsystem alone is (maximally) fluctuating. It later has been called 'Schrödinger's demon' [37] and is an important property of entanglement used for characterization and quantification.
Before continuing with quantifying entanglement, I would like to point out a few active research areas where the study of entanglement is central:

- **Bell and nonlocality test:** Based on the EPR paradox, Bell proved that quantum physics formally is incompatible with a hypothetical LHVM which would avoid the EPR paradox [48]. He conceived an afterwards called Bell inequality based on correlation measurements which is not allowed to be violated within a LHVM. Afterwards, the inequalities were further refined and tailored for experimental testing with the most notable example being the CHSH inequalities [49]. The first stringent violations of the Bell inequalities were performed by Aspect et al. [50], with a plethora of further important experiments either refining these results by closing so-called loopholes (for example see [51–55]), applying the concepts to quantum optics (for example [56]) or finite mass systems [24–26, 57, 58].
- **Quantum information and cryptography:** Quantum information evolved as a whole research field with entanglement used as a resource. For an overview see [37–39]. Early works include for example the no-cloning theorem [59]. Among other things, entanglement is used for teleportation [60, 61], quantum cryptography and key distribution [62, 63], dense coding [64, 65], error correction and computational tasks [66–69].

- **Study of many-body quantum systems**: Entanglement is also a key ingredient in studying the behaviour of many-body quantum systems. In general this is an exceedingly complicated endeavour. However, the increasing control over microscopic constituents in such systems, as I will discuss in detail later, allows for more and more entanglement studies. In particular quantum phase transitions are accompanied by a change in quantum correlations as quantified by entanglement [40, 70]. This is of special importance for topological states which are not described by local quantities or order parameters [71–74]. In addition, the important question of information spreading (or its absence in a many-body localized system) are intrinsically linked to entanglement properties [42–46].

- **Quantum metrology:** Non-classical (that is entangled) states can be used to limit intrinsic quantum noise in a metrology task by *squeezing* down the uncertainty in one quadrature component below the standard quantum limit at the cost of increasing the other (see [75, 76]).

In this thesis I am not aiming at testing quantum mechanics at an fundamental level as done for example in increasingly more involved Bell measurements. Instead, the relevant question will be whether a prepared quantum state, which we will characterize by correlation measurements, can be certified not to be formed by classical correlations alone. In this situation we will conclude that there has to be more to it, in the sense that pure quantum correlations have to be present. Those can be quantified by entanglement.

2.1.1. Quantifying entanglement

An important idea on quantifying entanglement is based on its usefulness for quantum communication [38]. This is referred to as the operational approach and treats entanglement as a resource. It was first introduced for a pure two-qubit system, where the basic task is to transfer a bit of information between two parties (usually labelled Alice and Bob). For this an entangled *e-bit*, given by the two-qubit Bell state $|\phi^-\rangle = \sqrt{\frac{1}{2}}(|00\rangle - |11\rangle)$, which can be interpreted as maximally entangled, is first shared between Alice and Bob and afterwards the actual information is transmitted via quantum teleportation [60, 61]. For a faithful teleportation we need the state $|\phi\rangle$, which is shared between Alice and Bob, to be exactly the e-bit, that is maximally entangled. This is usually not the case as any quantum transmission channel will always be noisy. Therefore, a purification stage has to be implemented. With this we might still be able to extract m_n e-bits

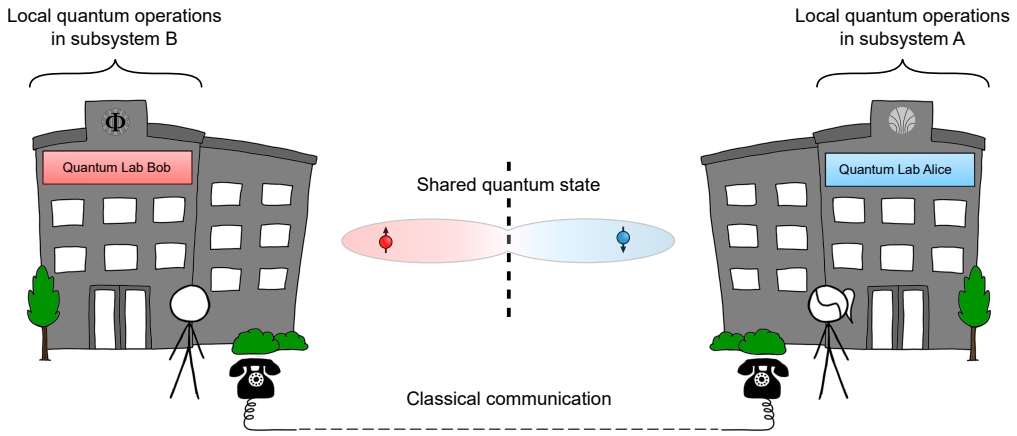

Figure 2.1.: **Quantum communication scheme.** A schematic illustration of the LOCC scheme. Alice and Bob first share a number of e-bits via a noisy quantum channel. Afterwards they are allowed to perform local quantum operations on their respective subsystems and communicate any instructions and strategies on LO to be performed and also measurement results through a classical communication channel. It is implicitly assumed that long range communication via the quantum channel is much more costly than local quantum operations and classical communication. The task at hand is now to use the shared entanglement for quantum communication. This means the entanglement is used as a resource for example for quantum teleportation. Equivalently this can also be used as a positive definition of entanglement: Given a certain shared state; how useful is it for a quantum task?

out of n identical shared states $|\phi\rangle$, by an adequately chosen distillation protocol based on so-called LOCC operations (see figure 2.1). These combine local quantum operations (LO) with classical communication (CC). Given a specific partitioning of the quantum system, LO describe generalized quantum operations on either of the subsystems. These can include applying unitary operations on the state, performing joint operations with a local ancillary state and projective measurement protocols. In addition, classical bits of information are allowed to be transmitted at any point by CC between the subsystems. Importantly, the concept of LOCC is not only relevant for technological purposes but can also be used to quantify entanglement. This is based on the fact that entanglement between the subsystems cannot be created by LOCC operations such that classical correlations are defined as those created by LOCC operations alone [38]. The other way around, if a target state, which cannot be simulated by classical correlations, is created out of an initial state (pure or mixed) by LOCC operations it can be concluded that already the initial state was entangled [77, 78]. This is the basis of entanglement quantification.

Coming back to the above communication task, for a fixed purification protocol, the distillation rate is obtained as the limit of $\lim_{n\to\infty} \frac{m_n}{n}$ and the *distillable entanglement* E_D as the supremum over all possible protocols. There also exist generalizations of this measure for mixed density matrices [79] and multipartite systems [80].

Here we have measured entanglement based on a very specific task. Therefore we will encounter equivalent notions which should not be confused: An entanglement measure can be classified based on its strictness. This means, a measure which is not perfectly strict might detect only certain states as entangled, while it misses others. On the other hand a specific (and not perfectly strict) measure also allows us to classify different types of entanglement. In the above example we detected distillable entanglement alone. It has been found [37] that in general there might be also *bound entanglement* present which cannot be used for teleportation. Thus distillable entanglement is in general only a sufficient but not a necessary condition for entanglement. However, for a quantum information task as described above, only this subset of entanglement is useful, such that the classification into distillable entanglement is of great practical interest.

As a dual measure to the distillable entropy E_D, there is also the concept of the entanglement cost E_C, which measures how many e-bits are at least (on average) needed to construct the above state $|\phi\rangle$ using LOCC. For a pure state the entanglement cost and the distillable entanglement are equivalent. This is not the case for a mixed state.[2]

The above measures are based on usefulness for a specific task. Note that this is fundamentally different to the negative definition of an entangled state being not separable [81]. In addition to the operational approach it is also possible to define a measure based on an axiomatic approach [37, 38, 82–84]:

- **A separable state has zero entanglement.** A fully separable state $\rho_{ABC\cdots}$ in a density matrix representation and the partitioning $ABC\cdots$ is defined to be separable if it can be written in the form

$$\rho_{ABC\cdots} = \sum_i p_i \rho_A^i \otimes \rho_B^i \otimes \rho_C^i \otimes \cdots \tag{2.3}$$

  in terms of a probability distribution p_i and ρ_X^i a state in the subsystem X. Importantly, all these states can be trivially created by LOCC alone due to the separable nature of the state. Thus it is postulated that all these states have zero entanglement.

[2] Note the similarity to a thermodynamic cycle, which has a finite efficiency. Similarly the cycle of distillation and formation has a limited efficiency for a mixed state.

- **Entanglement monotone [82].** Via LOCC operations, entanglement cannot increase [85]. Put more colloquially, the resource which is entanglement cannot be distilled out of thin air. From this postulate, it also directly follows that entanglement is invariant under local unitary operations (while for a general LOCC it might decrease). In addition for any bipartite state this implies that there exists only one maximally entangled state (the Bell state) out of which each mixed state can be created.

- **Other postulates.** A common additional postulate for bipartite entanglement is normalization which demands that the measure *counts* the number of e-bits, that is the measure is equal to n for a product state of n Bell pairs. A generalization to multipartite entanglement is not easily possible due to the lack of a unique target state. Other commonly used postulates are based on *continuity* and *convexity* [37] but are not strictly necessary for a closed axiomatic definition of entanglement.

This axiomatic approach allows us to directly detect entanglement with a measure which is non-zero only if entanglement is present. However entanglement can also be quantified by establishing an order such that ρ is more entangled than σ if the transformation $\rho \to \sigma$ is possible via LOCC (but not the other way around). This approach again has no straightforward generalization for multipartite systems due to the lack of a unique reference state. An overview of typical measures based on this axiomatic approach is presented for example in [37], with the important generalization to mixed states also covered in [86].

2.1.2. Multipartite entanglement

The most important difference between bi- and multipartite entanglement is that only in a bipartite system there exists a unique (up to local unitary transformations) maximally entangled state. For a $2 \otimes 2$ system we have already called this state e-bit, and similarly for a $d \otimes d$ system we have

$$|\phi_d^+\rangle = \frac{|0,0\rangle + |1,1\rangle + \cdots + |d-1,d-1\rangle}{\sqrt{d}} \tag{2.4}$$

This statement can be justified by showing that any pure or mixed state can be distilled out of $|\phi_d^+\rangle$ by LOCC alone. This becomes more complicated in higher dimensions. For example in tripartite systems (using here $2\otimes2\otimes2$ as an example) there are already 6 different classes of states: The completely unentangled state, three combinations of a product state of an e-bit with an additional qubit, the

Greenberger-Horne-Zeilinger (GHZ) state [87]

$$|GHZ\rangle = \frac{|000\rangle + |111\rangle}{\sqrt{2}} \tag{2.5}$$

and the W state [88]

$$|W\rangle = \frac{|001\rangle + |010\rangle + |100\rangle}{\sqrt{3}}. \tag{2.6}$$

These states cannot be converted into each other by local unitary operations. Also in terms of entanglement, they differ [88, 89]. To see this we have to introduce the notion of partial separability. Building on the definition of separability in 2.3, a d-partite system is defined to be k-separable if a new partitioning into $k \leq d$ subsystems can be found, such that the state can be written as a product state. Inverting this notion, the state is defined to be (at least) k-partite entangled, if such a partitioning cannot be found. In the above example the $|GHZ\rangle$ and the $|W\rangle$ state are three-partite entangled, while for the product state of a singlet with an additional qubit we, per definition, find a two-separable state such that we are left with bipartite entanglement. On top of this also the two tripartite states are fundamentally different, as they cannot be transferred into each other by local unitary operations.[3]

As a consequence, in general it can be hard to fully extend the measures to multipartite states as a unique target state (e-bit) is lacking. Typically we have to carefully choose which state we compare to. For example we might compare to the product state and thus identify entanglement without being able to differentiate between two-partite and multipartite entanglement. More in general we will oftentimes encounter measures able to quantify entanglement which is at least k-partite. All these measures can be arbitrarily hard to compute. Therefore an important task is to find measures which are of practical use.

2.1.3. A few important measures

Measures of particular importance for this thesis include:

- **Entanglement entropy:** The entanglement entropy on a partition A is defined via the Rényi entropy (of order α) $S_\alpha(\rho)$ as $S_\alpha(\rho_A)$, where ρ_A is the reduced density matrix of subsystem A. An entanglement measure can now be constructed by comparing the entanglement entropy of the given state to

[3] Note that the state $|W\rangle$ is in a certain sense more robust, as after measuring one qubit the remaining state is at least bipartite entangled which is not the case for the $|GHZ\rangle$ state.

that of a target state. Importantly, for a two-partite pure state, the distillable entanglement reduces to the entanglement entropy [90]. Intuitively this can easily be seen as a shared Bell state results in a maximum uncertainty of the measurement outcome in either subsystem and thus maximizes the entropy. Therefore the entanglement entropy can be interpreted as a quantification of Schrödinger's demon discussed above, quantified for example by introducing the conditional entropy $C(A|B) = S_\alpha(\rho_{AB}) - S_\alpha(\rho_B)$. For a mixed bipartite state we can use the conditional entropy as a lower bound to the distillable entanglement [86, 91].

- **Negativity:** The negativity is a measure of practical interest because it can be computed efficiently. For a density matrix ρ it is defined as

$$\mathcal{N}(\rho) = \frac{||\rho^{T_A}|| - 1}{2}, \tag{2.7}$$

in terms of the partial transpose ρ^{T_A} with respect to the partitioning A and the trace norm $||\cdot||$. For $2 \otimes 2$ and $2 \otimes 3$ systems the negativity is a sufficient and necessary condition for entanglement [92, 93]. Also for larger systems it remains sufficient but is no longer necessary. The importance of the negativity is mostly due to the fact that the computational complexity is reduced to the computation of eigenvalues of a density matrix.

- **Concurrence:** The concurrence can be used as a measure for the so-called entanglement of formation [94–97], which is closely related to the entanglement cost (albeit not the same [37]). For a pure state it is defined as $C = \sqrt{2\left(1 - \mathrm{Tr}\rho_A^2\right)}$ in terms of a reduced state ρ_A. It is mostly important for two qubit systems where an isomorphic map to the entanglement of formation exists. In this case we can define the concurrence of a pure state ϕ as $C(\phi) = |\langle\phi| \sigma_y \otimes \sigma_y |\phi^*\rangle|$ in terms of the Pauli y-matrix. For a mixed state we instead have to compute the infimum over all pure state decompositions such that $C(\rho) = \inf \sum_i p_i C(\phi_i)$. Importantly (and only for a two qubit system) there is also an explicit formula given by

$$C(\rho) = \max\left\{0, \lambda_1 - \lambda_2 - \lambda_3 - \lambda_4\right\}, \tag{2.8}$$

where λ_i^2 are the eigenvalues of the operator $\rho\left(\sigma_y \otimes \sigma_y\right)\rho^*\left(\sigma_y \otimes \sigma_y\right)$ in decreasing order.

2.1.4. Entanglement witnesses

Calculating an entanglement measure can be a very hard task. From a theoretical point of view, ruling out that any decomposition of a general mixed state separates is in general an NP-hard problem. Also from an experimental point of view we encounter an exponential scaling in the number of measurements needed as typically the full quantum state has to be known tomographically. One approach to limit the computational or experimental complexity is to consider an entanglement witness instead of a measure [92, 98]. An entanglement witness is a functional which is able to detect *some* entanglement, without however strictly being able to quantify entanglement, as schematically illustrated in figure 2.2. More formally we define the hermitian operator W to be a witness if for all separable states ρ we have $\mathrm{Tr}\{W\rho\} \geq 0$ but in turn there exists at least one state σ such that $\mathrm{Tr}\{W\sigma\} < 0$. Important witnesses include the CHSH (Bell) witness and also the negativity for larger quantum systems.

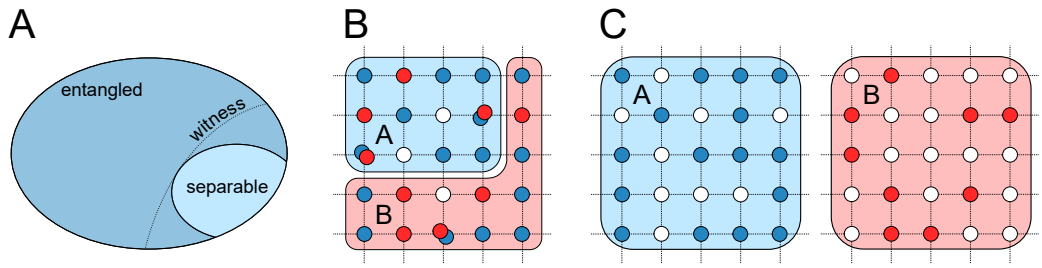

Figure 2.2.: **Measuring entanglement. A:** The full Hilbert space of a composite system can be separated into entangled (darker blue) and separable (lighter blue) states. A witness can certify that a given state is not separable, but on the other hand is not a necessary condition for entanglement. **B:** Mode partitioning: The system made up of different internal states used as particle labels (indicated by red and blue circles) in different external modes (crossing points of the dotted line) can be partitioned according to a specific boundary in-between the modes. Alice takes control over the subsystem A (blue shaded area) and Bob over subsystem B (red shaded area). **C:** Particle partitioning: The same system can be partitioned according to the internal state, where Alice takes control over the subsystem A of all blue particles and Bob takes control over the subsystem B of all red particles. Adapted from [99].

2.1.5. Particle vs mode entanglement and the role of symmetrization

Up to now the partitioning used was not explicitly specified, despite the notion of entanglement strongly depending on how the partitioning is chosen. Often times in literature, in particular in a quantum communication context, implicitly a partitioning according to particle labels is used (see figure 2.2). This is emphasized in literature by the personifications, Alice and Bob, used as labels. More precisely, particles or systems of particles, which are distinguishable by external parameters ('send to Alice/Bob') are used as the partitioning, where in turn some internal quantities (state 1 or state 0) are entangled. A prominent physical example is the decay of a spin 0 particle into two spin-1/2 particles. The total state of the two spin-1/2 particles has to be the singlet (that is the Bell state) while their relative momentum is diametral, such that we can identify the particle sent to one half-sphere as Alice's particle and the other one as Bob's.
There is a conceptual problem arising as soon as we have to consider the exchange symmetry. Consider for example the state of two indistinguishable fermionic particles in two distinct (spatial) modes. I will call the two modes in this case $|0\rangle$ and $|1\rangle$, to emphasize the connection to the above examples. Within a first quantized picture, we have to label the identical particles, which I will do as above as Alice for the first particle and Bob for the second. The price we have to pay for introducing labels to the indistinguishable particles is that we have to antisymmetrize the state by hand. Thus the state is given by

$$|\phi\rangle = \sqrt{\frac{1}{2}} \left(|1\rangle \otimes |0\rangle - |0\rangle \otimes |1\rangle \right). \tag{2.9}$$

At least formally this is a Bell state and (maximally) entangled. It is a long-lasting debate in literature if this non-separability which can be seen as an artefact of the antisymmetrization should be considered entanglement and if it can be used as a resource [100–113]. This topic will be discussed in more detail in section 6.4.
Particle entanglement is however not the only possible partitioning. We could also study entanglement in a mode partitioning. As an example we might have an ensemble of particles in an array of spatial modes (think for example of neutral atoms in an optical lattice [41, 114, 115], see also figure 2.2). This is particularly useful for delocalized particles. It is possible to partition the system according to the different modes and detect for example correlations in the particle occupation (or any other observable quantity) between the different modes [24]. Interestingly, as a pathological limit, already a single particle delocalized over several modes

features mode entanglement. As an example, one particle delocalized in two spatial modes could be written down as

$$|\phi\rangle = \sqrt{\frac{1}{2}}\left(|10\rangle + |01\rangle\right) \tag{2.10}$$

which at least formally is a Bell state. This is not restricted to position space. Also a spatially localized particle shows mode entanglement when the momentum modes are used as a partitioning. Intuitively it is not too surprising that we observe entanglement, as we can always map the two-level system given by the mode occupation number to a spin-1/2 system. The spin state is now entangled by the delocalization in conjunction with the atom number conservation. As with the identical particle entanglement above, it is also in this case crucial to identify the usefulness of such a mode entanglement [116, 117]. I will discuss mode entanglement in chapter 6 as well.

2.2. Correlation functions and the density matrix

A convenient way to represent a quantum mechanical state is the density matrix ρ. In order to write it down, the full set of information on the state has to be known. Determining all the entries of a density matrix describing a complicated many-body state can be a very demanding task. The experimental approach used in this thesis will be based on the measurement of correlation functions. Therefore, in this section, I will introduce the relevant basic notion on the density matrix and correlation functions. For a more detailed discussion the reader is referred to the literature (for example [3, 34, 118]).

2.2.1. Density matrix

Suppose that we have initialized a quantum system in the a-priori unknown normalized state vector $|\Psi\rangle$. This state could either be pure or mixed, such that $|\Psi\rangle = \sum_i p_i |\Psi_i\rangle$. We can define the density operator via

$$\hat{\rho} = \sum_i p_i \left|\Psi_i\right\rangle \left\langle\Psi_i\right| . \tag{2.11}$$

The density operator is a very useful concept as it greatly facilitates the notation of the quantum mechanical measurement process. For this we make use of the fact that the density operator is the projection operator onto the state $|\Psi\rangle$. Therefore, for a general observable $\mathcal{A}$, the expectation value of the measurement associated

to $\mathcal{A}$ is

$$\langle \mathcal{A} \rangle = \mathrm{Tr}\left(\mathcal{A}\hat{\rho}\right), \tag{2.12}$$

with the probability of an individual measurement outcome p_a (assuming the existence of a spectral representation) given by

$$p_a = \mathrm{Tr}\left(\mathcal{P}_a\hat{\rho}\right), \tag{2.13}$$

where $\mathcal{P}_a$ denotes the projection operator onto the eigenstate corresponding to the eigenvalue a.
This access to the eigenspectrum also allows for a convenient notation of measures quantifying the statistical spread over the space of eigenstates for example by virtue of the purity as well as the entropy. The purity is given by

$$\gamma = \mathrm{Tr}\hat{\rho}^2. \tag{2.14}$$

The density operator of a pure state is idempotent such that in this case the purity is unity. For a general state the purity is a measure for how mixed the state is. In a similar fashion we can write down the von Neumann entropy via

$$S_{vN} = -\mathrm{Tr}\left(\hat{\rho}\ln\hat{\rho}\right) \tag{2.15}$$

and the Rényi entropy of order α given by

$$S_\alpha = \frac{1}{1-\alpha}\ln\mathrm{Tr}\hat{\rho}^\alpha. \tag{2.16}$$

For a finite dimensional Hilbert space (as will be always the case in this thesis), the density operator can be represented as a matrix. This density matrix corresponding to the orthonormal basis $|e_i\rangle$ is defined via the entries

$$\rho_{i,j} = \langle e_i|\,\hat{\rho}\,|e_j\rangle\,. \tag{2.17}$$

The diagonal entries $\rho_{i,i}$ quantify the populations, that is the probability that the eigenstate $|e_i\rangle$ measured. For a classical state, this is all the information needed, as the full state is an incoherent sum over the eigenstates. For a general quantum mechanical state we have to take coherent superpositions into account. These are included in the density matrix by the off-diagonal entries which therefore quantify the coherences in the system.

2.2.2. Correlation functions

Another very useful object in a perturbative approach to a quantum field theory is the n-point correlation function χ_n of the form

$$\chi^n\left(i_1, i_2, \cdots, i_n\right) = \langle\Psi|\, \phi^{(\dagger)}(i_1)\phi^{(\dagger)}(i_2)\cdots\phi^{(\dagger)}(i_n)\,|\Psi\rangle\,. \tag{2.18}$$

This object is the conditional probability of n field annihilation (creation) operators $\phi^{(\dagger)}(i_j)$ evaluated with respect to the state (e.g. ground state) $|\Psi\rangle$ of the system. The index i_j with $j \in [1, \cdots, n]$ indicates n different points of the fundamental basis. Typically, these are n different spatial positions x_i. Note that in this thesis, I will focus on equal time correlations alone. Therefore I will suppress any reference to the time and in particular neglect any specific time ordering which in general has to be included in the definition of the correlation functions. We can gain some intuition on these correlation functions by considering two specific examples:
The one point function $\chi^1(x_1) = \langle\phi(x)\rangle$ measures the expectation value of the field amplitude. Typically (and in particular for theories with number conservation incorporated), this is zero as the field fluctuations average to zero. The two-point correlator $\chi^2(x_1, x_2) = \langle\phi(x_2)\phi^\dagger(x_1)\rangle$ is called propagator or Green's function. It measures the correlation between the field fluctuations at point x_1 and x_2. For two independent locations, also the fluctuations are independent and the propagator evaluates to zero. For a finite distance between the positions, within the so-called correlation length, the fluctuations are at least partially correlated resulting in a finite expectation value. Studying the propagator and in particular the divergence of the correlation length at a second order phase transition is one central topic in many-body (field) theory.
More in general we can express any (conditional) probability of *something happening* as a correlation function. Of course this can, and in general will be, a quite complicated object. Therefore, much of the success of quantum field theory is based on the fact that in a perturbative fashion the full correlation function can be reduced to a series expansion of correlation functions with respect to the free theory (that is with $|\Psi\rangle = |\text{Vac}\rangle$). There exists a large machinery to efficiently evaluate this perturbative series. In particular the pictorial series expansion in terms of Feynman diagrams can help in keeping track of different terms contributing. For an introduction into this the reader is referred to the standard literature such as [118], or [34] for a more condensed matter inspired approach.
Experimentally, we do not have access to the field operators directly, and instead have to rely on measurements of observables. In analogy to 2.18 the nth order

correlation function C_n of a set of observables $\mathcal{A}_i$ is defined as the conditional probability

$$C^n\left(i_1, i_2, \cdots, i_n\right) = \langle\Psi|\, \mathcal{A}(i_1)\mathcal{A}(i_2)\cdots\mathcal{A}(i_n)\, |\Psi\rangle\,. \tag{2.19}$$

Again the index i_j typically indicates different spatial positions x_i. Experimentally the expectation value is approximated by averaging the measurement result either over many different realizations of the same state $|\Psi\rangle$ or by taking a suitable average over a large statistical ensemble. In this thesis we will exclusively use spatial densities as an observable, $\mathcal{A}_i = \hat{n}(x_i)$. In order to get access to a broader range of observables, we will use a tailored experimental toolbox in order to map different observables onto real space densities. I will present this toolbox in section 5.3. The most important example will be the momentum p or wave vector k, where $\mathcal{A}_i = \hat{n}(x_i(k)) \equiv \hat{n}_{ki}$.

I would like to stress that throughout this thesis I will discriminate between an nth-order correlation function C^n, and an n-point correlation function χ^n. For example an nth order density correlator is a $2n$-point correlation function in the fundamental fields. In addition we will always consider finite systems with a fixed particle number N. Therefore any perturbative expansion will naturally stop at Nth order. For very large systems, an effective description in terms of an infinite system will nevertheless oftentimes be useful.

There is a close connection between the entries of the density matrix and correlation functions. To this end, consider that (assuming a pure state for simplicity)

$$\rho_{i,j} = \langle e_i|\, \hat{\rho}\, |e_j\rangle = \langle e_i|\Psi\rangle\, \langle\Psi|e_j\rangle = \langle\Psi|e_j\rangle\, \langle e_i|\Psi\rangle = \langle\mathcal{O}_{i,j}\rangle_\Psi\,, \tag{2.20}$$

where the expectation value is taken with respect to the state Ψ and $\mathcal{O}_{i,j} = |e_j\rangle\, \langle e_i|$. Therefore, by measuring a suitable set of correlation functions we can indeed reconstruct the state operator, as of course expected for a reasonable perturbation theory. Note however, that in general the evaluation of 2.20 might involve complicated correlation functions of high order and in particular the complexity will strongly depend on the choice of basis.[4] It is a-priori not clear how to connect measured correlation functions of nth order to these density matrix entries. I will discuss this in detail in chapter 6.

[4] This is also not surprising at all. The success of a perturbation theory strongly depends on a proper choice of the initial guess upon which higher perturbation orders are added. Crucially one should therefore be careful when inferring the presence of *interesting* physics based on high-order correlations measured.

2.3. Interactions between neutral atoms

In this section I will discuss some basic scattering properties of neutral atoms. I will focus on very low energy and momentum scattering via a short range isotropic potential, suitable for the description of ultracold quantum gases of ^{6}Li (see also section 2.4). I will first introduce the generic description of ultracold scattering in free-space and later introduce a few important concepts needed for trapped systems.
The fundamental elastic interaction potential for neutral ^{6}Li is given by a short range van-der-Waals potential V_{int}. As the range R_{vdW} of the potential is only of the order of a few hundred picometers and thus much smaller than the typical interparticle distance and the de-Broglie wavelength of ultracold atoms, the description can be significantly simplified by a partial wave expansion.

2.3.1. Partial wave expansion

In the centre-of-mass frame and using spherical coordinates, the elastic scattering process is described by the time-independent Schrödinger equation

$$\left[\frac{p^2}{2m_r} + V_{int}(r)\right]\Psi(r) = E\Psi(r), \tag{2.21}$$

with the reduced mass m_r of the two scatterers. Here, it is used that the scattering potential is spherically symmetric. Asymptotically for $r \gg R_{vdW}$ this can be solved by a superposition of an incoming plain wave (without loss of generality in z-direction) and a scattered spherical wave with a relative phase shift (or scattering amplitude) $f_{\vec{k}}(\theta)$

$$\Psi_{\vec{k}}(\vec{x}) = e^{ikz} + \frac{e^{ikz}}{r} f_{\vec{k}}(\theta). \tag{2.22}$$

The phase shift is directly related to the differential cross section

$$\mathrm{d}\sigma/\,\mathrm{d}\Omega = \begin{cases} \left|f_{\vec{k}}(\theta)\right|^2 & \text{for distinguishable particles} \\ \left|f_{\vec{k}}(\theta) - f_{\vec{k}}(\theta+\pi)\right|^2 & \text{for identical fermions} \\ \left|f_{\vec{k}}(\theta) + f_{\vec{k}}(\theta+\pi)\right|^2 & \text{for identical bosons.} \end{cases} \tag{2.23}$$

The scattering amplitude can be expanded in Legendre polynomials P_L, which is known as the partial wave expansion

$$f_{\vec{k}}(\theta) = \frac{1}{k}\sum_{L=0}^{\infty}(2l+1)e^{i\delta_L}\sin\delta_L P_L(\cos\theta). \tag{2.24}$$

The expansion coefficient δ_l can be interpreted as the phase shift which each partial wave, corresponding to a relative angular momentum L, acquires in the scattering process.
At low temperatures, only a few expansion orders have to be taken into account as higher angular momentum partial waves have negligible weight in the range of the effective potential. In particular for the ultracold systems considered in this thesis, only s-wave, that is $L = 0$ scattering has to be considered,[5] resulting in the s-wave scattering amplitude

$$f(k) = \frac{1}{k\cot\delta_0(k) - ik}. \tag{2.25}$$

Importantly, s-wave scattering for identical fermions is in conflict with the requirement of an antisymmetric relative wave function. Therefore, in accordance with equation 2.23, identical ultracold atoms are non-interacting and the lowest possible scattering order is of p-wave nature.
For ^{6}Li, at least in the regimes described in this thesis, we can further simplify equation 2.25 by an expansion of $k\cot\delta_0(k)$ to lowest order in k

$$f(k) = -\frac{1}{a^{-1} + ik}, \tag{2.26}$$

where the s-wave scattering length a is defined via $f(k \to 0) = -a$. The above equation has the two important limits of weak interactions $k|a| \ll 1$ where $f = -a$, and the unitary regime $k|a| \gg 1$ where the scattering amplitude $f = \frac{1}{k}$ becomes independent of the scattering length. For this description and the energy scales considered, as we do not resolve the scattering potential, we can replace the scattering potential by a conceptually much simpler pseudopotential chosen such that the low energy scattering properties are reproduced. We thus have

$$V_{eff}(r) = g\tilde{\delta}(r), \tag{2.27}$$

in terms of a suitably renormalized delta function and the scattering parameter $g = \frac{4\pi\hbar^2 a}{m}$. In addition, to gain some intuition on the scattering length, we can

[5] That is as long as other channels are not resonantly enhanced.

calculate the interaction shift on the mean field level of a homogeneous gas with density n to be

$$E_{int}(a) = gn = \frac{4\pi\hbar^2 n}{m}a. \tag{2.28}$$

In a similar approximation we can estimate the interaction shift of two (weakly interacting) distinguishable particles in the same spatial mode described by the wave function $\Psi(\vec{x})$ to be

$$U = \int \mathrm{d}\vec{x}|\Psi(\vec{x})|^2 g. \tag{2.29}$$

In both cases a positive scattering parameter results in an increased interaction energy, while a negative value reduces the energy. Based on this intuition we will call $a > 0$ ($a < 0$) repulsive (attractive) interactions.
The s-wave interactions support a single dimer bound state for any positive scattering length with a binding energy of [119]

$$E_B = \frac{\hbar^2}{2m_r a^2}. \tag{2.30}$$

There is no dimer state present in the spectrum for attractive interactions. For a very large repulsive interaction strength, the dimer binding energy becomes very small and accordingly the size of the molecule is large. Upon decreasing the scattering length, the dimer becomes more deeply bound and the size decreases until it is ultimately not resolved by typical momenta of the system. In this limit, the dimers can be described as effective point-like bosonic particles with an atom-dimer scattering length of $s_{ad} \approx 1.18a$ [119] and a dimer-dimer scattering length of $a_{dd} = 0.6a$ [120].

2.3.2. Scattering and pairing in lower dimensions

In the previous section I have discussed scattering properties of two particles in three dimensions. A similar analysis can be performed also in one and two dimensions. For a useful description of an experiment, however, we also have to take the trapping potential into account, which is needed to confine the atomic system to lower dimensions. A trapping potential always introduces an additional length scale, which competes with the intrinsic scales in the system such as the scattering length, the (inverse) density, or the Fermi length scale. In addition, a trapping potential always breaks the translation invariance[6], such that for example in- and outgoing plane waves cease to be a useful description of the scattering

[6]For specific lattice potentials it might be argued that the continuous translation is merely replaced by a discrete one, however every experimental lattice has to be of finite size of course.

problem. There are three important limiting cases for the length scales of the trapping potential compared to the intrinsic scales of the system

- **Trapping potential $\gg$ scales of the system:** In this limit the trapping potential is almost constant on the system length scales. Therefore it is often times convenient to impose a local density approximation (LDA), where the system is locally mapped onto a homogeneous system with a chemical potential offset originating from the local trap potential. It is crucial to notice that such an approximation is bound to fail when one of the intrinsic scales diverges. The most important example is a correlation length diverging at a second order phase transition.

- **Several scales of a similar order:** When at least one of the length scales of the trapping potential is of a similar size as an intrinsic scale, the confining potential has explicitly to be taken into account. In particular the density of states is radically changed and resonance in the scattering process can appear.

- **Dimensional freeze-out:** Engineering systems with fewer than three spatial dimensions is, strictly speaking, only possible theoretically. However, it is possible to kinematically freeze out one or more spatial dimensions by engineering the confinement length to be much smaller than all kinematic length scales. In this case the system behaves kinematically according to a lower dimensional density of states. Note, however, that it might still be possible that the interaction scale becomes even smaller (for a deeply bound molecule), such that while the molecules are 3D objects, the motional states are still restricted to lower dimensions.

For all that is to follow, we will always assume that the confining potential is a three dimensional harmonic potential. In this regime, theoretical results in various different geometries exist [121–125]. In the experiment, as I will discuss below, we typically have Gaussian traps instead. Within a second order Taylor expansion, these traps can be approximated by a harmonic confinement. However, for a fully quantitative theory, the full trap geometry has to be taken into account. This is in particular the case for tightly confined traps: A useful figure of merit in this respect is the ratio of the harmonic oscillator length of the trap (quantifying the scale on which anharmonicity starts to play a role) to the size of the ground state wave function set by the trap frequency.[7]

[7] For the same trap frequency, a large deep trap is more harmonic than a tight but more shallow trap. However, the latter case requires less laser power and is less prone to aberrations.

The most important example of a potential in this thesis is a radially symmetric trap approximated by the functional form (in cylindrical coordinate $x = (\rho, \phi, z)$)

$$V_c(x) = \frac{1}{2} m \left(\omega_{rad}^2 \rho^2 + \omega_z^2 z^2 \right), \tag{2.31}$$

in terms of the radial (axial) trap frequency ω_{rad} (ω_z) with an aspect ratio $\eta = \omega_{rad}/\omega_z$. A large positive aspect ratio corresponds to a quasi-1D system, while a ratio well below one describes the quasi 2D scenario. Here, I will discuss solutions for two distinguishable particles. In the limit where the interaction length scale is small compared to the harmonic oscillator length scales $a_{rad,z}^{HO} = \sqrt{\hbar/(m_r \omega_{rad,z}))}$, the wave function can be approximated by the non-interacting ground state; for stronger interactions, the description in the non-interacting basis has to involve higher lying states as well.

An analytical solution is given in [124] with the generalizations to a general 3D harmonic oscillator potential added in [125]. Given two particles and harmonic confinement, the centre-of-mass coordinate can be decoupled. In the following only the relative motion (in the relative coordinate r with the relative mass m_r) is discussed. It should be kept in mind, however, that in an experimental setting the anharmonicities present will couple the relative and centre-of-mass motion. Due to the decoupling and the point-like interaction potential, only states where the relative wave function is finite at $r = 0$ are shifted in energy by interactions. These are the angular momentum states with $m = 0$.

In the following paragraph, I will quote the solutions for the eigenenergies in the case where the aspect ratio or its inverse is integer obtained in [124]. For more general solutions and the corresponding wave functions see [124, 125]. The eigenenergies are given by the implicit formula

$$-\frac{\sqrt{\pi} a_z^{HO}}{a} = \mathcal{F}(-\mathcal{E}/2). \tag{2.32}$$

Here the eigenenergy $\mathcal{E} = \frac{E - E_0}{\hbar \omega_z}$ is given in units of the harmonic oscillator energy with respect to the ground state energy $E_0/\omega_z = 1/2 + \eta$. For an aspect ratio $n > 1$, that is a cigar-shaped trap, and in terms of the Gaussian hypergeometric function $F(a, b; c; d)$ and the Euler gamma function $\Gamma(x)$, $\mathcal{F}(x)$ is given by [124]

$$\mathcal{F}(x) = -2\sqrt{\pi} \frac{\Gamma(x)}{\Gamma(x - 1/2)} + \sqrt{\pi} \frac{\Gamma(x)}{\Gamma(x + 1/2)} \sum_{m=1}^{n-1} F(1, x; x + 1/2; e^{i \frac{2\pi m}{n}}). \tag{2.33}$$

For a very large aspect ratio, this result can be compared to the true 1D result already obtained in [121]. In terms of the 1D interaction potential $V_{int}^{1D}(x) =$

$g_{1D}\delta(x)$ the 1D solution is given by:

$$-\frac{1}{g_{1D}} = \frac{m_r}{2\hbar^2}\frac{\Gamma(-\mathcal{E}/2)}{\Gamma(-\mathcal{E}/2+1/2)}. \tag{2.34}$$

In [122], by comparison to the limit of equation 2.33 for very large aspect ratios it was shown that

$$g_{1D} = \frac{2\hbar^2 a}{m_r \left(a_{rad}^{HO}\right)^2}\frac{1}{1-Ca/a_{rad}^{HO}}. \tag{2.35}$$

In this formula $C = -\zeta(1/2) \approx 1.46$ in terms of the Riemann zeta function ζ. This is a very important result as it gives the proper renormalization of the 1D interaction parameter. In particular, we see that a confinement-induced resonance appears when the scattering length approaches the confinement scale. In addition, the resonance is shifted away from its bare position ($|a| \to \infty$) by the renormalization.[8] In figure 2.3, the energy levels of a quasi-1D system are presented and compared to the true 1D solution.

Based on equation 2.32, also the results for a quasi-2D system can be calculated. For an inverse aspect ratio $1/\eta = n$ the energy levels are determined by [124]

$$\mathcal{F}(x) = -2\frac{\sqrt{\pi}}{n} = \sum_{m=0}^{n-1}\frac{\Gamma\left(x+\frac{m}{n}\right)}{\Gamma\left(x-\frac{1}{2}+\frac{m}{n}\right)}. \tag{2.36}$$

Similar to before, we can now also compare equation 2.36 to the solutions obtained in a true 2D setting. In this case I will present it in a little more detail as it will be explicitly used in section 3.1. Additional background and an in-depth overview of the calculations can be found in [126] and references therein.

Again, we will start by a partial wave expansion which in 2D results in

$$f_l(k) = \frac{-4}{\cot\delta_l(k) - i}, \tag{2.37}$$

[8] A small excursion: It is interesting to compare this to the situation of (high energy) quantum field theories and the standard model. Also for these fundamental models, we have to regularize and renormalize the parameters of the model. This is done by fixing a set of parameters (for example a particle mass) to an experimentally determined value. Here we do the same thing: We fix the unknown g_{1D} by comparison to the binding energy (which is nothing but the excess mass of our composite system) determined by equation 2.33. The only difference is that as we discuss here a highly effective theory, we know the underlying microscopic theory and are - in principle - able to calculate the binding energy, while in high energy physics, theories describing the physics above the Planck scale are still to be found and the particle mass has to be experimentally measured.

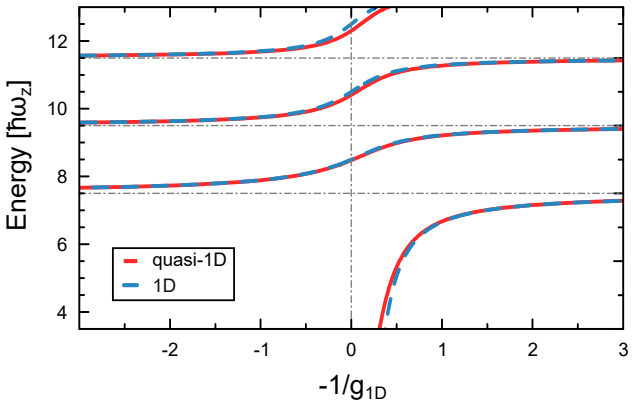

Figure 2.3.: **Energy levels in 1D.** Shown are the lowest eigenenergies of an interacting two-body system in a cigar-shaped trap as a function of the inverse 1D interaction strength calculated based on equation 2.35. An aspect ratio of $\omega_z/\omega_{rad} = 1/7$ is assumed. The quasi-1D solution according to equation 2.33 (red line) is compared to the true 1D limit according to equation 2.34 (blue dashed line). The 1D limit is a good approximation outside of the strongly interacting regime $-1 < 1/g_{1D} < 1$ for all energy levels except of the dimer state. Note that the energy is given with respect to the vacuum ground state such that the lowest non-interacting state has a ground state energy of $7.5\hbar\omega_z$. The true 1D solution is offset in energy accordingly.

with the differential cross section for distinguishable particles given by

$$\frac{\mathrm{d}\sigma}{\mathrm{d}\theta} = \frac{|f(k)|^2}{8\pi k}. \tag{2.38}$$

As before it suffices to consider the s-wave channel together with a low energy scattering process such that we can expand for a low k, resulting in

$$\cot \delta_0(k) = -\frac{2}{\pi} \ln\left(1/ka_{2D}\right) + \mathcal{O}(k^2). \tag{2.39}$$

In the above formula, the positive 2D scattering length a_{2D} was introduced. Before renormalizing the 2D scattering length by comparison of the above formula to the 2D limit of equation 2.36, I would like to point out a few observations. First of all, the scattering length appears here in the for of a logarithm. Therefore, if we want to describe the interaction strength using a dimensionless interaction parameter, the canonical choice is to use $\ln(ka_{2D})$ instead of ka in the 3D case. This will be heavily used in section 3.1, where, in terms of the *typical* momentum scale of the Fermi momentum k_F, the interaction regime is specified by $\ln(k_F a_{2D})$. Note that this quantity has the intuitive interpretation as the (logarithm of the) ratio between the scattering length and the interparticle spacing which is given

by $\frac{\sqrt{4\pi}}{k_F}$.
In addition, it can be seen that the definition of a_{2D} according to equation 2.39 is reasonable, as the binding energy is given by

$$E_B = \frac{\hbar^2}{2m_r a_{2D}^2}. \tag{2.40}$$

This is the same formula obtained already for the 3D case. The crucial difference is that a_{2D} is always positive such that a bound state is supported for any scattering length. Among other implications (see also section 3.1), an immediate consequence is that a unitary regime as in 3D does not exist in lower dimensions due to the additional length scale of the binding energy.
In [126] the renormalization of the scattering length in a quasi-2D scenario is performed. In terms of the 3D scattering length and the axial confinement length we arrive at

$$a_{2D} = a_z^{HO}\sqrt{\frac{\pi}{A}}e^{-\sqrt{\frac{\pi}{2}\frac{a_z^{HO}}{a}}}, \tag{2.41}$$

where $A \approx 0.905$. This can be also inverted to arrive at an implicit equation for the binding energy

$$\frac{a_z^{HO}}{a} = \int_0^\infty \frac{\mathrm{d}u}{\sqrt{4\pi u^3}}\left(1 - \frac{e^{-\frac{E_B}{\hbar\omega_z}u}}{\sqrt{\frac{1}{2u}\left(1-e^{-2u}\right)}}\right) \tag{2.42}$$

In figure 2.4, the binding energy of the dimer in the 3D as well as the 2D limit is shown together with the quasi-2D solution. In addition, also the energy levels for two particles in a harmonic quasi-2D trap are presented.

2.3.3. Many-body physics

The discussions in this chapter were up to now limited explicitly to few-body systems. In this section I would like to present a few relevant concepts of many-body physics, in particular related to two dimensions and low temperature behaviour. Importantly, many concepts introduced up to now, such as two-body bound states, will still play a major role also in the many-body context. For simplicity, I will restrict the discussion to homogeneous systems and balanced two-component Fermi gases alone. This step will be a-posteriori justified by a local density approximation in the context of the experiments presented in chapter 3. For additional details, the reader is also referred to [34, 119, 126, 127].
First of all we have to derive the relevant thermodynamic parameters. Given the density n of a single spin component, the Fermi energy E_F can be defined in 3D

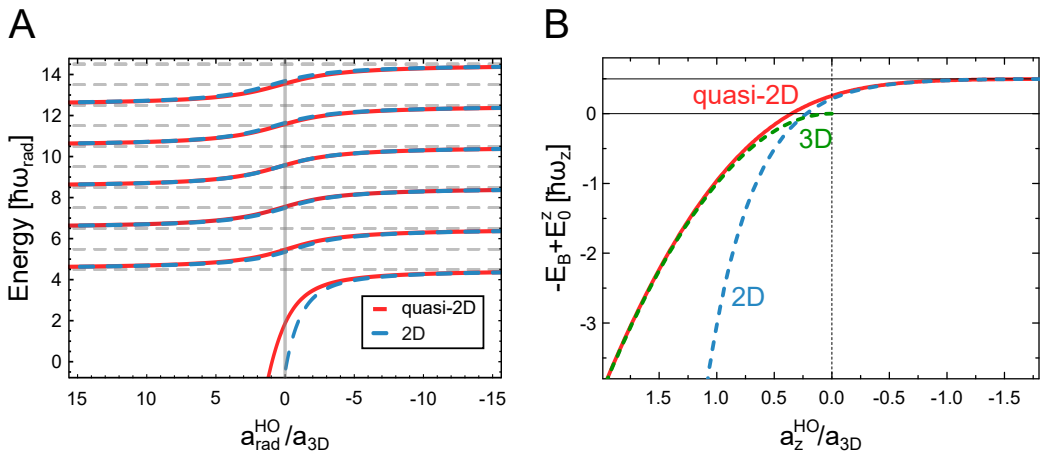

Figure 2.4.: **Energy levels in 2D. A:** Lowest eigenenergies of an interacting two-body system in a harmonic trap with $\omega_z/\omega_{rad} = 7$ as a function of the inverse 3D scattering length and in units of the inverse radial harmonic oscillator length. The quasi-2D solution (red line) according to equation 2.36 can be compared to the true 2D solution (blue dashed line) and the non-interacting energy levels (gray dashed line). The 2D limit is a good approximation outside the strongly interacting regime for all energy levels except for the dimer state. Note that the energy is given with respect to the vacuum ground state such that the lowest non-interacting state has a ground state energy of $4.5\hbar\omega_z$. The true 2D solution is shifted in energy accordingly. **B:** Comparison of the bound state energy in the 3D (green dashed line), the 2D (blue dashed line) and the quasi 2D (red line) limit. In order to compare the different energies, they are offset by the harmonic oscillator ground state energy in axial direction. For a negative 3D scattering length a_{3D}, there exists only a dimer state in the 2D solutions. For a small negative scattering length, the quasi-2D solution is well approximated by the true 2D solution. In contrast, for a small positive scattering length the size of the quasi-2D dimer is smaller than the harmonic oscillator length such that the bound state is not much influenced by the confinement, and mostly given by the 3D solution, while the 2D dimer is much deeper bound due to the limited density of states. In the regime of a large scattering length the quasi-2D solution interpolates between the 2D and the 3D solution.

as $E_F = \frac{\hbar^2}{2m}\left(3\pi^2 n\right)^{2/3}$ and in 2D as $E_F = \frac{\hbar^2}{2m}4\pi n$. Based on this definition, the Fermi wave vector $k_F = \frac{\sqrt{2mE_F}}{\hbar}$ and the Fermi temperature $T_F = E_F/k_B$ can be obtained as well. Note that the Fermi energy will be used as a *typical* energy scale also in the limit where the two-body binding energy is large, $E_B \gg E_F$, such that a Fermi surface is not present any more. If the absolute temperature T and the scattering length a or a_{2D} are known, all low temperature thermodynamic quantities can be described as a function of the dimensionless relative temperature T/T_F and the respective dimensionless interaction parameter $1/(k_F a)$ in 3D

or $\ln(k_F a_{2D})$ in two dimensions.
In the following section, I will first point out a few important considerations concerning condensation, before also discussing (quantum) phase transitions more in general and introducing the important concept of the BEC-BCS crossover in three and two dimensions.

Condensation

In this section I will very briefly discuss the phenomenon of condensation. Special interest will be put on two-dimensional systems which are considered to be 'marginal' [126] in the sense that ordered phases are less robust than in higher dimensions due to the more pronounced role of quantum fluctuations, ultimately destroying any *true long range order*, while in 2D at least some *quasi long range order* is still possible at finite temperature [126, 128, 129].
A Bose-Einstein condensate in three dimensions is ultimately characterized by long range order (LRO). This means the system features finite coherence for arbitrarily large spatial distances. This can be quantified by the first order correlation function g_1

$$g_1(r) = \frac{1}{n} \langle \hat{\psi}^\dagger(r) \hat{\psi}(0) \rangle \,, \tag{2.43}$$

in terms of the operator $\hat{\psi}^\dagger(r)$ ($\hat{\psi}(r)$) creating (annihilating) a single particle at position r and density n. A second order phase transition into a long range ordered phase corresponds to a spontaneously broken symmetry of the Hamiltonian. In the case of a (zero temperature non-interacting) BEC this is the phase ϕ of $\hat{\psi}$ which is fixed to an arbitrary value such that $\hat{\psi} = \sqrt{n} e^{i\phi}$. As a consequence

$$g_1(r) \equiv 1, \tag{2.44}$$

signalling full long range coherence. A similar symmetry-broken phase is not possible in two dimensions at finite temperature as fluctuations destroy any phase coherence beyond the thermal de-Broglie wavelength λ_{dB}. Thus, the first order coherence decays, even in the degenerate limit, for large distances r at least exponentially with [129]

$$g_1(r) \approx e^{-r/l} \tag{2.45}$$

where l is directly related to λ_{dB}. The only way around is to introduce another competing length scale. This can be done by introducing repulsive interactions quantified by the interaction strength g. A suitable length scale is given by the healing length $\zeta = \frac{\hbar}{\sqrt{mgn}}$. Crucially, the interaction energy can be minimized by reducing density fluctuations on length scales larger than the healing length.

As a consequence, these density fluctuations are strongly suppressed in the limit where the interaction energy is larger than the thermal energy. Even in this regime, true long range order can be excluded on general grounds based on the so-called Mermin-Wagner theorem [128].[9] Nevertheless, a topological and thus not symmetry-breaking phase transition as described by the Berezinskii-Kosterlitz-Thouless (BKT) mechanism is still possible [130, 131]. Instead of true LRO, this mechanism allows for quasi long range order in the form of algebraically decaying coherence described by

$$g_1(r) = r^{-\eta}. \tag{2.46}$$

with $\eta = 0.25$ for a homogeneous system.
Starting at already small temperatures, density fluctuation beyond the healing length can be assumed to be already strongly suppressed. Thus, in a simplified model, we can again try to start from a superfluid wave function of the form [129]

$$\psi_s(r) = \sqrt{n_s} e^{i\phi(r)} \tag{2.47}$$

On general grounds, it is possible to show that thermally excited, low lying phononic modes will eventually destroy LRO for very large distances based on the two-dimensional density of states in consistency with the Mermin-Wagner theorem. However, it is instructive to study this model in a little more detail. Within the approximations made, all interaction effects only affect the phase beyond λ_{dB}. Therefore, the relevant excitations are low energy phononic modes as anticipated, but also vortex excitations corresponding to a phase circulation of $\pm 2\pi$. The latter excitation is possible due to the vortex being restricted in size to the healing length and thus only contributing short range density fluctuations. In the limit where only the smooth phase fluctuations have to be taken into account, the effective Hamiltonian on length scales above the healing length is given by

$$H_\theta = \frac{\hbar^2}{2m} n_s \int \mathrm{d}^2 r \, (\nabla\theta)^2 \, . \tag{2.48}$$

Based on this, the first order correlation function g_1 takes the form $g_1(r) = \langle e^{i(\theta(r)-\theta(0))} \rangle$ which evaluates to [129]

$$g_1(r) = \left(\frac{r}{\zeta} \right)^{-1/\left(n_s \lambda_{dB}^2\right)} . \tag{2.49}$$

[9] Stating that LRO at finite temperature is not allowed in a lower dimensional system featuring only short range interactions and a Hamiltonion with a continuous symmetry in the thermodynamic limit.

This is an example of algebraic quasi long range order. Based on the assumption leading to the structure of the Hamiltonian, it is clear that the BKT transition is driven by vortex excitations. A possible way to see this is by studying the free energy needed for the vortex creation. It can be shown [129] that the free energy needed for creating a vortex changes sign at $n_s\lambda_{dB}^2 = 4$. Therefore, for large phase space densities, vortex excitations cost energy and vortices of different sign (that is the direction of the phase winding) pair up. In this limit, phase fluctuations are suppressed at length scales above the vortex pair length of $\mathcal{O}(\zeta)$ such that 2.48 becomes a valid (approximate) effective model and quasi long range order is established. On the other hand, for smaller phase-space densities, free vortices can proliferate, and the phase coherence is *scrambled* on length scales above the healing length.

Mean field picture of a second order phase transition

Phases classify the macroscopic behaviour of matter [132]. Above, I have already discussed the example of condensation, where a specific form of order developes at a critical temperature. In general, we have to distinguish between thermal and quantum phase transitions. In the former case, the system changes its phase as a function of the temperature, and thus the transition is driven by thermal excitations [133]. Therefore, even though the individual phases have to be described in a quantum formalism, the transition is of a classical nature. In contrast, in a quantum phase transition the system changes its phase as a function of a parameter of the system (for example due to the competition between two intrinsic energy scales) and is thus driven by quantum fluctuations [134].
We can classify phase transitions based on the free energy, where an nth order phase transition is defined to be a transition where the nth derivative of the free energy shows a discontinuity. As a consequence, first order transitions involve latent heat (as for example seen in the vaporisation process), which is not the case any more for higher order transitions which are referred to as continuous. I will here focus on second order phase transitions which will be relevant in particular in chapter 7. Note that in this formalism, topological phase transitions (such as the BKT mechanism discussed above) are of infinite order and cannot be described within the framework of spontaneous symmetry breaking and local order parameters applied here. For a full theoretical discussion the reader is referred to [34, 118, 134].
Finite order phase transitions are accompanied by a spontaneous symmetry break-

ing, such that the ground state in the symmetry-broken phase has a lower symmetry than the underlying Hamiltonian. This mechanism gives rise to a (locally defined) order parameter, which takes a finite expectation value only when the symmetry is broken. I will illustrate this in one of the most basic, yet experimentally relevant, cases of a $U(1)$-symmetric Hamiltonian. I will use an effective and purely phenomenological low energy theory, the so-called Landau theory [135]. To this end the free energy F, linked to the (effective) action S of the system via $F = \frac{T}{V}S$, is expanded in powers of the order parameter. In a mean field approach, the order parameter in the $U(1)$ system is *guessed* to be the macroscopic wave function $\Psi(r) = |\Psi|e^{i\theta}$. Now, we can expand the static part of the action to lowest order, still reflecting the symmetry of the Hamiltonian [34]

$$S_{static}[\Psi] = \int \mathrm{d}^3 r \left(\xi|\nabla\Psi|^2 - r|\Psi|^2 + \frac{u}{2}|\Psi|^4\right). \tag{2.50}$$

As this model is purely phenomenological and generic for any $U(1)$ symmetric system, the parameters ξ, r and $u > 0$ are a-priori unknown and have to be determined by comparison to a microscopic model. In order to calculate the expectation value of the order parameter, we have to minimize the free energy with respect to Ψ. Crucially the expectation value, and thus the ground state properties, depend on the sign of r. When $r < 0$ we obtain $\langle\Psi\rangle = 0$, and the symmetry is preserved. On the other hand, for $r > 0$, we have $|\langle\Psi\rangle| = \frac{r}{u}$. Therefore we have identified $r = 0$ as the critical point. Based on the construction of Ψ as a macroscopic wave function, we can interpret the expectation value $\langle\Psi\rangle_{r>0} =: \Psi_0 = \frac{r}{u}$ as the condensate density. Here, without loss of generality $\theta = 0$ was chosen. This process of symmetry breaking can also be visualized by defining a mean field potential of the order parameter based on the above action via

$$V(\Psi) = -r|\Psi|^2 + \frac{u}{2}|\Psi|^4. \tag{2.51}$$

This potential is shown in figure 2.5. It has its minimum at zero for $r < 0$, while the minimum is shifted to finite values for $r > 0$.

In this thesis, I will at several instances discuss fundamental excitations on top of the ground state. We might be tempted to directly infer the nature of the modes based on this mean field potential. For example, the shape of the potential suggests two (to lowest order) uncoupled modes: A gapped (that is of finite energy for $k \to 0$) amplitude mode and an ungapped phase mode corresponding to oscillations in $|\Psi|$ and θ respectively. While this naive approach certainly helps to gain intuition, it has to be kept in mind that it is based on the static part of the action alone, and thus not capable of correctly predicting excitations on top of

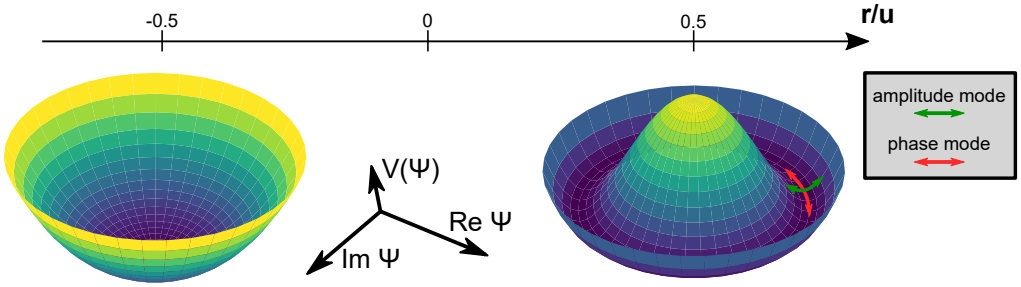

Figure 2.5.: **Mean field potential.** The mean field potential $V(\Psi)$ of the order parameter Ψ can be extracted from the static part of the action. The potential is shown for a fixed $u = 2$, assuming $r = -1$ (left panel) and $r = 1$ (right panel). For $r < 0$, the minimum of the potential is at zero, such that the ground state reflects the symmetry of the potential. For $r > 0$, the minimum of the potential is at a finite $|\Psi_0| = \frac{r}{u}$, such that the ground state with a spontaneously chosen fixed phase θ has a lower symmetry than the potential. Indicated, based on a fixed $\Psi_0 = \frac{r}{u}$ with $\theta = 0$, are oscillations in the phase θ (phase mode, red arrow) and amplitude $|\Psi|$ (amplitude mode, green arrow). Upon varying the phase the potential stays constant, such that a massless (Goldstone) mode might be anticipated, while by varying the amplitude, $V(\Psi)$ increases (to lowest order) quadratically such that a massive (Higgs) mode is expected. It is important to stress that this serves only to build up intuition, as for a valid characterisation of the fundamental modes, the kinetic part of the action has to be included as well.

the mean field ground state. In order to make progress in this direction, also the lowest order time derivatives have to be included. For the example of a (spinless) non-relativistic Bose gas, such an equation is given by the famous Gross-Pitaevskii equation [136]. The crucial result is that in general for a non-relativistic dispersion relation, the first-order derivatives couple the phase and amplitude excitations. In the specific case of a non-relativistic Bose gas, the linearized excitation spectrum is given by the Bogoliubov dispersion relation (with the mass set to one) [34]

$$\omega^2 = \xi^2 k^2 u |\Psi_0|^2 + (\xi^2 k^2)^2. \tag{2.52}$$

This dispersion relation features both massless long wavelength phononic excitations ($\omega \propto k$) as well as particle-like short wavelength excitations ($\omega \propto k^2$), without any independent second stable mode due to the coupling of phase and amplitude oscillations. Note that in a relativistic setting, there are no first-order derivatives and the two modes remain indeed uncoupled. In this setting, the gapless mode is referred to as the Goldstone mode, with the amplitude mode referred to as the Higgs mode. It is important to note that even in non-relativistic systems, a (significant) coupling between phase and amplitude mode can be avoided

by a suitable density of states and in particular by an (approximate) particle-hole symmetry, such that (albeit strongly damped) Higgs modes were also observed in a non-relativistic setting in [22, 137–143].

The 3D BEC-BCS crossover

After the more general remarks on condensation and phase transitions, I will now discuss the specific case of two-component Fermi gases. I have discussed above that depending on the scattering length a, vastly different scattering regimes can be reached. In addition, below I will introduce a method to smoothly change the scattering length from very large negative to very large positive values. In this section, I will introduce a very successful theoretical framework which aims at a unified description of the low-temperature phases of a two-component many-body Fermi system interacting via s-wave scattering throughout all these scattering regimes. This so-called BEC-BCS crossover was first studied theoretically by Eagles and Leggett [144–146] and later on realized in an ultracold atomic system [147, 148], with its application however not restricted to atomic systems alone [146, 149]. It smoothly links the limits of molecular Bose-Einstein condensation for weakly repulsive interactions to the weakly attractive regime described by a BCS phase. Strictly speaking, the BEC-BCS crossover is a pure 3D model, which I will describe in this section. In the context of this thesis, however, also the (quasi-)2D limit is of interest. Thus I will discuss the application on two-dimensional systems in the next section.
The limit of weak attractive interactions is well described by BCS theory, where at the critical temperature T_C the Fermi surface becomes unstable towards Cooper pairing already for arbitrarily weak interactions [4, 34]. On the other hand, weak repulsive interactions support a deeply bound molecular dimer state. In the limit where the dimer binding energy is the dominating energy scale in the system, a description in terms of bosonic molecules (with a renormalized dimer-dimer scattering length [120]) as the fundamental constituents of the model becomes favourable. Consequently, like their atomic counterparts, also the molecules condense into a molecular BEC (mBEC) at the critical temperature [150–152]. The BEC-BCS crossover links these two marginal limits smoothly (that is, there is no phase transition in-between) via the strongly correlated crossover or unitary regime. Based on equation 2.26, the unitary regime is characterized by the condition that the scattering length is much larger than the interparticle distance such that $k_F|a| \gg 1$. Therefore, the scattering amplitude assumes the unitary form $f_0 = \frac{1}{k}$, independent of the scattering length. As a consequence, the only

relevant length scales remaining are the (inverse) Fermi wave vector and the thermal de-Broglie wavelength, such that all thermodynamic quantities are uniquely determined by E_F and T/T_F. Due to the strongly correlated nature and the fact that it can neither be described purely in terms of bosonic nor fermionic degrees of freedom, no complete theoretical description of this regime is available up to date [119].

Despite the fact that a full theory of the BEC-BCS crossover is missing, its success is rooted in the fact that at least a consistent treatment is possible already on the mean field level. In fact, it is possible to directly extend the standard zero-temperature BCS mean field theory over the whole crossover [144, 145]. Within a standard BCS treatment and based on a Bogoliubov transformation [119], the spectrum of elementary quasi-particle excitations is given by the familiar expression[10]

$$E_k^{BCS} = \sqrt{\Delta^2 + \eta_k^2}, \tag{2.53}$$

in terms of the position-dependent order parameter

$$\Delta(r) = -\int \mathrm{d}s V(s) \left\langle \hat{\Psi}_\downarrow(r + s/2)\hat{\Psi}_\uparrow(r - s/2)\right\rangle, \tag{2.54}$$

defined as the weighted average of the short-range potential $V(r)$ over the pairing field, and the kinetic energy $\eta_k = \frac{\hbar^2 k^2}{2m} - \mu$ relative to the chemical potential μ. The crossover can be realized by tuning μ as calculated self-consistently within the Bogoliubov treatment. In the weak coupling limit, the chemical potential coincides with the Fermi energy $\mu = E_F$ such that the standard BCS superfluid gap $\Delta_{sf} = \Delta$, with a minimum of the excitation spectrum at $k = k_F$, is recovered. Upon decreasing μ, the minimum shifts towards $k = 0$ and reaches zero exactly when the chemical potential changes sign on the BEC side where ultimately $\mu \to -E_B/2$ such that the single-particle pair breaking excitations with $\Delta = E_B$ are also incorporated in the BEC limit.

Similar observations can be made for the ground state wave function given by

$$|BCS\rangle = \prod_k \left(\cos\theta_k - \sin\theta_k \hat{a}_{k\uparrow}^\dagger \hat{a}_{-k\downarrow}^\dagger\right)|0\rangle, \tag{2.55}$$

where $\sin\theta_k = \sqrt{(1 - \eta_k/E_k)/2}$. If we project the wave function onto the subspace of a fixed particle number N, the wave function can be expressed in terms of pair orbitals [119]

$$\Psi_{BCS}(r_1, \cdots, r_N) = \hat{A}\left[\psi(r_{1\uparrow 1\downarrow}) \cdots \psi(r_{N\uparrow N\downarrow})\right]. \tag{2.56}$$

[10] compare this to the Bogoliubov spectrum for a spinless Bose gas given in equation 2.52.

Here $\hat{A}$ denotes the antisymmetrization operator and $r_{i\uparrow i\downarrow} = |r_{i\uparrow} - r_{i\downarrow}|$ the relative coordinate of pair i. Importantly, the pair function for a single pair $\psi(r) \propto \int \mathrm{d}k \tan\theta_k e^{ikr}$, describing weekly bound Cooper pairs in the weak coupling limit, smoothly evolves into the molecular wave function $\psi(r) \propto \frac{1}{\sqrt{2\pi a r}} e^{-r/a}$ upon approaching the deep BEC limit. As a consequence, pairing and the fundamental excitations are consistently described across the full crossover, becoming exact in the limiting cases of weak attractive or repulsive coupling.

2.3.4. The 2D BEC-BCS crossover

In two dimensions, true long range order is prohibited for contact interactions in a homogeneous gas by virtue of the Mermin-Wagner theorem. Nevertheless, also in two dimensions the ground state smoothly changes nature from a weakly interacting fermionic system for $\ln(k_F a_{2D}) \gg 1$ to an effective description in terms of weakly interacting bosonic entities for $\ln(k_F a_{2D}) \ll 1$. Therefore, this crossover is again entitled (2D) BEC-BCS crossover; despite the fact that the mechanisms of Bose-Einstein or BCS condensation have to be replaced by their respective BKT counterparts. Apart from the topological nature of the phase transition, the most profound difference to the three-dimensional crossover is that a two-body bound state exists for all values of the interaction parameter. However, a fermionic regime can still be defined in the many-body limit by ensuring $E_B \ll E_F$ such that the typical interparticle distance is much smaller than the two-body pair size. As this constraint directly translates into $\ln(k_F a_{2D}) \gg 1$, this is already naturally incorporated in the description used so far. Importantly, this implies that the regimes within the BEC-BCS crossover cannot only be reached by changing the scattering length, but also by varying the density.[11] In [126, 127], an overview of the current status towards a theoretical description of the 2D BEC-BCS crossover is given. Here, I will restrict the discussion again to a few key results of a zero temperature mean field treatment. Note however, that in two dimensions a mean field treatment is expected to be even less accurate due to the increased role of quantum fluctuations.
Similar to before, the quasi-particle excitation energies are given by [126]

$$E_k^{BCS} = \sqrt{\Delta^2 + \eta_k^2} \tag{2.57}$$

[11] Covering the whole crossover only by changing the density is experimentally impractical due to the logarithm in the definition of the interaction parameter. As we will see in the next sections, drastically changing the scattering length is the better way to go.

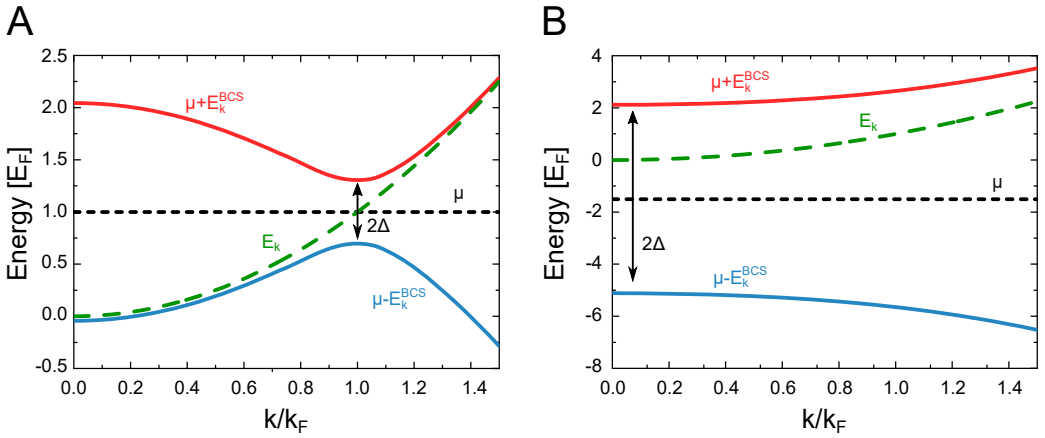

Figure 2.6.: **BCS dispersion relation. A:** Assuming a gap of $\Delta = 0.3E_F$, corresponding to $E_B = 0.045E_F$, the chemical potential (black dashed) is approximately given by the Fermi energy $\mu \sim E_F$. The paired branch (blue line) is given by $\mu - E_k^{BCS}$ and calculated with the help of equation 2.57. The unpaired branch (red line) is calculated according to $\mu + E_k^{BCS}$. As a reference, the single particle kinetic energy $E_k \propto k^2$ (green dashed line) is shown as well. The minimum excitation gap is approximately at the Fermi wave vector k_F. **B:** The BCS formula can also be applied more on the BEC side (same colour scheme used). Here $\Delta = \sqrt{10}E_F$, corresponding to $E_B = 5E_F$, is assumed. As a consequence, the chemical potential becomes negative, $\mu = -1.5E_F$, and the minimum excitation gap is at $k = 0$.

in terms of the gap parameter Δ and $\eta_k = \frac{\hbar^2 k^2}{2m} - \mu$. The chemical potential takes the general form $\mu = E_F - E_B/2$ and thus smoothly evolves from E_F in the BCS limit to $-E_B/2$ in the BEC limit. In addition, the order parameter is given by $\Delta = \sqrt{2E_F E_B}$. As a consequence, the single-particle excitations are again captured both in the BEC and the BCS limit. The corresponding dispersion relations in the BCS limit ($\Delta = 0.3E_F$, $E_B = 0.045E_F$) and further down on the BEC limit ($\Delta = \sqrt{10}E_F$, $E_B = 5E_F$) are shown in figure 2.6. Equivalently, equation 2.55 can also be recovered with $\sin^2\theta_k = \frac{1}{2}(1 - \eta_k/E_k)$, such that the pair wave functions are again consistently included for the limiting weakly interacting regimes.

While there is also in 2D no full analytical treatment of the BEC-BCS crossover, more quantitative results can be obtained at least in the limiting cases by perturabtive calculations or quantum Monte Carlo methods (see [126, 127] for an overview). Remarkably, upon perturbing slightly away from the strict 2D limit towards a regime where $E_F \approx \omega_z$, an increase in the gap Δ is expected, already based on a mean field treatment. Going beyond the zero temperature limit, equivalently also an increased critical temperature is expected [126], consistent

with observations in high-T_C superconductors [153].
As in the three dimensional system, also in 2D special interest lies in the strongly correlated crossover regime. However, in this case a unitary regime does not exist due to the additional length scale set by the dimer state. Therefore, a reasonable definition of the crossover 'point' is given by the interaction strength where the chemical potential changes sign and consequently the last remnants of a Fermi surface disappear. Based on the BCS treatment, $\ln(k_F a_{2D}) = 0$ could be interpreted as the crossover interaction strength. This is however inconsistent with a current experimental understanding based on for example [15] and [18] as will be discussed in detail in section 3.1. In addition, a more detailed theoretical QMC calculation [126] locates the sign change of μ rather at $\ln(k_F a_{2D}) \simeq 0.5$. The crossover into a BKT superfluid was studied in our group in [15, 16], confirming the BKT nature of the phase transition and measuring an enormously large critical temperature of more than 15 % of the Fermi temperature in the crossover regime. There are however still a number of exciting mysteries to unravel, including in particular the microscopic (pairing) correlation mechanism responsible for the unconventional thermodynamic behaviour observed.

2.4. The atom of choice: ^{6}Li

All our experiments employ ^{6}Li, a fermionic isotope of Lithium, which is the lightest alkali atom with a proton number of $Z = 3$. The fermionic nature of ^{6}Li is set by the single valence electron in combination with the nuclear spin of $I = 1$. A detailed overview of all relevant properties of ^{6}Li can be found in [154]. The level structure up to the hyperfine splitting is shown in figure 2.7. For all our experiments, we will work in the electronic ground state manifold $2^2S_{1/2}$, which itself is split by the hyperfine coupling into the $F = 1/2$ and $F = 3/2$ submanifolds with a splitting of $\Delta = h\cdot 228.2\,\mathrm{MHz}$. The relevant optical excitation energies which we will use for (near) resonant tapping and cooling as well as imaging are the D_1 and in particular the D_2 line at $\lambda_1 = 670.992\,421\,\mathrm{nm}$ and $\lambda_2 = 670.977\,38\,\mathrm{nm}$, coupling the ground state to the $2^2P_{1/2}$ and $2^2P_{3/2}$ manifolds, respectively. The natural line width of the D_2 transition is $\Gamma = 5.8724\,\mathrm{MHz}$ with a saturation intensity of $I_{sat} = 25.4\,\mathrm{W/m^2}$. Therefore, the hyperfine structure of the D_2 line is not resolved without any magnetic field applied. Two additional details on the D_2 line will be of importance later on. First of all, the recoil velocity, which is the velocity change after scattering a single photon on the D_2 line, is given by $v_{rec} \approx 0.1\,\mu\mathrm{m/\mu s}$. As will be discussed in detail below, this has important consequences for imaging the atoms. In addition, the splitting between

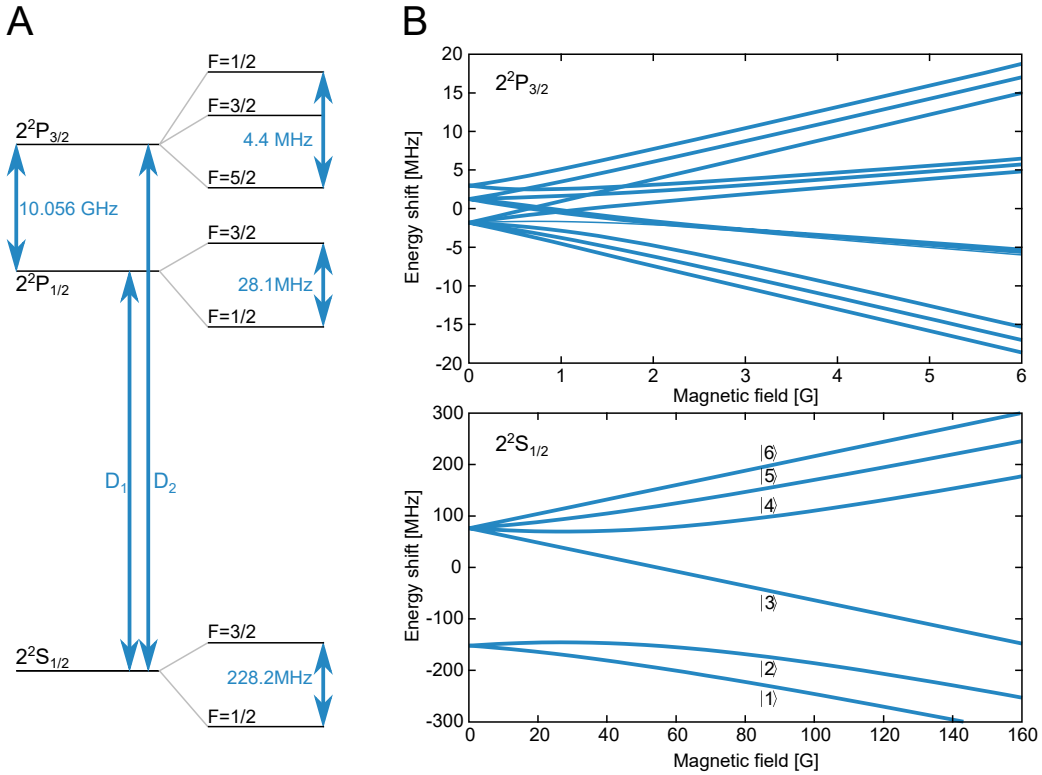

Figure 2.7.: **Level structure of ^{6}Li. A:** Hyperfine structure of the lowest manifolds at $B = 0$. The $2^2S_{1/2}$ ground state is split by around 228 MHz into the $F = 3/2$ and $F = 1/2$ submanifolds. The relevant optical transitions are the D_1 and D_2 line at around 671 nm ($\sim$ 446.8 THz) coupling the ground state to the $2^2P_{1/2}$ and $2^2P_{3/2}$ manifolds, respectively. The splitting between the D_1 and D_2 line is around 10 GHz, with the splitting between the different F submanifolds significantly smaller than for the ground state manifold. **B:** Level structure of the ground state (lower panel) and the D_2 (upper panel) manifold as a function of an applied magnetic offset field. For the ground state, only at $\mathcal{O}(100\,\mathrm{G})$ the approximate Paschen-Back regime is reached, while for the $2^2P_{3/2}$ manifold this is already at $\mathcal{O}(1\,\mathrm{G})$ the case. The energy levels of the ground state are labelled $|1\rangle$ to $|6\rangle$ in ascending order of energy.

the D_1 and D_2 line is with around 10 GHz rather small, which can pose challenges in the strong coupling regime as will be briefly discussed in section 5.4.6.

All the experiments presented in this thesis will be performed at a magnetic offset field in the range $B \in [250\,\mathrm{G}, 1000\,\mathrm{G}]$. Therefore, in figure 2.7 also the Zeeman splitting of the relevant manifolds is shown. For small magnetic fields, F is still a good quantum number and the manifolds split up linearly according to the m_F projections. On the other hand, in the regime where the magnetic interaction energy is larger than the hyperfine coupling, we are in the Paschen-Back regime of the hyperfine structure, where the nuclear and total electronic

angular momentum fully decouple. Therefore, we again have a linear scaling of the energies, now with the m_J projection. Due to the small hyperfine coupling of the excited state manifolds, the decoupling in this case already happens at around 1 G. As a consequence, for all practical purposes, we can neglect the residual coupling between nuclear and total electronic angular momentum at large magnetic fields. This is not possible for the ground state manifold. Even though the general level structure is well captured by the Paschen-Back effect, I will have to take the small but finite residual hyperfine coupling into account when presenting our imaging scheme in chapter 5. We label the different hyperfine states of the ground state manifold by $|1\rangle - |6\rangle$ in ascending order of energy. Their analytic form and the limiting cases for large magnetic fields in the $|m_j, m_I\rangle$ basis are given by [154]

$$\begin{aligned}
|1\rangle &= A_+ \,|1/2, 0\rangle - B_+ \,|-1/2, 1\rangle \quad &\rightarrow \quad |-1/2, 1\rangle \\
|2\rangle &= A_- \,|1/2, -1\rangle - B_- \,|-1/2, 0\rangle \quad &\rightarrow \quad |-1/2, 0\rangle \\
|3\rangle &= |-1/2, -1\rangle \\
|4\rangle &= B_- \,|1/2, -1\rangle - A_+ \,|-1/2, 0\rangle \quad &\rightarrow \quad |1/2, -1\rangle \\
|5\rangle &= B_+ \,|1/2, 0\rangle - A_- \,|-1/2, 1\rangle \quad &\rightarrow \quad |1/2, 0\rangle \\
|6\rangle &= |1/2, 1\rangle \,,
\end{aligned} \tag{2.58}$$

where in terms of the magnetic dipole energy $A_d = h \cdot 152.136\,840\,7\,\mathrm{MHz}$ and the neutron (electron) magnetic moment μ_n (μ_e) the magnetic field dependent prefactors are given by $A_\pm = 1/\sqrt{1 + (Z^\pm + R^\pm)^2/2}$, $B_\pm = \sqrt{1 - A_\pm}$, $Z^\pm = (\mu_n + 2\mu_e)\frac{B}{A_d} \pm 1/2$ and $R^\pm = \sqrt{(Z^\pm)^2 + 2}$.
In this thesis, we will employ the hyperfine states $|1\rangle, |2\rangle$ and $|3\rangle$. They can be individually addressed by the D_2 line due to the splitting of around $h \cdot 80\,\mathrm{MHz}$ between the individual states. In addition, we can transform the states into each other by driving radio-frequency (rf) transitions. More specifically, all experiments presented in this thesis will use a mixture of two out of the three hyperfine states (albeit in a varying composition). Therefore, we will heavily make use of the fact that any two-level system can be mapped onto a spin-1/2 description. The two hyperfine states will thus be described as the spin-up and spin-down projections of an isospin-1/2 state. As we will work at (thermal and interaction) energies much below $h \cdot 80\,\mathrm{MHz}$, the spin projection will always be a conserved quantity in the dynamics of the quantum systems presented.

2.4.1. Feshbach resonances of ^{6}Li

The exact value of the scattering length is a parameter of the effective description given in section 2.3.1. It can be calculated using first principles based on the microscopic (van-der-Waals) scattering potential or measured experimentally. For ^{6}Li (in a mixture of the lowest hyperfine states), this so-called background scattering length is given in units of the Bohr radius a_0 by approximately $a_{bg} = -1600a_0$ [155]. Much of the versatility of ultracold quantum gases is based on the fact that we are not stuck with the scattering length ^{6}Li happens to have, but instead are able to tune and in particular resonantly enhance the scattering length. The most common tool, which will also be used in this thesis, are magnetic Feshbach resonances.

Such a Fano-type Feshbach resonance appears when a virtual bound state in the scattering potential between two atoms is tuned into resonance with the relative kinetic energy of the scatterers. In the specific case of a magnetic Feshbach resonance, the closed channel featuring the bound state has a different magnetic moment compared to the open scattering channel such that their relative energy can be tuned by an applied magnetic field. For a detailed description of Feshbach resonances, the reader is referred to [11]. Here it suffices to state that the scattering length as a function of the magnetic field in the vicinity of a Feshbach resonance is approximately given by the phenomenological model

$$a(B) = a_{bg}\left[1 - \frac{\Delta_B}{B - B_0}\right], \tag{2.59}$$

in terms of the resonance position B_0 and width parameter Δ_B. For ^{6}Li, and all combinations of relevant hyperfine states, there are convenient Feshbach resonances in the range $B_0 \in [689\,\mathrm{G}, 832\,\mathrm{G}]$. Details on the resonances can be found in [155] and in figure 2.8, where the scattering length as a function of the magnetic field is shown. Importantly, we can experimentally reach (almost) every scattering length including the limiting cases of vanishing ($a = 0$) and strongly repulsive and attractive ($a \to \pm\infty$) interactions. Note that the Feshbach resonances of ^{6}Li are broad in the sense that they have a very weak energy dependence (signalled also by Δ_B being large). This a-posteriori justifies neglecting the k-dependence of the scattering phase shift in the derivation of equation 2.26.[12]

[12] ^{6}Li also features narrow s-wave and p-wave resonances. In this case, (at least) the next leading term given by the effective range has to be included in equation 2.26.

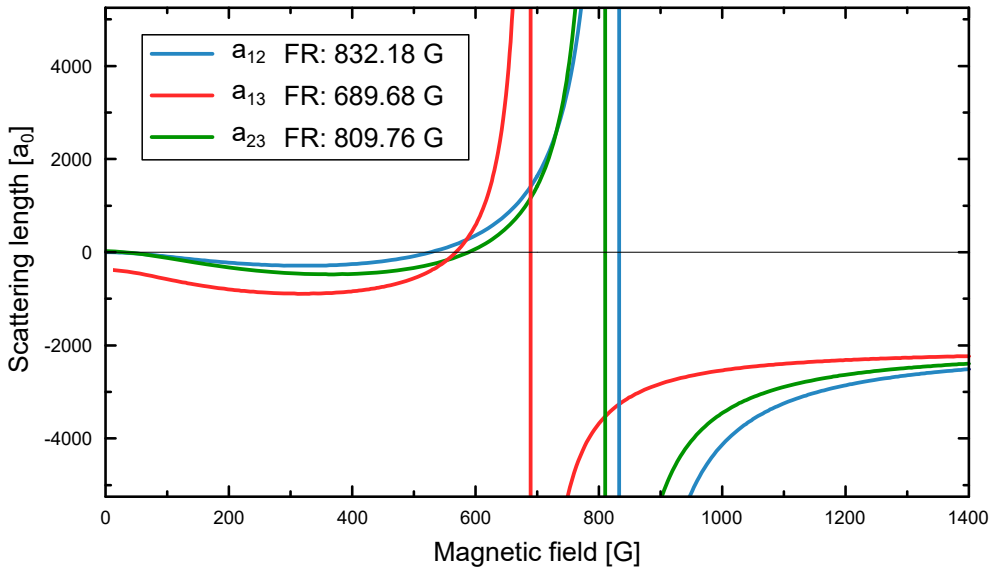

Figure 2.8.: **Feshbach resonances of ^{6}Li .** Shown is the s-wave scattering length as a function of the magnetic offset field in the vicinity of the broad Feshbach resonances in the three combinations of the states $|1\rangle$-$|3\rangle$. The Feshbach resonance in the $|1\rangle$-$|2\rangle$ mixture (blue line) is located at around 832 G, the resonance in the $|1\rangle$-$|3\rangle$ mixture (green line) at around 690 G and the resonance in the $|2\rangle$-$|3\rangle$ mixture at around 810 G.

2.5. Preparing ultracold quantum gases

The preparation of ultracold quantum gases is, for the most part, based on very well established techniques and both the general concept [11] and the specific implementations in our experiment [32, 99, 156–159] have already been described extensively. For this reason, in this chapter, I will only very briefly outline the preparation of ultracold atomic samples as well as the deterministic preparation of number states. Note that the experiments described in this thesis were performed at two different experimental setups. The general experimental procedure and the techniques used are identical, though.

2.5.1. Cooling and trapping

All experiments are performed in ultra-high vacuum (around 10^{-11} mbar) in an octagon steel chamber providing both optimum isolation from the environment and good optical access through high numerical aperture (NA) viewports, with the top and bottom re-entrant with $NA = 0.65$ (see figure 2.9). We can set an offset magnetic field in the range of 0 G to 1000 G by controlling the current through a set of coils placed directly above (below) the upper (lower) re-entrant

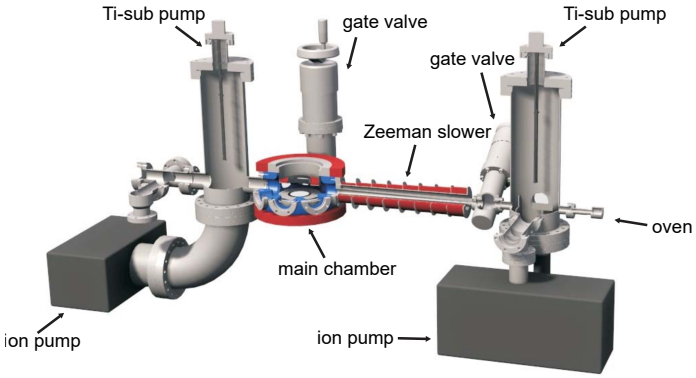

Figure 2.9.: **Mechanical design of the vacuum system.** Ultra-high vacuum conditions are ensured by two ion pumps and two titanium sublimators. The atoms are heated up in the oven and can evade through a nozzle into the Zeeman slower and the main experimental chamber where they are trapped first in a MOT and than in optical dipole traps. All experiments are performed in the octagon main chamber. Good optical access is provided by the high NA viewports, in particular the re-entrant viewports on the top and the bottom of the chamber. The full setup has a length of around 1.5 m.

viewport. This also defines the quantization axis to be the z-axis. At a finite magnetic field we can drive rf transitions between the different hyperfine states by an oscillatory current through a single-loop coil placed below the experimental chamber. The ultracold gas starts out as hot vapour evading at a rate of around 10^{16} atoms/s out of a nozzle in the oven where an enriched sample if ^{6}Li is heated up to above 300 °C. A fraction of the atoms is resonantly (on the D_2 line) pre-cooled and trapped in the vacuum chamber using a Zeeman slower and a magneto-optical trap (MOT).[13] After this stage we are left with a few times 10^8 atoms in the hyperfine states $|1\rangle$ and $|2\rangle$ at a temperature of a few hundred µK. In order to cool below the Doppler temperature of $T_D = 136\,\mu\text{K}$ which is set by the recoil energy, we have to use non-resonant techniques. For this reason we transfer the atoms into a far off-resonant optical dipole trap (ODT) formed by a focused laser at a wavelength of 1064 nm.[14] On the timescales considered in this thesis, the potential formed by the off-resonant light can be assumed to be fully conservative. In the ODT we can set the relative population of the hyperfine states through a suitable rf pulse. Typically, we are working either in a balanced $|1\rangle - |2\rangle$ or a balanced $|1\rangle - |3\rangle$ mixture. Also in the ODT, we perform forced evaporative cooling in order to create a sample at a much lower temperature at

[13] The light is derived from a Toptica tapered amplifier at 671 nm, beat offset locked onto a reference laser stabilized with the help of a spectroscopy cell.
[14] 200 W Yb-doped fibre amplifier YLR-200-LP-WC from IPG Photonics.

the expense of significant atom loss. We either perform the evaporation step a few Gauss below the Feshbach resonance at a large positive scattering length, or at around 300 G where the scattering length is negative. In the latter case we end up with a degenerate Fermi gas of around 40 000 atoms per spin state well below the Fermi temperature ($T \lesssim 0.5 T/T_F$ for the experiments described here). During the repulsive interaction based evaporation step, already at a rather large temperature $k_B T^* \approx E_B$ a molecular gas is formed (see equation 2.30). As the molecule-molecule scattering length is also large and positive ($a_{dd} \approx 0.6a$ for deeply bound molecules), we end up with a molecular Bose-Einstein Condensate (mBEC) of around 40 000 dimers at temperatures as low as $T/T_F \approx 0.1$. Due to the larger scattering length and in particular the bosonic statistics, the evaporation into a mBEC is with around 1 s much faster than the evaporation into a Fermi gas, which takes at least 5 s.

After the forced evaporation, we transfer the gas into a range of different optical dipole traps, again acting as a conservative potential, which allow us to study the quantum gas in various different geometries. In addition, we can also use the degenerate Fermi gas as a starting point for the preparation of few-body number states, as described below.

After the preparation and manipulation stage we infer information on the prepared state by imaging with resonant light[15], as will be described in detail in chapter 5. Importantly, resonant imaging is both projective, in the sense that we project the wave function onto the measurement basis, and destructive, as we strongly perturb the state by the imaging process. Therefore, we have to repeat the whole preparation and imaging scheme over and over again if we are to sample the many-body probability distribution of our system. For different experimental measurement campaigns, the number of repetitions for a fixed set of physical parameter, ranges from a few single ones to several ten thousands. Each experimental run takes on average around 10 s.

For all experiments, we create a sequence of timings for various triggers as well as target values for all the intensities, frequencies and currents used in the experiments with the help of a specific LabView interface and send it to a real-time processor unit.[16] The processor unit features high resolution and high speed digital and analogue out- and inputs (16bit and 18bit). It distributes the digital timings in the form of TTL logic triggers to the various experimental instruments. In addition, with the help of the analogue in- and outputs, we can regulate the various laser and rf powers and frequencies as well as electric currents through

[15] Using different Toptica DL100(-pro) diode lasers at 671 nm.
[16] Jaeger AdWin Pro II.

magnetic field coils using digital PID loops running at 400 kHz.

2.5.2. Preparation of deterministic few-body states

In our group we have specialized in creating deterministically prepared fermionic few-body states [160]. The general scheme of creating states in one spatial dimension is well established by now, however, based on the physical system of interest it is continuously refined and adapted to the specific needs. In this chapter, I will present the basic techniques for the preparation of number states in a single optical tweezer (synonymously also called microtrap) as a starting point for the preparation of interacting but still deterministic few-body states in a multi-well geometry. I will introduce specific refinements of this general scheme when needed in later chapters and in particular in chapter 7, I will present the novel generalization to two-dimensional potentials.

Preparation of number states

In order to prepare a state where with almost unity probability, a few distinct energy levels are occupied while all other levels are empty, we have to ensure two things: First of all we have to isolate the eigenstates which should be occupied in energy, such that we can selectively remove all atoms in other states. Secondly, unity occupation of the relevant states has to be ensured. Both prerequisites can be fulfilled at the same time using the dimple trick [161]: We start with a mostly degenerate Fermi gas in a rather large optical dipole trap (waist around 100 µm) as described above. Typical temperatures are around 250 nK corresponding to $T/T_F \approx 0.5$. Now we superimpose the ODT with an optical tweezer formed by a tightly focussed infrared laser beam. We use a laser power of several 100 µW which is derived from a 1 W Innolight Mephisto laser at 1064 nm wavelength. The beam is collimated to a diameter of around 2 cm and focussed through a custom made high resolution objective which is mounted directly above the upper re-entrant viewport. The objective has a numerical aperture of NA= 0.55 and an effective focal length of $f = 20.3$ mm such that the beam is focussed down in the atom plane to around 1 µm, which is close to the design diffraction limit of 0.72 µm. In order for the atoms to thermalize into this microtrap, we set a finite interaction strength via the magnetic offset field and ramp on the tweezer potential slowly within several 10 ms. As the trap volume of the microtrap, with a few hundred trapped states, is small compared to the large ODT which thus acts as a reservoir, the overall temperature stays close to the temperature of the reservoir.

However, locally in the microtrap, the Fermi energy is drastically increased, as illustrated in figure 2.10. As a consequence, the degeneracy of the lowest levels in the microtrap is basically unity ($P(E_0) > 99.99\,\%$). In addition, the lowest eigenstates have very distinct eigenenergies, which allows us to individually address them. We will quantify typical energy spacings throughout this thesis by the trap frequency in the harmonic approximation. That means the typically Gaussian potential shape is Taylor-expanded to second order around the minimum. Note that this approximation, in particular for such a tightly focussed trap, is accurate at most for the lowest lying states and thus should be interpreted as a figure-of-merit alone. For quantitatively accurate calculations the full potential shape has to be taken into account. Typical axial trap frequencies (that is along the z-axis) are around 1 kHz, with the aspect ratio, which is defined as the radial trap frequency divided by the axial trap frequency, being roughly 7. As a consequence, the lowest lying (non-interacting) states in the microtrap are in the radial ground state with a few distinct axial excitations.

After the thermalization step, we switch off the reservoir, such that we are left with a few hundred atoms in the microtrap. We tune the magnetic field to typically around 530 G where the atoms are non-interacting. Therefore the lowest lying single-particle eigenstates are occupied by one atom of each of the two hyperfine states (see figure 2.10). Afterwards we remove all but the lowest lying states by a suitable trap deformation. We will call this step *spilling* of the microtrap. In practice, this is achieved by superimposing a linear magnetic field gradient $B' \approx 20\,\mathrm{G/cm}$ - $60\,\mathrm{G/cm}$, which induces a tilt of the potential according to $V_{mag} = \mu B'$ in terms of the magnetic moment μ. In the Paschen-Back regime for large magnetic fields, the magnetic moment becomes state independent with $\mu \approx \mu_B = \frac{e}{2m_e}\hbar$. At around 530 G the magnetic moments differ by around 1 %. With the gradient applied, all states are tunnel-coupled to the continuum. However, the tunnelling timescales are vastly different for states below the tunnel barrier height (at least several 100 ms) and above the barrier ($\lesssim 1\,\mathrm{ms}$). Therefore, by adjusting the the magnetic field gradient strength, the time the gradient is turned on and the potential depth of the tweezer during spilling, we can have all atoms above a certain energy scale tunnel out while the atoms at smaller energies remain trapped. This process is illustrated in figure 2.11. With this technique we can prepare atom numbers of (at least) one, two and three atoms per spin state almost deterministically. In this thesis, we will mostly use the situation of one atom per spin state in the ground state. We can prepare this state with a fidelity of typically 97 %. The fidelity is limited by the separation of tunnelling timescales for the given potential and the trap frequency. As we saturate this

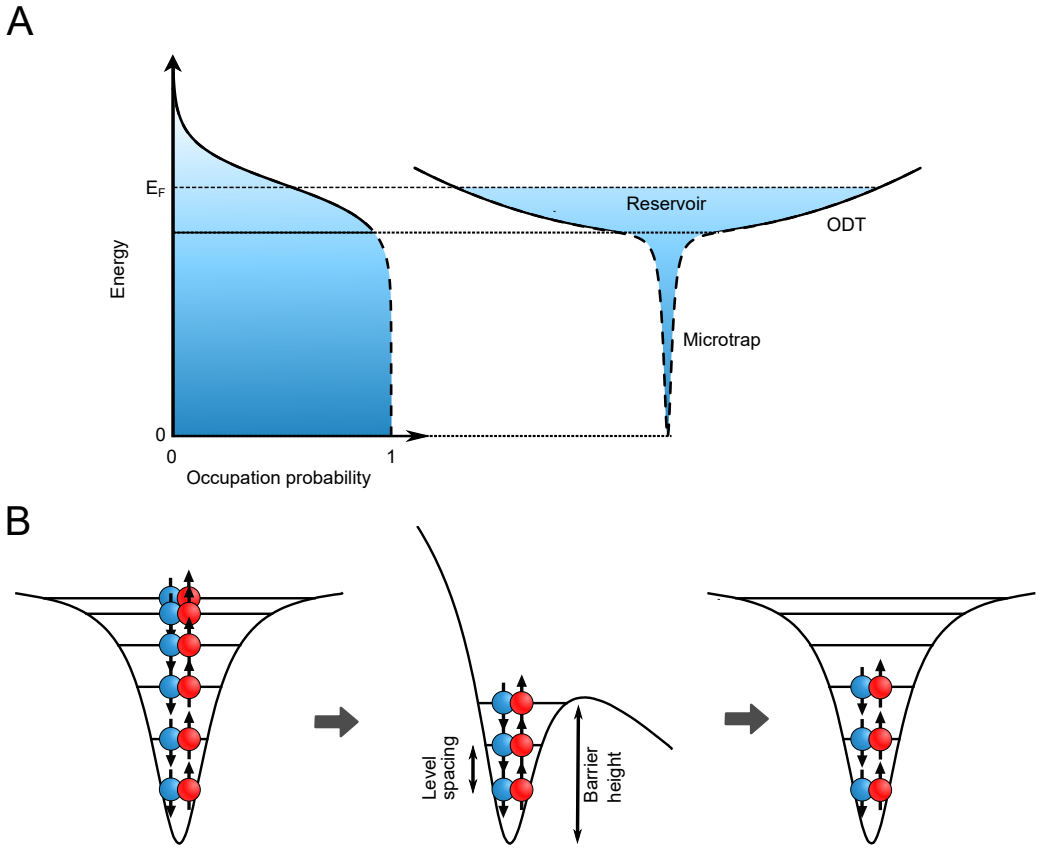

Figure 2.10.: **Spilling of the optical tweezer. A:** Loading of the microtrap. In the right panel, the potential landscape of the combined trap out of the ODT serving as a reservoir and the microtrap is schematically illustrated. The trap volume of the microtrap is significantly smaller but in turn the potential is much deeper. In the left panel, the occupation probability of different energy states of a Fermi gas based on a finite temperature of $T/T_F \sim 0.5$ is shown. While the absolute temperature is globally the same, the local Fermi energy (relative to the potential depth) is increased in the microtrap, resulting in an almost unity occupation probability of the ground state. **B:** Schematic illustration of the spilling procedure. Starting from the full microtrap, a magnetic field gradient is applied such that only a certain number of levels remains bound. The atom number is tuned by the ratio between the barrier height and the level spacing. After typically around 20 ms the gradient is slowly ramped off and a specific number of atoms is prepared. In this example, three filled levels corresponding to six atoms are prepared.

limit, we can conclude that the finite degeneracy of gas and technical noise on the optical and magnetic potentials are not deteriorating the preparation. With the current geometry of the microtrap it is not easily possible to create states of more than $3 + 3$ atoms due to the finite aspect ratio and the specific geometry of the tweezer. When needed, the geometry can be adapted, though [160, 162].

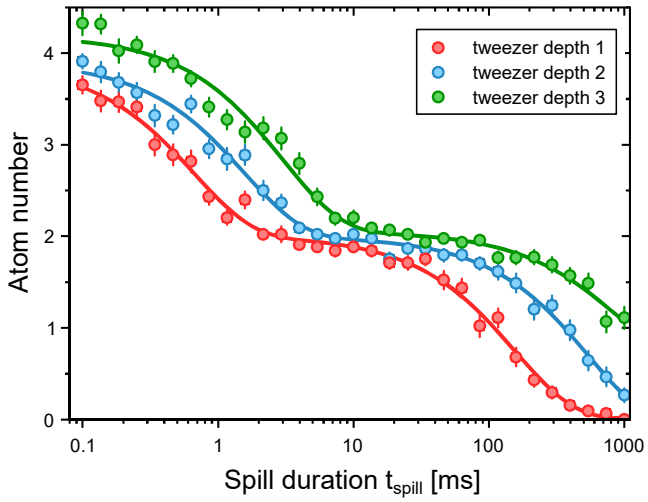

Figure 2.11.: **Tunnelling timescales.** For a fixed magnetic field gradient, the height of the tunnel barrier can be fine-tuned by adjusting the depth of the tweezer. Here, for three slightly different depths (green, blue and red data points), the atom number remaining in the tweezer as a function of the spill duration where the gradient is turned on is shown in a semi-logarithmic plot. The tweezer depths are chosen such that the tunnel barrier is in-between the lowest and the first excited state. Two different tunnel timescales can be identified. The timescale in which the first excited state tunnels into the continuum is $t_{spill} \lesssim 1\,\mathrm{ms}$ while the tunnelling time for the ground state is at least two orders of magnitude larger. The observed mean atom number is well described by a sum of two exponential functions (solid lines). In order to optimize the spilling process, the tweezer depth, the spill duration and in an additional data set (not shown) the magnetic field gradient have to be optimized such that the correct atom number is prepared with the highest fidelity.

In addition, similar fidelities are reached not only for spilling of a non-interacting gas, but also for weak interactions where the energy levels are still well separated from each other. In addition, we can make use of the fact (see figure 2.7) that at low magnetic fields of $B \approx 5\,\mathrm{G}$ - $30\,\mathrm{G}$ the magnetic moments are vastly different between the different hyperfine states. Thus, by slightly modifying the spilling protocol, we can also engineer spin imbalanced states, where we prepare a different number state for the different hyperfine states. We can prepare all the combinations $(0+3, 0+2, 0+1, 1+2, 1+3, 2+3)$ near deterministically with fidelities above $95\,\%$.

A few tunnel-coupled wells

The spilling technique described above allows us to prepare number states in a single tweezer. We are however also interested in preparing specific states in a

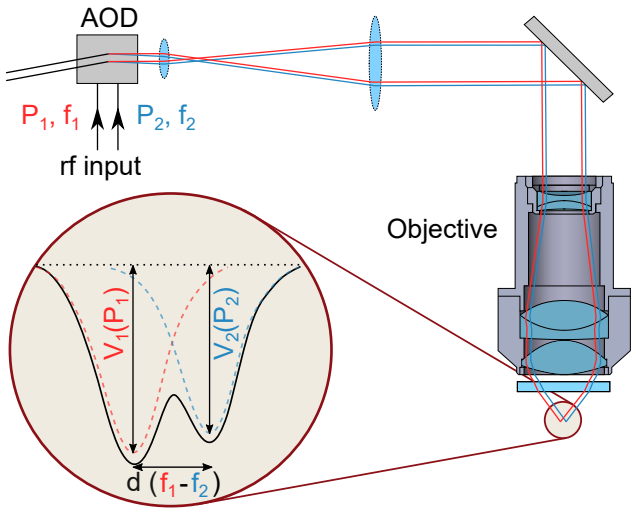

Figure 2.12.: **Creating a tunnel-coupled double-well potential.** The light going through the AOD is partially deflected by means of an rf input signal sent to the AOD. The fraction of the light deflected is controlled by the rf power and the angle by the frequency. The undeflected light is blocked (not shown). If we use two different rf tones (tone one/two with power $P_{1/2}$ and frequency $f_{1/2}$, respectively), light is deflected at two different angles (red and blue beam path). The light is collimated to a size of $\sim 2\,\mathrm{cm}$ and focussed onto the atom plane through the objective. In the case where the two tweezers projected in this way overlap, the lowest lying excitation energies are well approximated by those of a double-well potential. The distance d between the wells and the respective potential depths $V_{1/2}$ are controlled by the frequency and power of the rf signal and can be tuned. Adapted from [163].

multi-well geometry formed by an array of tweezers. For this, we utilize a two-axis acousto-optic deflector (AOD), which is driven by an rf control signal. In the AOD a certain fraction of the light (set by the rf intensity) is deflected at an angle set by the frequency of the rf pulse. We block the undeflected part and use the deflected light for the creation of the tweezers. If we use a multi-frequency rf signal, the light is deflected into multiple angles. We expand the beams using a telescope and focus it with the objective onto the atom plane. Different deflection angles therefore correspond to different positions of the focus on the horizontal plane, which allows us to create multi-well potentials. With the relative power of the frequency components we control the relative depth of the potentials and via the frequencies the distance between the individual tweezers, as schematically shown in figure 2.12.

The AOD has a bandwidth of around 30 MHz corresponding to a position shift of 15 µm in the atom plane, thus corresponding to 15 times the waist of a single

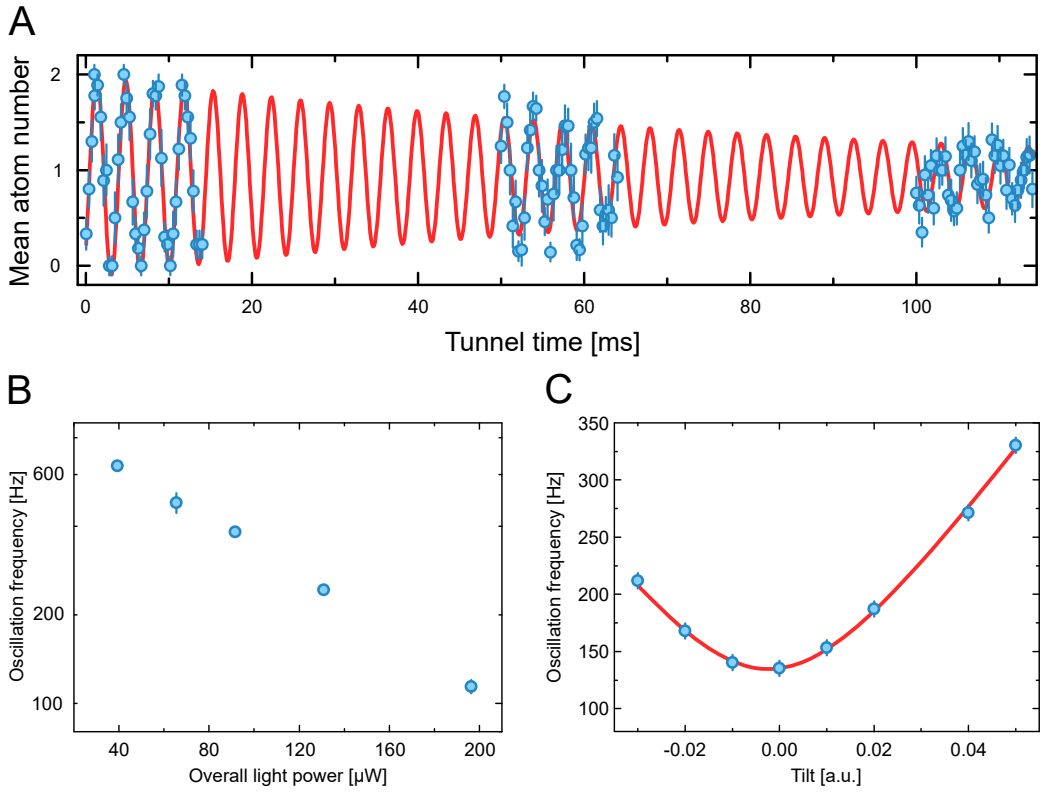

Figure 2.13.: **Tunnelling in a double-well. A:** Resonant tunnel dynamics of two non-interacting particles. Recorded is the mean atom number in one of the wells as a function of the time where the tunnelling is enabled (blue data points). Coherent oscillations in the population are observed due to the effective two-level dynamics. A decay time of about 80 ms is observed which is consistent with a small drift in the resonance position by about 25 Hz, due to the relative power in the wells drifting (red line). **B:** We can tune the tunnel coupling by adjusting the overall light power and thus also the tunnel barrier height. In this thesis we work mostly at around 100 Hz oscillation frequency. **C:** By introducing a relative tilt between the two wells, we can tune the tunnel dynamic off-resonant, resulting in a larger oscillation frequency (and a smaller amplitude). In order to calibrate the tilt, we fit the expected tunnel coupling based on a two-level system given by $J' = \sqrt{J^2 + \Delta^2}$ in terms of the resonant tunnel coupling J and the tilt Δ (red line).

microtrap. In this thesis we will use only one axis of the AOD and as a consequence create a 1D array of tweezers. More precisely, we will use 1 to 3 tweezers resulting in a single trap or a double- and triple-well respectively. We deliberately work at very low diffraction efficiencies of the AOD on the sub-percent level corresponding to low rf powers in order to minimize non-linearities both due to heating effects and the finite percentage of light being deflected off. We stabilize the total deflected lightpower using a digital PID loop. Crucially, we do not sta-

bilize the relative power difference between the different wells. Instead, we set it passively by fixing the rf power in the different frequencies. Implications of this limitation will be discussed in chapter 6.

We can either separate the tweezers as much as possible such that they are mostly independent, or we can have them partially overlapping, as shown in figure 2.12. In the latter case we can engineer tunnel coupling between the different tweezers or, adapting the terminology of larger systems, lattice sites. For a fixed spacing we tune the tunnelling rate by adapting the potential depth of the tweezers. This is shown in figure 2.13. In addition, we can tune the tunnelling dynamics in and out of resonance by means of the relative depth of the microtraps. We typically separate the tweezers by around 1.5 µm, resulting in ground state tunnelling rates of around 100 Hz. Crucially, for these parameters only nearest neighbour tunnelling has to be taken into account. We always work in a regime where the tunnel coupling is much smaller than the trap frequency. Thus, for single-particle tunnelling, we only have to take the lowest energy level in each well into account and arrive at a system fully described by a Rabi-coupled two-level system.

In addition, we can turn on attractive or repulsive on-site interactions by tuning the magnetic field. I will discuss a theoretical treatment of such a tunnel-coupled interacting few-body and few-well system in terms of a one-dimensional Fermi-Hubbard model in section 6.1. In order to avoid confusion, I should point out that by now we have used two distinct notions of 1D. In a single well, the lowest lying excitations are along the axial (that is z) direction, while the dynamics in a few-well system as described here is along the axis of the tweezer array, which is along one of the horizontal axes. In turn, for this to be a true 1D model, we have to make sure that both the tunneling and the interaction energy scale are well below the single-particle excitation energy in axial direction.[17] This is equivalent to the lowest band approximations in an infinite lattice model.

[17] In particular, the tunnel rate is dependent on the axial excitation levels, such that these cannot be ignored.

Part II.

Motivation:
A strongly correlated 2D Fermi gas

3. Correlations in many-body quantum systems

This chapter is centred around a summary of the results obtained on high temperature many-body induced pairing in a quasi-2D ultracold Fermi gas. These results have been published in [18]. In the discussion, it will become clear how a set of complex techniques and tricks can be used to learn a lot about the fascinating pairing correlations in such a system. However, even with all these techniques, we will be limited to probing the global collective response of the system with no direct access to fundamental microscopic correlations granted. The crucial insight is that these limitations are not specific to the exact system described in this chapter but inherent to at least a broad class of ultracold quantum gas experiments, and even more general almost for the whole field of many-body physics. Therefore, it is imperative to find a general scheme to surpass them. Thus, after the discussion of the high temperature pairing results, in the next part of this thesis, I will lay out a roadmap, combining general concepts with specific measurements, on how to make progress towards measuring microscopic correlations also in a macroscopic quantum system. As a consequence, the many-body pairing experiments discussed in this chapter can be seen as an important step towards a better understanding of strongly correlated Fermi gases on their own, as a motivation for the remainder of the thesis to build up a toolbox for correlation measurements, and as the ideal system to test this toolbox on.

3.1. High temperature pairing in a strongly correlated 2D Fermi system

At the most fundamental level, quantum exchange statistics prevents any macroscopic occupations of a single quantum state by fermionic particles. Therefore, a pairing mechanism is the central mechanism required for fermionic superconductivity and superfluidity. As discussed in section 2.3.3, a very useful framework to discuss a system interacting via s-wave scattering with a variable scattering length

is the BEC-BCS crossover. The two limiting cases differ fundamentally in their pairing properties. BCS theory describes the phase transition by an instability of the Fermi surface towards pair formation at the critical temperature T_C [34], in conjunction with the opening of a superfluid gap. The gap, Δ_{sf}, represents the order parameter of the system and accounts for a suppression of the density of states at the Fermi surface. Crucially, these Cooper pairs are only stabilized by the presence of the Fermi surface and can thus be considered many-body induced. Within BCS theory, the temperature scale T^* where the pairs form coincides with the critical temperature $T_C = T^*$. This is quite different in the BEC limit. Here, tightly bound two-body molecules are populated thermally already at very high temperatures $T^* \gg T_C$. Subsequently, at the critical temperature T_C, orders of magnitude lower ($k_B T_C \ll E_B$), these point-like bosonic compound particles condense into a mBEC. Of particular interest is the strongly interacting regime, between the limiting cases, where the system is still fermionic in the sense that the chemical potential is positive, $\mu > 0$, such that a Fermi surface is present. Thus, paired states are still expected to form at a finite momentum. In this regime, fermionic pairing and superfluidity are still closely related phenomena, however not equivalent [164], such that pairs can form even without any macroscopic phase coherence established. Understanding this so-called pseudogap phase, where $T^* > T_C$, on a fundamental level is an outstanding question in many-body physics, also in the context of high-temperature superconductivity [149, 165–167]. Of particular interest are (quasi-)two-dimensional systems where, due to the increased role of quantum fluctuations, the pseudogap region is expected to be more pronounced [126]. A prominent example of a pseudogap region is found in high-T_C cuprates with a finite doping factor [168] or, more directly connected to the s-wave BEC-BCS crossover, in high-T_C iron selenide films [149, 167]. When discussing 2D systems, it has to be kept in mind (as discussed in section 2.3) that unlike in 3D, a two-body molecular bound state exists for arbitrarily small attractive interactions (and thus in a quasi-2D system for all 3D scattering lengths). In addition, the second order phase transition at T_C has to be replaced by a topological BKT transition.

According to the above considerations, it is tempting to identify the BEC limit of the crossover with a pseudogap phase, since here $T^* > T_C$. However, we will apply a more rigid definition according to which a pseudogap is accompanied by a reduced spectral weight at the Fermi surface above T_C [126]. As a consequence, this implies the pairing mechanism to be many-body induced with the excitation spectrum gapped at a finite momentum k. In particular, we demand the chemical potential to be positive, $\mu > 0$. This is expected only to happen for

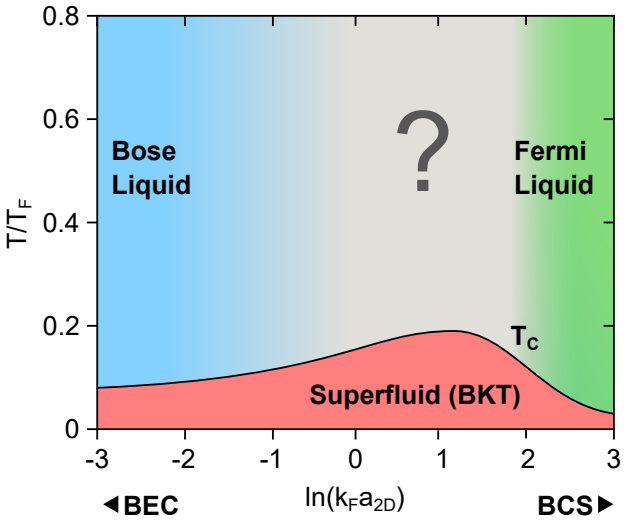

Figure 3.1.: **Schematic phase diagram of the 2D BEC-BCS crossover.** The ground state of the the 2D BEC-BCS crossover is a BKT superfluid for all interaction parameters. In the BCS limit, the critical temperature becomes exponentially small, with the normal phase above T_C described by a Fermi liquid of unpaired fermions. In the BEC limit, the normal phase is instead described by a (weakly interacting) Bose liquid of tightly bound molecules. In the crossover regime, the critical temperature is anomalously large, as experimentally studied in [15]. The nature of the normal phase above T_C is neither captured by a Bose nor a Fermi liquid description and is not yet fully understood. Adapted from [18].

$\ln(k_F a_{2D}) \gtrsim 0.5$ [126].

In figure 3.1 a schematic drawing of the finite temperature phase diagram is shown. Measurements of the critical temperature, the nature of the phase transition and the equation of state have previously been performed in our group [15–17]. In turn, the nature of the normal phase above the critical temperature in the crossover regime has proven elusive so far. Only in the limiting regimes of weaker interactions, descriptions in terms of a weakly interacting Bose or Fermi liquid exist.

There have been a range of measurements on pairing above the critical temperature for superfluidity in the BEC-BCS crossover [169–175]. Crucially, none of the measurements has shown any evidence of pairing above T_C or a pseudogap behaviour in a regime where it cannot be explained by two-body (that is bosonic) correlations alone [126, 165, 176–179].

In this chapter, I will present measurements on the normal phase in a strongly correlated quasi two-dimensional two-component Fermi system, revealing a region in the phase diagram which significantly deviates from a Bose or Fermi liquid behaviour. In this region, a pairing mechanism influenced by many-body

correlations allows for pairing far above the critical temperature for superfluidity.

3.1.1. Remarks on a mean field treatment

In this chapter, I will oftentimes refer to a BCS treatment of the BEC-BCS crossover as already introduced in section 2.3.3. I should stress again that while it is a consistent theory [126] and thus to a large part responsible for the success of the BEC-BCS crossover as a concept, it is not expected to be accurate in the crossover regime. In particular, the critical temperature is dramatically overestimated for strong interactions [15], partially due to the fact that the enhanced role of quantum fluctuations in two-dimensional systems is not included in a mean field model. In this context, in [169], an interesting (but purely qualitative) conjecture was presented. To this end, consider a complex BCS type order parameter given by $\Delta(x) = |\Delta(x)|e^{i\theta(x)}$. We know that below the critical temperature T_C a gapped (BKT) superfluid forms, such that the expectation value of the gap becomes finite, that is $\langle\Delta(x)\rangle =: \Delta_{sf} > 0$. Above the critical temperature, thermal fluctuations in conjunction with quantum fluctuations destroy any (quasi) long range order. In other words, the phase factor is scrambled such that $\langle e^{i\theta(x)}\rangle = 0 = \Delta_{sf}$. Nevertheless, the amplitude of the gap parameter $\langle|\Delta(x)|\rangle =: \Delta_{pseudogap}$ is potentially still finite up to a higher temperature scale T^*. The conjecture states that BCS theory, at least approximately, correctly predicts the onset of a finite pairing gap $\langle|\Delta(x)|\rangle$ at T_C^{BCS}. At the same time, the prediction that phase coherence establishes at the same temperature is incorrect due to the negligence of quantum fluctuations. This would suggest identifying $T^* = T_C^{BCS}$. While this model is clearly oversimplified, it helps in gaining intuition and also motivates, why a pseudogap regime is expected to be more prominent in lower dimensions. In particular, this interpretation becomes exact again in the weakly interacting BEC limit.

3.2. Measurement of high temperature pairing

In this section, I will present the experimental measurements on high temperature many-body induced pairing in the strongly correlated regime of a 2D BEC-BCS crossover. I will start with brief overview of the preparation scheme and continue with a step-by-step presentation and interpretation of the measurements.

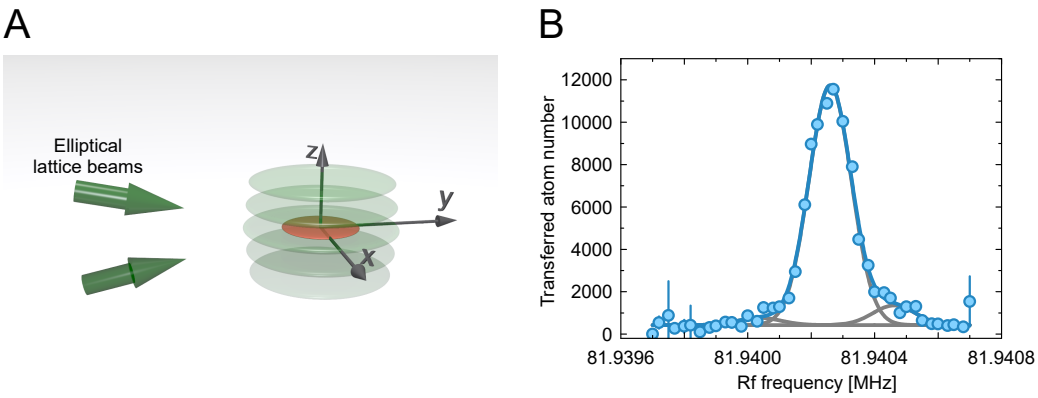

Figure 3.2.: **Preparing a single layer of the SWT. A:** Sketch of the SWT. The standing wave potential (light green) is formed by the interference of two phase-stable laser beams derived from the same source. The atoms (red) are loaded into the central layer. **B:** Rf tomography method to experimentally confirm loading into a single layer. Starting from a gas of atoms in state $|1\rangle$, an rf pulse with a variable frequency in the vicinity of the $|1\rangle - |2\rangle$ transition is applied. During the whole time, a magnetic field gradient is turned on such that the transition frequency becomes spatially dependent due to the locally varying magnetic offset field. The transferred atom number in state $|2\rangle$ is recorded. The central peak corresponds to atoms in the central layer while small side peaks indicate a small population in adjacent layers. From a multi-peak fit to the data (blue: full model given by sum of three Gaussian functions; grey: individual peaks) we can estimate that at least around 90 % of the atoms are loaded to the central layer.

3.2.1. Preparation of a quasi-2D system

In order to perform measurements in quasi-2D, it is necessary to strongly confine the atoms along one of the spatial axes. In our case this is the z-axis. The confinement is induced by a far off-resonant standing wave optical dipole trap (SWT). The trap potential is derived from a single elliptical (aspect ratio 1 : 8, elongated along z-direction) laser beam of wavelength $\lambda = 1064\,\mathrm{nm}$.[1] The beam is split using a 50:50 beam splitter and subsequently both beams are focussed onto the atoms intersecting under an angle of 14°. The potential formed by the two interfering beams is given by a layered stack of potential discs, each with a tight confinement along the vertical axis and a much weaker, almost isotropic confinement in radial direction as schematically illustrated in figure 3.2. The distance between the different potential maxima is around 4.4 µm. At a typical trap depth of $V_0 = 500\,\mathrm{nK}$ the trap frequencies of the central disc are measured

[1] Light from a 50 W NUFERN SUB-1174-22 fibre amplifier, seeded by an Innolight Mephisto-S 500NE is used in this setup. This laser setup features a very low intensity-noise spectrum in the range of the typical trap frequencies such that parametric heating is minimized.

to be $\omega_z \approx 2\pi \cdot 6.95\,\mathrm{kHz}$ for the strongly confined axis and $\omega_x \approx 2\pi \cdot 23.4\,\mathrm{Hz}$, $\omega_y \approx 2\pi \cdot 21.2\,\mathrm{Hz}$ along radial directions. Therefore, the aspect ration is $\omega_x : \omega_y : \omega_z \approx 1.1 : 1 : 327$. Note that a significant contribution to the radial confinement is made by an additional magnetic saddle point potential due to the Feshbach coils (deliberately) placed slightly off of a Helmholtz configuration (see [156, 157, 180] for details). By comparing the spacing between the potential maxima to the vertical harmonic oscillator length $a_z^{HO} \approx 550\,\mathrm{nm}$ it is clear that at least for the ground state (or lowest band) tunnelling between layers is negligible.

Loading of a single layer

Loading of a single layer of the SWT is described in detail in [156, 157]. The starting point is a mBEC prepared as described in section 2.5.1. Loading a molecular gas is more efficient due to the absence of the Fermi pressure otherwise enlarging the cloud size. For this set of experiments, the ODT used for evaporation is already flattened with the help of elliptically focussed beams. In addition, we can increase the mode overlap with a single layer by creating a time-averaged potential. For this, the potential is *smeared out* in horizontal direction by modulating the position of the ODT beams with a frequency far above typical trap frequencies [156]. Finally, it is necessary to tune the vertical position of the atomic cloud with respect to the interference pattern by applying a small magnetic field gradient of up to $\pm 6\,\mathrm{G/cm}$. After careful alignment of all the traps involved and a suitable trap frequency matching, we can transfer at least 90 % of the atoms into the central layer of the SWT. There are two complementary experimental techniques available to us in order to determine the single layer loading efficiency. Firstly, a tomographic method based on rf transitions which are made spatially dependent by an applied magnetic field gradient (see figure 3.2 and [156, 157] for more details). Secondly, a suitably tailored time-of-flight method (based on [181], see section 5.3 for a detailed discussion of the broader picture in terms of so-called matter wave optics). After loading a single layer, an additional evaporation step incorporating a strong magnetic field gradient of typically $30\,\mathrm{G/cm}$ is performed to remove atoms excited to higher bands during the loading procedure and to set the atom number. After this second evaporation, we are left with around 35000 atoms per spin state at a temperature of around 50 nK.

Reaching the 2D regime

In addition to loading a single layer of the SWT we have to ensure that the system is in the (quasi-)2D regime. This is achieved when all the atoms are in the

motional ground state along the vertical direction. For an ideal Fermi gas at zero temperature, the number of states available within the ground state can be easily estimated. Based on the measured trap frequency and the density of states of a fully harmonic trap, around 49 000 atoms (per spin state) could be accompanied. However, there are a few more details to consider: First of all, any interactions will alter the density of states. In addition, a finite temperature allows for occupations above the Fermi-energy, while on the other hand, the emergence of Bose statistics for a deeply paired system allows for larger occupation numbers of individual states. Furthermore, as discussed in section 2.3.2, for deeply bound molecules we will encounter the situation where the molecular wave function is three-dimensional, while the kinematics of the molecule are fully restricted to two dimensions. Therefore, I should clarify that despite the fact that we carefully ensure initiating the system in the kinematic 2D regime, all observations made in the following are indeed expected to be at least somewhat influenced by admixtures of higher lying states in axial direction.
In order to check experimentally that we are in the quasi-2D regime [182], we tune the system into the weakly interacting regime, limited only by the background scattering length. Afterwards, we switch off the SWT potential instantaneously and let the cloud expand for a short free time-of-flight of 3 ms. Subsequently, we image the cloud along the horizontal axis and record the cloud width by a Gaussian fit to the data. We can measure the width for different atom numbers, corresponding to a different second evaporation depth in the SWT. The width is compared to the theoretical expectation of a ground state wave function according to the measured trap frequencies. This measurement is shown in figure 3.3. It is observed that up to around 50 000 atoms per spin state, there is no significant population in vertically excited states. The experiments described in this chapter are thus performed with around 30 000 atoms, where the quasi-2D assumption is well fulfilled for weakly interacting systems. A similar measurement is not easily possible for stronger interactions. However, when tuning towards the BEC side by increasing the attractive interactions we expect this measurement to be rather an upper limit on the atom number allowed.

Estimating the parameters of the regime

For a homogeneous quasi-2D system we can combine the thermodynamic parameters into two dimensionless quantities, fully determining the phase diagram. They are given by the interaction parameter $\ln(k_F a_{2D})$ and the relative temperature T/T_F. In order to determine these quantities, in this chapter, we will apply the

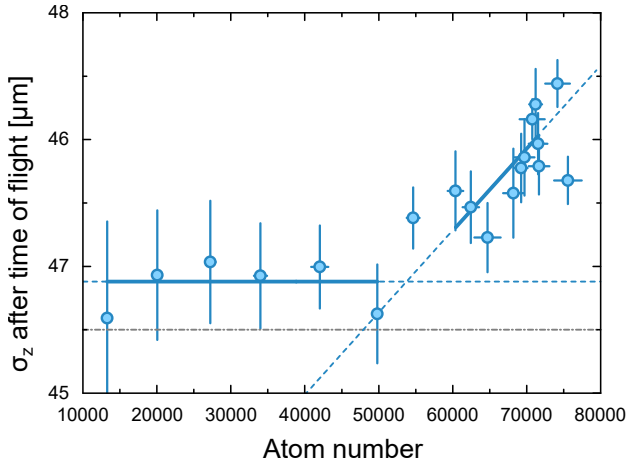

Figure 3.3.: **The quasi-2D limit.** Measured axial cloud width after a short time-of-flight of 3 ms. The kink in the measured width indicates the population of higher axial excitations for atom numbers larger than around 50 000. The position of the kink is extracted from the intersect of two linear fits to the data (solid blue line: linear fit; dashed blue line: guide to the eye). In grey, also the expected ground state width based on the measured particle number and trap frequencies, assuming fully harmonic potentials, is indicated. We conclude that, when working at around 30 000 atoms, we are well within the quasi-2D regime.

local density approximation introduced in section 2.3.2. This means we will assign the thermodynamic quantities T/T_F and $\ln(k_F a_{2D})$ of a homogenous system to a density region with a local density $n_{2D}(r)$. In the normal phase, the approximation made that the potential varies slowly on the scale of typical correlation length scales in the system, translates to the requirement of $k_F(r)R \gg 1$. Here, k_F accounts for the typical momentum scale of the system (and thus the thermal de-Broglie length) and R is the typical spatial extent of the cloud. Based on typical experimental parameters, we can faithfully apply the local density approximation for temperatures below $T/T_F \approx 1.5$.

In order to determine the thermodynamic quantities, we need the local density $n_{2D}(r)$, fixing $k_F = \sqrt{4\pi n_{2D}(r)}$ and $T_F = \frac{\hbar^2 k_F^2}{2mk_B}$, as well as the global temperature of the sample and the 2D scattering length a_{2D}. We can calculate the renormalized 2D scattering length and the two-body binding energies based on the 3D scattering length and the trap parameters using equations 2.41 and 2.42. We measure the density spatially resolved by a carefully calibrated absorption imaging scheme. As we are working with a single-layer 2D sample, when imaging along the vertical dimension, we can directly measure the in-situ density $n_{2D}(r)$ (as opposed to a 3D sample were one dimension is always averaged over). We

are probing the system using an imaging beam with an intensity comparable to the saturation intensity of the optical transition. Due to the large number of scattered photons, we have to compensate Doppler shifts during imaging. In addition, we also have to account for dark state losses due to not fully closed optical transitions (see also chapter 5). I have carefully calibrated and discussed the imaging system already in a previous work, therefore the reader is referred to [157, 183] for more details. In total, after calibration, we estimate the systematic uncertainty in the density to be around 7 %.

Finally, also the temperature is needed for a full description of the system. We determine the global temperature of the sample by fitting reference equations of state (EOS) to our sample. This procedure is based on the techniques developed in [17] and furthermore described in detail in [157]. In order to infer the functional form of the EOS, $n(\mu, T, r)$, in terms of the temperature and chemical potential μ, the underlying physics has to be fully known, which is here clearly not the case. However, we can estimate the temperature based on the asymptotic limiting cases. For example, the very low density wings of the atomic cloud correspond to a very high relative temperature T/T_F (within a local density approximation). We can therefore try to fit this regime with a Boltzmann EOS

$$n_0 = \frac{\alpha}{\lambda_T^2} e^{\alpha\beta\mu}, \tag{3.1}$$

where λ_T is the thermal de-Broglie wavelength and $\beta = \frac{1}{k_B T}$. The factor $\alpha \in \{1, 2\}$ accounts for the fact that the system is molecular for $\ln(k_F a_{2D}) \leq 0$, corresponding to $\alpha = 2$, and fermionic for $\ln(k_F a_{2D}) \geq 2$. In-between these two limiting cases, we interpolate α (see [156]). We refine the temperature determination by comparing also to different EOSs such as a virial expansion in the low density regime and a Thomas-Fermi EOS in the high density regime, as well as comparing to Luttinger-Ward and quantum Monte-Carlo simulations [17, 18, 156, 157]. All methods show consistent results leading to a faithful temperature estimation.

To summarize, for a fixed realization of an atomic cloud in the quasi-2D regime we assume a fixed global temperature T and a two-body binding energy E_B. In addition, based on the local density we introduce a local interaction parameter $\ln(k_F a_{2D})$ and relative temperature T/T_F dependent on the radial distance from the cloud. This is shown in figure 3.4 for a typical example. Note that the atomic cloud is slightly elliptical such that for this density profile an elliptical averaging scheme has been used. We will frequently refer to specific datasets by the values of $\ln(k_F a_{2D})$ and T/T_F in the centre of the cloud. However, it has to be

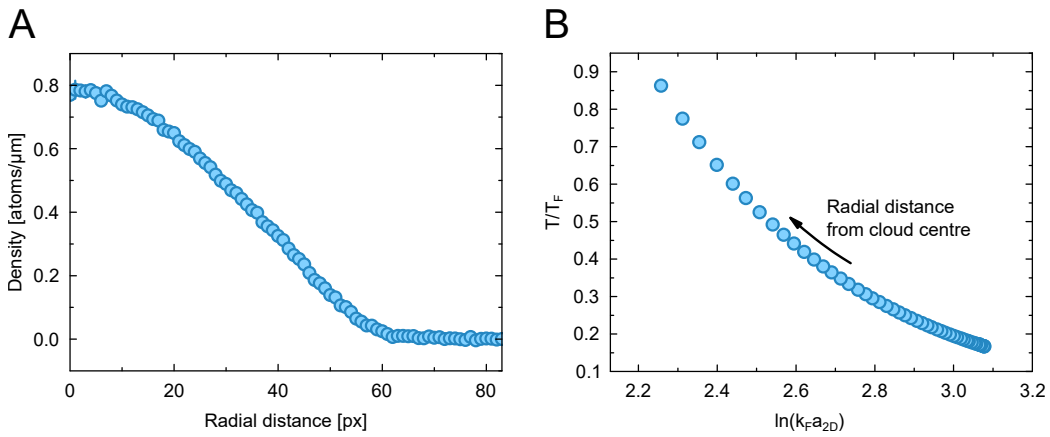

Figure 3.4.: **Relating the measured cloud profile to local parameters. A:** Typical example of a measured density profile. The data is elliptically averaged in accordance with the symmetry of the trap potential. **B:** Corresponding local parameters for the same dataset within the LDA, calculated using the global temperature and magnetic offset field. The central region of the cloud profile corresponds to the largest $\ln(k_F a_{2D})$ and the smallest relative temperature T/T_F. For a larger radius, the density is reduced and correspondingly the system becomes more bosonic (smaller $\ln(k_F a_{2D})$) while the relative temperature increases.

always kept in mind that, as we go towards the lower densities further away from the centre, T/T_F increases while $\ln(k_F a_{2D})$ decreases. Therefore, for sufficiently small densities, we are always in the high temperature, bosonic regime. This can be understood intuitively by comparing the fixed two-body pair size to the interparticle distance. The latter is increasing while reducing the density, such that at some point it is much larger than the molecular size and the system becomes bosonic. At the same time, due to the reduced density, all intrinsic energy scales are lower such that in turn the relative temperature increases.

3.2.2. Spatially resolved rf spectra

We probe our system by rf spectroscopy. This has been a very successful tool in studying quantum gases, in particular with respect to their pairing properties. The general scheme is sketched in figure 3.5. Our sample consists of a two component mixture of states $|a\rangle$ and $|b\rangle$ (in the actual experiment this will be either a $|1\rangle - |2\rangle$ or a $|1\rangle - |3\rangle$ mixture). Suppose that some fraction of the atoms is bound into molecules with a binding energy E_B, and (for simplicity) that the gas is otherwise non-interacting. In addition, we have a third initially unoccupied state $|c\rangle$ available (either state $|3\rangle$ or $|2\rangle$). The energy difference between state $|b\rangle$ and $|c\rangle$ is typically around $E_{|c\rangle-|b\rangle} = 2\pi \cdot 80\,\mathrm{MHz}$, and thus conveniently in the

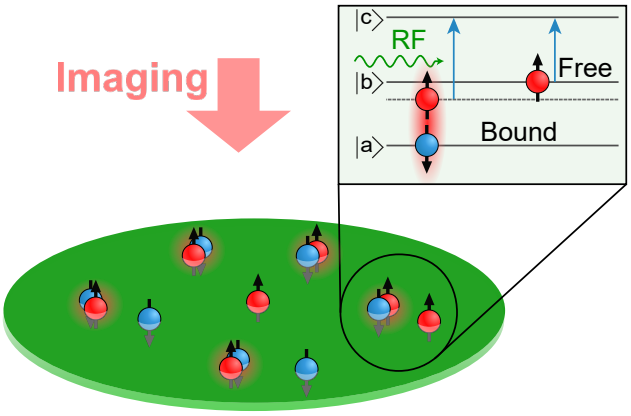

Figure 3.5.: **Schematic illustration of the rf spectroscopy method.** A mixture of paired dimers and free atoms is assumed. By an rf pulse, a fraction of the atoms in state $|b\rangle$ is transferred into an initially unoccupied state $|c\rangle$. The transition frequency of the paired atoms is blue-shifted with respect to the free atoms due to the binding energy.

rf range.[2] Therefore, by applying a short (global) rf pulse at the corresponding frequency, we can transfer a fraction of the free atoms into state $|c\rangle$. The atoms bound into molecules are not resonant with the pulse if the binding energy is sufficiently large. However, we can tune this transition into resonance by detuning the centre frequency of the rf pulse accordingly. Therefore, by recording the fraction of atoms transferred into state $|c\rangle$ as a function of the applied frequency, we can get a measure for both the fraction of atoms paired and the binding energy. In a real system, there are a few more details to consider. First of all, it should be noted that the recoil energy of the rf photon is small compared to the mass of a ^{6}Li atom. Therefore, the momentum of the atom remains approximately constant upon absorption of one photon. In addition, we have to take the full dispersion relation of our initial and final state system into account. Therefore, in figure 3.6 a more realistic sketch of the rf spectroscopy method is shown. Here, we have chosen rather generic single-particle dispersion relations of a (mean field) BEC and BCS state[3], which account for the limiting cases of a weakly interacting bosonic or fermionic system close to $T = 0$. Indicated are the lowest (bound) branch, which is fully occupied for $T = 0$ and the branch of quasi-particle excitations (which were referred to as 'free' particles in the above discussion). In addition, well separated in energy, the dispersion relation of the final state is indicated,

[2]The rf transition flips the nuclear spin, therefore we can drive transitions with $\Delta m_I = \pm 1$, see equation 2.58.

[3]The BEC limit might look unexpected. Note that shown here is the *single-particle* and thus fermionic dispersion relation and not the dispersion relation of the bosonic molecules.

which is assumed to be the quadratic relation of non-interacting particles (final state interactions to be discussed later).
It is important to realize that, depending on the dispersion relation, the minimum of the quasi-particle branch can be at around $k \sim 0$ (in the BEC limit) or $k \sim k_F$ (in the BCS limit). Therefore, also the excitation of the quasi-particle ('free') branch branch into the continuum happens preferably at a finite momentum in the latter case. In this set of experiments, we do not have access to the momentum of the transferred atoms. Nevertheless, we can observe signatures of this behaviour in the rf response, which is also schematically drawn in figure 3.6. In the BEC limit, we expect a response of the unpaired atoms centred around zero frequency offset (relative to the non-interacting transition frequency). It is symmetrically broadened by the finite temperature with an integrated weight proportional to the fraction of free particles. In addition, offset by the binding energy, the bound peak appears. An asymmetric peak shape with a sharp threshold is expected. While the minimum transition shift is given by E_B at $k = 0$, there are additional contributions at finite momentum corresponding to a larger shift due to the finite momentum width of the pairing wave function. In the BCS limit, we expect an asymmetric peak from the (Cooper) bound atoms offset again by E_B. In addition, there is a peak from quasi-particle excitations. In this limiting case, they are at finite momentum and offset in frequency by the gap. This 'free' peak is slightly asymmetric due to the functional form of the dispersion relation. It is remarkable that (at least within mean field BCS theory) in two-dimensional systems the threshold for the bound state is always at E_B relative to the non-interacting transition frequency. Therefore, only by recording the free branch in addition, the shift due to the superfluid gap becomes visible.
We do not expect our system to be fully described by either of these two dispersion relations. Nevertheless, we can get a good intuition on how to interpret the rf spectroscopy data. In particular, we have learned that it is instructive to compare the measured energy difference between bound and free peak with the two-body binding energy. In addition, in the case where we have *any* dispersion relation with a gap at finite momentum, we expect this gap, and therefore also the rf response, to be dependent on the density. For the specific example of the BCS limit, we can read off the density dependence from the functional form of the gap, $\Delta = \sqrt{2E_F E_B}$.
At this point it is clear that an important experimental step is to record the rf response locally resolved in order to apply the LDA and observe possible shifts of the transition frequency with the density. In principle, we can record the atoms transferred into the final state locally using absorption imaging (or equivalently

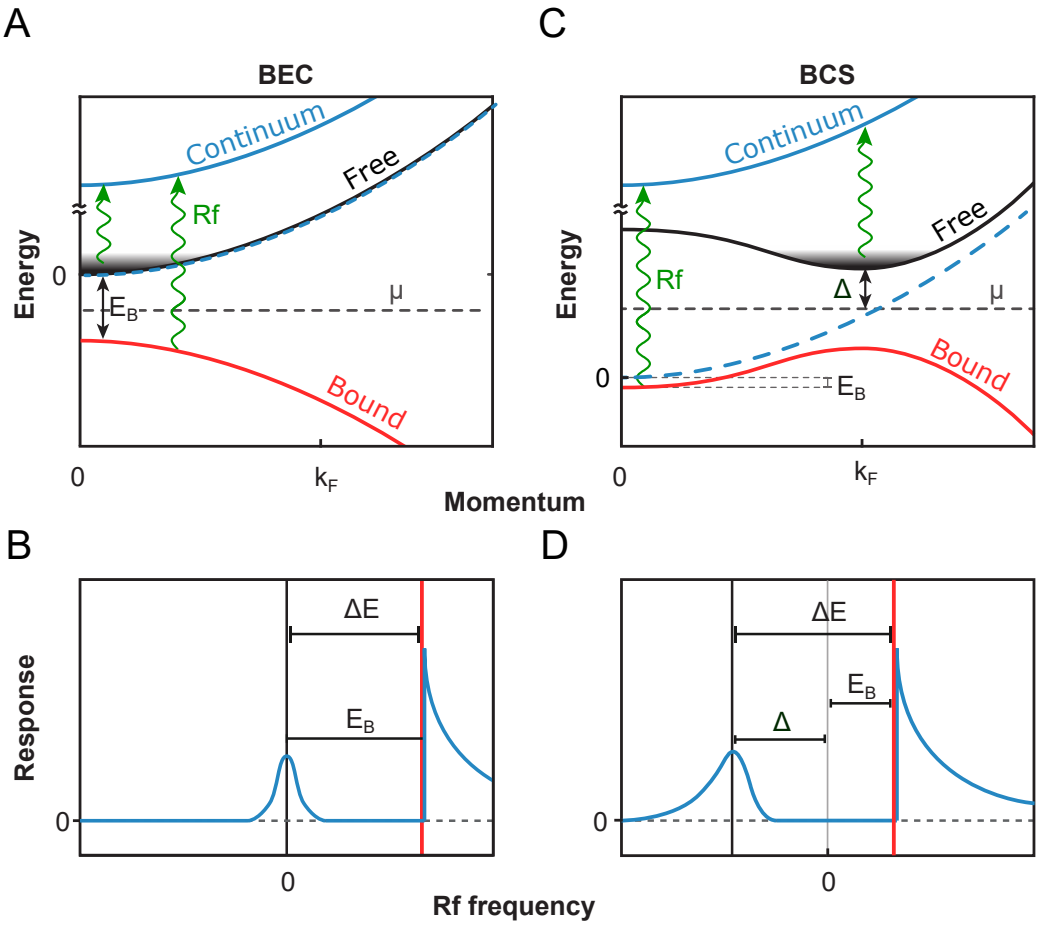

Figure 3.6.: **Rf spectroscopy in the BEC and BCS limit. A:** Single-particle dispersion relation in the BEC limit. At $T = 0$ only the bound branch (red line) at negative energies (relative to the non-interacting free branch) is occupied. The chemical potential (grey dashed line) is negative with $\mu = -E_B/2$. At finite temperature there is also some population in the unpaired free branch (black), predominantly at $k \sim 0$. We drive rf transitions (green arrow) from either the bound or the free branch into the continuum (blue line). Indicated as a reference (dashed blue line) is also the non-interacting dispersion relation. **B:** Corresponding idealized rf spectrum. Free atoms contribute a symmetric peak at around zero frequency shift relative to the non-interacting transition. The onset of the asymmetric paired peak is at E_B, corresponding to the $k = 0$ contribution, with the distance between the two peaks given by $\Delta E = E_B$. **C:** Single-particle dispersion relation in the BCS limit (colour scheme as in A), with the many-body gap Δ at $k = k_F$ and a positive chemical potential. As opposed to A, the unpaired particles first occupy the free branch around $k \sim k_F$. **D:** Corresponding idealized rf spectrum. Free atoms contribute a slightly asymmetric peak based on the signal from $k \sim k_F$ which is shifted by Δ relative to the non-interacting transition. The onset of the asymmetric paired peak is again at E_B for the $k = 0$ contribution, with the distance between the two peaks now given by $\Delta E = E_B + \Delta$ and density dependent. Adapted from [18].

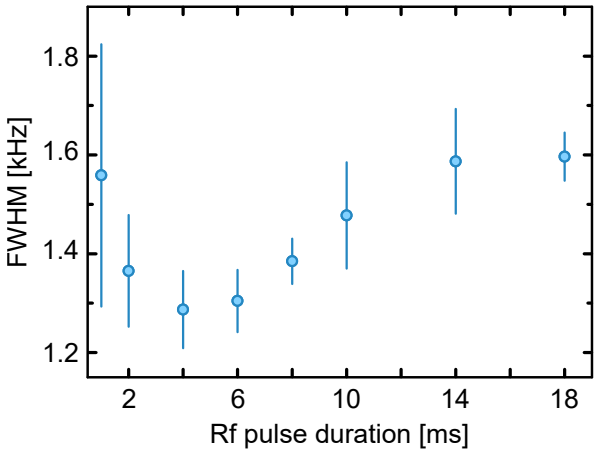

Figure 3.7.: **Validity of the LDA.** Experimentally determined full width at half maximum of the rf peak (free peak) as a function of the pulse duration. For short rf pulses, the width is limited by Fourier broadening. For longer pulse durations, the width increases due to diffusion in the trap. We choose to work at a pulse duration of 4 ms corresponding to a frequency resolution of $\Delta\nu = 222\,\mathrm{Hz}$. Adapted from [18].

record the atoms remaining in the initial state). However, on the scale of the trap period, the atoms diffuse within the cloud and the rf signal is smeared out. On the other hand, if the rf pulse is much shorter than the trap frequency (and other intrinsic timescales), local resolution is at least partially retained. Based on these considerations, it seems favourable to choose the rf pulse as short as possible. However, if the pulse is too short, the energy resolution is reduced due to the Fourier limit. We use an rf pulse which is approximately rectangular in the time domain with a pulse duration τ_{rf}, such that the frequency resolution is given by $\Delta\nu \approx 0.9\frac{1}{\tau_{rf}}$. For this set of experiments, we choose to work at a pulse duration of $\tau_{rf} = 4\,\mathrm{ms}$ corresponding to a Fourier limited rf resolution of $\Delta\nu = 222\,\mathrm{Hz}$, which has to be compared to the typical radial trap frequency of $\omega_{rad} \gtrsim 2\pi \cdot 20\,\mathrm{Hz}$, or equivalently a trap period of $T_{rad} \approx 50\,\mathrm{ms} \gg \tau_{rf}$. We experimentally confirm that the chosen pulse duration is reasonable by recording the width of a rf response at a fixed density as a function of τ_{rf}. This measurement is presented in figure 3.7.

As expected, we observe that for small $\tau_{rf} < 4\,\mathrm{ms}$, the width is larger in accordance with the Fourier limit. In turn, for $\tau_{rf} > 4\,\mathrm{ms}$ the width also increases, which we attribute to diffusion during the rf pulse. By choosing $\tau_{rf} = 4\,\mathrm{ms}$ from here on, partial position resolution is retained. We adapt the power of the rf pulse separately for each experimental setting in order to retain a similar fraction of

transferred atoms (Rabi rate Ω between 60 Hz and 250 Hz). For these settings, we are not limited by power broadening. Due to the interaction-induced decoherence rate of the order of 1 ms, the transfer has to be described in a (partially) incoherent framework (see below), in its most basic implementation given by Fermi's golden rule. We work in the approximate linear response regime.
We are now in the position to record spatially resolved rf spectra. Note that depending on the situation, we will choose to work either with a $|1\rangle - |2\rangle$ or a $|1\rangle - |3\rangle$ initial state mixture. In order to avoid confusion, I will always define relative energies in such a way that a positive energy offset corresponds to an attractive shift or pairing. In figure 3.8, an experimentally measured spectrum is presented for a $|1\rangle - |2\rangle$ mixture, with $\ln(k_F a_{2D}) \approx 1.5$ and $T/T_F \approx 0.3$ in the centre of the cloud. In the upper panel, the density profile of the cloud, averaged over a few realisations, is depicted with, $n'(r, \omega_{rf})$, and without, $n_0(r)$, application of the rf pulse. We infer the profile of the transferred density by taking the difference $\delta n(r, \omega_{rf}) = n_0(r) - n'(r, \omega_{rf})$. Indeed, a distinct feature can be observed: Only at a certain density, corresponding to a specific radius, atoms are transferred into state $|3\rangle$. This strongly indicates that density-dependent effects are required for the correct physical description of the system. In order to quantify this, the response function is shown in figure 3.8. It is defined by

$$I(r, \omega_{rf}) = \frac{\delta n(r, \omega_{rf})}{n_0(r)}. \tag{3.2}$$

Experimentally, it is obtained by first averaging the the difference δn over pixels corresponding to equal densities. For the trap geometry employed here, this corresponds to an elliptical average, where the short radius is denoted by r. Afterwards, the transferred fraction is calculated by normalizing δn to $n_0(r)$, and the experiment is repeated for a range of different rf frequencies. In this way, a 2D map of the rf response is obtained, where the frequency relative to the transition of the non-interacting system is denoted on the y-axis while on the x-axis the radius, corresponding to a specific density and thus also $\ln(k_F a_{2D})$ and T/T_F, is shown. The response is plotted in a colour scale. In the response, a single peak which is clearly density-dependent is observed. Based on this, we can now try to find an interpretation in terms of (many-body) pairing.

3.2.3. Interpretation of the rf spectra

Given the complexity of the system, for a consistent interpretation of the data, a range of different additional aspects has to be considered.

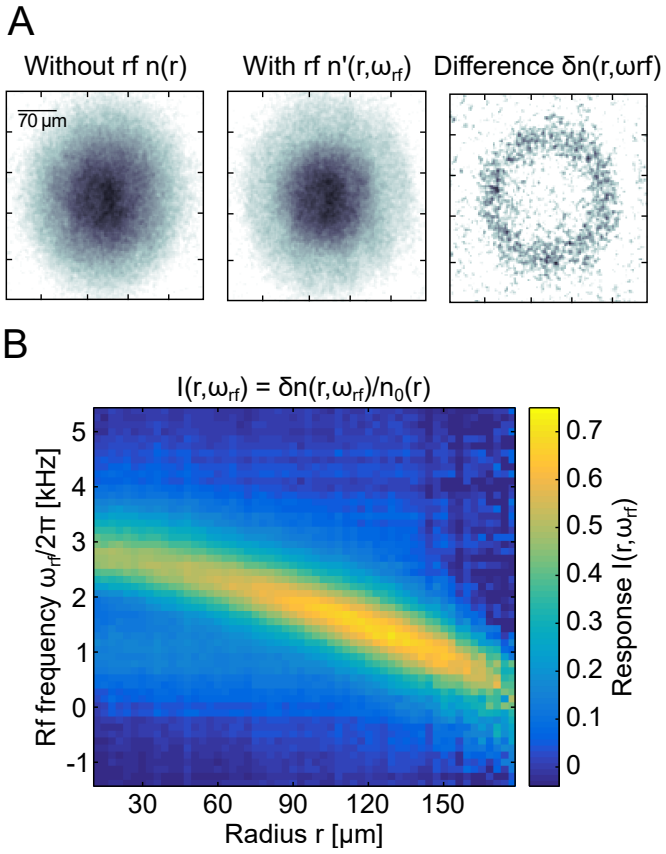

Figure 3.8.: **Measured rf response in the crossover regime.** The system is prepared in the $|1\rangle - |2\rangle$ mixture, with $\ln(k_F a_{2D}) \approx 1.5$ and $T/T_F \approx 0.3$ in the centre of the cloud. **A:** Measured cloud profile, with and without an rf pulse applied at a specific frequency ω_{rf} relative to the non-interacting transition frequency. The transferred fraction δn is calculated by taking the difference of the profiles. Only at a specific density, there are atoms transferred. **B:** By repeating the measurement from A for different rf frequencies, the response function $I(r, \omega_r f)$ is extracted. There is a single and strongly density-dependent peak visible. Adapted from [18].

Interaction shifts

An important hurdle to overcome when trying to interpret the measured rf response is accounting for the final state interactions, as for ^{6}Li the Feshbach resonances in all three combinations of states $|1\rangle, |2\rangle, |3\rangle$ are partially overlapping. The short rf pulses used in our experimental setting are still partially coherent. As a consequence, due to the absence of clock shifts in such a scenario [184, 185], only the interactions between states $|a\rangle$ and $|c\rangle$ have to be taken into account. Nevertheless, final state interactions can in principle be as complicated to describe as the ones in the initial states. Therefore, I will explain an observable

mostly independent of these shifts in section 3.2.4. It is nevertheless important to at least estimate their influence.

First of all, we have the freedom to switch between different initial state mixtures, depending on the ratio between initial and final state interaction strength. Thus it is possible to cover the full crossover regime with a central $\ln(k_F a_{2D}) \in [-0.5, 2]$ in the initial state, while at the same time avoiding working in the crossover regime of the final state altogether, such that the central $\ln(k_F a_{2D}) \notin [-7, 4.5]$ in the final state (calculated using k_F of state $|a\rangle$ and the $|a\rangle - |c\rangle$ scattering length). In addition, we can use the fact that we transfer only a small fraction of the atoms in state $|b\rangle$ into state $|c\rangle$. This suggests a description of the final state in terms of a Fermi polaron quasi-particle, that is a single impurity of a $|c\rangle$ dressed by a background of $|a\rangle$ atoms [185–187]. Importantly, the (zero momentum) spectral function of the Fermi polaron in two dimensions is split into two distinct branches. For negative (and also small positive) $\ln(k_F a_{2D})$, a broad short lived repulsive polaron exists that is shifted towards positive energies. In addition, for positive (and also small negative) $\ln(k_F a_{2D})$, there is a much more narrow attractive polaron correspondingly shifted towards negative energies [186]. In [186], the polaron energies are calculated via a T-matrix approach. In the context of this thesis, we can restrict ourselves to the limiting cases of small $|1/\ln(k_F a_{2D})|$, where perturbative results are applicable [185, 187].

In the limit $E_B/E_F \to \infty$, the repulsive polaron energy E_+ is given by [187]

$$E_+ = \frac{2E_F}{\ln(E_B/E_F)} \tag{3.3}$$

while the attractive polaron energy E_- can be calculated via [185]

$$E_- = E_F \int_0^1 \mathrm{d}u \frac{-2}{-\ln(E_B/E_F) + \ln\left(\sqrt{\left(1 - \frac{E_-}{2E_F}\right)^2 - u} + \left(1 - \frac{E_-}{2E_F} - \frac{u}{2}\right)\right)}. \tag{3.4}$$

In figure 3.9, the energy shifts calculated according to equations 3.3 and 3.4 are shown as a function of $\ln(k_F a_{2D})$. For the interaction regimes considered in this chapter, we expect the spectral weight of the polaronic quasi-particle to be $\gtrsim 90\,\%$ [186] such that a description of the final state in terms of a Fermi polaron seems to be a promising approach. Note that, in addition, final state effects such as the polaron also lead to a change in the expected line shape of the rf response, and a finite lifetime of the final state quasi-particle results in a broadened transition. This will be discussed below.

In addition, clock shifts in the initial mixture $|a\rangle - |b\rangle$ (with respect to the final

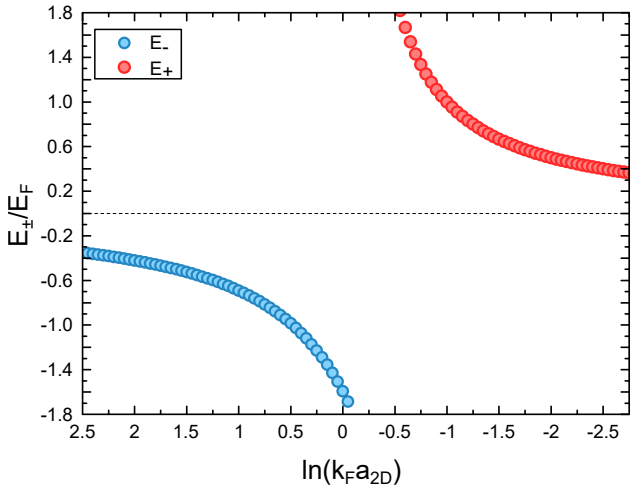

Figure 3.9.: **Polaron energies.** Perturbative results for the repulsive (red) and attractive (blue) polaron energy shift as a function of the Fermi energy and the (final state) interaction strength given in units of $\ln(k_F a_{2D})$.

mixture) can result in an overall shift of all the transitions. We take these shifts into account on a mean field level by considering the Hartree contribution U given by

$$U = g n_{|a\rangle}, \tag{3.5}$$

with respect to the density $n_{|a\rangle}$ in state $|a\rangle$ and the interaction parameter

$$g = \frac{\hbar}{2m} \frac{\ln(k_F a_{2D})}{\ln(k_F a_{2D}) + \pi^2}. \tag{3.6}$$

We will include both the polaron and the Hartree shift in the following. Ultimately, we are however interested in an observable which is (mostly) unaffected by these interaction shifts. I will come back to this in section 3.2.4.

Suitable Fit function

In order to quantitatively describe spectra such as the one shown in figure 3.8, we have to find a suitable functional form of the excitation spectrum. However, the line shape and position are influenced by both the initial and final state interactions, rendering this a very complicated task. Here, I am going to describe a generic function which can account for different possible initial and final state effects. In principle, the (free) parameters of the line shape model, extracted from a fit to the data, are a valid set of observables to describe the relevant many-body physics on their own. As the line shape is significantly broadened by the finite

frequency resolution and the parameters are prone to statistical fluctuation, the only parameters extracted from the model will be the position of the unpaired peak and the threshold frequency of the paired peak. Note that small systematic shifts, in particular on the threshold position, cannot be fully excluded due to the methodology used. However, the further discussion will be based mostly on either qualitative or very large effects, where small systematic shifts are not limiting.
We will try to describe the measured spectra with a line shape function $\Gamma(\omega)$ in terms of the centre frequency of the rf pulse ω. The model is given by the sum of the unbound and bound branch line shapes:

$$\Gamma(\omega) = \Gamma_{bound}(\omega) + \Gamma_{free}(\omega) \tag{3.7}$$

We will see below that the peak $\Gamma_{free}(\omega)$ originating from the unpaired particles is mostly symmetric. Even if there are small asymmetries due to a more complex dispersion relation, they are washed out by the finite frequency resolution. Therefore, it is sufficient to describe this part of the spectrum by a Gaussian profile with peak position, width and amplitude left as free parameters. We will interpret the peak position as the unpaired or quasi-particle excitation frequency. The bound branch line shape $\Gamma_{bound}(\omega)$ is more complex. Based on a Fermi's golden rule treatment of a bound-free transition, we get a threshold function

$$\Gamma_{bound}(\omega) \propto \frac{\theta(\hbar\omega - E_{th})}{\omega^2}, \tag{3.8}$$

in terms of the step function θ and the threshold energy. We will be interpreting the threshold energy as the excitation energy of the paired branch, that is $E_{th} = E_B$. There are a few additional effects which we have to account for. The frequency ω is given relative to the reference frequency. We have defined $\omega = 0$ to be the non-interacting transition frequency, while the proper reference in equation 3.8 is affected by (mean field) interaction shifts of the initial state. This shift directly influences the line shape due to the $\frac{1}{\omega^2}$ factor. We account for this effect by introducing an additional free parameter η replacing $\frac{1}{\omega^2} \rightarrow \frac{1}{(\omega-\eta)^2}$. In [170, 188], a correction factor to the above line shape was presented which takes into account final state interactions. It depends on the two-body binding energy E_B^f of the final state mixture and takes the 2D nature of the scattering process into account. Here, we include this factor to our line shape as well. Importantly, it shifts the maximum away from the threshold frequency, such that the naive approach of interpreting the peak position of the line shape as the binding energy would have lead to an overestimation of this parameter. Finally, we account

for additional broadening of the line shape, mostly due to the finite (Fourier) frequency resolution, and the finite lifetime of the final state polaron, by a Gaussian convolution. The fit function to describe the paired branch excitations is therefore given by

$$\Gamma_{bound}(\omega) = \left(A_b \frac{\theta(\hbar\omega - E_{th})}{(\omega - \eta)^2} \frac{\ln^2\left(E_{th}/E_B^f\right)}{\ln^2\left((\hbar\omega - E_{th})/E_B^f\right) + \pi^2} \right) * \left(\frac{1}{\sqrt{2\pi\sigma_{broad}^2}} e^{-\frac{\omega^2}{2\sigma_{broad}^2}} \right). \tag{3.9}$$

In this formula, E_{th} is given relative to the non-interacting transition frequency and we have included the relative amplitude A_b of the bound branch contribution as well as the width σ_{broad} of the Gaussian broadening. Together with the frequency shift η, these are kept as free parameters, while the final state binding energies calculated based on the magnetic field and are fixed.
In addition to the line shapes described above, we observe some additional signal, which contributes a 'shoulder' to the recorded line shape (visible for example at around 1 kHz in figure 3.8). We attribute this contribution to the spectrum to a small number of atoms in adjacent layers of the SWT [183] and exclude the corresponding frequency region from the fitting procedure.

Limiting cases

Before coming back to the discussion of spectra in the crossover regime, such as shown in figure 3.8, it is instructive to discuss a few limiting cases. In figure 3.10, two example spectra for rather large positive and negative interaction parameters (yet still strongly interacting) are shown.
More on the BEC side, we observe a single excitation peak at a large energy offset, showing the typical asymmetric shape of a bound to free transition. In this situation, we can unambiguously identify the system to be mostly paired. This is supported by the observation that the threshold energy is very similar to the two-body binding energy and not significantly density-dependent. Also, as the thermal energy scale ($T_F/k_B \approx h \cdot 7\,\mathrm{kHz}$) is well below the dimer binding energy, a description in terms of a fully paired Bose liquid seems appropriate. This is quite different for the second spectrum shown on the BCS side of the crossover. Again, we observe only a single peak (and in addition the shoulder feature mentioned above). The slight density dependence is consistent with a Hartree shift. Otherwise we cannot draw too many conclusions in this situation. It is not possible to distinguish any possible paired branch from a unpaired one,

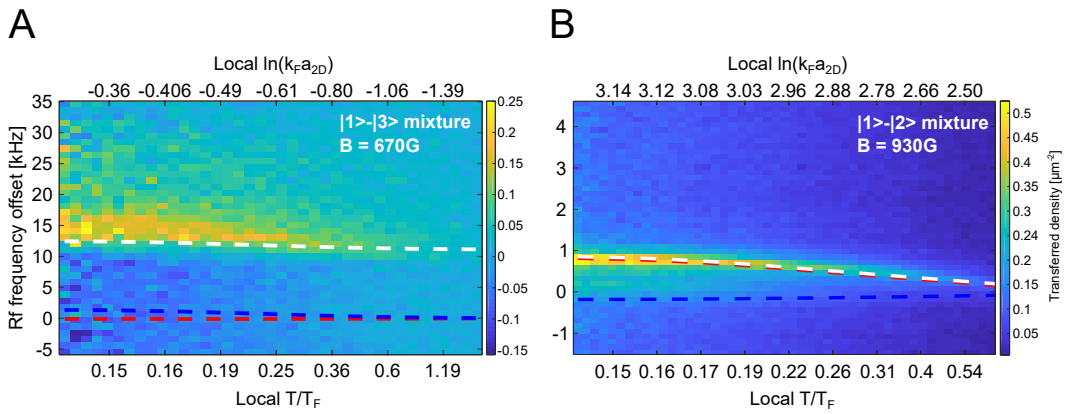

Figure 3.10.: **Rf response in the limiting regimes. A:** BEC limit. There is a single, strongly asymmetric peak visible, corresponding to the bound state transition. In red and blue, the contributions from the Hartree and the polaron shift are indicated, respectively. For the white line, also the dimer binding energy is added on top of the other interaction shifts. It is consistent with the observed onset of pairing. **B:** Towards the BCS limit. There is again only a single symmetric peak visible. No definite statement can be made regarding the paired and unpaired contributions to the observed spectrum. The peak position is consistent with a Hartree shifted transition of unpaired atoms alone. The scale of the dimer binding energy ($E_B = 2\pi \cdot 40\,\mathrm{Hz}$) is not resolved in this case.

as the energy scale set by the two-body binding energy scale ($E_B = 2\pi \cdot 40\,\mathrm{Hz}$) is well below our frequency resolution. It should be noted that, in this limit, any pairs are expected to be broken up thermally. In addition, going further towards the BCS limit, the temperature T^* where the pairs form has to converge to the critical temperature $T^* = T_C$ as given by BCS theory. The most interesting regime is the crossover regime in-between, where for a reasonable temperature regime $T \in [T_C, T_F]$, we observe only a single excitation branch as for example shown in figure 3.8. It is not a-priori clear whether to attribute this peak to a paired or unpaired branch. We can presume, based on the line shape and the fact that the threshold position is not at all described by interaction shifts as introduced above alone, that this should be a bound branch. However, a theory also including the two-body bound state is still not sufficient, as the energies do not match. This is shown for one example in figure 3.11. In addition, based on the expected molecular binding energy E_B and the temperature, a significant part of the pairs should be broken up resulting in two peaks in the spectrum, which is not observed.

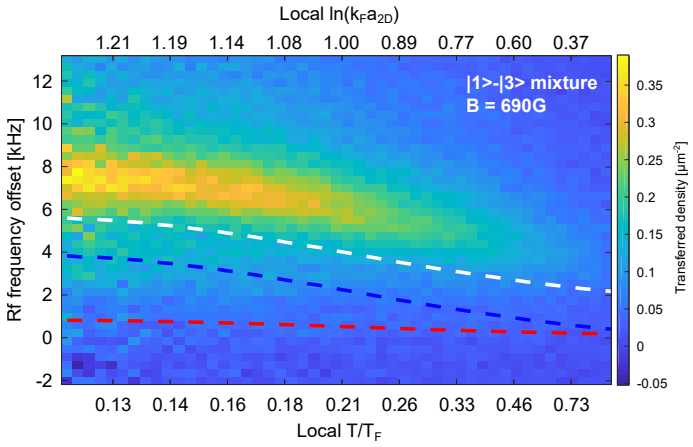

Figure 3.11.: **Spectrum in the crossover regime.** Indicated are the expected Hartree (red) and polaron (blue) shifts with the two-body binding energy on top of these shifts (white). In this regime, the observed spectrum is not consistent with these shifts alone.

The onset of pairing

Before I discuss an important technical trick which we will use to unambiguously identify the distance between the unbound and the bound branch, I will introduce two important crosscheck measurements, which already allow us to draw some conclusions based on the spectra shown above. First of all, we can prepare a system which is in the centre of the cloud well below the critical temperature for superfluidity (which we check with the methods developed in [15, 16]). A local density approximation is in this regime not fully valid any more. However, we will still have *thermal wings* at lower densities[4], which can be interpreted as a region above T_C. In figure 3.12, a measurement of the threshold energy for different local densities converted into different local T/T_F is presented. Interestingly, for all densities only a single peak is observed again, with the threshold position showing a smooth dependence on the density. This indicates that we indeed only see the paired branch and the pairing gap opens up significantly above the critical temperature and features a smooth evolution across the critical temperature in accordance with a pseudogap behaviour.

The second important crosscheck measurement is to study the onset of pairing at very high temperatures. As stated before, below $T/T_F \lesssim 1.5$ no significant unpaired fraction is observed. Nevertheless, for very low densities or very high temperatures, a regime with a significant fraction of unpaired atoms is eventually

[4]The finite correlation length of a 2D superfluid indeed allows for something like a constricted local density approximation.

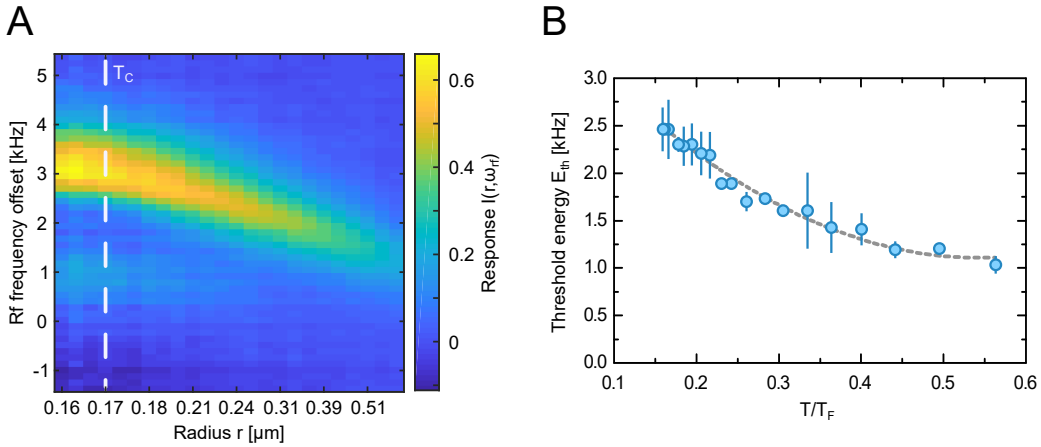

Figure 3.12.: **Threshold energy across the superfluid transition. A:** Spectrum where the central $\ln(k_F a_{2D})$ is well below the critical temperature (the corresponding radius is, based on an LDA, indicated in white). Only a single peak is visible for all densities. **B:** Threshold energy extracted by a fit to the data shown in A (blue points; grey: guide to the eye). The applicability of the LDA in this regime is limited. Nevertheless, it can be stated that only a single peak with a continuously changing threshold energy is observed even when approaching the low density thermal wings of the cloud. Adapted from [18].

reached. This is shown in figure 3.13, for a system prepared at 844 G (central $\ln(k_F a_{2D}) \sim 1.4$) in the $|1\rangle - |2\rangle$ mixture. By a slightly different evaporation scheme, we have prepared a similar sample at different temperatures. Note that the higher temperature sample has, at a similar total atom number, a slightly smaller central density. With these settings we indeed observe two branches above $T/T_F \approx 1.5$. We can compare the fraction of unpaired atoms to the expectations based on the simplified model of a non-interacting mixture of free atoms and dimers in thermal equilibrium. Here, the fraction of unpaired atoms is given by the so-called Saha formula

$$\frac{n_f^2}{n_d} = \frac{m k_B T}{4\pi\hbar^2} e^{-\frac{E_B}{k_B T}}, \tag{3.10}$$

in terms of $n_f(n_d)$, the free (bound) density of particles. It is shown in figure 3.13 for the experimental parameters that the Saha formula is drastically overestimating the unpaired fraction. For a temperature of $T/T_F = 0.54$, around 35 % of the atoms should be unpaired while experimentally, we do not observe a significant unbound contribution. Also at very high temperatures, no consistency is seen.

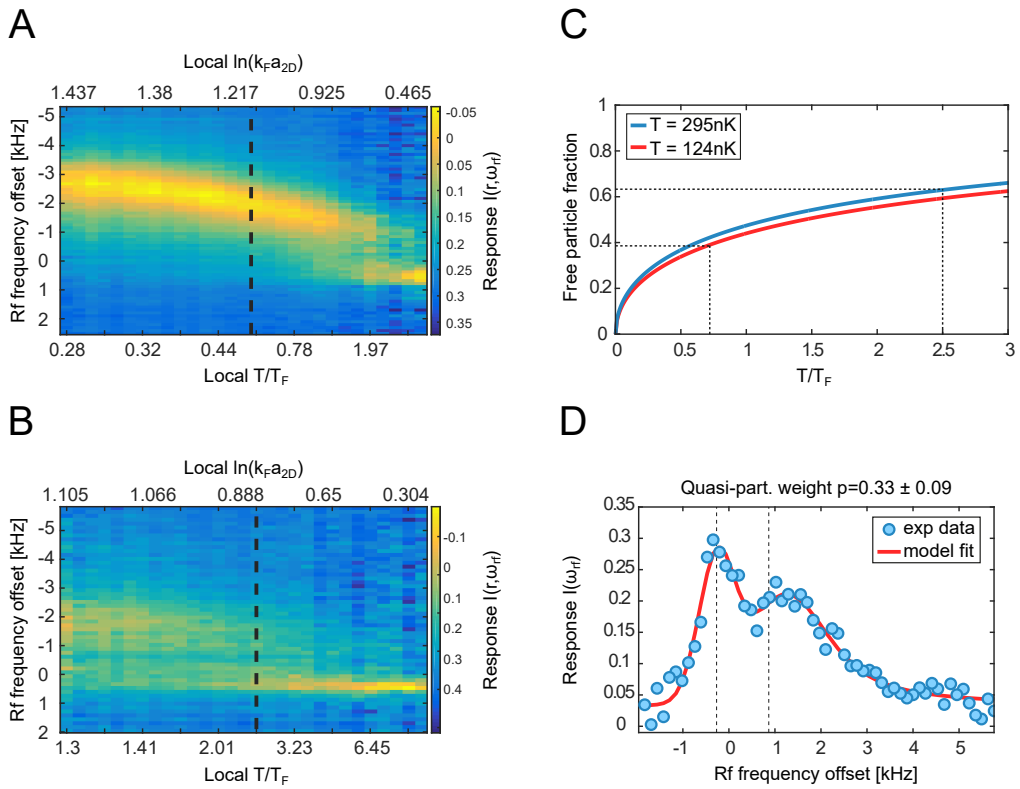

Figure 3.13.: **Onset of pairing. A:** Rf response in the crossover regime, where also the very low density regime is shown. Above $T/T_F \approx 1.5$, two peaks are visible. **B:** The same rf response at a higher initial temperature. Two peaks are visible up to very high temperatures. **C:** Comparison to the Saha formula. The expected unpaired fraction is plotted for global temperatures corresponding to the spectrum in A (red line) and B (blue line). At the local temperatures indicated by the dotted black lines in A and B, an unpaired fraction significantly higher than observed experimentally is expected. **D:** Based on a fit to the cut (black dotted line) through the spectrum in B, an unpaired fraction of around one third is expected (blue: data points; red: model fit, grey dotted lines: determined free particle peak position and threshold energy, respectively). The Saha formula predicts a fraction almost twice as large. Adapted from [18].

Preliminary conclusions

All the measurements presented so far, including measurement in limiting regimes and several crosscheck measurements, support the conjecture made that we indeed observe pairing above T_C which is going beyond physics described by simple molecular bound states. We observe only a single branch of bound particles in the crossover regime. This is the case even for $\ln(k_F a_{2D}) \gtrsim 0.5$, where, based on theory calculations and other experiments [126], the chemical potential is expected to be greater than zero. In addition, the pairing energy does not seem to be

consistent with a two-body molecular binding energy, and appears to be density-dependent. The latter two points are certainly the most important. However, up to now, they are also the weakest statements as they are dependent on the models used. In the following section, I will describe a final set of measurements which will fix this issue and will allow me to draw a set of remarkable conclusions about the normal phase of a strongly correlated 2D quantum fluid.

3.2.4. Observation of many-body pairing

I have concluded, based on the observations presented above, that the fraction of paired atoms is strikingly enhanced in the crossover regime. This result alone is already a very important step towards understanding the strongly correlated regime in 2D. However, it is still challenging to draw any conclusions about the value of the pairing energy and in particular its density dependence, as the results obtained so far are highly dependent on a model-based theoretical description of final state effects. Importantly, we are missing a suitable reference energy, which already includes (most of) the final state effects. The canonical reference scale would be given by the excitations of the unpaired branch. In particular, all mean field (Hartree) shifts as well as polaronic shifts only depend on the density and the scattering length, such that the paired and unpaired branches are shifted common mode.

From these considerations, we can conclude that a sufficient population in the unpaired branch is needed in order to make any progress. It is possible to achieve this based on a quasi-particle spectroscopy method first used in [189] in the context of measuring the gap of a 3D Fermi superfluid. The key idea is to inject a very small fraction of additional atoms in one of the spin-states into the system. Due to the resulting density mismatch, these atoms remain unpaired and occupy the unpaired branch of the dispersion relations (see figure 3.6). The imbalance has to be large enough to result in a resolvable rf response but small enough in order to not significantly alter the dispersion relations. Here we use a spin-imbalance P of around

$$P = \frac{n_{|b\rangle} - n_{|a\rangle}}{n_{|b\rangle} + n_{|a\rangle}} \lesssim 0.15. \tag{3.11}$$

The imbalance is created by sequence of Landau-Zener sweeps, transferring a fraction of the atoms in state $|a\rangle$ into $|c\rangle$ at a large magnetic offset field $B = 1000\,\mathrm{G}$ where the interaction strength is comparably weak. For ^{6}Li, a three-component mixture is unstable and the atoms in state $|c\rangle$ (together with some of the atoms in states $|a\rangle$ and $|b\rangle$) are lost via three-body recombination. Due to these three-body losses, we are limited to temperatures above $T/T_F \gtrsim 0.4$.

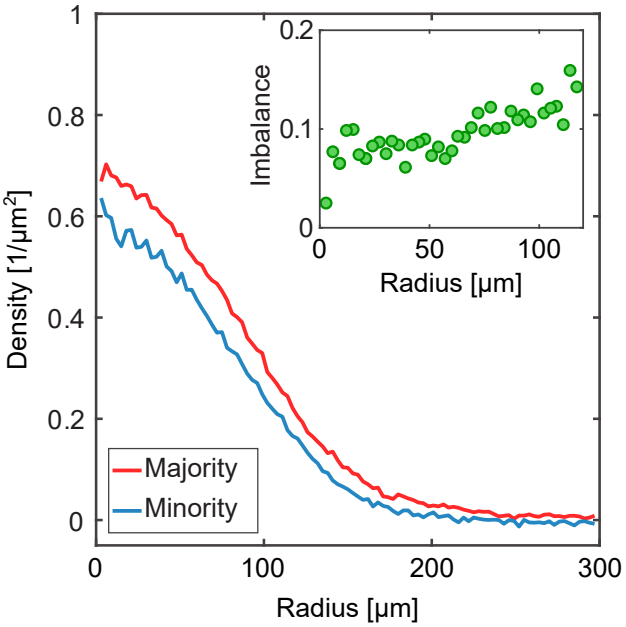

Figure 3.14.: **Density imbalance.** Measured radial density profile of the majority (red) and minority (blue) component. In the inset, the imbalance P is shown as a function of the radius. The measured imbalance is observed to be mostly uniform. Adapted from [18].

The resulting density profile for a typical realization is shown in figure 3.14. Importantly, as opposed to similar experiments with superfluids [189, 190], no separation into a balanced central region and spin polarized wings is observed. The local polarization varies only very weakly with the local density. Based on the fitting procedure presented above, we can now determine the energy difference ΔE between the centre position of the unpaired peak and the threshold position of the paired peak. We will identify ΔE with the pairing energy (see also figure 3.6). This allows us to distinguish different pairing regimes. In a regime where the pairing is dominated by two-body effects, that is molecular pairing, we expect $\Delta E = E_B$. On the other hand, if a density-dependent pairing energy with $\Delta E > E_B$ is observed, we can associate this with many-body pairing. More precisely, we can at least conclude that the relative wave function is strongly altered by the presence of the surrounding strongly interacting medium. In addition, we are working in a temperature regime where without the medium the paired fraction would be almost negligible. Therefore, the pairing is not only altered by the medium but also induced by it. In order to gain intuition, this can be compared to the limiting case of a BCS state where the Cooper pairing is induced only by the presence of the Fermi surface. In particular within BCS theory, the difference

between the pairing energy and the two-body binding energy is exactly given by the gap parameter,

$$|\Delta| = \Delta E - E_B \tag{3.12}$$

Despite the fact that we do not want to rely on BCS theory in the crossover regime, Δ, as defined in equation 3.12, is still a useful figure of merit quantifying the excess pairing energy on top of the two-body pairing.

In figure 3.15, two examples of spectra measured in the crossover regime are presented. In the left panel, a spectrum with a central $\ln(k_F a_{2D})$ of around -0.5 is shown ($B = 672\,\mathrm{G}$ in a $|1\rangle - |3\rangle$ mixture with $E_B = 2\pi \cdot 9.31\,\mathrm{kHz}$). Therefore, while the system is still strongly interacting, the chemical potential is expected to be negative for the whole cloud [126] such that the state mostly governed by bosonic statistics. Indeed, we observe two distinct branches, which we attribute to unpaired (close to zero offset frequency) and paired (around 10 kHz to 15 kHz offset frequency) atoms. Note again that the unpaired branch is only visible due to the imbalance introduced, as we have observed that it is not thermally occupied. Both the paired and the unpaired branch shift slightly with density, the distance between the two peaks mostly stays constant however and is to a good approximation given by the two-body binding energy. This is in stark contrast to the second spectrum shown ($B = 692\,\mathrm{G}$ in a $|1\rangle - |3\rangle$ mixture with $E_B = 2\pi \cdot 1.37\,\mathrm{kHz}$). It has a central $\ln(k_F a_{2D})$ of around 1, such that, at least in the central region, the system is expected to be governed by fermionic statistics with a positive chemical potential. Again, we observe two branches. While the unpaired branch shifts only weakly with density, there is a much more dramatic (yet continuous) shift of the paired branch. This can be attributed to additional many-body correlations strongly altering the pairing mechanism. Therefore, only in the outer wings of the cloud (that is at large radii), the distance between the peaks is approximately given by the two-body binding energy. In the central region, this gap even increases to around twice E_B.

Based on these spectra, it is now possible to extract the pairing energy in units of E_B for various different thermodynamic parameters. The measurements of the pairing energy are presented in figure 3.16, with a set of representative cuts, including a fit to the data, shown in figure 3.17. The two crucial observations are that first of all the pairing energy, well above T_C can be as large as 2.5 times the two-body binding energy (comparable to the Fermi energy, $\Delta E \approx 0.6 E_F$). In addition, the effect of an enhanced pairing energy is surprisingly robust against thermal fluctuations as the effect persists up the Fermi temperature and even above. We can use this data to generate a map of $\Delta E / E_B$ as a function

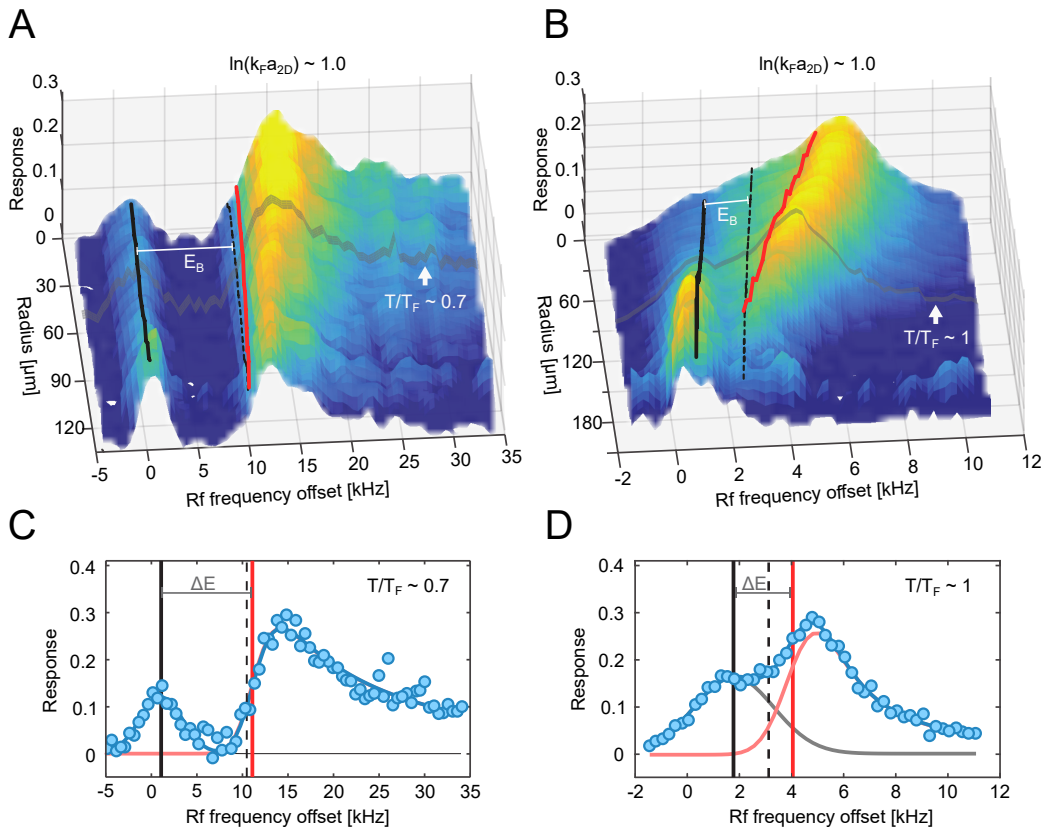

Figure 3.15.: **Quasi-particle injection spectroscopy. A:** Spectrum of the rf response (indicated both on the vertical axis and the colour scale) slightly on the bosonic side of the resonance. Only due to the small imbalance, two peaks are visible. Both peaks shift slightly with density (black line: free particle peak, red line: threshold energy), with the distance mostly given by the dimer energy E_B (binding energy gap indicated by the black dotted line). In light grey, the radius corresponding to $T/T_F \approx 0.7$ is indicated. **B:** Spectrum of the rf response (same colour-scheme as in A) in the crossover regime. The free particle peak shifts slightly in energy, while the bound peak shows a pronounced density dependence. The distance between the peaks is consistent with E_B only in the low density regime. In light grey, the radius corresponding to $T/T_F \approx 1.0$ is indicated. **C,D:** Cuts along the grey lines of the spectra in A and B with a fit to the data (blue). Again, the peak position of the free peak (black), the threshold of the bound peak (red), as well as the distance ΔE between these two energies are indicated. In C, ΔE is mostly consistent with E_B, as opposed to the situation in D where $\Delta E \gg E_B$. Here, in addition, the individual contributions of the free peak (light grey) and bound peak (light red) to the total fitted model are shown. Adapted from [18].

of $\ln(k_F a_{2D})$ for a fixed T/T_F. Here we choose $T/T_F \sim 0.5$. It this context this is a very high temperature, as it is far above the highest observed critical temperatures for fermionic superfluidity of $T/T_F \approx 0.17$ [15], which in turn are

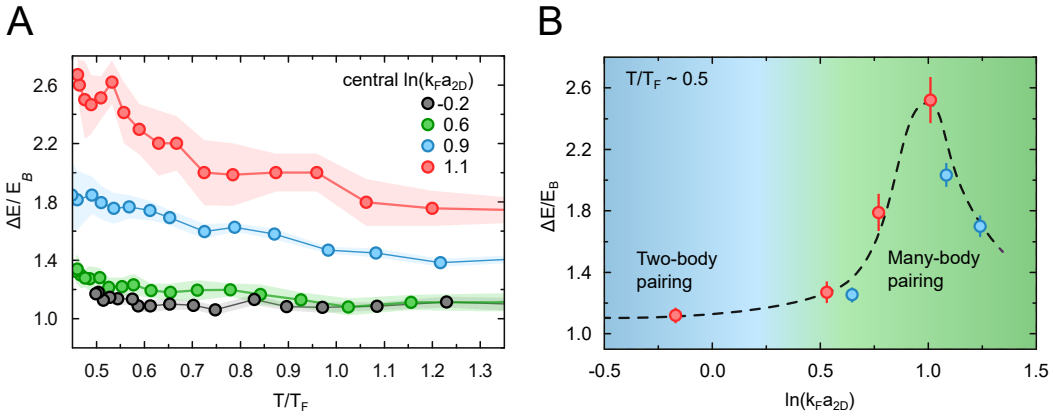

Figure 3.16.: **The high temperature pairing regime. A:** Measured pairing gap ΔE in units of the dimer binding energy for different experimental settings (different colours, points indicate measurements, the shaded region the statistical uncertainty. In order to increase the visual clarity the data points are connected by lines.). Indicated is the central interaction parameter for each dataset. A significant enhancement of the pairing gap is observed in the crossover region. **B:** Measured pairing gap as a function of the interaction strength for a fixed relative temperature of $T/T_F \sim 0.5$. Red data points are measured using a $|1\rangle - |3\rangle$ mixture, blue data points using a $|1\rangle - |2\rangle$ mixture. The data taken with the two different mixtures show consistent results. The dashed line is a guide to the eye. Indicated is the approximate regime where the pairing mechanism shifts from a two-body effect (blue) to a many-body phenomenon (green). Adapted from [18].

already considered anomalously large. This 'phase diagram' is also shown in figure 3.16. Despite the fact that we expect the influence of final state interactions to be mitigated, at least to leading order, we always choose the specific mixture of hyperfine states such that the interaction parameter $\ln(k_F a_{2D})$ of the final state is minimized. Based on this map of the pairing energy we can draw the following conclusions:

- We identify a parameter regime around $\ln(k_F a_{2D}) = 1$ where we have pairing in the normal phase above the critical temperature with a strongly enhanced and density-dependent pairing energy. This observation is robust against thermal fluctuations up to at least the Fermi temperature.

- The regime of many-body pairing is consistent with the regime where the interparticle spacing reaches the order of the scattering length and where the chemical potential changes sign.

- Due to the anticipated presence of a Fermi surface and the strong density dependence, we expect the pairing correlations to be centred around a finite

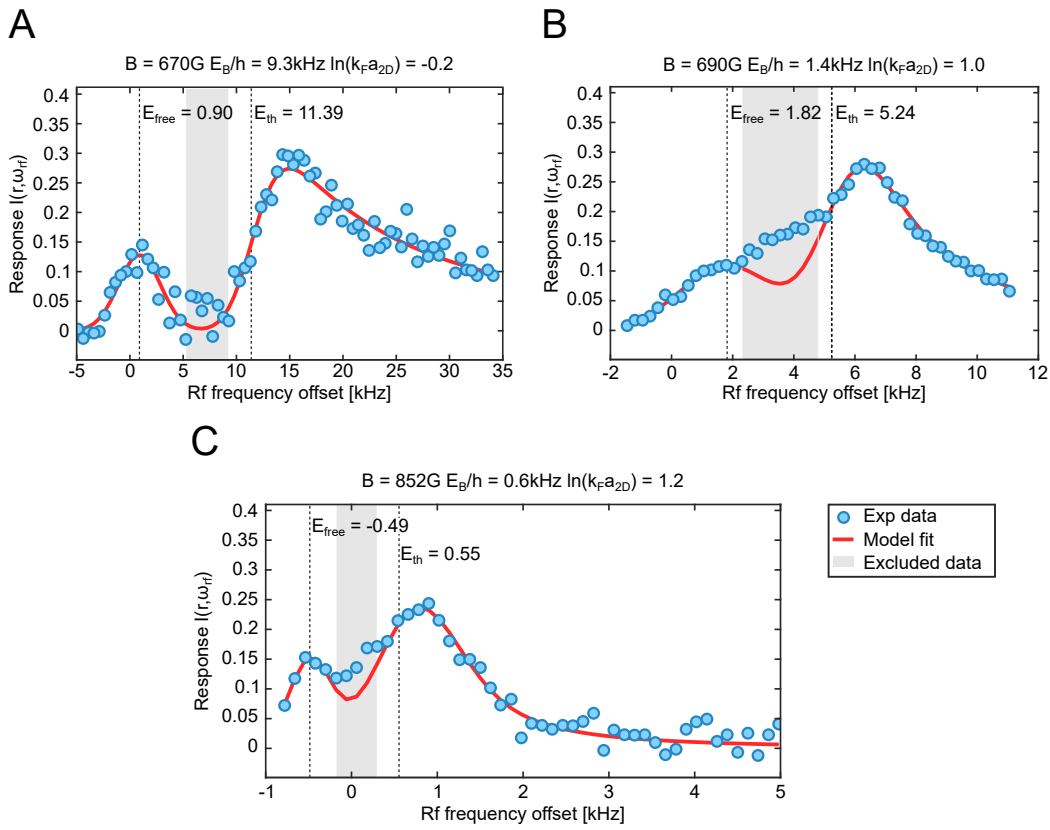

Figure 3.17.: **Spectra in different regimes.** Typical example spectra across the crossover. Indicated in blue are the measured data points and in red the model fit to the data. Both the threshold and the free particle peak positions are indicated, in addition to the region (grey shaded area) which we exclude from the fit due to contributions from adjacent layers of the SWT. The plots range from slightly on the bosonic side (**A**, $|1\rangle - |3\rangle$ mixture), to the crossover regime (**B**, $|1\rangle - |3\rangle$ mixture), including an example for a different initial and final state configuration (**C**, $|1\rangle - |2\rangle$ mixture). Adapted from [18].

single-particle momentum. This has to be rigorously confirmed, however, with another experimental scheme.

- Towards the BEC regime, we observe that the pairing in the normal phase becomes consistent with the presence of a two-body molecular state. This is a trivial version of a pseudo gap regime. These results are consistent with previous studies such as [170].

- For very large $\ln(k_F a_{2D})$, towards the BCS regime, where the pairing temperature T^* and the critical temperature are expected to coincide, we expect the relative pairing energy $\Delta E/E_B$ to converge to one. We observe first indications of such a behaviour, however, we are limited by the finite

frequency resolution (and at some point also by the finite temperature) when approaching the BCS regime. Above $\ln(k_F a_{2D}) \approx 1.5$ we observe only a single branch for all temperatures (above and below T_C) signalling any gap is below our experimental resolution. This is consistent with the expectation of a gapless Fermi liquid above T_C [191].

On a qualitative level, it is also instructive to go back to the (very much) simplified intuitive model presented in the beginning, according to which a mean field BCS theory is applied also to the crossover regime. In this case, the BCS critical temperature is identified with the pairing temperature T^* instead of T_C. Therefore, the model acknowledges that (at least in 2D) quantum fluctuations destroy phase coherence down to the actual critical temperature, while it still assumes that the absolute value of the gap is left intact. We therefore identify the absolute value of the superfluid gap with the pairing gap $|\Delta|$. In figure 3.18, the BCS pairing gap is plotted for a range of different relative temperatures. It is an

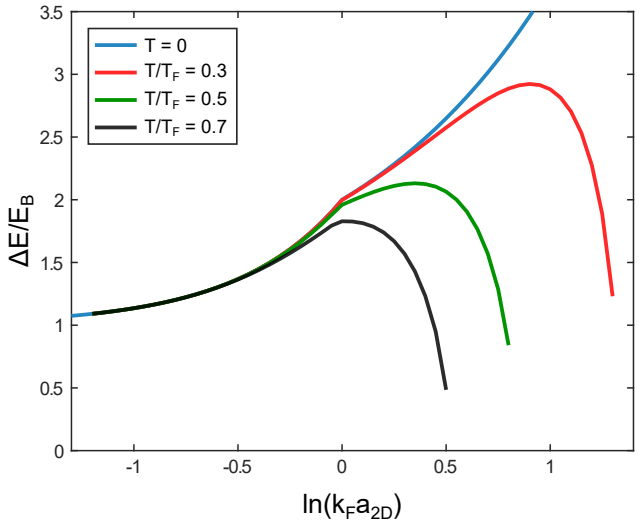

Figure 3.18.: **Finite temperature BCS theory.** The paring gap is plotted as a function of the interaction parameters for different temperatures (different colours). BCS theory is not expected to be accurate in the strongly interacting regime. Adapted from [18].

interesting observation that at least on a qualitative level, the BCS gap appears to be consistent with the experimental results of figure 3.16. However, let me point out again that here, the theoretical model has been applied well outside its expected range of applicability. In particular, the position of the crossover is inaccurately predicted to be around $\ln(k_F a_{2D}) = 0$ within this mean field model. Finally, I would like to stress that a full theoretical description of the crossover

regime is currently not within reach, underlining the importance of experiments studying these intricate strongly-correlated quantum fluids.

3.2.5. Concluding remarks

In the experiments presented in this chapter, major progress was made identifying a regime where many-body induced pairing in the normal phase is a defining feature. The careful analysis of the strongly correlated many-body system allowed us to draw a range of different conclusions. It became clear that pairing above the critical temperature is indeed present and a defining feature of a rather large region of the phase diagram (see figure 3.16). The pairing is surprisingly robust against thermal fluctuation. In addition, it was possible to map out what I called the pairing gap $|\Delta|$ across the BEC-BCS crossover. Finally, and crucially, we concluded, based on the density dependence of $|\Delta|$, that all these phenomena are driven by correlations going beyond simple two-body correlations. Further studies are needed, however, to unambiguously confirm that the pairing takes place at finite single-particle momenta. A promising path would be to adapt techniques used in a recent measurement of the momentum dependence of the superfluid gap [192] to the normal phase, or to record the momentum of the transferred atoms in the rf measurement similar to an angle-resolved photoemission spectroscopy method [169, 193].

In any case, we infer information on microscopic (pairing) correlations based on macroscopic observables, such as the rf response. Similar situations also occur for a much broader range of systems, where relevant density dependences are observed [11]. Progress can, for example, be made by carefully recording the scaling with density, which allows us to draw conclusions on the order of density correlations which play a role. In addition, these measurements can be combined with other results on global collective effects such as phase coherence [15, 16], the equation of state [17], the superfluid gap [192] as well as fundamental excitation modes [21, 22] to name just a few. However, it should be clear now that a major breakthrough in studying and understanding many-body systems would be constituted by the ability to directly measure the microscopic correlations, ideally on a single-particle level. In the example presented in this chapter, this would mean to start by calculating pairing correlations based on density correlations measurements either in momentum or position space. The limiting cases of Cooper pairing and molecular pairing would already be covered by correlations up to second order in the density, while in the crossover regime, possibly also higher order correlations are needed.

Currently, a scheme to experimentally measure correlations in such a system does not exist, at least for continuous systems [194]. In this thesis, I will however outline an agenda allowing us to approach this vision step by step. I will present the progress we made during my the course of thesis along this path and point out interesting physics which can already be learned at intermediate steps.

Part III.

The next step: Single-particle resolved correlation measurements

4. Strategy and roadmap

In the previous part, results on high temperature pairing in the normal phase of a strongly interacting quasi-2D Fermi gas were discussed. Based on the unexpectedly large and density-dependent pairing gap, we concluded that pairing in this regime is induced and influenced by many-body physics. However, to unambiguously confirm this, microscopic correlations have to be measured. This will be an important observable for other general many-body systems, as well. Therefore, it is instructive to set up an agenda, to achieve this goal:

- **Prepare the system of interest.**
- **Take an educated guess of what the system looks like.**
- **Find the best possible measurement basis.**
- **Develop a method to record arbitrary correlations.**
- **Measure the relevant correlation function.**

Of course, none of these steps is straightforward. Already the preparation step imposes a major challenge. Due to the overall small energy scales in ultracold atoms, low entropy phases of matter (in particular in quantum spin models) can be shifted to extremely low temperatures [11]. Even if we only focus on intriguing quantum states at relatively high temperatures, as discussed in the previous chapter, we have to acknowledge that these states are quite *messy*. This is due to thermal fluctuation, varying density, final state interactions, fluctuations in the preparation scheme and many additional aspects. Let me stress again that ultracold atom systems are still astonishingly clean and separated from the environment compared to other condensed matter systems. However, identifying individual microscopic correlations and relating them to macroscopic behaviour is still extremely challenging, as the individual contributions to the full system cannot be studied in isolation.
An alternative approach is to use the microscopic control over individual atoms to prepare and study very small but in turn deterministic systems with exquisite control [160]. They can show minimal instances of the microscopic correlations

within the Hamiltonian studied [163], yet lacking of course the many-body nature of large scale systems. The naive approach would now be to combine many of these small systems to form a macroscopic system. This has proven to be very difficult however (with first steps taken for example in [195]), mostly due to non-local correlations (and thus exactly what renders the many-body system interesting) in the macroscopic system. For example, a - on first sight - promising idea is to build up the antiferromagnetic ground state of a Fermi-Hubbard model by coupling many states of local singlets. However, the actual ground state is far more complicated and in fact has a significantly reduced singlet fraction due to quantum fluctuations [196, 197]. Thus, the state built up only of local singlets is not the ground state and again of higher temperature.[1] While for this specific model there are a few ideas, for example based on so-called resonant valence bond states, on how to approach this problem [195, 202–204], a general scheme to assemble a many-body state in this way has yet to be developed.

Establishing intuition on what correlations to expect in the system is equally important and challenging. The prime example in this respect are results of Bardeen, Cooper, and Schrieffer over 40 years after the discovery of superconductivity [4]. Based on the BCS theory, we now have the intuition that measuring momentum-momentum correlations is a promising approach to identify Cooper pairing [27]. Similarly, only due to the trial wave function proposed by Laughlin [205], we can infer the best way to measure the correlations in specific quantum hall systems. Without any such prior intuition, an unfortunate choice of basis or observables to measure the correlations can significantly complicate the interpretation of the results. We will see examples of this in the following chapters.

Finally, in order to measure arbitrary correlations, the properties of all the constituents have to be measured with a high fidelity. This means that in particular both single-particle and position or momentum resolution are desirable. It is possible to get away without full single-particle resolution, when studying strong, low order correlations [27]. This is not the case any more when small, subtle higher order correlations are relevant.

Due to these reasons, I have to conclude that directly following the above agenda is currently not within reach. Here, I would instead like to point out an alternative, more realistic, route which I followed during my doctoral studies. Therefore, this agenda can also be understood as an outline of the remainder of this thesis. I have structured the agenda into different milestones. In this part of the thesis,

[1] This can also, in a formal way, be phrased on more general grounds in terms of (many-body) gaps closing up at quantum critical points and the Kibble-Zurek mechanism [198–201]. See also chapter 7.

I will discuss how each of these is reached.

- **MILESTONE 1:** Develop an imaging scheme suited for correlation measurements.
- **MILESTONE 2:** Identify the most basic few-body systems which feature prototypical correlations or pose typical challenges interpreting the results.
- **MILESTONE 3:** Develop a toolbox for measuring correlation functions. Apart from the above prototypes, this includes also intuition on which basis to choose, where the limitations of all used methods or interpretations lie, and how to further extend them.
- **MILESTONE 4:** Scale up the system size. The crucial questions will be: A) what is the minimum instance model which incorporate the many-body features of interest and B) how much control over imaging and preparation fidelity am I allowed to sacrifice in order not to lose the access to interesting correlations when scaling up the system size.
- **MILESTONE 5:** Characterize a mesoscopic system which features first signatures of many-body effects.
- **MILESTONE 6:** Characterize a strongly correlated many-body state based on suitable correlation measurements.

In the following chapters I will discuss our progress towards these goals. In chapter 5, I will discuss a new imaging scheme which is single-particle and hyperfine state resolved, has a good position resolution, and works in free space. I will explain how this imaging scheme allows for measuring correlations with full single-particle resolution in a range of different basis sets, at least for small and medium-sized atomic quantum systems. With this first milestone, many possibilities to precisely measure microscopic correlations, also at higher orders, open up.
Before jumping right back to full many-body systems, it is instructive to first identify and study smaller systems. I will present in chapter 6 a set of measurements, where we prepare and fully characterize few-body systems based on correlation studies. In this way, I develop a toolbox for characterizing correlations and entanglement in interacting Fermi systems. In particular, it will become clear that there are still a lot of relevant open questions concerning the correlation and entanglement properties already for very small systems. This is in particular true when indistinguishability is involved. Therefore, first isolating and understanding

the basic ingredient, constitutes the second and third milestones.
Even with small systems fully understood, there is a large conceptual step in between the microscopic and macroscopic world. In particular, collective behaviour and the notion of phases of matter and phase transitions only come into play when approaching the thermodynamic limit. In chapter 7, I will present results on a mesoscopic system, where we study the emergence of a pairing phase transition in a system closely related to the BEC-BCS crossover studied in the previous chapter. Taking this intermediate step on the road towards many-body systems is very relevant, even beyond the major conceptual importance of mesoscopic systems itself: In these systems we can still achieve deterministic control, thus taking thermal fluctuations out of the equation. In addition, all the energy gaps are still finite, such that an adiabatic preparation scheme of the ground state is still feasible. Finally, in a mesoscopic system the imaging scheme remains fully applicable without compromises. Therefore, the milestones 4 and 5 are defined to be preparing and studying a mesoscopic 2D system.
Ultimately I am interested in studying many-body physics. Therefore the final, ambitious milestone is to fully characterize a many-body system based on correlation measurements. I will recapitulate in the outlook in chapter 8 how far we got on this path and which ingredients are still missing.

5. Imaging

In this chapter, I will present the first important milestone outlined in section 4: A single-particle and hyperfine-state resolved imaging scheme, with a good position resolution and a focus on versatility. Parts of the results shown in this chapter are published in [28].
Before delving into any detail, I will summarize the fundamental requirements the imaging scheme has to meet:

- **Single-particle resolution:** Ultimately, we would like to measure arbitrary microscopic correlations between the individual constituents of our quantum system as outlined in section 2.2. Therefore, full single-particle resolution combined with unity detection probability is required. Slightly lifting this strict requirement will result in noise on the particle densities and thus reduced measured correlation amplitudes. This will limit the smallest amplitude we can detect as well as up to which order we can measure correlations for a fixed finite measurement time.[1] Therefore, we aim at almost unity detection probability at least for small system sizes. In certain situations, it can however be beneficial to relax the requirement of perfect single-particle resolution in order to be able to measure lower-order correlation functions of - in turn - larger systems. This situation is similar to the so-called noise-correlation scheme [27]. In any case, it is important to note that in addition to a rather innocent reduction of contrast, imperfect single-particle resolution can also add spurious correlations if false positives or false negatives appear in a correlated way. This will be relevant in the context of a *detection hole* discussed below and in chapter 6.

- **Hyperfine state resolution:** In the systems described in this thesis, different hyperfine states will act as iso- or pseudospins. Therefore, we have to image all populated hyperfine states in the same realization in order to measure correlations between different spin projections and avoid averaging

[1] In a slight oversimplification, if you measure a correlation function of order $\mathcal{O}(n^j)$ in the density n with a single-particle fidelity f, you can expect a reduction in the correlation amplitude of $\mathcal{O}(f^j)$.

over different subsets of the Hilbert space. In this thesis, I only discuss two-component hyperfine mixtures. The imaging scheme will however also be applicable to three-component systems.

- **Position resolution:** We will always measure correlations between individual particles at different positions. Even if we are interested in other quantities (e.g. the momentum or a specific relative phase), we will use time-of-flight methods together with generalized interference methods in the spirit of *matter wave optics* in order to map the desired quantity onto position-dependent densities. Therefore, the position resolution is crucial and will determine how well we can represent individual states in position space. We always have to ensure that the position resolution is significantly better than the smallest correlation feature of interest.

- **Free-space:** The imaging system is designed with bulk systems and generalized interference measurements in mind, which are typically realized by a tailored time-of-flight measurement. Therefore, ideally the imaging system does not require any trapping potential during imaging exposure, and thus can be used for any continuous system. In situations where the resulting position resolution is not sufficient, the next best option is to sample the density in a grid formed by a so-called *pinning lattice* potential prior to imaging. However, this comes at the price of additional collective effects in the light scattering (light assisted collisions in particular) due to locally increased densities. When starting out with a lattice system, it is in principle also possible to realize all interference measurement without time-of-flight by a specific set of quantum gates [39] and therefore avoid any free expansion. Due to limited gate fidelity in conjunction with a large number of gates needed, this is extremely challenging and not pursued any further in the context of this thesis.

- **Simplicity:** Developing an imaging system with the above prerequisites poses by itself an enormous technical challenge. This alone justifies keeping everything - wherever feasible - as simple as possible. In addition, oftentimes simplicity and versatility complement each other. Other highly successful but also highly involved position- and single-particle resolved imaging schemes, the *quantum gas microscope* [206] scheme in particular, offer an outstanding performance in the specific situation they are designed for (in-situ imaging in a lattice system in this case). On the other hand, it can be extremely challenging (albeit not impossible [194]) to adapt it to

imaging a quantum system after a set of general matterwave optics operations. Similar statements can be made about other high resolution lattice imaging schemes [207] or specific time-of-flight detection methods such as multichannel plate imaging of helium [208]. With the imaging scheme described in this chapter, we are aiming at a conceptually more simple, and therefore possibly more versatile approach.

In the following sections, I will first briefly introduce a few common and relevant imaging methods before presenting our newly developed scheme. Apart from the status-quo, I will also elaborate on possible further improvements. Furthermore, as it can be a hard task to choose the best possible imaging scheme for a system at hand, I will afterwards elaborate on which imaging scheme to use for a specific task. As the imaging system was specifically designed for rather small systems, this discussion is of great interest for the endeavour of scaling up the system size. Finally, I will summarize how far I got in my agenda outlined in section 4.

5.1. Overview of different imaging methods

There is a large variety of possible imaging schemes for ultracold atoms. The vast majority[2] is based on light scattering. Most of the times this is resonant or near-resonant scattering. It is destructive in the sense that the recoil energy scale of a single photon is much larger than typical energies in the system, such that the state is strongly altered in the imaging process. There are however also efforts towards a weakly destructive imaging scheme, where off-resonant light elastically scatters off the atoms which can afterwards be detected by phase shifts [209]. In this thesis, only resonant imaging schemes, more specifically absorption and fluorescence imaging, will be covered.

In absorption imaging, the sample is illuminated with resonant light and the shadow cast by the atoms due to absorption is imaged. This is a very versatile and easy to implement imaging method and well suited for extracting densities of larger systems as described in section 3.1. It is usually not possible to identify individual atoms with absorption imaging, though, as the photon number absorbed per atom is typically smaller than the photon number fluctuation of the probe beam. The only way to circumvent this is by resonantly enhancing the scattering cross section by for example a cavity in combination with a non-classical light source, or by choosing extremely long exposure times. For a certain regime of densities and rather strong correlations of lower order (typically second order in

[2]Ionisation detection being an important exception which I will not cover here.

density), it is nevertheless possible to extract some correlations. This analysis method goes by the name of noise correlations [23, 27, 183]. In the experiments presented below, absorption imaging is only used for diagnostic purposes.
In fluorescence imaging, the sample is also illuminated by resonant light, however this time the fluorescence light scattered into a certain solid angle is imaged. Here, single-particle resolution is in principle possible, as the (statistically fluctuating) number of collected fluorescence photons competes with the imaging noise alone, rather than the probe light fluctuations on top of this. Therefore, for a sufficiently large number of collected photons (for example by a long exposure time), single-particle resolution is achieved. There are hurdles to overcome though: First of all, with many photons scattered, the atoms are significantly heated up. If a long exposure and thus many scattered photons are needed, it is often necessary to cool the atoms during imaging. One method, which is used in our experiment to count small atom numbers with almost unity fidelity, is to recapture them in a MOT [210]. Here, the near-detuned probe light also acts as the cooling light and the atomic sample is kept at a temperature slightly above the Doppler temperature. In this realization, any position information is lost, and, as the pseudo-spinstates are not well defined at zero magnetic field, also the spin information. To circumvent this, the atoms have to be trapped locally (as opposed to one global trap formed by the MOT). For this, the space is discretized and each spatial region is attributed to an individual trap. One possible implementations is an array of optical tweezers as formed for example by a lattice potential. As these lattice wells are typically orders of magnitude more shallow compared to the MOT confinement, the atoms have to be kept at a lower temperature for example by Raman sideband cooling. This is the (simplified) idea behind so-called *quantum gas microscopes*, which have proven to be very successful in recent years (see [206] and references therein). It should be stressed, however, that the actual implementation is highly demanding as a number of complications arise [206].
All this complexity of achieving singe-particle resolution is rooted in the fact that a lot of photons per atom are needed to unambiguously identify it. The natural question arising is: Can we work out a way to identify atoms and their positions based on only a few scattered photons? In this chapter, I will present a successful imaging scheme based on only a few hundred scattered photons.

5.2. Spin-resolved single-atom imaging of ^{6}Li in free space

The results obtained with our first generation of a spin-resolved single-atom imaging of ^{6}Li in free space have been published in [28]. This section is based on this publication. Further details can also be found in [158, 159]. In addition, similar ideas have been used in [211–213].

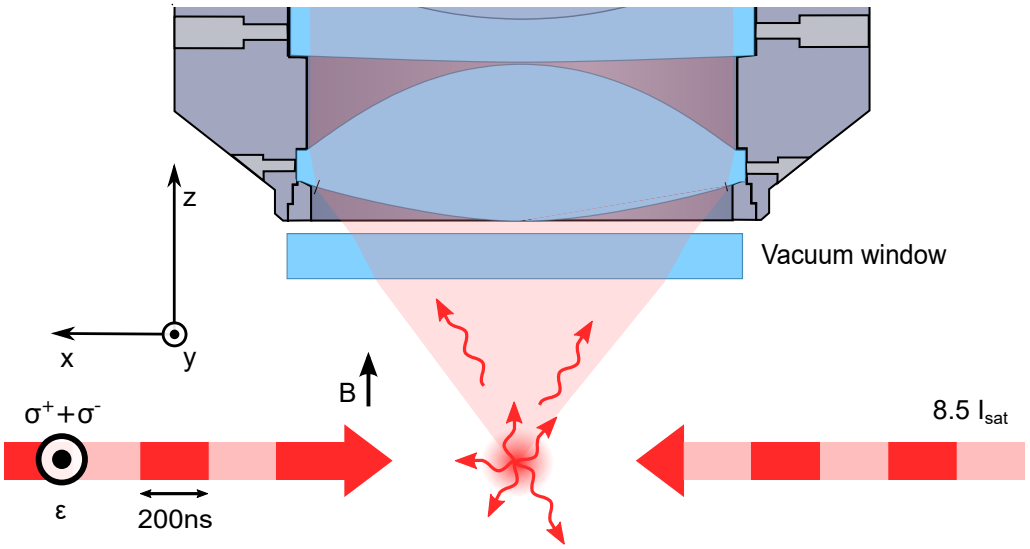

Figure 5.1.: **Schematic illustration of the imaging scheme.** The atoms (red circle) are probed via fluorescence imaging. The two probe beams are counter-propagating along the x-axis and are pulsed on and off alternatingly in rapid succession (total pulse length typically 20 µs, individual pulse length 200 ns). The quantization axis is set by the uniform magnetic field of strength B aligned along the z-axis in the lab frame. Therefore, the probe beams, which are linearly polarized along the y-axis, can drive the $\sigma_\pm$ transitions. Around 11 % of the scattered light is collected via the objective with a high numerical aperture of NA= 0.55. Adapted from [28].

The general idea is quite simple: As shown schematically in figure 5.1, we illuminate the atoms for a certain exposure time with light resonant to the D2 line of ^{6}Li and collect the fluorescence photons through an objective with high numerical aperture (NA) on an electron-multiplying CCD (EMCCD) camera. In addition, we use the fact that for all magnetic fields of interest, the different hyperfine states labelled $|1\rangle, |2\rangle, |3\rangle$ (see section 2.4 and also figure 5.5) can be addressed selectively as the resonance frequencies differ by around $\omega = 2\pi \cdot 80\,\mathrm{MHz}$ (to be compared to the natural line width of the D2 line of around $\Gamma = 2\pi \cdot 6\,\mathrm{MHz}$) [154]. Therefore, we can image all spin states in quick succession, without scattering

photons on atoms in other hyperfine states. All this is conceptually quite simple (as it should be in accordance with the above requirement list), but - as always - the devil is in the detail.

5.2.1. Diffusion in momentum space

Every time an atom absorbs a photon, it gets a momentum kick. For ^{6}Li and the D2 line, the velocity change is on the order of 0.1 µm/µs per scattering event. Therefore, if an atom absorbs, for example, a very modest number of 300 photons with the same k-vector, this would result in a linear velocity of 30 m/s (or equivalently an impressive 600 µm travelled within 20 µs). We can avoid this by making sure that the mean k-vector of the absorbed light is zero. In the experiment, we achieve this by two counter-propagating probe beams, which are linearly polarized perpendicular to the magnetic field axis, driving the σ_- transition. As we noticed that the standing wave potential of the counter-propagating beams can have a negative impact on the imaging performance, we instead alternatingly and rapidly ($f = 5\,\mathrm{MHz}$) *flash* the beams on and off (see figure 5.1). While we have now eliminated any net momentum transferred to the atoms, they nevertheless diffuse during imaging due to a random walk in momentum space driven by spontaneous emission momentum kicks. The diffusion is particularly detrimental for ^{6}Li as it is very light compared to other elements typically used for cold atom experiments. The width of the position-distribution after an exposure time t in the horizontal plane is given by a Gaussian with width [211, 214]

$$\sigma(t) = \sqrt{\frac{R\alpha}{3}} v_{rec} t^{3/2}, \tag{5.1}$$

in terms of the scattering rate R, the recoil velocity v_{rec}, and a correction factor α taking into account the dipolar nature of the emission. While the position *after* the exposure follows a Gaussian distribution, the measured width of the mean signal from a single atom, which is obtained by integrating the mean position over time, is not Gaussian anymore and has slightly more weight in the wings (for details see section 5.4.4, equation 5.2 and in addition [28, 214]). A typical mean fluorescence signal of a single atom (averaged over several realizations) is displayed in figure 5.2.

Due to the diffusion, we have to find a suitable trade-off in order to detect enough photons for reliable atom identification without losing too much position information. Increasing the exposure time and the scattering rate both linearly increases the number of scattered and also detected photons. According to equation 5.1,

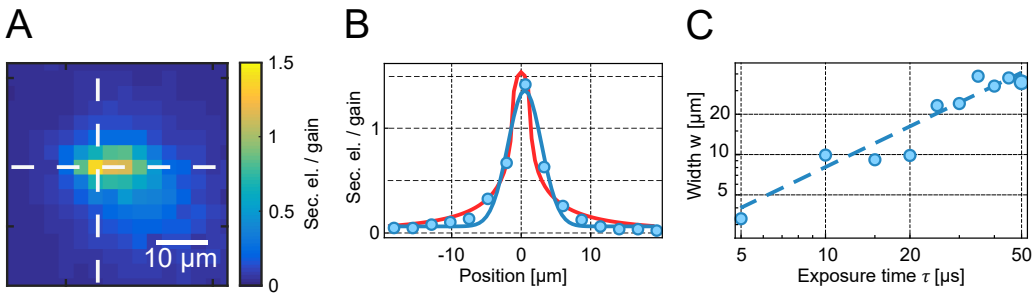

Figure 5.2.: **Mean fluorescence signal of a single atom. A:** Map of the mean signal recorded for a single atom at a fixed position with a probe light intensity of $I = 8.5 I_{sat}$ and $t = 20\,\mu s$ exposure time. A single pixel corresponds to $2.7\,\mu m \times 2.7\,\mu m$ in the atom plane. The colour scale indicates the number of secondary photoelectrons in units of the gain of the amplification register, which is an estimate for the number of primary photoelectrons. **B:** Cut along the white dashed vertical line in A. In blue, a Gaussian fit to the data is shown. This simplified model does not account for the increased weight at larger position offsets. In red, also a fit of the full momentum space random walk model is shown. **C:** The root-mean-square width w of the measured signal distribution is shown as a function of the exposure time. The blue line is a guide to the eye. For the exposure time $t = 20\,\mu s$ shown in A, a spread of $w = 10.1 \pm 1.4\,\mu m$ is measured. Adapted from [28].

it is beneficial to rather saturate the transition, thus increasing the scattering rate, instead of choosing longer exposure times. However, this also cannot be done without limit. For intensities far above the saturation intensity, the scattering rate only changes marginally while the transition gets increasingly power broadened.[3] Therefore, the off-resonant scattering rate in other hyperfine states is increased, which becomes problematic as soon we try to image both spin states in the same realization (see below). The optimum imaging intensity slightly depends on the mixture of hyperfine states employed and the physical system to be imaged. For a typical application with a few atoms, an intensity of $I = 8.5 I_{sat}$ (corresponding to a power broadened linewidth of $\Gamma' = 2\pi \cdot 18.1\,MHz$) in units of the saturation intensity $I_{sat} = 2.54\,mW/cm^2$ of the ^{6}Li D2 line is used. With the exposure time set to $t = 20\,\mu s$, we scatter a mean number of around 330 photons and measure a root-mean-square radius of the signal from a single atom of $w = 10.1 \pm 1.4\,\mu m$. Note that this is significantly larger than the optical resolution of the imaging system of around $1\,\mu m$.

[3] Explicitly, the resonant scattering rate γ scales as $s/(1+s)$ as a function of $s = I/I_{sat}$ and the linewidth Γ scales as $\sqrt{1+s}$.

5.2.2. Identification of single atoms

As explained above we have to rely on only a few hundred photons scattered per atom in order to retain sufficient position resolution. It is therefore important to collect as many of these photons on our camera as possible. For this, we make use of a custom made high resolution objective with a numerical aperture of NA= 0.55. With an effective focal length of $f = 20.3\,\mathrm{mm}$, it is placed directly above the upper re-entrant viewport of the vacuum chamber (see figure 5.1) and has a lateral (axial) resolution of 0.8 µm (4.4 µm) and a field of view of roughly 200 µm. In order to calculate the fraction of photons collected by the objective, we have to integrate the anisotropic dipole radiation pattern of the σ_- transition over the NA (with the NA of 0.55 corresponding to 8.2 % of the full sphere covered), which leaves us at a 11.4 % collection efficiency. We image the emitted light onto an EMCCD camera[4], which for the parameters used has a quantum efficiency of around $\eta = 0.85$. In addition we have to suppress any stray light at other optical frequencies as much as possible and therefore add a bandpass filter to the optical setup.[5] Together with all other optical elements, we are left with around 90 % transmission of the fluorescence light and thus can expect to detect around 9 % of the total scattered photons on the camera, leaving us with around 25 primary photoelectrons (PPE) per atom to work with.

Due to the diffusion during imaging, the signal from a single atom is spread on average over around 10 µm × 10 µm in the atom plane. Our imaging system has a magnification of 5.9 such that our effective resolution is neither limited by the pixel size nor the finite resolution of the objective, even if we take into account the defocussing due to diffusion along the axial direction. Each pixel of the camera corresponds to an area of 2.7 µm × 2.7 µm in the atom plane.

We identify individual photons impinging on the camera using the photon counting mode provided by the EMCCD as shown in figure 5.3. This read-out mode is based on a stochastic multiplication of the primary photoelectrons of each pixel. Therefore, each PPE is amplified to several hundred secondary electrons. The exact distribution of secondary electrons is described by a so-called Erlang distribution [216, 217]. Most importantly, the ratio of the gain of this amplification to the read noise of the camera is very large, $g/\sigma_{read} = 64$, such that we have a very good discrimination between the signal from one or more PPEs and the readout noise [215]. In turn, the discrimination capability between one and two PPEs per pixel is quite limited, such that the information we can extract from the images

[4] ANDOR iXon DV887, back illuminated. For a discussion of the role of the specific camera model on the overall performance, see 5.4.

[5] Semrock, FF01-675/67-25 centred at 675 nm.

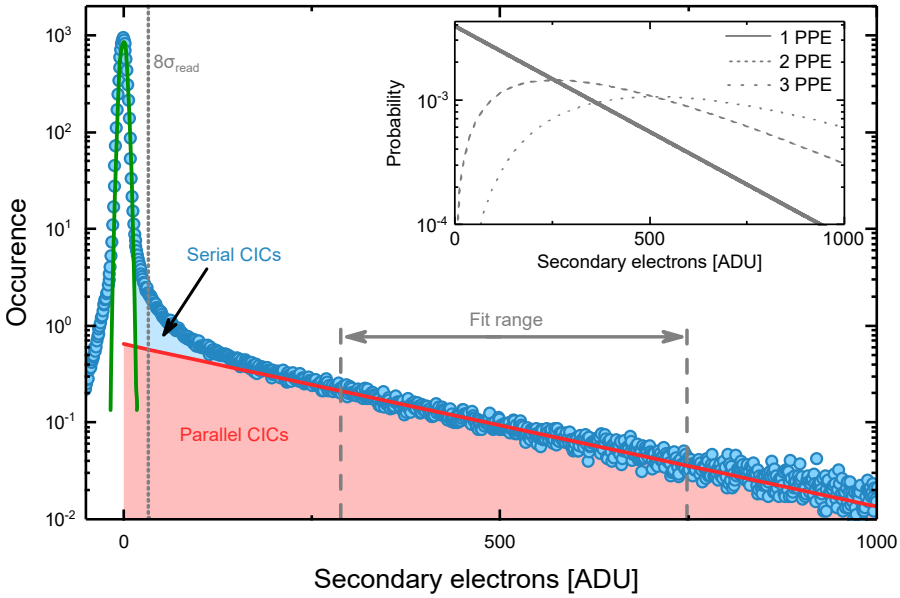

Figure 5.3.: **Single photon counting with an EMCCD camera.** A histogram of the pixel values (in ADU) of a dark image in photon counting mode. The histogram can be explained by a large contribution of empty pixels (without a PPE present), and a few (around 1.7 %) pixels with a single PPE. Each PPE is amplified stochastically, leading to an exponential secondary photoelectron distribution. The read-out noise can be accounted for by a convolution with a Gaussian read-noise distribution. In the semi-logarithmic plot, the exponential distribution manifests itself as a linear slope. We extract the gain (red line) and the read-noise (green line) by a fit to the slope of the distribution and the region around zero ADU, respectively. A gain over read-noise of $g/\sigma_{read} = 64$ is extracted. In addition to the parallel CICs which are produced in the parallel shifting process and thus fundamentally cannot be differentiated from signal PPEs, additional serial CICs can be created at different stages of the serial multiplication register. They can partially be suppressed, at the cost of a reduced extraction efficiency, by choosing a larger binarization threshold of $8\sigma_{read}$. This is possible as the CICs created at different (on average later) stages in the serial multiplication register feature (on average) a smaller gain [215]. **Inset:** Probability density function of the stochastic amplification for different PPE numbers, in a semi-logarithmic plot according to an Erlang distribution. Only a partial discrimination between the distributions is possible. Adapted from [28].

is mostly binary. Based on this discussion, it is now clear that the main noise contribution are spurious PPEs, as they fundamentally cannot be discriminated from signal PPEs. One major source of noise photons can be stray light. By carefully shielding the imaging path and the experimental table and reducing unwanted reflections (in particular in and close to the vacuum chamber), we can reduce the stray light to around 0.004 PPE/px. The dominant noise contribution

left are clock induced charges (CICs), which occur on the camera chip in the parallel transport process prior to readout, when shifting pixel lines on the chip towards the readout register. While these result in the same signature as any other PPE, in addition we observe a small contribution of *serial* CICs with (on average) smaller secondary photoelectron numbers.
We choose to binarize our images with a threshold of $8\sigma_{read}$. In doing so, we suppress most of the serial CICs while retaining a sufficient *extraction efficiency* of 88.5 %. We measure a CIC occurrence rate of 0.017 /px (see figure 5.3). In the binarization process, we indeed achieve single photon counting, while we lose any information on the occurrence of two or more PPEs. Note, however, that this discrimination ability was small from the beginning, and, in addition, for the imaging parameters chosen, the probability of having two PPEs per pixel is (by construction) small. Putting everything together, we are now left with around 20.0 ± 4.5 bright pixels per atom, spread over an area of around 25 pixels with about half a CIC on average for the same area. This means that if we exactly know the position where an atom might be, we can discriminate one atom from none with almost 100 % fidelity. The task left, as shown in figure 5.4, is now to reliably identify the positions of all the atoms.
To this end, we use the fact that bright pixels caused by CICs are spatially uncorrelated while the signal is clustered. We therefore have a clear separation in spatial frequencies, and by applying a low-pass filter with a cut-off frequency of 3 px in-between the characteristic frequencies of noise $f_{noise} = 1/\text{px}$ and signal $f_{signal} \approx 1/4\,\text{px}$, we suppress the noise without deteriorating the spatial resolution. Local maxima in the low-passed image are now potential positions of single atoms. For each of these maxima, we can estimate the likelihood that the maximum is due to an atom. Importantly, the detection fidelity for a single atom *somewhere* depends on our prior knowledge on the approximate position of the atom, which manifests itself in an appropriately chosen region of interest (ROI). The larger this ROI, the more likely it is that an accidental cluster of CICs occurs. For a small image size of 21 px × 21 px we reach single detection fidelities of 99.4 ± 0.3 %, while for around 5000 px^2 the fidelity drops to about 98 %. For these settings, we achieve a spatial resolution - defined by the spread of positions determined for an atom prepared at a fixed position - of $\sigma_{pos} = 4.0 \pm 0.4\,\mu\text{m}$. It is important to keep in mind that while we can pinpoint a single atom to 4 µm, two atoms on the same image (that is, in the same spin state) have to be much further away from each other in order to distinguish them as the identification method relies on the signal distributions not significantly overlapping. We determine the minimum distance two atoms have to have to be discernible with

over 90 % probability to be 32.4 µm. I will present in section 5.4.4 an alternative analysis method which is capable of improving these numbers.

5.2.3. Spin resolution

We are mostly interested in quantum systems consisting of atoms in several different hyperfine states.[6] Each hyperfine state therefore takes on the role of a pseudospin state where we would like to measure correlations between different spin states. Therefore, in the same realization, we have to selectively detect both (all) states. In this context, it is instructive to take a closer look at the actual imaging transitions used in experiment.

As discussed above in section 2.4, and shown in figure 5.5, we employ the lowest three hyperfine states of the $^2S_{1/2}$ manifold in the experiment. We image on the D2 line by shining in light resonant on the σ_- transition from the $m_j = -1/2$ to the $m_j = -3/2$ manifold. As already sketched in figure 5.1, we employ a probe light beam which is linearly polarized in the lab frame, therefore in general it is also possible to drive σ_+ transitions from $m_j = -1/2$ to $m_j = +1/2$. They are however energetically fully suppressed, due to a detuning of at least 1.1 GHz above 300 G. From the $m_j = -3/2$ manifold, only a decay back to $m_j = -1/2$ is possible. At high magnetic fields above 300 G we are already perfectly in the Pashen-Back regime of the hyperfine structure of the excited state $m_j = -3/2$ manifold, while due to the larger hyperfine coupling this is only approximately the case for the ground state $m_j = -1/2$ manifold (see section 2.4 and [154]). Except for the *stretched-state* $|3\rangle = |m_j = -1/2, m_I = -1\rangle$, our states of interest are therefore only approximate eigenstates of the total electron angular momentum operator $\hat{J}$ and the optical transitions are not fully closed. Atoms in states $|1'\rangle$ and $|2'\rangle$ have a probability of a few permille per optical cycle to decay into states $|5\rangle$ and $|4\rangle$, respectively. We can circumvent these atoms from going dark by also imaging states $|5\rangle$ and $|4\rangle$ with a separate imaging beam at the corresponding frequency. These σ_+ transitions from the $m_j = +1/2$ to the $m_j = +3/2$ manifold are again (only) approximately closed and with a small probability they decay back into the original states $|1\rangle$ or $|2\rangle$. It should be stressed that this is in fact not a repumping scheme, but rather should be described as a bichromatic imaging as both involved transitions are almost closed. As shown in figure 5.5, without the second imaging beam, there is only limited discrimination capability between the signal from a single atom in state $|1\rangle$ or $|2\rangle$ and the background distribution.

[6] Typically two, however with ^{6}Li also the preparation of three-component systems is possible. While we are able to create stable weakly interacting quantum few-body states with three components, larger and strongly interacting systems are limited by three-body loss [218].

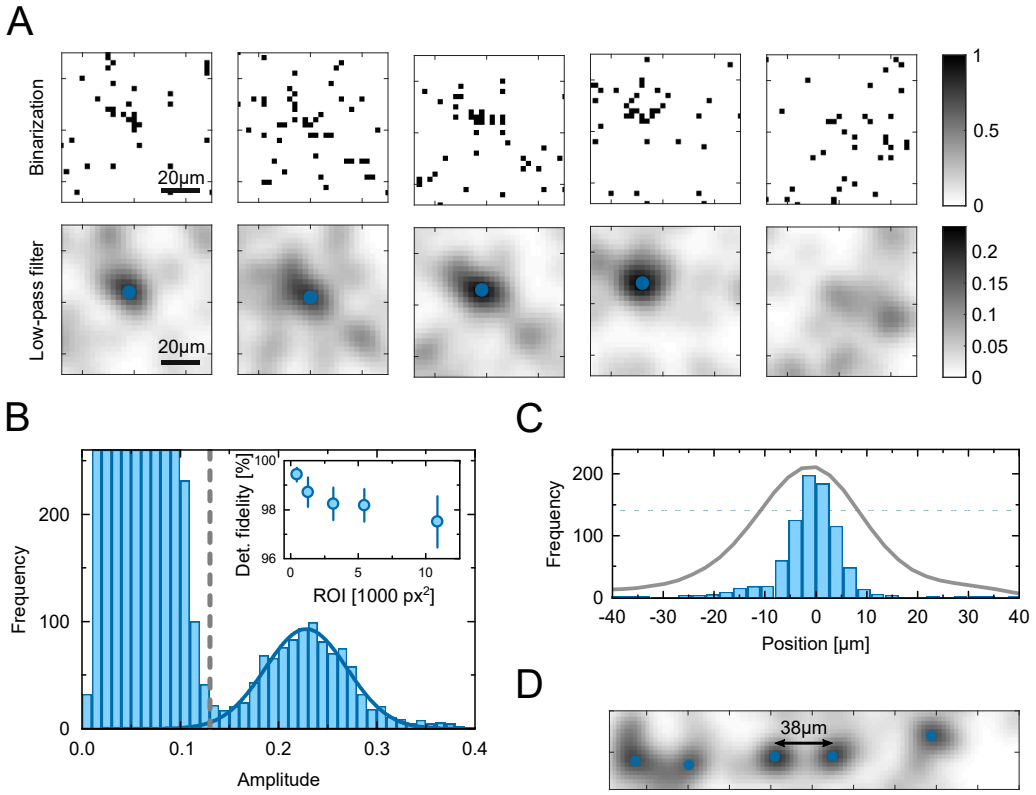

Figure 5.4.: **Single atom detection. A:** Example regions of interest of camera images after binarization (upper panel) and application of a low-pass filter (lower panel). In the first four images, a single atom is present, indicated by a signal-cluster on top of an uncorrelated background and the large-amplitude local maximum, respectively. **B:** Histogram of all local maxima obtained in a set of images with at most one atom present in the region of interest. A bimodal distribution is observed. We identify atoms by selecting a threshold in the amplitude. The threshold is determined by comparing the signal distribution (blue line, obtained by a Gaussian fit) with the background distribution (obtained by analysing a region of interest without atoms). Local maxima above the threshold are identified as atom positions (blue dots in A). **Inset:** Detection fidelity measured for different ROI sizes. **C:** Histogram of the determined atom positions for a system where the atom before the imaging process is always fixed to the same position. We obtain a root-mean-square resolution of 4 µm, significantly smaller than the spread of the mean signal (grey line). **D:** Section of an image with five atoms present. Indicated is the distance between two of the local maxima which is still sufficient to identify the maxima as different atoms. Adapted from [28].

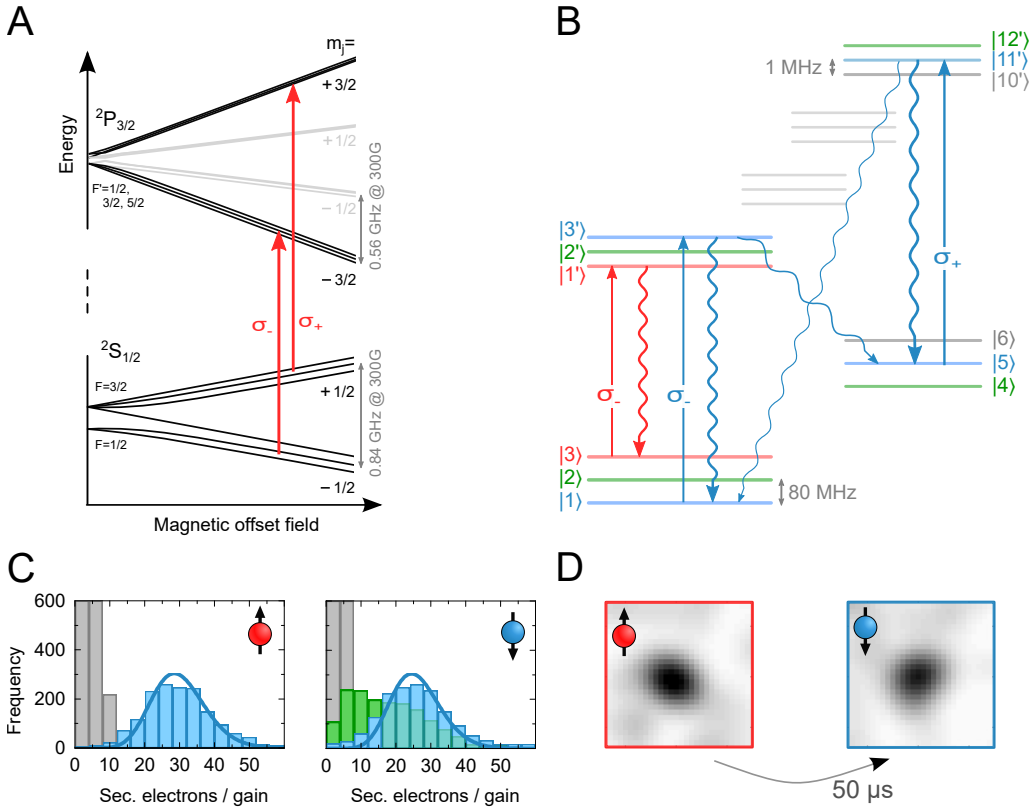

Figure 5.5.: **Hyperfine resolution. A:** Schematic drawing of the $^2S_{1/2}$ and $^2P_{3/2}$ manifolds in the range from 0 G to 300 G, together with the σ_- and σ_+ transitions employed in the bichromatic imaging scheme. **B:** The same level scheme at a fixed finite magnetic field. Indicated are the relevant optical transitions for imaging states $|3\rangle$ (red) and $|1\rangle$ (blue) (with $|2\rangle$, which is similar to $|1\rangle$, not shown for visual clarity). The σ_- transition of the D2 line is fully closed for the stretched state $|3\rangle$ (red arrows). When imaging state $|1\rangle$, after being optically excited with a σ_- transition the state $|3'\rangle$ decays back to state $|1\rangle$ with above 99 % probability (strong blue arrows), but with a small probability may also decay into state $|5\rangle$ as well (weak blue arrow). Therefore, also state $|5\rangle$ is imaged on the σ_+ transition. **C:** Distribution of the integrated signal of a single atom in blue (left panel: $|3\rangle$, right panel: $|1\rangle$) using the bichromatic imaging scheme. The blue lines represent the expected signal distributions based on a mean photon number of 24.7 and 21.0, respectively. In grey, the distribution without an atom present is shown and in green (for state $|1\rangle$) the distribution without using the second imaging beam on the σ_- transition. **D:** Mean signal of a single atom in state $|3\rangle$ and $|1\rangle$, each imaged in the same experimental run. Adapted from [28].

However, with the bichromatic imaging in place, the signal distributions become mostly independent of the state imaged.

At high magnetic fields, the resonance frequencies for the different hyperfine states differ by approximately $\omega = 2\pi \cdot 80\,\mathrm{MHz}$. This is more than a factor 10

larger than the natural line width of the transitions (and still significantly larger than the power broadened linewidth for the parameters used above). This allows us to selectively address the different spin states. We therefore first image one of the spin states as explained above. Then we shift the laser frequency within around 30 µs to the resonance frequency of the second spin state while at the same time triggering the fast kinetics mode of the EMCCD camera, which shifts the collected signal out of the exposed sensor area at a rate of 0.5 µs per line. Therefore, after typically 50 µs to 100 µs (depending on the image size), we can take the image of the other spin state. This method works as long as any typical internal timescale of the system imaged is much larger than the time between two images. While this strongly depends on the actual system of interest, this requirement can typically be fulfilled. Furthermore, off-resonant scattering due to the imaging light of the first image on atoms in the second transition cannot be neglected. Therefore, the in this respect more favourable $|1\rangle - |3\rangle$ mixture is used whenever possible. In addition, there is some potential for optimizing the imaging parameters, in particular with respect to the saturation intensity used. In a typical scenario, we measure a position uncertainty which is 10 % larger in the second image, corresponding to one off-resonantly scattered photon on average.

5.3. Matter wave optics

Because the imaging method is designed to work in free space, we are not restricted to in-situ measurements but are free to use standard time-of-flight methods to access different measurement bases. To this end, we will always measure the position of the atoms in the imaging process. Before the exposure, however, we can use a toolbox explained below to map a basis of interest onto position space. This will be of particular importance for more complicated quantum systems, where it might be useful to engineer a basis transformation into a suitable basis by *matter-wave optics* methods. As the name suggests, these methods can be understood by an analogy to (quantum) optical systems. For this thesis, in particular measurements in momentum space will be of importance. In analogy to an optical Fourier-transform in (quantum-)optics, this will be the most important fundamental building block of the matter wave optics framework. In principle, a Fourier transform can be achieved by a free (that is ballistic) time-of-flight expansion as long as the final spread of the signal is much larger than the initial in-situ distribution (analogy: the far field distribution of a diffraction pattern). In turn, in analogy to a perfect lens in optics, we can bring the far field (long time) distribution to a finite *focal* length (time), by using a suitable

phase imprinted onto the atoms. This can be achieved by a quarter period time ($T/4$) evolution in a harmonic confinement [180, 219]. The basic idea can be easily understood for a classical harmonic oscillator, where after a $T/4$ time evolution, any initial deflection is converted into momentum and vice versa. This principle can be generalized also for the phase-space distribution of a quantum state due to the quadratic nature of the phase imprinted. In the implementation for the imaging scheme described here, we have to make sure in addition that we always stay in the focal plane of the objective. Therefore, the atoms are always confined with an optical potential in all three spatial dimensions. If the potential is separable in all directions, the free time evolution spatially decouples and the expansion for a quarter of the trap period $T/4$ along one of these directions maps the initial momentum along this axis onto the respective positions (see figure 5.6). Therefore, if we are interested in extracting the 1D momentum along a specific dimension (for example the axis of a double-well system), we use a weak harmonic confinement along the double-well axis in conjunction with a tighter confinement along the other axes. Experimentally, this is achieved by an optical dipole trap formed by a single focussed far off-resonant trap beam. After a $T/4$ time evolution in the weak axis, we image the system and extract the position along this axis, effectively integrating out the two other spatial dimensions. We are thus left with a measurement of the 1D momentum. We can set the size of the proportionality factor between position after time of flight and momentum by adapting the trap frequency (analogy: focal length of a lens). It is important to note, however, that both non-separable contributions to the trap geometry and interactions between atoms during time-of-flight couple the different axes. A further limitation arises from anharmonicities of the potential, which cause aberrations and distort the mapping to momentum space. Therefore, only if the potential landscape is very well under control, more complicated matter wave optic methods can be employed. This is typically very challenging with optical potentials. Consequently, magnetic potentials should be employed if possible. On the other hand, engineering small-scale and very specific magnetic potentials at the centre of our vacuum chamber is an almost impossible task, such that we often times have to rely on optical potentials.

Building on the fundamental block of a matter wave Fourier transform, also other methods of possible benefit directly come to mind. The only additional ingredient will be locally applied phase shifts, which could be engineered for example by locally changing the energy landscape by quenching on an optical tweezer potential for a short time. These methods include:

- A mixed basis measurement somewhere between position and momentum

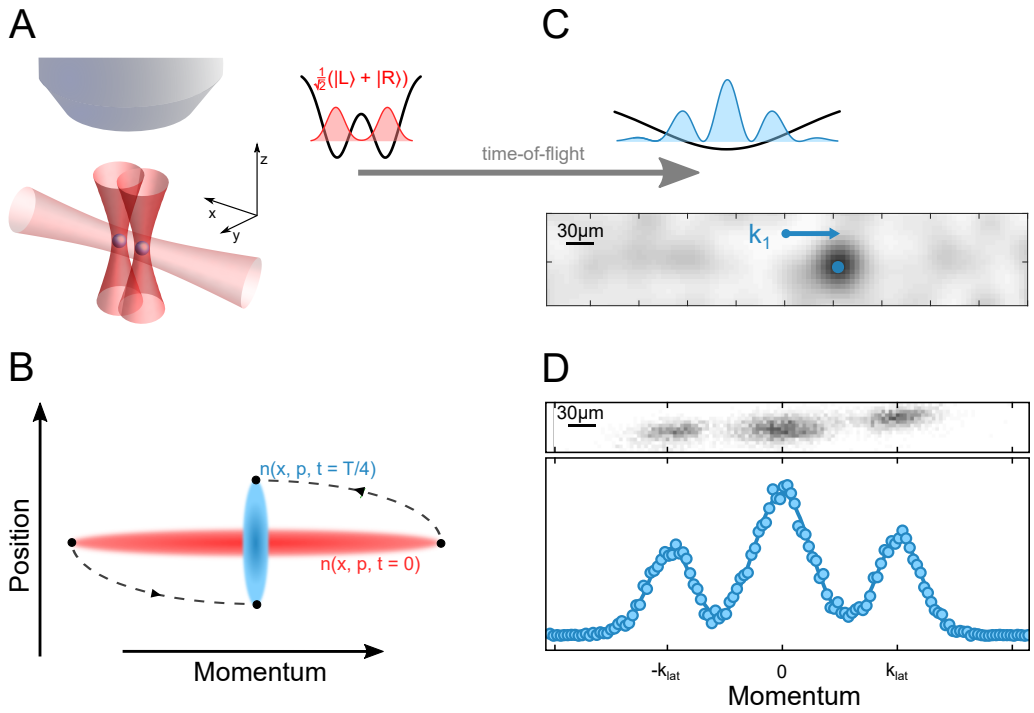

Figure 5.6.: **Momentum space measurements.** Illustration of the matter wave Fourier transform on the example of the single-particle ground state of a balanced double-well. **A:** The ground state of a single atom in the balanced double-well created by two tunnel-coupled optical tweezers (vertical red beams) is given by $\sqrt{\frac{1}{2}}(|L\rangle + |R\rangle)$. Time-of-flight expansion is performed in a single beam ODT oriented along the double-well axis, as indicated by the light red beam ($\omega_{ax} = 2\pi \cdot 75\,\mathrm{Hz}$, $\omega_{rad} = 2\pi \cdot 300\,\mathrm{Hz}$). **B:** Schematic illustration of the phase space evolution during a $T/4$ time evolution. A distribution initially well localized in position space (red ellipse) is mapped at $t = T/4$ onto a distribution well localized in momentum space (blue ellipse), with the position after time-of-flight proportional to the initial (in-situ) momentum. **C:** In analogy to Young's double-slit experiment with a single-particle, we sample the single-particle interference pattern by repeatedly measuring the position of the atom after time-of-flight. **D:** Reconstruction of the interference pattern in the form of a histogram of the individual measurement results from C. Top-panel: Two-dimensional distribution in the horizontal plane. Bottom panel: The axis orthogonal to the double-well axis is integrated out. The contrast of the interference pattern is a measure for the initial state purity in addition to the fidelity of the time-of-flight expansion and the imaging system.

space. This can help to extract certain coherence factors as will be seen in the next chapter.

- A matter-wave telescope build out of two $T/4$ expansions with different

trap periods in order to magnify the in-situ distribution.

- Filtering methods based on momentum. For example, it might be interesting to study the in-situ distributions of atoms with momenta close to the Fermi momentum. This could be realized with the telescope explained above and a local filter after the first $T/4$ expansion.

- Phase-contrast imaging as the most prominent example of self-interference, where in addition to the above telescope setup at the Fourier time an additional phase shift (by lifting the energy) is added to the zero frequency component.

In a slight oversimplification, it could be stated that such a toolbox would represent the (continuous system) quantum gas analogue to digital quantum gates as employed successfully in for example ion chains and superconducting qubits [220]. This intuition will be of importance in the context of quantum state tomography discussed below.

5.4. Margins of improvement

With the single-particle and hyperfine state resolved imaging scheme, which allows us to measure in both position and momentum space (and possibly also more complicated bases), the first milestone outlined in section 4 is reached. Coming back to the list of requirements presented in the beginning of this chapter, for the microscopic systems used as examples here, all five[7] prerequisites have been met. While this is clearly an important step towards detecting correlations in small systems, there are however also clear limitations is terms of spatial resolution and scalability to larger systems. Therefore, before discussing the application of this imaging system to correlation measurements, I will explain margins of improvement. A particular focus will be on the scalability towards larger systems.
As we have learned above, the actual imaging fidelity and the spatial resolution are a result of a suitable trade-off between several key ingredients, such as exposure time, magnification, signal filtering, and others. Importantly, the optimum parameter set can quite significantly differ when imaging different physical systems. Therefore I will try to also outline a general strategy for choosing the optimum imaging system and parameter set below. These considerations will be very important when trying to scale up the system size, and may provide a

[7] Single-particle resolution, hyperfine resolution, position resolution, working in free-space and also (relative) simplicity.

guideline when to choose a imaging scheme like this.
There are a number of possible improvements which I will consider:

1. Choosing a different atomic species.
2. Implementing a better camera and objective.
3. Implementing a pinning lattice.
4. Improving the image analysis procedure.
5. Optimizing the imaging parameters.

In addition, all measurements based on time-of-flight require that interactions are fully quenched during the expansion. Therefore, I also discuss possible schemes for this purpose, which are based on Raman and microwave transitions.

5.4.1. Different atomic species

While it is clearly beyond the scope of this thesis to implement a different atomic species into the experiment, for the imaging alone it would have been the most effective. Going back to equation 5.1, we see that for a fixed number of scattered photons, the width of the integrated photon signal scales according to $1/(m\lambda\Gamma)$. It is clear that ^{6}Li is - in this respect - an unfortunate choice as it is rather light.[8] Other examples of atomic species which can be laser cooled are typically much heavier while featuring similar optical transition. Two examples are ^{87}Rb ($\Gamma = 2\pi \cdot 6.1\,\mathrm{MHz}, \lambda = 780\,\mathrm{nm}$) or ^{168}Er ($\Gamma = 2\pi \cdot 29.7\,\mathrm{MHz}, \lambda = 400\,\mathrm{nm}$) which potentially would allow for a 20 times or even 80 times smaller diffusion with the same number of scattered photons. This would push us to a regime where the resolution of the signal is limited by the optical point spread function rather than the diffusion. As will be briefly discussed below, in this regime it might be actually favourable to replace the EMCCD by a regular sCMOS camera with a very low read-noise.

5.4.2. Different camera and objective

If it is not possible to lower the diffusive spread per scattered photon, the next best option is to reduce the number of photons scattered, ideally by reducing the exposure time. For a reliable atom detection, this has to be counterbalanced

[8] On the other hand, this can be a huge advantage in terms of interaction and tunnelling timescales.

by either reducing the noise of the imaging system or increasing the effective photon collection rate. For the latter, the NA of the objective as well as the quantum and extraction efficiency of the EMCCD camera are possible candidates for improvements. The margins are typically quite small, though. I am not aware of any commercially available EMCCD camera which performs significantly better in terms of quantum and/or extraction efficiency, and even if this changes in the near future, there is nothing more than a few percent improvement to be expected. There is a little more potential in the NA: The objective employed in this thesis is already well optimized for the situation of optical access through one viewport of a steel chamber. A glass cell might provide a slightly higher NA, and in particular imaging from two optical axes with two objectives and two cameras can provide a significant benefit. While the effectively doubled collection efficiency comes at the price of also doubling the noise, correlating the two individual images instead of simply adding them up can suppress additional noise. Within the scope of this thesis, instead of improving the collection efficiency, reducing the noise in form of CICs is the more promising path to take. Through a specific optimization of the read-out process, NüVü camēras claims to provide a significantly reduced CIC rate at similar read-out settings for their EMCCD cameras [221]. We have tested a few versions of the camera in-house and indeed can expect an improvement in CIC rate of almost one order of magnitude, as shown in figure 5.7. A few hard- and software features needed for our imaging scheme are still in an advanced prototype phase and we expect to upgrade the camera in our experiment soon. I will provide some more details on the consequences of reduced CICs below.

5.4.3. Pinning lattice

In certain situations, it might be beneficial to give up the *free-space* aspect of our imaging system in order to improve the position resolution. For this, we would need to confine the atoms during imaging with a confinement depth of approximately the total recoil energy transferred during imaging. With the one photon recoil energy of $E_R = k_B \cdot 3.5\,\mu\mathrm{K}$, we need $\mathcal{O}(\mathrm{mK})$ confinements. In figure 5.8, the effect of confining the atoms during imaging is presented. In this example, a single atom is confined during the exposure time in a microtrap with a depth of $290E_R$. It can be observed that the measured width of the mean signal is mostly constant for exposure times below around 15 µs. As during this time around 250 photons are scattered, this is consistent with the depth of the pinning potential employed.

As we are typically dealing with continuous density distributions (this is of course

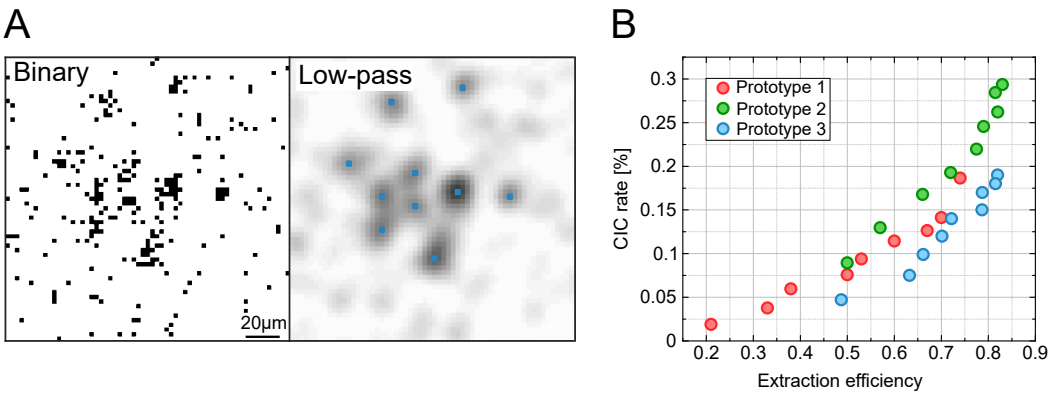

Figure 5.7.: **Performance of the NüVü. A:** Example image illustrating the performance of the NüVü camera, where 10 atoms spread out in the horizontal image were identified based on binarization and a low-pass analysis **B:** CIC performance of the NüVü measured for different read-out parameters and different prototypes. Typically, the camera is used at a lower gain setting (relative to the read-out noise) such that the extraction efficiency is slightly lower. Therefore, a cut-off of $5\sigma_{read}$ instead of $8\sigma_{read}$ is chosen. Importantly, the CIC rate is significantly reduced compared to the Andor camera with around 1.7 % CICs.

the fundamental implication behind the free-space aspect), we would have to discretize space by ramping on an optical *pinning lattice* with a lattice spacing significantly smaller than the resolution we want to achieve. There are two options for an experimental implementation: Either a conservative potential using (infrared) far detuned light, as in the example above, or a lattice formed by near resonant light. In the latter case, the optical power needed would be vastly reduced. However, close to the optical resonance, the trap potential is significantly different for the ground and excited states. In addition, spin resolution is much harder to achieve due to off-resonant scattering. Up to now, a pinning lattice has not been implemented in our experiments.

5.4.4. Optimizing image analysis

An important question to raise is which fraction of the information available to us we actually use in the image reconstruction. I have already mentioned that we discard (albeit very little) information by the binarization of all the images. In particular, two PPEs on a single pixel result in exactly the same signal as one PPE. Furthermore, we effectively identify atoms by checking if the number of bright pixels in a certain area (as defined by the point spread function of the filter applied) surpasses a chosen threshold. We ignore at this point that we know a lot more about the signal distribution. Either from first principles or based on

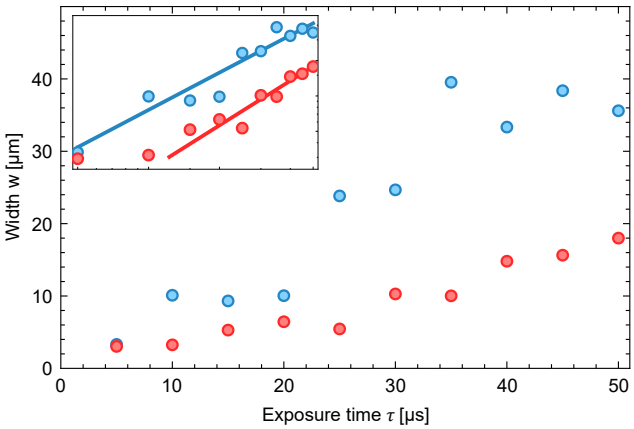

Figure 5.8.: **Effect of confinement during imaging.** Shown is the measured width of the mean signal obtained for a single atom initially fixed at the origin. A probe light intensity of $I = 8.5 I_{sat}$ is used and the exposure time is varied. The blue data points are obtained without confinement during the exposure (data identical to figure 5.2). The experiment is repeated with the atom confined in a pinning potential (formed by the microtrap) with a depth of $290 E_R$. Solid lines are a guide to the eye. Adapted from [28].

measurements of the effective point spread function, we have access to the following three quantities in ascending order of complexity: Firstly, the mean point spread function. Secondly, the fluctuations on top of the mean distribution, which differ, due to the random-walk nature, from simple binomial statistics. And finally, the full statistics of individual signal occurrences, which add information on the spatial connectivity to the pixel-wise fluctuations considered in the second point. This suggests two possible approaches based either on a maximum likelihood approach or machine learning techniques.

For a likelihood estimation, we would rasterize the image (with a subpixel grid-size), restrict ourselves to a range of possible atom numbers, and then calculate for each configuration of positions and number of atoms a likelihood of this distribution to describe the observed signal. We then guess the actual distribution of atoms to be the one corresponding to the highest likelihood. Obviously, the computational effort scales very badly with raster size and possible atom number. For a possible range of atoms between $N_{atom} \in [\alpha, \beta]$ and a grid of $d \times d$ positions, the number of configurations is $\frac{d^{2\beta+2} - d^{2\alpha}}{d^2 - 1}$. As an example, take a region of interest of $100\,\mathrm{px} \times 100\,\mathrm{px}$ and a grid spacing of around $0.5\,\mu\mathrm{m}$. Let us assume for this example that we expect the atom number to be restricted to below 20. The number of possible configurations is now $\mathcal{O}(10^{108})$, which shows that a straightforward application is impossible for already modest atom numbers. However,

it might be possible to further restrict the possible number of configurations by either independently measuring the particle number, or only specifically testing situations which are inconclusive based on a simpler analysis method. For example, each time the low-pass method identified the presence of *at least* one atom at a certain position, within a region of interest around this position, various hypotheses based on configurations of one or two atoms could be tested against each other. Note that similar considerations are actually well known in other fields of physics, in particular in the context of clusterfinding in astrophysics [222–224].
As an alternative to likelihood methods, also machine learning techniques can be of interest. The biggest challenge here is to provide a sufficiently good reference set for a supervised training approach. While it is possible to provide a set of data where with a fidelity of around 98 % an atom was at a point-like position (as used in figure 5.4), it is not possible to have a perfect training set and any experimental imperfections which might occur for example after time of flight are not taken into account. For these reasons, in exploratory studies including various cluster finding algorithms and machine learning techniques we did not achieve significant gains so far for small systems of a few atoms. It will, however, become very important to revisit these ideas when studying larger systems where any simple image analysis tool begins to fail.
As a first step in this direction, and as a benchmark of possible margins of improvement, I will here presents results obtained by with likelihood analysis on simulated data. For this I set up a three-step framework

- **Step 1:** Simulate atom positions.
- **Step 2:** Simulate diffusion of the atoms and the camera response.
- **Step 3:** Perform image reconstruction and correlation detection.

The first step is, at least for this benchmark, straightforward. For simplicity, I will restrict the discussion to the situations of either no atom present, one atom at a fixed position, or two atoms at fixed positions with a variable distance between each other. I will however make sure that in-between runs, the position of the atoms relative to the pixel grid is not fixed. For future applications, also a sampling of a more complicated many-body wave function is implemented in this step.
The diffusion of the atom is implemented with the help of a 2D probability density function (PDF). The PDF used here is based on the time integral of

the momentum space diffusion [214],

$$P = \frac{5}{6\pi w}\left(\frac{w^2}{x^2+y^2}\right)^{1/6} \Gamma\left(\frac{1}{6}, \frac{x^2+y^2}{w^2}\right). \tag{5.2}$$

Here, $\Gamma(s,x) = \int_x^\infty t^{s-1}e^{-t}\,\mathrm{d}t$ denotes the incomplete gamma function and w is the width parameter. In principle, w can be calculated from first principle with $w \propto \sqrt[3]{t}\sqrt{Rv_{rec}^2}$. Here, we will use the width as a free parameter to adjust the PDF to the measured distribution [28, 214]. It is perfectly reproduced for $w = 3\,\mathrm{px}$.[9] From this PDF, the (fluctuating) number of primary photo electrons detected on the camera is sampled. Based on this PPE map, the readout response of the camera is simulated. This includes the stochastic amplification based on an Erlang distribution, the read noise, and the distribution of parallel CICs. The resulting images resemble very well those experimentally measured, as presented in figure 5.9. Note, that spatial correlations within individual atomic signal distributions are not included in this analysis. However, for the exposure times used in this thesis, they were not unambiguously detectable in the experimental data either.

Based on these simulated images, the reconstruction algorithm is tested. As a first test, the standard reconstruction algorithm is employed and indeed the fidelities and the spatial resolution are very close to those presented in this chapter. In addition, also a likelihood algorithm is employed. For all images, three hypotheses - none, one and two atoms present - are tested. A likelihood map is calculated by explicitly calculating the logarithm of the likelihood for each combination of the atom positions on a sub-pixel grid; here using 5×5 super-sampling. For the hypothesis test, the known PDF of the PPEs as well as the known camera response is used. It is important to state that the full statistics of the fluctuations on top of the mean value (which are explicitly not Gaussian) are taken into account. In this analysis, a uniform (i.e. unity) prior is used, as no prior knowledge on the atomic position can be employed. The results based on 400 simulated images per setting and a region-of-interest of $40\,\mathrm{px} \times 40\,\mathrm{px}$ are presented in figure 5.9 and table 5.1.

Based on this analysis, we can make the following observations: We have a slightly better position resolution for a single atom using the maximum likelihood method, as we now use the full information on the signal distribution. The improvement is however not very large, as the centre of a distribution can be quite reliably determined even without knowledge of the exact distribution. However, while

[9] Note that this is exactly the functional form of the red line in figure 5.2.

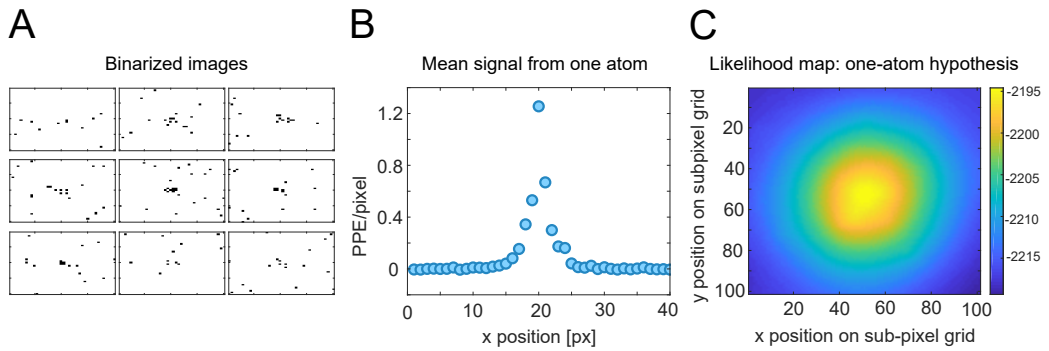

Figure 5.9.: **Illustration of the likelihood study. A:** A set of simulated example images after binarization, based on the assumption of a single atom in the centre of the image, with parameters otherwise close to those presented in this chapter. **B:** Cut through the mean signal from one atom within the simulation. The distribution is consistent with the experimentally observed signal presented in figure 5.2. **C:** Two-dimensional likelihood map of the one-atom hypothesis. The most likely position of a single atom is at the maximum of this distribution, while the width of the peak is a measure for the credibility interval in the position of the reconstructed atom. This likelihood map has to be compared to the likelihood value of the zero atom hypothesis, and the four-dimensional map of the two-atom hypothesis in order to draw a conclusion on the most likely configuration of atoms.

the low-pass method fails to identify two atoms closer than 30 µm together, the likelihood method is capable of reliably detecting two atoms only 10 µm apart from each other. In addition, only with this method we can at least partially distinguish two atoms from one even in the case that they are sitting directly on top of each other. It is crucial to keep in mind that this will fundamentally never be possible with full fidelity, as first of all the number distributions of primary photo electrons for two and one atom overlap, and in addition the Erlang distribution only allows for a partial discrimination capability between one and two PPEs per pixel. In this context, it is also clear why the fidelity of detecting a single atom is smaller for the likelihood method than for the low-pass method, as the latter method effectively only tests for at least one atom present instead of exactly one. In conclusion, it is clear that the likelihood analysis method indeed offers potential for significant improvement. Only within this approach it is possible to include all the information available on the system and the imaging in the reconstruction. In particular, any additional a-priori knowledge can also be directly included. For example, the independently measured particle number distribution can be directly implemented in the form of a prior. At the same time, the improved reconstruction capability comes at the expense of an increased com-

0.5 % CICs

Setting	Low-pass method		Maximum likelihood method	
	[p(0),p(1),p(2)]	rms spread	[p(0),p(1),p(2)]	rms spread
0 atoms	[1,0,0]	-	[1,0,0]	-
1 atom	[0.013,0.987,0]	3.3 µm	[0.003,0.867,0.13]	2.8 µm
2 atoms d=30 µm	[0,0.065,0.935]	3.3 µm	[0,0,1]	2.7 µm
2 atoms d=20 µm	[0,0.84,0.16]	-	[0,0.005,0.995]	3.1 µm
2 atoms d=10 µm	[0,1,0]	-	[0,0.02,0.98]	3.7 µm
2 atoms d=0 µm	[0,1,0]	-	[0,0.033,0.967]	-

1.7 % CICs

Setting	Low-pass method		Maximum likelihood method	
	[p(0),p(1),p(2)]	rms spread	[p(0),p(1),p(2)]	rms spread
0 atoms	[0.997,0.003,0]	-	[0.965,0.033,0.003]	-
1 atom	[0.018,0.98,0.003]	3.3 µm	[0,0.837,0.163]	3.0 µm
2 atoms d=30 µm	[0,0.078,0.922]	3.4 µm	[0,0,1]	3.0 µm
2 atoms d=20 µm	[0,0.813,0.187]	-	[0,0,1]	3.3 µm

Table 5.1.: **Results of the likelihood study.** For this study parameters as presented in section 5.2 are assumed. Two different CIC rates are used, in order to also reflect a possible improvement using a new camera. Several configurations are simulated: No atom present, one atom roughly in the centre of the image (however not exactly, in order to avoid a possible bias due to the symmetry of the problem), and two atoms at variable distance d. For all settings and based on 400 images each, the occurrence rate p to reconstruct zero, one or two atoms is calculated alongside the rms spread of the detected positions (where applicable). This procedure is performed for the low-pass based method as well as the likelihood approach.

putational cost. Therefore, it will be necessary to restrict the relevant region of interest in a pre-analysis of the images. In addition, the reconstruction presented above is a limiting case in the sense that it was the theoretically best possible reconstruction (up to numerical errors and the finite grid size). The same fidelities can only be reached if, like in this case, the exact statistical distribution of signal counts is known. By a careful imaging calibration this is however within reach. For the experiments presented in this thesis, the likelihood approach was not yet employed.

5.4.5. Optimizing imaging parameters

In this section, I will outline how to optimize the imaging parameters, with a focus on the specifications discussed in section 4. The discussion is based both on the current status of the imaging system, as well as possible future improvements. The following physical situations are of particular interest:

- Very few atoms per spin state. This is the situation where the imaging performs best. As the initial atom number is fixed and known, postselection

is possible to mitigate the effects of a finite detection probability.

- $\mathcal{O}(10)$ atoms per spin state. These are system sizes where we can still near deterministically prepare a quantum system and observe the emergence of many-body effects. In order to make full use of our preparation capabilities, also a full single detection scheme is needed. This will be the limiting case for a true single-particle imaging and postselection will already be challenging.

- $\mathcal{O}(100)$ atoms per spin state. For these atom numbers, we will have to rely on (quasi) thermal systems without a fixed particle number and cannot hope for full single-particle resolution.

I will assume that the following experimental tools are at hand. These are based on existing state-of-the-art equipment or tools which will be available in the near future.

- A high NA objective
- EMCCD camera
- sCMOS camera
- Pinning lattice

For the objective, I will use the parameters of the objective used in our experiment. The parameters of importance will be the photon collection efficiency, the field of view, and as a limiting case for any point spread function the optical resolution. The magnification M will be an optimization parameter but for all realistic situations be approximately in the range $M \in [5, 10]$. I will compare the performance of an EMCCD camera to the performance of a scientific complementary metal-oxide-semiconductor (sCMOS) camera. For the EMCCD, the relevant parameters are the effective extraction efficiency and the CIC density. I will use the parameters of the NüVü camera but assume the functionality of the Andor camera used in the previous sections. In figure 5.7, the extraction efficiency is plotted as a function of the CIC density. For an sCMOS camera, the signal has to be compared to the read noise (dark current is typically negligible for our application). As a typical example, I will use the Andor Neo 5.5 sCMOS camera. It features a quantum efficiency of $QE = 0.55$ and a read noise of $\sigma_{read} = 2.5e^{-}$ with settings applied that allow us to take two images in quick succession. Note that there are back-illuminated sCMOS cameras with significantly higher quantum efficiency and lower read noise. However, none of these feature a (true) global

shutter needed for this imaging scheme.[10] Finally, I will also take into account additional pinning potentials. I will assume a far off-resonant pinning lattice, as this is the only configuration which can readily be integrated into our experiment. For example, in a bow-tie configuration a lattice depth of several 100 µK can be reached.

A few spread out atoms

As outlined above, based on an average of 330 scattered photons within 20 µs, of which we collect around 20, we reach a detection fidelity of 99.4 ± 0.3 %. This is combined with a position uncertainty of 4.0 ± 0.4 µm while keeping full hyperfine state resolution. By virtue of a $T/4$ expansion in a waveguide potential with a trap frequency of for example $\omega_{wg} = 2\pi \cdot 75$ Hz (see [28]), we can spread out the atom distribution across around 100 µm. Therefore, in this example the position uncertainty translates into a momentum uncertainty of $\sigma_{mom} = 0.18\,/\mu\text{m}$ (or 4 % of the maximum momentum).

All these values are optimized for the parameters of the Andor. With the NüVü, due to a reduced CIC rate, we can get away with fewer scattered photons and thus a better position uncertainty. This can already be seen in the most basic model: We assume that our signal is spread over around n x n pixels, such that there are rarely more than two PPEs per pixel in order to keep the full counting statistics. Now we compare the number distribution of the signal to the probability of a coincidental cluster of CICs. As a function of for example the exposure time, the signal distribution is given by a binomial distribution with N photons/decision where the probability is set by the effective collection efficiency, given by the collection efficiency of the imaging system as well as the quantum and extraction efficiency of the camera. If the position of the atom is already known beforehand, the appropriate noise distribution is also easy to calculate and given by a binomial distribution as well (with n^2 decisions with a probability given by the CIC rate). Here, we rather calculate the probability that *somewhere* on the image of size R x R pixels, a number of k CICs occurs within a region of interest of size n x n pixels.[11] For the parameters of the NüVü and the Andor, this is shown in figure 5.10. Note that these plots in general have a third axis,

[10] There exists a first prototype of a back-illuminated camera which might be used with a global shutter, however not yet matching any other requirements needed for scientific use [225].

[11] The number of total CICs C is given in terms of the binomial distribution B and the CIC rate p_{CIC} via $B(C|R{\cdot}R, p_{CIC})$. The number N of potential clusters of size k, possible to form out of C CICs, is given by $N = \binom{C}{k}$. Assuming periodic boundary conditions, the probability that the CICs are within the region of interest n x n is given by $\left(\frac{n}{R}\right)^{2(k-1)}$. Finally we have for the mean number M of clusters of size k: $M(k) = \sum_C B(C|R \cdot R, p_{CIC}) \cdot N \cdot \left(\frac{n}{R}\right)^{2(k-1)}$.

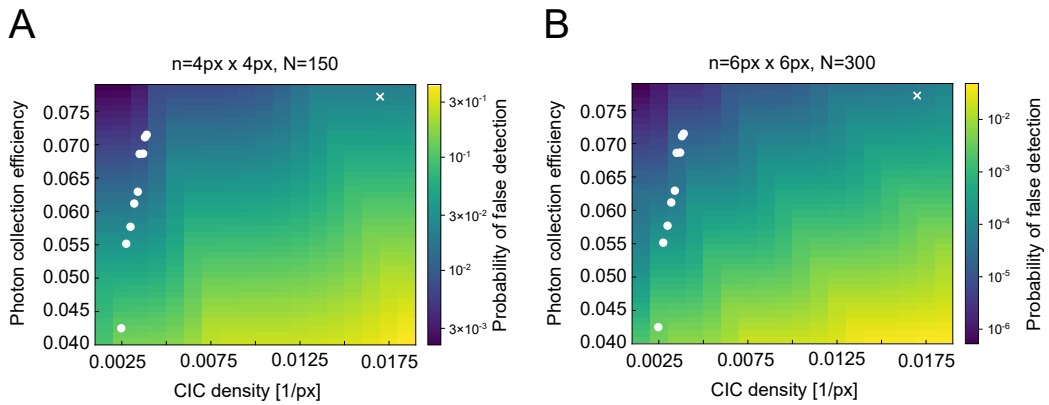

Figure 5.10.: **Detection efficiency of a single atom.** Calculated probability of at least one false negative or false positive occurring (logarithmic colour scale) as a function of the total photon collection efficiency and the CIC density. A typical image size of 200 px by 200 px is assumed, with the results depending on this specific choice. The probability of less than k photons detected on the camera is compared to the probability of at least one coincidental cluster of k CICs in a region of interest n, set by the typical spatial extent of the signal from one atom. An optimum cut-off size k_{opt} is chosen such that the sum of false positives and negatives is minimized. White dots show combinations of photon collection efficiency and CIC density possible with the NüVü camera, while the white cross corresponds to the respective value of the Andor camera. **A:** For a mean number of 150 scattered photons, a region of interest $n = 4\,\text{px} \times 4\,\text{px}$ is suitable (see figure 5.8). According to this model, for typical parameters of the Andor, the probability of a false positive/negative is around 1.3 %. With the best Nüvü settings, the probability is at 0.9 % slightly lower. In turn, the number of scattered photons could be reduced to ~ 140 photons in order to have the same fidelity as the Andor. **B:** For a mean number of 300 scattered photons, a region of interest $n = 6\,\text{px} \times 6\,\text{px}$ can be chosen. Both with the best Nüvü and the typical Andor values, the probability of a false positive/negative is below 10^{-4}. With the best Nüvü settings, the number of scattered photons could be reduced to ~ 270 photons in order to have the same fidelity as the Andor. All experimentally measured fidelities are slightly lower, due to additional technical limitations.

as the exposure time also changes the size of the point spread function and thus the size of the region of interest n. From the plot, we can read off that there is indeed some prospect of optimization by using the NüVü. As we will be able to use a slightly smaller number of scattered photons, the position resolution will improve. Note that this simple model underestimates the improvements expected from switching the camera model, as the effect of a reduced counting statistics due to more than one PPE per pixel is not included.

It is important to state that in this regime, an EMCCD is always the better

choice compared to an sCMOS:[12] Even if the effective point spread function is on the order of one pixel, as the position of the atom is not fixed with respect to the pixelgrid, the signal is spread over a few pixels. Therefore, a typical photon number of 15 to 25 is not enough for reliable atom detection in an sCMOS based approach, if a typical quantum efficiency $QE = 0.55$ and electron readnoise $\sigma_{read} = 2.5e^-$ is assumed. Increasing the number of photons further without massively deteriorating the resolution would require active cooling and thus result in a full quantum-gas-microscope setup.

Several spread out atoms

One additional complication arising when several atoms per spin state are imaged, is that the probability of two signal distributions overlapping becomes finite. Assuming roughly 20.0 ± 4.5 PPEs collected per atom and accordingly 40.0 ± 6.3 PPEs for two atoms, there is some discrimination potential. However, at the same time, we do not want to deteriorate the spatial resolution by spreading out the signal over more pixels, such that the approximation of at most one photon per pixel made in the context of figure 5.10 does not hold any more. Thus, we have to account for the imperfect discrimination potential between one and two photons per pixel. We have seen above that at least up to distances of around 10 µm, a likelihood approach is still capable of identifying single atoms, nevertheless.
In this regime, we also first encounter the important hierarchy of length scales: The size of the correlation feature we are interested in has to be much larger than the effective resolution. In addition, the system size itself has to be much larger than the size of the correlation feature, as the finite system size also introduces a correlation length scale (manifesting itself typically as an envelope on top of the correlation features of interest). Experimentally, we will first encounter this hierarchy in chapter 6. For smaller and in particular discrete systems, it will be still possible to deal with the different scales. However, for larger and continuous systems it becomes much more challenging as we will see in chapter 8.
Playing into this and not considered explicitly so far is the magnification. With a smaller magnification, and as a consequence a larger part of the field of view of the objective imaged on the camera, we can spread out the atoms more. Thereby, the overlap of the imaging point spread functions is reduced. On the other hand, we have to make sure that we spread the signal of one atom over several pixels for the identification procedure. For our camera, we work at a magnification of $M = 5.9$ and thus both image the whole field of view and spread the signal suf-

[12] The situation is different in [213], where several hundred photons are collected per atom.

ficiently. In the case of a pinning lattice (or in general a smaller effective point spread function), a camera with more pixels or a smaller magnification can be beneficial however.
Independently of the exact image analysis method used, we will always have to deal with a reduced probability of detecting atoms of the same hyperfine state which are close to each other. Crucially, this *detection hole* will result in (strong) spurious correlations on the length scale set by the minimum distance at which atoms can still be discerned from each other. In the worst case (think of fermionic antibunching), these spurious correlations can also look very similar to expected physical correlations. We will therefore always make sure to carefully exclude the parameter range influenced by the detection hole from the analysis of the underlying physical system. In addition, as a general rule, it has to be ensured that the typical interparticle distance is (much) larger than the scale set by the detection hole (ideally taking into account correlations leading to increased/decreased typical distances between particles).
There is another more subtle complication arising for intermediate scale systems. We can prepare very small systems with a very high fidelity of typically 95 % to 98 %. Together with the detection fidelity, which is even for larger regions of interest at least 98 %, we have only a very small fraction of false positives/negatives. Therefore we can compensate a drop in either the preparation fidelity or the detection fidelity by postselection without significantly introducing noise on the correlation measurement. This is much harder for intermediate scale systems. Assuming 98 % single-particle detection fidelity we have a combined detection fidelity of only 67 % for 20 particles. Also the preparation fidelity will have dropped to typically 70 % to 85 %.[13] Thus, postselection to the correct atom number results in significant false positives or negatives and reaches its limitations. For even larger atom numbers as will be briefly discussed below, we thus have to slightly adjust perspectives away from deterministic preparation and detection.

Around 100 spread out atoms

If the atoms are uniformly spread out over the whole field of view, for example with a box potential, 100 atoms correspond to a mean interparticle distance of almost 18 µm. However, there are very few situations where such a uniform density seems realistic: Any in-situ preparation of a low entropy state in an optical box potential would be extremely challenging due to excitation energies at the

[13] Note that the preparation fidelity of the combined state does not drop with the single-particle fidelity to the power of the number of atoms, as we typically make use of closed shell configurations or gapped many-body states in the preparation.

Fermi surface of $\mathcal{O}(1\,\mathrm{Hz})$. This is a general problem for any in-situ measurement, as a length scale can always be converted into an appropriate energy scale. A particular useful one, in the context of pairing, is the energy of a two-body bound state (in two dimensions). Here, 10 µm correspond to $E = h \cdot 16\,\mathrm{Hz}$.
Despite the fundamental difficulty of preparing systems in-situ at such small energy scales, a time-of-flight expansion from a smaller trap to the size of the field of view can be still possible.[14] In order to include realistic measurements of systems in a harmonic trap with larger densities in the central region, a typical interparticle distance of 10 µm is assumed in the following discussion of a system of around 100 particles.
A few observations can be made straight away:

- The general picture, that within a suitably defined region of interest the presence of at least a certain photon number indicates the presence of at least one atom, remains exactly the same.
- As the probability of having two atoms closer than the point spread function size is rather large, we have a significant signal overlap and individual single atom detection is impossible for any number of scattered photons even with a pinning lattice built in.
- For 20 PPEs on average we are still (albeit barely) in a regime were we have on average less than one photon per pixel detected. Thus, we can still expect significant granularity in the reconstructed density.
- We are in a regime where it might prove beneficial to reduce the number of photons scattered in order to lose less information due to having more than two photons per pixel.

As long as there is significant granularity in the density which is (mostly) due to atom number fluctuations, there is potential to extract correlation functions. The correlation signal will be of course reduced by the convolution of the density with the point spread function, the granularity caused by the CIC noise, and the information loss due to more than one photon per pixel being present.
Importantly, there is a smooth transition to the case of correlations between individually identified atoms, when reaching the limit where the point spread functions are well separated.[15] Postselection is not possible in this regime anymore, while there is again a smooth transition from perfect postselection to discrete

[14] With the help of a matterwave telescope this nevertheless can be an in-situ measurement.
[15] There is a subtle difference in the autocorrelation peak appearing for density correlations wich is not present when individual particles are correlated, which will be discussed in section 6.3.

noise caused by false positives and negatives to continuos noise by imperfect single atom resolution.

The advantage of these correlation measurements described here to *standard* noise correlation measurements [23, 27, 183] based on absorption imaging is that the contribution from atom noise compared to other noise source can be much larger. This is true in particular when working close to the single atom resolution limit, resulting in smaller correlation amplitudes which still can be detected. I will present first preliminary results in this regime in chapter 8. In order to illustrate the potential of this method, I present in addition also an example of simulated data in figure 5.11. Shown here is a simplified toy model of real space pairing in the crossover region (compare to chapter 3). I simulate an ensemble of $N = 150$ atoms without number fluctuations in a Gaussian cloud of size $\sigma = 54\,\mu\text{m}$. A fraction of $f = 0.5$ of the atoms is paired with a pairing wave function of Gaussian shape. The size of the pairing wave function is chosen to be the inverse of the interparticle distance corresponding to $11\,\mu\text{m}$, in line with the two-body pair size in the crossover regime. This model is of course not capable of capturing the true many-body nature of the atomic ensemble in the crossover regime. However, it constitutes a reasonable limiting case of purely two-body pairs and can be used to benchmark the correlation reconstruction. Shown in figure 5.11 are the normalized second order density correlations obtained by directly correlating the EMCCD images without any image reconstruction in the spirit of a (near) perfect noise correlation analysis. Indeed, we can reconstruct the pairing correlations. However, it also becomes apparent that it will always be a major challenge to realize a separation of the scales between the resolution of the correlation feature (pair size) and the size of the envelope set by the system size. In particular in an experimental correlation analysis, we will have additional spurious correlations due to time-dependent fluctuations of the cloud geometry [183]. Here we consider a situation where the cloud already covers a significant fraction of our field of view. Even for this situation, the pair size has to be finely tuned to a range where it is slightly larger than the effective resolution while still being smaller than the cloud size.

Also in this regime an sCMOS camera offers no improvement. Without any pinning, we have around one photon per pixel and therefore are dominated by read noise. However, it is crucial that this is very specific to our imaging scheme collecting only a few photons per pixel. As soon as there are more than $\mathcal{O}(10)$ photons per pixel, an sCMOS camera is always advantageous, as the EMCCD has limited photon number resolution.

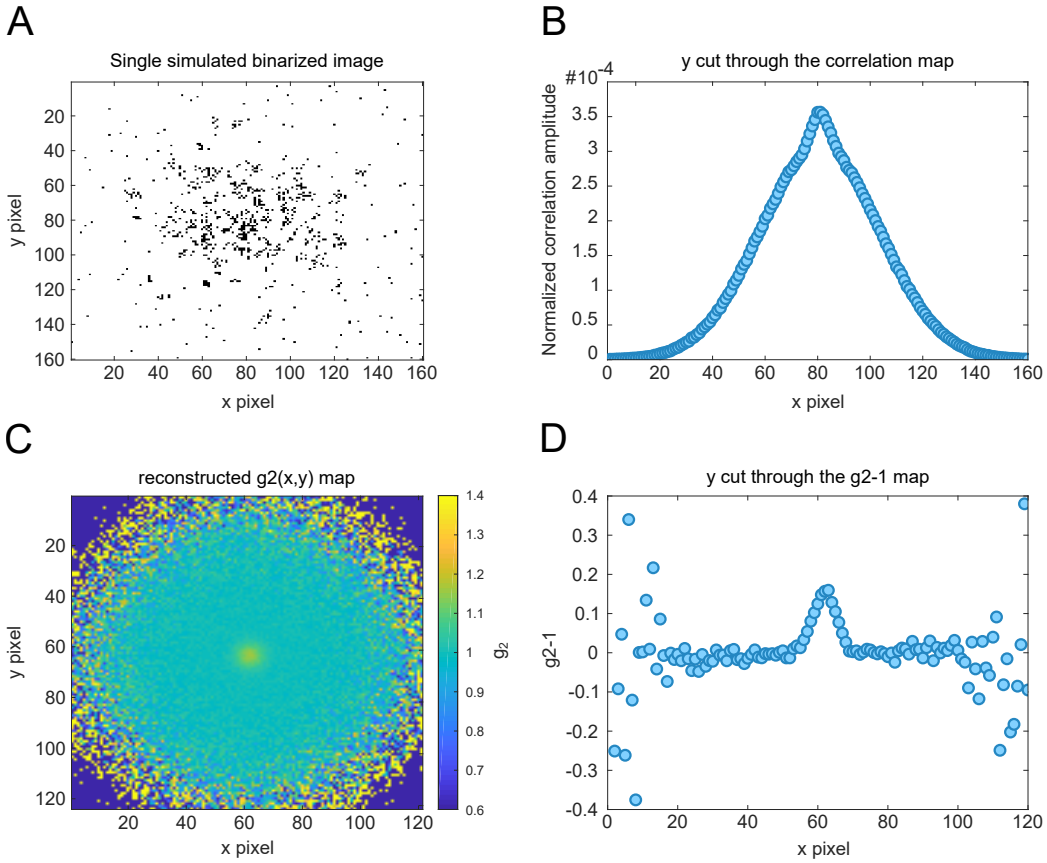

Figure 5.11.: **Simulated in-situ correlations.** Simulation for 150 atoms per spin state with a paired fraction of 50 %. On the camera, there are on average 15 photons per atom impinging. Correspondingly $w = 1.5$ is chosen for the effective point spread function according to equation 5.2. The Gaussian width of the cloud is $\sigma = 54\,\mu\text{m}$, corresponding to a peak density of 0.06 atoms/pixel. The pair size is set to be equal to the central interparticle spacing of 11 µm **A:** Example image of a single realization after binarization. **B:** Cut through the calculated second order density correlation map (G_2). Details on the correlation analysis are discussed below. The correlations are dominated by the envelope set by the system size. **C:** Correlation map with the envelope divided out (g_2 map). In the centre a correlation peak due to the real space pairing can be observed. **D:** Cut through the correlation map of C. The pair correlations are clearly visible. The correlation amplitude is however already significantly reduced below the ideal value of 0.5, based on the paired fraction.

5.4.6. Quenching interactions

For the interacting few-body systems discussed below in chapter 6, we will not explicitly quench interactions by tuning the scattering length. We rely on the fact that due to the fast initial expansions after the tight optical tweezers are switched off, the reduced density quasi-instantaneously quenches the interactions. As we

have shown and used to our advantage in [33], this assumption does not hold in general. For a straightforward improvement, the time-of-flight could be performed in a 2D trap similar to the one employed in section 3, and discussed further in chapter 7. This is a valid option even for a 1D system, in order to reduce the density during time-of-flight. Nevertheless, in particular for larger scale systems, a strategy to actively quench the scattering length is necessary. A possible method is to (quasi-) instantaneously change the hyperfine state composition of the system into a mixture with a small scattering length. Similar to the rf methods employed in chapter 3, these transitions do not change the momentum of the transferred atoms and thus do not alter the quantum state encoded in the atoms. Unfortunately, all possible combinations of the states $|1\rangle - |3\rangle$ feature broad overlapping Feshbach resonances. Therefore, we have to rely on a different mixture. A possible candidate is the $|1\rangle - |4\rangle$ mixture, which is expected to be mostly collisionally stable and very weakly interacting [154]. The energy difference between the states $|3\rangle$ and $|4\rangle$ is typically around $E/h \approx 1.7\,\mathrm{GHz}$ for the employed magnetic field range and thus in the microwave regime. Hence, driving microwave transitions in analogy to the rf transitions considered before seem to be a promising approach. As the microwave transitions change the electron spin, the matrix element between state $|3\rangle = |m_j = -1/2, -1\rangle$ and state $|4\rangle \approx |+1/2, -1\rangle$ is comparably large. Therefore, with a resonant microvave circuit at reasonable powers of around 10 W, we achieve Rabi rates of around $\omega_{mw} = 2\pi \cdot 400\,\mathrm{kHz}$ at specific magnetic offset fields. Unfortunately, most likely due to resonant behaviour of the vacuum chamber and setup, it is currently not possible to freely shift the resonance frequency of the microwave circuit. Therefore, it is not yet possible to use the microwave setup at arbitrary magnetic offset fields.

An alternative to microwave pulses is given by optical transitions. As we have to couple two hyperfine states of the electronic ground state, we can make use of two-photon transitions in a Raman configuration. In this setup, we phase coherently drive a two-photon transition formed by either a π transition up in energy and a σ_- down, or a σ_+ transition up and a π transition down, in order to change the m_j projection of the atom by $+1$. The two-photon detuning is set to the energy splitting between states $|3\rangle$ and $|4\rangle$. In addition, the probe beams are counter-propagating such that there is no net momentum transfer. The individual beams are detuned in-between the D1 and D2 line, far off-resonant from both single photon transitions. The following considerations are based on the explicit calculation of transition rates, a set of measurements performed with a phase locked laser setup described in [226], and comparison to literature [227]. The calculations are taking into account the actual light polarisations in the lab

frame[16], and all optical transitions of the D1 and D2 line with their respective matrix transition elements including the full hyperfine structure.
The contributions from the D1 and the D2 line to the total Rabi rate interfere constructively for a detuning in-between them, however destructively if both transitions are blue or red detuned with respect to the Rabi beams. Since for ^{6}Li the splitting between the two lines is approximately 10 GHz and therefore rather small, residual off-resonant scattering becomes limiting. The theoretical best ratio between the timescale of a $\pi/2$ pulse and the off-resonant scattering rate is at typical magnetic fields of a few hundred Gauss around or below 100. In the experimental implementation, this factor is worse, roughly by a factor of two, most likely due to deviations of the employed laser from a purely monochromatic light source. Additional complications arise due to the strong magnetic field dependence of the transition of around $2\pi \cdot 2500\,\mathrm{kHz/G}$, requiring both exquisite magnetic field control and large Raman rates. In addition, as the intensity of the Raman beams is directly proportional to the coupling strength of the hyperfine states, the intensity has to be homogeneous across the sample and very well stabilized. Due to these constrains, it would be advantageous to drive a Landau-Zener sweep to transfer the hyperfine population instead of a single $\pi/2$ pulse. However, this is (even in theory) not possible with a fidelity of above 95 % due to the off-resonant scattering. In the experiment, we measure Raman rates of around 300 kHz at intensities of the individual beams of around $44\,\mathrm{mW/mm^2}$. While Landau-Zener passages are out of reach, this is significantly faster than the timescale of fluctuations of the magnetic field of $\mathcal{O}(10\,\mathrm{mG})$, such that these values still allow for a single $\pi/2$ pulse to be performed with 98 % fidelity (see also [227]). In addition, the optical powers needed for a beam which is homogeneous across a mesoscopic quantum system with a size of $\mathcal{O}(10\,\mu\mathrm{m})$ still are feasible.
Currently, both a setup based on Raman-transitions and on microwave transitions is implemented at a prototype stage, with a final setup under construction.

5.5. Concluding remarks

In conclusion, in this chapter I have described an imaging scheme which allows us to measure correlations with single-particle resolution in real and momentum space. Correlation measurements between both different and identical hyperfine

[16] As it is not possible to have counter-propagating beams which drive only $\pi + \sigma_-$ transitions (or $\sigma_+ + \pi$), we use two linear polarized beams in the lab frame and have to take additional off-resonant scattering processes into account.

components are possible. Therefore, it is ideally suited for systems featuring an interplay between interaction-based correlations between different hyperfine components and symmetrization-based correlations between identical particles. Due to its versatility based on the free space nature of the scheme, a set of matter-wave manipulations are possible prior to imaging. Together, these achievements constitute the first important milestone of chapter 4. The imaging scheme is first and foremost developed with small and medium scale systems in mind. Nevertheless, in this chapter, I have also discussed to which extend it is applicable to significantly larger systems as well. Before going back to many-body systems however, in the following chapter, I will discuss correlation measurements in small few-body systems which became possible due to this imaging scheme.

6. Correlations in microscopic systems

In the previous chapter, I have discussed how to record the position and hyperfine state of all the atoms in a small or medium scale quantum system. Following the strategy outlined in section 4, the next step will be to utilize these capabilities for detecting correlations in a quantum system of interest, while trying to distil as much information on the underlying state as possible out of these measurements. Despite the huge progress made in terms of detection capabilities, it is not advisable to directly go back to studying full large scale many-body systems, however. On the technical side of things, we would be again reaching limitations of the imaging scheme in terms of scalability towards larger system sizes. But this is not even the most important argument: Also conceptually, it is a priori not at all obvious how to identify and interpret different correlations which might be present in a many-body system. Typically, only in the very weakly interacting limits, there is a clear expectation for the relevant correlation structure measurable based on low-order correlation measurements (see for example [27]). In a general, strongly correlated system, the complex interplay of indistinguishability and interactions can and will lead to a complex correlation structure, with the relevant features needed for a better understanding of the underlying physics oftentimes hidden in plain sight. There is not yet an established method to characterize correlations in this limit such that existing measurements (see for example [228]) are often times very hard to interpret. For these reasons, I will instead start out by discussing very small systems of up to three particles. I will furthermore conceptually simplify matters by only studying systems with a few discrete spatial modes as given by different wells of our double- or triple-well microtrap geometry introduced in section 2.5.2. Parts of the results presented here have been published in [29–31]. We have also studied systems where many spatial modes are of relevance in [33], these results will not be discussed in detail here though.

Based on these small systems, I will outline how we build up a toolbox for classifying different states based on correlation measures. We will focus on correlations

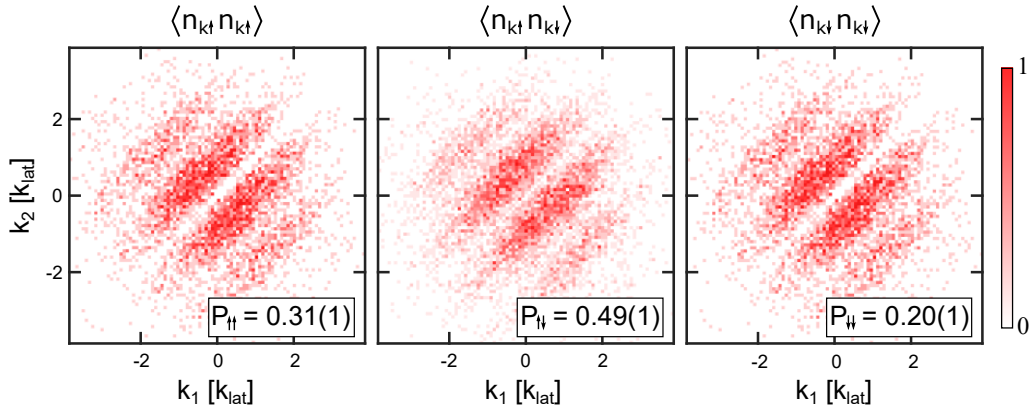

Figure 6.1.: **Second order momentum density correlations.** Experimentally measured correlation functions $\langle n_{k\alpha} n_{k\beta} \rangle$ with $\alpha, \beta \in [\uparrow, \downarrow]$, together with the population of the spin modes $P_{\alpha\beta}$. The correlation map is obtained by a histogram of coincidence measurements, thus sampling the correlation function. More details will be given below. Adapted from [31].

which are prototypical for larger systems as well, and will develop a procedure to learn as much as possible about the prepared states. This will include a reconstruction of the density matrix and a discussion of entanglement properties. At first glance, all this might sound like a very technical procedure and merely an intermediate step towards *interesting* larger states. However, it will turn out that there are a lot of open questions even for rather small systems, in particular when delving into entanglement properties. Crucially, the approach presented here will go beyond the description of states with exactly one immobile particle per site, as typically encountered in trapped-ion [220] or superconducting-qubit systems [229] but also often times engineered in optical lattice or tweezer arrays [230–232]. For these immobile particles, which behave classically in their external degrees of freedom, pure spin models can be applied, while the description becomes conceptually more challenging for mobile particles in itinerant systems. This is in particular the case in combination with indistinguishability introduced, as individual particles at individual sites can no longer be used as a natural *partitioning* of the system.

As an appetizer, and to illustrate these points, consider the correlation measurements of a - for now - unknown state shown in figure 6.1: Presented are second order correlation measurements between momentum space densities (extracted via time-of-flight methods) of two atoms initially prepared in a double-well potential. We observe very strong correlations (as indicated by a correlation structure with very high *visibility*) for all combinations of the hyperfine states. Naively, I might

therefore try to infer that this has to be a complicated state, possibly even highly entangled. As it will turn out however, the state prepared is conceptually very simple, namely two identical particles prepared independently from each other in two close-by microtraps. The *mistake* I made, which lead to the conclusion of a complicated state, was on the one hand that I ignored the fact that already the Pauli principle can lead to strong correlations; and on the other hand, that the measurements were performed in an unfavourable basis by choosing a spin projection basis which was rotated with respect to the natural quantization axis. From this example it can already been seen that an essential discussion point in this chapter has to be how to choose the basis and observable you describe and measure your states in. This can be of practical interest, as for a complicated many-body state knowing or at least guessing a suitable basis can dramatically simplify the description and the measurement protocols. In addition, the whole notion of entanglement, as introduced in section 2.1, is based on a specific choice of partitioning, as a state is defined to be entangled if it is not separable into a product state with respect to a specific partitioning of the Hilbert space. For example, if the total Hilbert space H is subdivided into two subsystems A and B with $H = H_A \otimes H_B$, a general state $|\Psi\rangle \in |\Psi\rangle_{A\otimes B}$ is bipartite entangled if it cannot be written down as a product state of $|\psi\rangle_A \in |\Psi\rangle_A$ and $|\psi\rangle_B \in |\Psi\rangle_B$. Similar concepts apply also for tri- and higher order partite entanglement as introduced in section 2.1. The notion of entanglement is of course invariant under a local basis change within subsystem A or B, but strongly depends on the global basis and thus partitioning choice.

Let me illustrate this while at the same time introducing the basis states used in this chapter. From here on, for the ease of notation and visual clarity I will always label the hyperfine states by a (pseudo-)spin projection $|\uparrow\rangle$ and $|\downarrow\rangle$. Note that therefore $|\uparrow\rangle$ and $|\downarrow\rangle$ might correspond to different specific hyperfine states for different sets of experiments. I assume that each site of the double or triple-well will contribute exactly one spatial mode which I will denote by left L, right R, and for the triple-well also central C.

We will encounter situations where we can distinguish the atoms by their spin projection. In these situations, the *particle partitioning* can be the most obvious choice where each atom is its own subsystem. Thus, we might denote a single atom of spin up in the leftmost well by $|L\rangle_\uparrow$. If we add another atom of spin down to the leftmost well, the state is given by $|\phi\rangle = |L\rangle_\uparrow \otimes |L\rangle_\downarrow =: |LL\rangle$. The state space of two distinguishable atoms in a double-well is thus spanned out by

$$\{|LL\rangle, |LR\rangle, |RL\rangle, |RR\rangle\}. \tag{6.1}$$

By construction, the above state $|LL\rangle$ is a product state and thus not entangled. A prototypical example of an entangled state is the Bell state $|\psi^+\rangle = \frac{1}{\sqrt{2}}(|LR\rangle + |RL\rangle)$. I will discuss a scheme to prepare this and also other bi- and tripartite entangled states below.
Another possible choice is the *mode partitioning*, where we subdivide the system according to the different spatial modes given by the different sites of the double- or triple-well potential. For example, the state of two distinguishable particles both in the left well of the double-well is now given by $|LL\rangle = |\uparrow\downarrow\rangle_L \otimes |0\rangle_R =: |\uparrow\downarrow, 0\rangle$, or more in general, any state is spanned out by

$$\{|\uparrow\downarrow, 0\rangle, |\uparrow, \downarrow\rangle; |\downarrow, \uparrow\rangle, |0, \uparrow\downarrow\rangle\}. \tag{6.2}$$

This partitioning is also quite useful for particles of the same spin projection, which cannot be labelled based on internal parameters. Nevertheless, also for indistinguishable atoms, a particle partitioning is possible. In this case, and in a first quantization description, formal labels 1 and 2 are introduced for the particles, which in turn forces us to manually symmetrize the state afterwards. Thus, the state of two particles in two wells can be written down as $|\psi^-\rangle = \frac{1}{\sqrt{2}}(|1, 2\rangle - |2, 1\rangle)$, where in analogy to above $|i, ii\rangle$ denotes the state where the particle i (ii) is in the left (right) well. This state is formally identical to a Bell state and thus maximally entangled. On the other hand, this 'entanglement' is only an artefact of the first quantized description. It is heavily discussed in the literature whether such a state should be considered entangled [37, 100–104]. I will try to shine some light on this question in section 6.4, and even more importantly discuss how this indistinguishable particle entanglement manifests itself in measurements and how to differentiate between correlations rooted in symmetrization and interactions.
To summarize, the questions I would like to address in this chapter are:

- **Interaction-induced correlations and entanglement:** Is it possible to characterize small but strongly interacting few-particle systems by measuring correlation features? Can we connect the correlations measured also to entanglement? Can we identify prototypical correlation and entanglement features which will also help us to study larger many-body systems?

- **Identical particle correlations:** The necessity for antisymmetrization of fermionic wave functions already results in strong correlations. Can we measure these and what do we learn about indistinguishability?

- **Identical particle entanglement:** Does this also mean that these states

feature entanglement? Is it somehow possible to differentiate between correlations and entanglement caused by interactions and by symmetrization and how can we make sure that if we measure (strong) n-th order correlations in a system, this actually tells us something about how *complicated* your state is?

6.1. Preparing and detecting few-body states

In this section, I will describe the preparation of the relevant two and three particle states of either the same or different spin projection in two or three tunnel-coupled microtraps. From this pool of states, we will avail ourselves of the correlation and entanglement studies presented. For the preparation, we will make heavy use of our capabilities of preparing deterministic quantum states in individual microtraps as introduced in section 2.5.2. We will use that by applying spin-selective gradients during the spilling process, we can prepare the number states almost independently for the different hyperfine states. In addition to the preparation scheme, I will explain how we detect the atoms afterwards. This will of course build upon the methods introduced in chapter 5 making use also of the matterwave manipulations introduced in section 5.3.

6.1.1. Preparation of few-body states

The relevant states used in this chapter are sketched in figure 6.2. They include: Two or three identical particles in two or three wells (states $|A\rangle$ and $|B\rangle$), two identical particles in two wells with the quantization axis on the equatorial plane (state $|C\rangle$), two interacting and tunnel-coupled atoms in two wells (a Hubbard dimer state $|D\rangle$), the same state with an uncoupled spectator atom next to it (state $|1\rangle$), and three interacting and tunnel-coupled atoms in three wells (state $|2\rangle$).

Identical particles in two or three wells

The most straightforward extension of the preparation of a number state in a single well is to prepare n independent copies of this state in n copies of the microtrap. As explained in section 2.5.2, we can apply an rf signal, built up of the sum of different frequencies, to the AOD in order to create multiple copies of our tweezer potential. If we separate the microtraps in the atom plane by at least 10 µm, the lowest lying states are not coupled even if a magnetic field gradient is applied for the spilling process. In this way, we can prepare for example

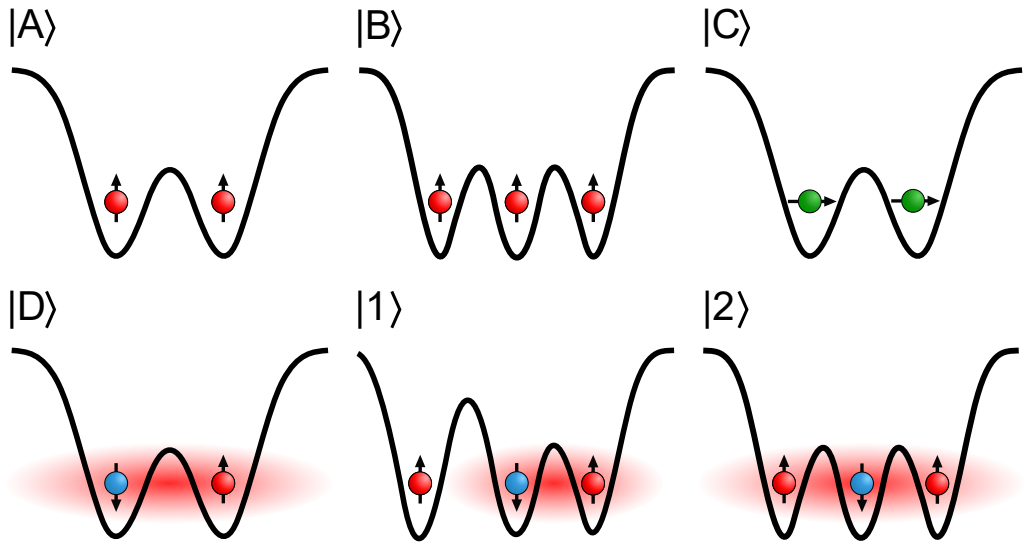

Figure 6.2.: **Schematic illustration of the relevant classes of states.** $|A\rangle$: Two identical particles (spin triplet) in the lowest spatial modes of a double-well without tunnel coupling. $|B\rangle$: Three identical particles in the lowest spatial modes of a triple-well. $|C\rangle$: Two identical particles in the lowest spatial modes of a double-well, with the total spin polarized along the horizontal axis. $|D\rangle$: Hubbard dimer of two particles distinguishable by their hyperfine state and approximately in the lowest band of a tunnel-coupled double-well. Repulsive or attractive interactions can be turned on. $|1\rangle$: Hubbard dimer with an additional spectator atom in an isolated microtrap close-by. $|2\rangle$: Three atoms (two spin-up, one spin-down) in a triple-well with tunnel coupling and interactions turned on.

two (three) atoms of state $|\uparrow\rangle = |1\rangle$ in two (three) independent wells. We can adiabatically bring the wells closer to each other after preparation, making sure that there is no overlap between the on-site wave functions, such that the lowest band (more precisely lowest mode) approximation is well met. Note that this is equivalent to the above assumption that each site contributes exactly one mode. We reach a preparation fidelity of typically 0.95 (0.92) for two (three) particle states (labelled $|1\rangle$ and $|2\rangle$) compatible with the assumption of an independent preparation in each well. It is important to stress that these identical particles in different wells are fully independent[1] and *blind* to each other except for constraints due to the Pauli antisymmetrization. Thus, any correlations observed can solely be caused by the fermionic nature of the particles.

[1]Being slightly pedantic, it could be noted that the particles do share a common history before the loading into the microtraps. However, at the corresponding temperatures and densities there are no correlations at the length scale of $\gtrsim 10\,\mu\text{m}$. In the language of Bell tests, this could be considered a loophole nevertheless.

(Partially) distinguishable particles in two or three wells

In addition to the product states of indistinguishable particles, we also prepare interacting states of two distinguishable (by their hyperfine state) particles, in addition to states with three or more particles, where both interactions and spin statistics play a role. In each case, we start by a product state of $n_{i,\sigma}$ particles of spin-projection σ in well i with the tunnel coupling switched off. Afterwards we can turn on the tunnelling by bringing the wells closer towards each other. If at this stage the different wells still have a different depth, the coupling is off-resonant, though. Now we can adiabatically turn on interactions by means of tuning the magnetic field, or tune the tunnel coupling into resonance by adjusting the relative depth of the wells. We calibrate the tilt of the tweezers by mapping out the tunnel resonance for a single-particle tunnelling between two of the wells as shown already in figure 2.13. Based on this set of experimental steps, a broad range of different states can be prepared, as I will present in this section. In order to discuss this in a systematic way, first a theoretical treatment of the system is needed:
To describe the system of interacting particles theoretically, we assume that it is described by a Fermi-Hubbard Hamiltonian of the form [163]:

$$H = -J \sum_{\{i,j\}} \sum_{\sigma} \hat{c}^{\dagger}_{i,\sigma} \hat{c}_{j,\sigma} + U \sum_{j} \hat{n}_{j\uparrow} \hat{n}_{j\downarrow} + \sum_{j,\sigma} \hat{n}_{j\sigma} \Delta_i, \tag{6.3}$$

where $\hat{c}^{(\dagger)}_{j\sigma}$ is the fermionic annihilation (creation) operator on site j corresponding to spin state $\sigma \in \{\uparrow, \downarrow\}$, $\hat{n}_{j\sigma} = \hat{c}^{\dagger}_{j,\sigma} \hat{c}_{j,\sigma}$ denotes the particle density, and $\{i, j\}$ runs over nearest neighbours alone. J denotes the tunnel coupling and U the on-site interaction energy. In addition, Δ_i is a site-dependent (but spin-independent) offset of the potential, taking over the role of a chemical potential. The relevant approximations made are that the tight-binding approximation holds, and that the relevant physics is described by a single band only. Within the tight binding approximation, a basis of local Wannier states on the individual lattice sites j is chosen, resulting in only next neighbour tunnelling. For not too large tunnel rates, this is well fulfilled as the tunnel rate of $T \approx 2\pi \cdot 100\,\mathrm{Hz}$ is much smaller than typical trap frequencies of $\omega_{ax} \approx 2\pi \cdot 5\,\mathrm{kHz}$. Within the tight binding approximation, we can also describe the interaction strength by an on-site interaction strength U alone, which is calculated according to equation 2.29. We can calibrate U either by comparison to the Hubbard model, more directly by a shift in the tunnel resonance or by direct calculations based on the known scattering length and the trap parameters.

For the single band approximation to hold, the on-site interaction energy U has to be smaller than the single-particle excitation energy. These assumptions are reasonably fulfilled for intermediate scales of the interaction energy (see [163] for a qualitative discussion of the case of two wells and two particles, in addition to a description of the experimental calibration of the parameters). Note however, that we are also specifically interested in the limit $|U|/J \gg 1$ where this approximation will be less accurate. Nevertheless, the Hubbard results will provide valuable intuition in this regime as well. For a few wells, we can easily write down the Hamiltonian in a matrix form. For example, for two particles in a double-well where the single-particle modes are given by $|L\rangle, |R\rangle$ and we have a tilt of $\Delta_R = \Delta$ and $\Delta_L = -\Delta$, we can write down the Hamiltonian in the two-particle basis $\{|LL\rangle, |RL\rangle, |LR\rangle, |RR\rangle\}$:

$$H = \begin{pmatrix} U-2\Delta & -J & -J & 0 \\ -J & 0 & 0 & -J \\ -J & 0 & 0 & -J \\ 0 & -J & -J & U+2\Delta \end{pmatrix} \tag{6.4}$$

We can solve for eigenstates and eigenenergies by diagonalizing the Hamiltonian for any parameter of the model. In particular for more complicated N-body Hamiltonians, the diagonalization is performed in this thesis with the help of the Python package QuSpin [233, 234]. We can use the results in two distinct ways. We can identify interesting states and in addition work out a possible adiabatic scheme for their preparation. This is shown for two particles of different hyperfine states (corresponding to the Hamiltonian in equation 6.4) in figure 6.3: For $\Delta = 0$ we have for each ratio of U/J four eigenstates labelled $|a\rangle$ to $|d\rangle$. State $|d\rangle$ is the spatial singlet and thus not influenced when varying U/J. Similarly, the state $|b\rangle$ scales trivially with U/J. More interesting are the states $|a\rangle$ and $|c\rangle$ where the competition between delocalization and interactions leads to a change in nature as a function of U/J. For this thesis, mostly the ground state, which is in a spin singlet, is considered. Its functional form is given by

$$|a\rangle = \sqrt{\frac{1}{2}}\left(\sqrt{\frac{1}{1+\mathcal{N}^2}}\left(|LL\rangle + |RR\rangle\right) + \sqrt{\frac{\mathcal{N}^2}{1+\mathcal{N}^2}}\left(|LR\rangle + |RL\rangle\right)\right), \tag{6.5}$$

where

$$\mathcal{N} = \frac{U}{4J} + \sqrt{1+\left(\frac{U}{4J}\right)^2}. \tag{6.6}$$

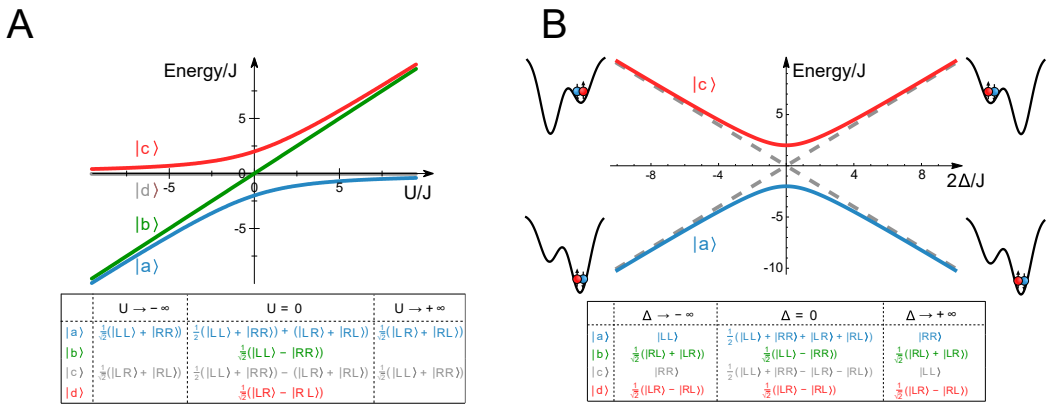

	U → − ∞	U = 0	U → + ∞
|a⟩	$\frac{1}{\sqrt{2}}(\|LL\rangle + \|RR\rangle)$	$\frac{1}{2}(\|LL\rangle + \|RR\rangle) + (\|LR\rangle + \|RL\rangle)$	$\frac{1}{\sqrt{2}}(\|LR\rangle + \|RL\rangle)$
|b⟩		$\frac{1}{\sqrt{2}}(\|LL\rangle - \|RR\rangle)$	
|c⟩	$\frac{1}{\sqrt{2}}(\|LR\rangle + \|RL\rangle)$	$\frac{1}{2}(\|LL\rangle + \|RR\rangle) - (\|LR\rangle + \|RL\rangle)$	$\frac{1}{\sqrt{2}}(\|LL\rangle + \|RR\rangle)$
|d⟩		$\frac{1}{\sqrt{2}}(\|LR\rangle - \|RL\rangle)$	

	Δ → − ∞	Δ = 0	Δ → + ∞
|a⟩	|LL⟩	$\frac{1}{2}(\|LL\rangle + \|RR\rangle + \|LR\rangle + \|RL\rangle)$	|RR⟩
|b⟩	$\frac{1}{\sqrt{2}}(\|RL\rangle + \|LR\rangle)$	$\frac{1}{\sqrt{2}}(\|LL\rangle - \|RR\rangle)$	$\frac{1}{\sqrt{2}}(\|RL\rangle + \|LR\rangle)$
|c⟩	|RR⟩	$\frac{1}{2}(\|LL\rangle + \|RR\rangle - \|LR\rangle - \|RL\rangle)$	|LL⟩
|d⟩	$\frac{1}{\sqrt{2}}(\|LR\rangle - \|RL\rangle)$	$\frac{1}{\sqrt{2}}(\|LR\rangle - \|RL\rangle)$	$\frac{1}{\sqrt{2}}(\|LR\rangle - \|RL\rangle)$

Figure 6.3.: **Energy spectrum of the Hubbard dimer. A:** Lowest band eigenstates of the balanced double-well as a function of the interaction strength U. Indicated are the states written down in the particle basis for the limiting cases of $U/J = 0$ and $U/J \to \pm\infty$. **B:** Eigenstates as a function of the tilt Δ for $U = 0$. Indicated are the states for the limiting cases of $\Delta = 0$ and $\Delta \to \pm\infty$. Importantly, the relevant state $|a\rangle$ takes the form of a product state for a large tilt, indicating a possible path for an adiabatic preparation scheme. Adapted from [163].

For very strong attractions, $U \to -\infty$, it takes the form of what can be interpreted as the few-body analogue of a charge-density wave: The symmetric coherent superposition of both particles left and both particles right $|a\rangle_{U\to-\infty} = \sqrt{\frac{1}{2}}(|LL\rangle + |RR\rangle)$. When tuning towards strong repulsive interactions ($U \to \infty$) the state develops an 'antiferromagnetic' order, with the symmetric coherent superposition of particle one left and particle two right and vice versa, $|a\rangle_{U\to+\infty} = \sqrt{\frac{1}{2}}(|LR\rangle + |RL\rangle)$.
Also from figure 6.3, we can identify a preparation scheme for these states. Here, the eigenenergies and states for $U = 0$ as a function of Δ/J are shown. It can be observed that for a strongly tilted double-well, the eigenstate are given by the trivial product state of both particles in one of the wells. Such a state can be prepared with a high fidelity using the methods introduced above. Subsequently, we can slowly and adiabatically balance the wells to end up either in state $|a\rangle$ or $|b\rangle$. From this starting point, we can then also adiabatically tune the interaction strength in order to reach any desired state. Experimentally, we obtain a measure for the fidelity of preparing the desired state by first (adiabatically) ramping into the state and than on the same adiabatic path back to the product state. Here, we can measure the full occupation statistics and extract the overlap with the initial state. From this, a lower bound of the preparation fidelity is extracted. We infer that we can prepare the ground state of the interacting double-well

with above 90 % fidelity (corresponding to a purity of ~ 0.86, when modelling the experimental state by the theoretical ground state with a 10 % white noise contribution). It is also possible to compare the realized state with the expected state in a Hubbard model. This procedure is presented in [163] with more details presented in [158, 235] and shows good agreement for intermediate tunnel rates and interaction strength. In figure 6.2, the state of two interacting tunnel-coupled atoms forming a Hubbard dimer is labelled $|D\rangle$.

In a similar fashion, we can also study a system of three atoms in three wells. I will restrict the discussion to the case of two atoms in state $|\uparrow\rangle$ and one atom in state $|\downarrow\rangle$. In the most interesting case of very strong repulsive interactions, double occupancies will be suppressed. Therefore, to get a first intuition, we can assume that the eigenstates are built up out of the states $|\uparrow\uparrow\downarrow\rangle$,$|\uparrow\downarrow\uparrow\rangle$ and $|\downarrow\uparrow\uparrow\rangle$. The corresponding Hamiltonian in this basis is thus given by

$$H = \frac{J_{se}}{2}\begin{pmatrix} -1 & 1 & 0 \\ 1 & -2 & 1 \\ 0 & 1 & -1 \end{pmatrix}, \tag{6.7}$$

where $J_{se} = \frac{4J^2}{U}$ is the second order tunnelling process called superexchange coupling. First order tunnelling is fully suppressed in this limit, as it always leads to double occupancies. The next leading perturbative term, given by J_{se}, is thus the process where the doubly occupied state is only a virtual intermediate state, resulting in the expression for the superexchange coupling [236]. The ground state for the balanced triple-well is given by

$$|W\rangle = \frac{1}{\sqrt{6}}\left(|\uparrow\uparrow\downarrow\rangle - 2\,|\uparrow\downarrow\uparrow\rangle + |\downarrow\uparrow\uparrow\rangle\right) \tag{6.8}$$

This is the so-called W state [88, 237] which is tripartite entangled and thus not biseperable.[2] The energy gap from the ground state to the first excited state (of the same symmetry) is J_{se}. For a realistic parameter set with $U = 10J$, we have $J_{se} = 0.25J$ which is only on the order of $2\pi \cdot 25\,\mathrm{Hz}$ such that the preparation of such a state is very challenging but not yet fundamentally impossible. We numerically confirm that for $U = 10J$, now taking into account all states within the Hubbard model, the ground state is indeed close to the W state. A possible adiabatic route to this state is illustrated in figure 6.4 and builds on the same ideas as

[2] For two qubits, as in the case of the double-well, all maximally entangled states can be transformed into each other by local operations and thus fall into the same class of Bell states. As introduced in section 2.1, this is not the case for three qubits any more as there exists both the class of W and GHZ states which cannot be transformed into each other by local operations [88].

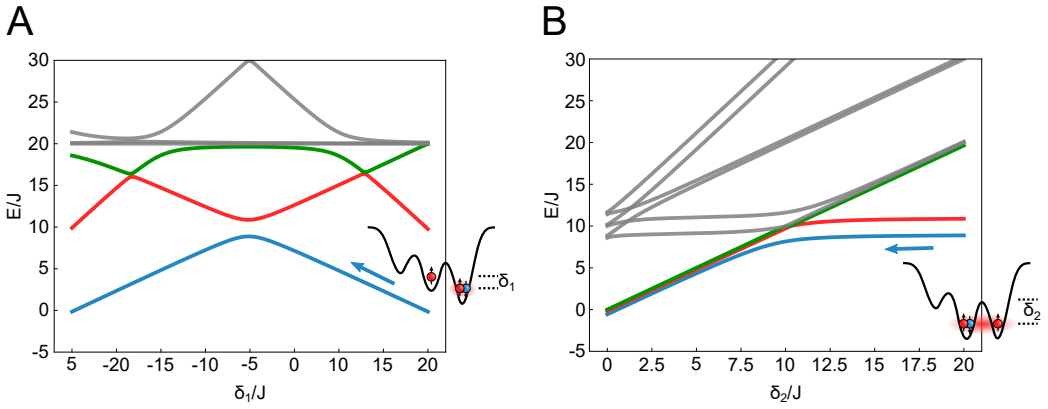

Figure 6.4.: **Energy spectrum of the lowest band Hubbard model of three particles in three wells. A:** Lowest band eigenstates of the balanced double-well as a function of the tilt δ_1. Here $U = 10J$ and $\delta_2 = 20J$. This is conceptually very similar to figure 6.3 B, and for a large detuning δ_1 the state again separates into a product state. **B:** Eigenstates as a function of the tilt δ_2 for $U = 10J$ and $\delta_1 = 0$. For $\delta_2 = 0$ the state is to a good approximation given by the (maximally) tripartite entangled W state. Therefore these plots show that there is a suitable adiabatic route from a product state to the W state with the energy gap always larger than the final state gap J_{se}.

used before in the double-well case. Here, the tilt δ_1 between the middle and the right well, as well as the tilt δ_2 between the leftmost and the middle well, is introduced. The experimental preparation of this state pointed out some fundamental limitations of our preparation scheme: We set the depth of the individual wells by stabilizing the optical power of the microtraps recorded with a photodiode via a digital PID loop. In order to enable tunnel coupling, the individual light distributions have to overlap. Therefore, it is not possible to directly record the power of the wells independently, and we instead measure only the total power of all tweezers. In turn, we have to rely on the assumption that the relative power between the wells is stable and does not drift over time. This is approximately the case, as we precisely control the rf power which sets the percentage of light deflected into the respective microtrap path in the AOD. However, in particular as this is an active element, we can have (among other effects) temperature drifts. Note that, as the small energy scale of the tunnel coupling of $\mathcal{O}(100\,\mathrm{Hz})$ is, for a fixed distance between the wells, set by the much larger energy scale of the overall trap depth of $\mathcal{O}(50\,\mathrm{kHz})$, we need a very high relative stability of at least 10^{-4} in order to study itinerant systems. For a fixed experimental sequence we can indeed achieve this. The requirements for studying systems where the relevant energy scale is given by the superexchange instead of the regular tunnelling become even

more stringent, however. In addition, adapting the experimental sequence (for example with a different time when the microtraps are switched on) can also lead to a different steady state temperature. As a consequence, we have to calibrate the relative depth between all pairs of microtraps in principle for each different sequence. This is already extremely challenging for three wells and nearly impossible for larger systems.[3] Due to these limitations, it was not possible to prepare the W state near deterministically. Instead, the prepared state (labelled $|2\rangle$ in figure 6.2) will be used as a test ground to study a priori unknown (mixed) states with the methods which will be developed in this chapter.
In addition to the states outlined above, we can also prepare *hybrid* states by placing a spectator atom in an isolated microtrap next to a double-well of interacting and tunnel-coupled atoms (state $|1\rangle$). In addition, we can use tailored rf pulses to drive transitions between $|\uparrow\rangle$ and $|\downarrow\rangle$ atoms. By applying a global $\pi/2$ pulse to the state $|\uparrow\uparrow\rangle$, we prepare the state $|C\rangle = \frac{1}{2}\left(|\uparrow\rangle + |\downarrow\rangle\right)_L \otimes \left(|\uparrow\rangle + |\downarrow\rangle\right)_R$ which will provide an important example of a simple state (as it might be symbolically written down as $|{\rightarrow}{\rightarrow}\rangle$), which can appear to be strongly correlated if measured in an unfortunate choice of basis. In fact, as will be discussed later, the results shown in figure 6.1 above are for exactly this state.

6.1.2. Detection of atoms in real and momentum space

For the state reconstruction and entanglement certification, we will rely on measuring the single-particle resolved densities of the different spin states in real and momentum space based on the scheme introduced in chapter 5.

In-situ measurements

The typical spacing between different wells for the experiments described in this chapter are on the order of 1 µm to 10 µm. Unfortunately, this is smaller than our resolution of the imaging method, thus prohibiting direct in-situ imaging. However, we still have the the matterwave optics toolbox described in section 5.3 at our disposal. In-situ imaging is thus achieved with a three-step protocol as illustrated in figure 6.5:

- **Projection:** We project the wave function onto the individual wells by rapidly increasing the depth of the tweezers to a depth were tunnelling is

[3] In order to make progress in this direction, a stabilization of the individual wells is needed. One possible idea is to use that the AOD not only deflects the light in different directions but also changes the frequency. The frequency difference between the wells is typically on the order of a few MHz. It might be possible to resolve it with a very fast photodiode. Such a stabilization setup is not yet implemented.

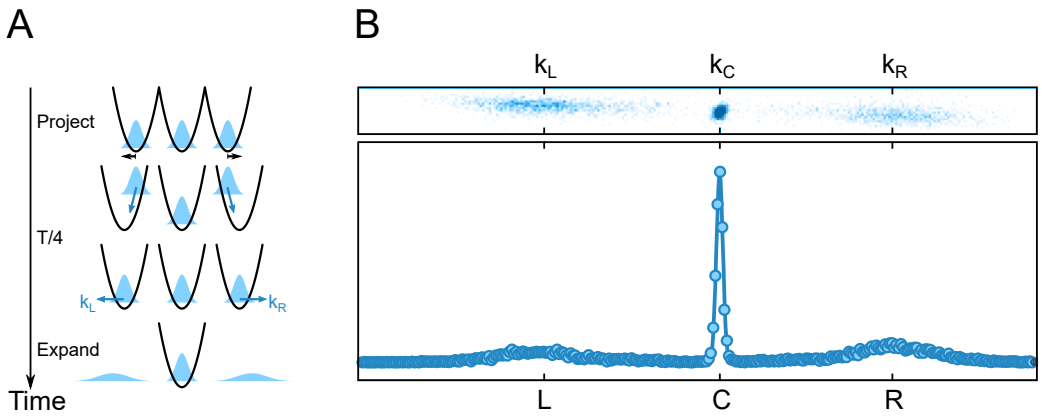

Figure 6.5.: **In-situ measurements in a three well system. A:** Schematic illustration of the three-step protocol based on projection, imprinting a momentum and time-of-flight expansion. The protocol for a two-well system follows analogously. **B:** Typical example of an in-situ measurement. Shown is the histogram of measured positions after time of flight expansion in the waveguide potential before (upper panel) and after (lower panel) integrating out the momentum orthogonal to the 1D axis. Note that the middle well features a much more narrow distribution, as the atoms were confined during the time-of-flight. As the distributions from different wells fully separate, we discretize the measured positions into three bins and recover the in-situ populations with a fidelity of above 99 %. Adapted from [99].

fully suppressed.

- **Imprinting momenta:** We imprint a distinct relative centre-of-mass momentum k_i onto the wave function of each well by displacing the position of the wells, followed by a time evolution of a quarter of the trap period in the microtrap.

- **Time-of-flight expansion:** After the first $T/4$ evolution, we switch off the microtraps and let the atoms expand in a much more shallow waveguide potential (as in figure 5.6) aligned onto the axis connecting the microtraps to extract the momentum of the atoms.

Note that this procedure is an implementation of the matterwave telescope explained in section 5.3. The only difference is that in particular for the first $T/4$ expansion, the tight tweezer potential is not well approximated by a harmonic confinement. Therefore, we measure a significant distortions of the wave functions. Crucially, as we imprint a relative centre of mass momentum k_i which is much larger than any momentum spread of the on-site wave function δk, we can nevertheless reliably infer the population of each well with around 99 % fidelity.

Momentum space measurements

We measure the momentum space density by a $T/4$ time-of-flight expansion in a very elongated optical waveguide potential as explained in section 5.3. To this end, we use various configurations of optical dipole traps with typically around 40 Hz trapping frequency along the multi-well axis, resulting in expansion times of around 6 ms. The weak axis of the waveguide is misaligned with respect to the multi-well axis by about 1°, which manifests itself in a slightly reduced correlation amplitude measured as discussed below. In addition, we also slightly probe the anharmonicity of the waveguide potential such that the mapping between momentum and position after time of flight becomes non-linear. We compensate this to first order by a quadratic rescaling of the measured momenta [99].

6.1.3. Single-particle coherence

Before discussing correlations of two and more particles, it is instructional to first understand the results of a single particle in one or two wells.
The on-site wave function of a single particle in the ground state of a single well is given by the corresponding Wannier function. For this discussion, it is fully sufficient to assume a Gaussian shape. Therefore, also the momentum space wave function is Gaussian with an inverted width. If we detect the atom after time-of-flight and repeat the experiment many times, we thus sample this wave function. This is fully analogous to a single slit diffraction experiment, where the on-site wave function takes the role of the aperture function of the slit. In turn, if a single-particle is delocalized over two wells, this is analogous to a Young's double-slit experiment. Experimentally, we can directly prepare the states $|\phi_\pm\rangle = \sqrt{\frac{1}{2}}\left(|L\rangle \pm |R\rangle\right)$ (in the double-slit analogy, in case of the '-' sign an additional π phase shift has to be imprinted on one of the slits). A histogram of the measured momenta, which corresponds to the sampled momentum space wave function, was already shown in figure 5.6. We observe only a few diffraction orders as the scale of the inverse lattice spacing is not much smaller than the scale of the Wannier function in momentum space, which is inherent to the scheme of tunnel-coupling the sites by partially overlapping the individual microtraps. This challenge of scale separation will show up also for large systems, where in general we have to ensure that the length scale of the full system is larger than the typical correlation length, which in turn has to be larger than the spatial resolution.

6.2. Correlations and entanglement in a double-well

The first important set of states to be considered are the ground states of the balanced double-well populated with two particles, distinguishable by their spin projection in a broad range of U/J, covering both the strongly attractive and repulsive regime. For very strong attractive interaction, the ground state is approximately given in the particle basis by $|\psi_{-\infty}\rangle = \sqrt{\frac{1}{2}}\left(|LL\rangle + |RR\rangle\right)$, while for strong repulsive interactions it is given by $|\psi_{+\infty}\rangle = \sqrt{\frac{1}{2}}\left(|LR\rangle + |RL\rangle\right)$. Both states cannot be written as a product state in this partitioning and thus feature particle entanglement. On the other hand, the state for vanishing interaction strength $|\psi_0\rangle = \frac{1}{2}\left(|LL\rangle + |LR\rangle + |RL\rangle + |RR\rangle\right) = \sqrt{\frac{1}{2}}\left(|L\rangle + |R\rangle\right)_\uparrow \otimes \sqrt{\frac{1}{2}}\left(|L\rangle + |R\rangle\right)_\downarrow$ is fully separable and thus does not have particle entanglement. How do we characterize these states and ultimately also certify the entanglement? We could start by measuring in-situ correlations. For example for the state $|\Psi_{+\infty}\rangle$, we expect very strong correlations of the form that each time the spin up atom is detected in the one well, the spin down atom is detected in exactly the other well. These correlations therefore tell us that the state is built up of the basis states $|LR\rangle$ and $|RL\rangle$. We could however still have any incoherent superposition of these basis states. In order to reconstruct the state and certify the entanglement, we have to additionally extract the coherence between the two states $|LR\rangle$ and $|RL\rangle$, by a suitable (two-particle) interference experiment. As I will explain in detail below, we can achieve this by measuring second order density correlations in momentum space. The intuition is that the two states are connected by an exchange process (here this is the tunnelling dynamics) with a certain momentum scale associated to it. If there is a fixed phase relation between these states, this coherence thus manifests itself in a two-particle correlation feature of the corresponding momentum scale. This is very similar to the case of Bell measurements, where also a measurement in two different (conjugate) bases is needed to extract the entanglement [36, 48, 238].

It should be stressed that we can also apply the second natural partitioning, namely the different spatial modes. Here, the state $|\psi_0\rangle$ can be written down as $|\psi_0\rangle = \frac{1}{2}\left(|\uparrow\downarrow, 0\rangle + |0, \downarrow\uparrow\rangle + |\uparrow, \downarrow\rangle + |\downarrow, \uparrow\rangle\right)$, which is in fact not a separable state. Thus this non-interacting state of delocalized particles features mode entanglement.

In the experiment, we prepare the ground state of our two-site Hubbard model for different values of U/J. We fix the tunnelling rate to $J = 2\pi \cdot 77 \pm 1\,\mathrm{Hz}$ and tune the on-site interaction strength U by tuning the magnetic field in the range $B \in [525\,\mathrm{G}, 625\,\mathrm{G}]$, corresponding to $U/J \in [-5.9, 18.5]$. Experimentally, it is

easier to prepare states with strong repulsive interactions compared to strong attractive interactions, as we are limited by the stability of the relative depth of the tweezers, which is less detrimental for $U/J \gg 1$ where the atoms are forced onto different tweezers by the repulsive interaction strength. As described above, we record the in-situ position of all atoms for approximately 1000 independent realizations. In addition, we measure the (in-situ) momentum distribution of all atoms for approximately 4000 independent realizations. We postselect the data for all images where we identify exactly one atom per spin state. The postselection rate, which is a combination of preparation and detection fidelity, is $\geq 80\,\%$ for all datasets. In order to visualize the data, we construct a two-dimensional histogram of position (momentum) of the first atom in one dimension and the position (momentum) of the other atom in the second dimension using a bin-size of $5.4\,\mu\text{m} \times 5.4\,\mu\text{m}$. Therefore, each entry in the histogram is the result of a combined coincidence measurement of both particles. This is shown for a selection of datasets in figure 6.6. In the in-situ distribution, we observe that for strong attractive interactions the probability of detecting both particles in either the left or the right well is strongly enhanced over detecting one in the left and the other in the right well. In return, for strong repulsive interactions the atoms populate almost exclusively different wells. In-between, for vanishing interactions, all four combinations $\{|LL\rangle, |LR\rangle, |RL\rangle, |RR\rangle\}$ are approximately equally likely. Note that while the conditional probabilities have this interesting structure, if we integrate out the position of one of the particles by integrating out the corresponding axis of the 2D histogram, we do not observe any structure as each particle individually is equally likely to be observed in each of the wells. From this we can infer that indeed the second order correlations are relevant in this situation.[4] As we are only interested in the discretized position of the atoms, we can subdivide the histogram into four quadrants corresponding to $\{|LL\rangle, |LR\rangle, |RL\rangle, |RR\rangle\}$ and thus interpret the data as a direct measurement of the correlation function $\langle n_\uparrow(x_1), n_\downarrow(x_2)\rangle$, where $x_1, x_2 \in [L, R]$. For the momentum space density measurement, we can similarly interpret the data as a measurement of the momentum correlation function $\langle n_\uparrow(k_1) n_\downarrow(k_2)\rangle$. Here, already the non-interacting case seems to show quite intricate behaviour. This can be understood by first integrating out one of the atoms, by again integrating out one of the axes of the histogram. We arrive at a single-particle distribution which corresponds to the interference pattern of a single particle delocalized over the double-well as discussed above. The full two-dimensional pattern is thus consis-

[4] More formally, we could extract the *connected* part of the second order correlation function to arrive at the same conclusion. I will come back to this below.

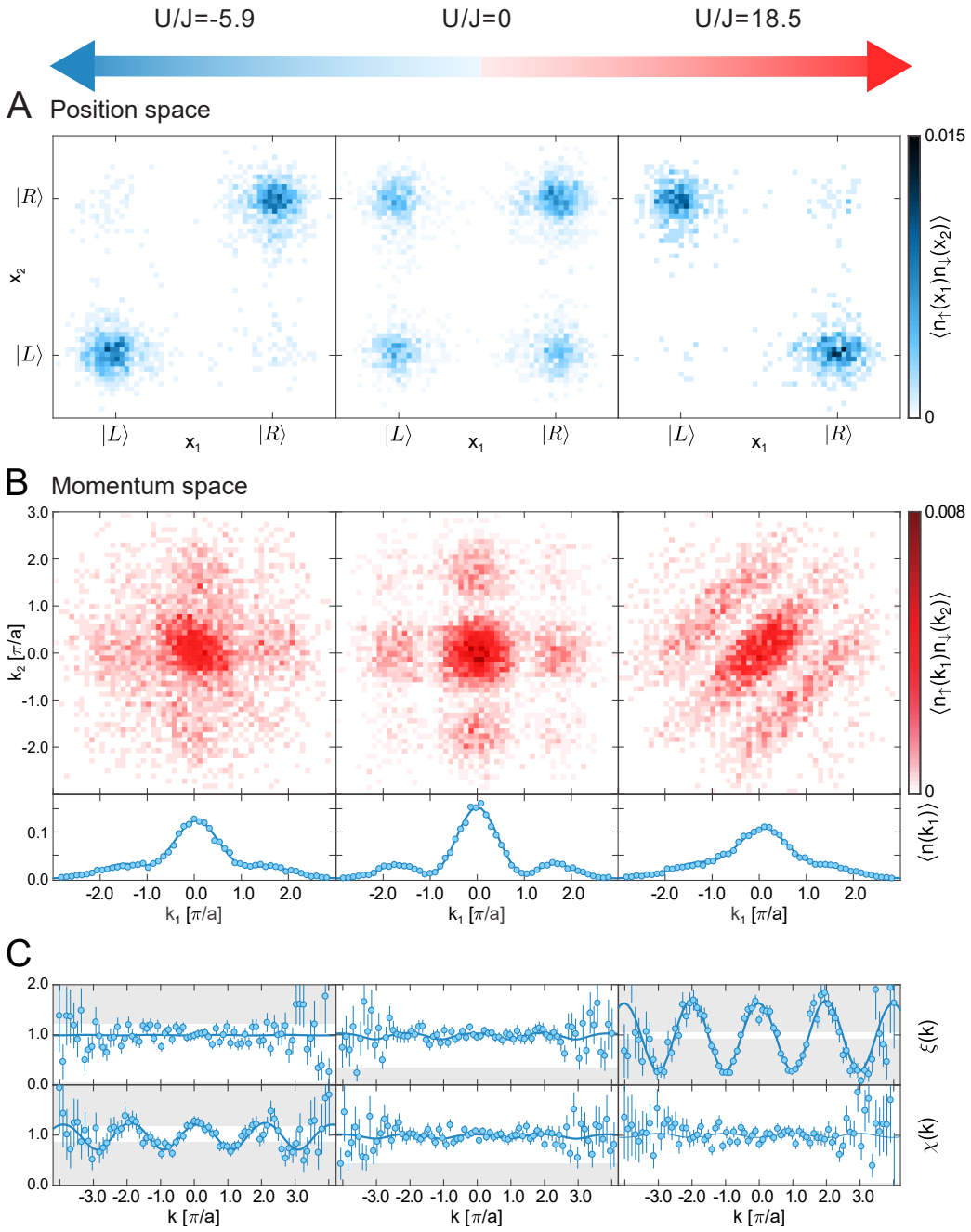

Figure 6.6.: **Correlations in the Hubbard dimer. A:** Measured in-situ correlations. Shown are the spatial coincidence measurements after the in-situ measurement protocol introduced above. By discretisation into the four quadrants, the populations in the different two-particle modes can be extracted. **B:** Measured momentum correlations. Shown in the upper panel are the spatial coincidence measurements after the momentum measurement protocol introduced above. In the lower panel, the single-particle momentum distribution, obtained by integrating out the momentum of one of the particles (corresponding to one spatial dimension of the above correlation map), is shown. **C:** Measured pair and centre-of-mass correlators $\xi(d)$ and $\chi(s)$ extracted from the data shown in B. Indicated by the grey shaded area is the regime of momentum correlation strength which, in conjunction with the measured in-situ correlations, cannot be explained without any entanglement present. Adapted from [29].

tent with the pattern of two independent delocalized particles, as given by the outer product of the single-particle interference pattern (just like in position space as well). This correlation structure directly reflects the expected two-particle state, which also can be written as the product state of two delocalized particles $|\psi_0\rangle = \sqrt{\frac{1}{2}}\left(|L\rangle + |R\rangle\right)_\uparrow \otimes \sqrt{\frac{1}{2}}\left(|L\rangle + |R\rangle\right)_\downarrow$. In turn, we expect the two-particle coherence, which would indicate that we indeed realize a strongly correlated and even (particle-) entangled state, to show up as a deviation of the correlation function from the outer product structure. Indeed, for strong attractive and repulsive interactions, a 'stripe pattern' along the diagonal and antidiagonal, respectively, is observed in the correlations. At the same time, the single-particle distribution approaches the single slit pattern of a localized particle. In the momentum density correlations shown in figure 6.6, the diagonal axis represents the relative momentum between the two particles, while the antidiagonal represents the centre-of-mass momentum. Therefore, the results indicate that for strong repulsion, there are certain relative momenta which are strongly suppressed or enhanced while for strong attractions, there are certain centre-of-mass momenta enhanced or suppressed. Together with the periodicity of the pattern, we can indeed conclude that this effect is a consequence of the two-particle coherence between $|LR\rangle$ and $|RL\rangle$ or $|RR\rangle$ and $|LL\rangle$, respectively. In order to make this even clearer and more quantitative, we extract the pair correlators in the relative momentum coordinate $d = k_1 - k_2$ as

$$\xi(d) = \int \mathrm{d}\kappa \frac{\langle n_\uparrow(\kappa - d/2) n_\downarrow(\kappa + d/2)\rangle}{\langle n_\uparrow(\kappa - d/2)\rangle \langle n_\downarrow(\kappa + d/2)\rangle}, \tag{6.9}$$

and in the centre-of-mass coordinate $s = k_1 + k_2$ as

$$\chi(s) = \int \mathrm{d}\kappa \frac{\langle n_\uparrow(\kappa + s/2) n_\downarrow(s/2 - \kappa)\rangle}{\langle n_\uparrow(\kappa + s/2)\rangle \langle n_\downarrow(s/2 - \kappa)\rangle}. \tag{6.10}$$

Here, we have also divided out the envelope on top of the correlations due to the finite spread of the individual momentum distributions.

The pair correlator is also shown in figure 6.6. We observe oscillations in the relative coordinate for repulsive interactions with almost full visibility. For attractive interactions, we observe oscillations in the centre-of-mass coordinate. They have a slightly reduced contrast due to the limited stability of the relative depth of the tweezers as explained above. Without interactions, we do not observe oscillations. From the discussions above we anticipate that we indeed have particle entanglement for strong interactions, as we observe strong correlations in two conjugate basis sets. We certify this by constructing, in close analogy to typical

Bell measurements, an appropriate entanglement witness. The exact form of the witness is worked out in [29, 239] and indicated in figure 6.6 by a grey shaded area. Indeed, we can certify particle-entanglement for $|U|/J \gtrsim 5$.
At this point, it is useful to take one step back and recapitulate what we did and also did not achieve so far. We have prepared a strongly correlated initial state of two distinguishable particles. By the combined measurement of second order correlations in position and momentum space, we showed that the systems indeed features two-particle coherence for sufficiently strong interactions which does not allow for a description in terms of product states alone. However, we did not draw any quantitative conclusions on for example the purity or fidelity of the state prepared or on the amount of entanglement, and we also did not discuss the extension of these methods towards larger systems. Therefore, what is left to discuss is:

- **Entanglement measure:** Instead of only certifying that we have *some* entanglement by using a witness, we could try to quantify it with the help of an entanglement measure.
- **State reconstruction:** We can try to characterize the initial state completely, corresponding to a reconstruction of the density matrix. From there on, we can calculate any given quantity of interest.
- **Larger systems:** We can try to identify quantities which will be also useful for larger systems.

For a qualitative discussion, it was enough to only compare to the pure ground state of the Hubbard model. For a quantitative discussion, however, we have to consider the full density matrix of the potentially partially mixed state. We write it down in the particle basis $\{|LL\rangle, |LR\rangle, |RL\rangle, |RR\rangle\}$ where it takes the general form

$$\rho = \begin{pmatrix} P_{LL} & \rho_{1,2} & \rho_{1,3} & \rho_{1,4} \\ \rho_{1,2}^* & P_{LR} & \rho_{2,3} & \rho_{2,4} \\ \rho_{1,3}^* & \rho_{2,3}^* & P_{RL} & \rho_{3,4} \\ \rho_{1,4}^* & \rho_{2,4}^* & \rho_{3,4}^* & P_{RR} \end{pmatrix}, \tag{6.11}$$

with the real valued population on the diagonal and the complex valued coherences. Thus, we have in total 16 real parameters fixing the state. The density matrix is also shown in figure 6.7. We can extract the populations directly from the in-situ measurement. Similarly, we can expect to extract the coherences from the momentum space correlation measurements, where the magnitude of a coherence factor will be determined by the strength of a correlation pattern and the

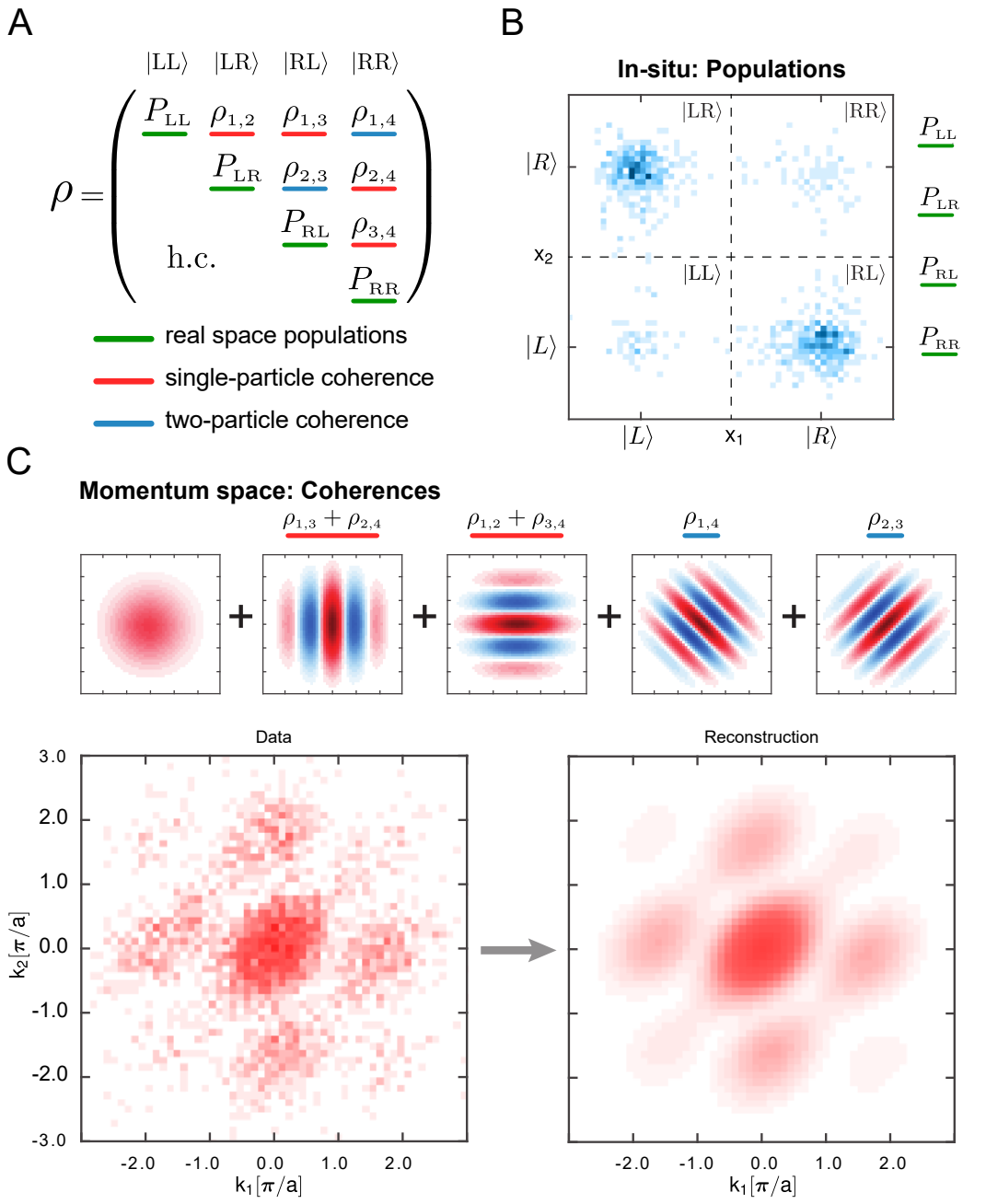

Figure 6.7.: **Reconstruction of the density matrix. A:** Density matrix of the Hubbard dimer. The diagonal entries are given by the (in-situ) populations (green), the off-diagonal entries by the two-particle coherences (blue), and the other entries by single-particle coherences (red). **B:** The populations can be directly extracted from the measured in-situ correlations by discretizing the coincidence histogram into the four quadrants. **C:** The two-particle coherences and the sum of two respective single-particle coherences can be extracted by fitting the basis functions obtained from equation 6.16 to the momentum space coincidence histograms. Adapted from [29].

phase set by the phase of the pattern. More explicitly, within the framework of the Hubbard model we can define the operator annihilating (creating) a particle of spin $\sigma \in \{\uparrow, \downarrow\}$ centred at position $x_i \in \{L, R\}$ or momentum k in terms of the Wannier function Φ and its Fourier transform $\tilde{\Phi}$ by

$$\hat{\Phi}^{(\dagger)}_{\sigma,i} = \Phi^{(*)}(x - x_i)\hat{c}^{(\dagger)}_{\sigma,i}, \tag{6.12}$$

$$\hat{\tilde{\Phi}}^{(\dagger)}_{\sigma} = \sum_{i\in\{L,R\}} \tilde{\Phi}^{(*)}(k)e^{-ikx_i}\hat{c}^{(\dagger)}_{\sigma,i}. \tag{6.13}$$

Neglecting, for the ease of notation and visual clarity, the envelope given by the Wannier function from now on, we can write down the second order momentum correlation function

$$\begin{aligned}\langle \hat{n}_{k_1\uparrow}\hat{n}_{k_2\downarrow}\rangle &= \langle \hat{\tilde{\Phi}}^{\dagger}_{\uparrow}(k_1)\hat{\tilde{\Phi}}_{\uparrow}(k_1)\hat{\tilde{\Phi}}^{\dagger}_{\downarrow}(k_2)\hat{\tilde{\Phi}}_{\downarrow}(k_2)\rangle \\ &= \sum_{k,l,m,n\in\{L,R\}} e^{ik_1(x_l-x_k)+ik_2(x_n-x_m)}\left\langle \hat{c}^{\dagger}_{\uparrow,k}\hat{c}_{\uparrow,l}\hat{c}^{\dagger}_{\downarrow,m}\hat{c}_{\downarrow,n}\right\rangle .\end{aligned} \tag{6.14}$$

Already here we can observe, that the intuition of coherences being related to a certain correlation pattern given above, is reflected in the formal structure of the density matrix by the oscillating phase factors. In particular, it is clear that the discrete nature of the double-well leads to discrete frequencies in the correlation function. To carve out the connection to the density matrix, we also write out the correlation matrix C in the same representation as the density matrix

$$C_{\hat{n}_{k_1\uparrow}\hat{n}_{k_2\downarrow}} = \begin{pmatrix} 1 & e^{-iak_2} & e^{-iak_1} & e^{-ia(k_1+k_2)} \\ & 1 & e^{-ia(k_1-k_2)} & e^{-iak_1} \\ & & 1 & e^{-iak_2} \\ h.c. & & & 1 \end{pmatrix}, \tag{6.15}$$

where $a = x_L - x_R$ denotes the spacing of the double-well. In writing down the correlation function in the matrix representation, we explicitly calculated the expectation values of the various combination of creation and annihilation operators $\hat{c}^{(\dagger)}_{\sigma,i}$, encountered in 6.14, with respect to the different combinations of basis vectors.

Finally, we can relate the measured correlations $\langle \hat{n}_{k_1\uparrow}\hat{n}_{k_2\downarrow}\rangle = \mathrm{Tr}\left(\rho C_{\hat{n}_{k_1\uparrow}\hat{n}_{k_2\downarrow}}\right)$ to

the density matrix

$$\begin{aligned}\langle \hat{n}_{k_1\uparrow}\hat{n}_{k_2\downarrow}\rangle = & P_{LL} + P_{LR} + P_{RL} + P_{RR} \\ & +2\mathcal{R}\left[(\rho_{1,3}+\rho_{2,4})\, e^{iak_1}\right] \\ & +2\mathcal{R}\left[(\rho_{1,2}+\rho_{3,4})\, e^{iak_2}\right] \\ & +2\mathcal{R}\left[\rho_{1,4}e^{ia(k_1+k_2)}\right] \\ & +2\mathcal{R}\left[\rho_{2,3}e^{ia(k_1-k_2)}\right],\end{aligned} \tag{6.16}$$

or, equivalently, written down in quadrature components and using that $P_{LL} + P_{LR} + P_{RL} + P_{RR} = 1$

$$\begin{aligned}\langle \hat{n}_{k_1\uparrow}\hat{n}_{k_2\downarrow}\rangle = & 1 \\ & +2\mathcal{R}\left[\rho_{1,3}+\rho_{2,4}\right]\cos\left(ak_1\right) + 2\mathcal{I}\left[\rho_{1,3}+\rho_{2,4}\right]\sin\left(ak_1\right) \\ & +2\mathcal{R}\left[\rho_{1,2}+\rho_{3,4}\right]\cos\left(ak_2\right) + 2\mathcal{I}\left[\rho_{1,2}+\rho_{3,4}\right]\sin\left(ak_2\right) \\ & +2\mathcal{R}\left[\rho_{1,4}\right]\cos\left(a(k_1+k_2)\right) + 2\mathcal{I}\left[\rho_{1,4}\right]\sin\left(a(k_1+k_2)\right) \\ & +2\mathcal{R}\left[\rho_{2,3}\right]\cos\left(a(k_1-k_2)\right) + 2\mathcal{I}\left[\rho_{2,3}\right]\sin\left(a(k_1-k_2)\right).\end{aligned} \tag{6.17}$$

This leads us to an important conclusion: By extracting different correlation patterns with a discrete frequency, set by the distance between the wells, we can directly extract the two-particle coherences $\rho_{1,4}$ and $\rho_{2,3}$, showing up as (anti-) diagonal patterns, and in addition constrain the one-particle coherences $\rho_{1,3}+\rho_{2,4}$ and $\rho_{1,2}+\rho_{3,4}$ showing up as horizontal and vertical patterns. In total, we can thus extract 12 out of the 16 real parameters. In practice, we determine the parameters by fitting the different basis patterns to the data. Here, the spacing a and the envelope function, which now has to be reintroduced, are is fixed and extracted independently. For a typical example, this is also shown in figure 6.7. With most of the entries of the density matrix fixed, we can can come to more qualitative conclusions. In [29], we have for example used this information to construct a bound on the concurrence (see also section 2.1) based on the measured entries. The concurrence is a measure of entanglement (of formation) and thus not only certifies the existence of entanglement, but also quantifies it in units of the entanglement of a perfect Bell pair. This is a quite important step for the exact system at hand, but it is only applicable to a two-qubit system as the relation between the concurrence and the entanglement of formation has no known extension to larger systems (in particular as no single class of entanglements exists beyond two qubits). Therefore, I will not elaborate on the concurrence here and rather focus on concepts where there is some potential of scalability.

A very successfully concept also for larger systems is the entanglement entropy [37, 114]. The general intuition is the following: For a pure state, the entropy as measured by the Rényi or von Neumann entropy is by construction exactly zero. If this state is a product state in a certain partitioning, also the entropy of the individual subsystems has to be zero. Only if there is entanglement between the systems, each subsystem individually has a finite entropy (and even might appear to be thermal [41]) despite the total entropy remaining zero.[5] More in general, an entropy of a subsystems in a specific partitioning which is higher than the total entropy of the combined system indicates entanglement [86]. Importantly, this concept is not limited to the particle partitioning but instead can also be used when partitioning the system into modes.
For this discussion, we will use the Rényi entropy of second order which is defined as

$$S = -\ln \mathrm{Tr}\left(\rho^2\right) = -\ln P, \tag{6.18}$$

where P is the purity of the density matrix and ρ can be either the full density matrix or the reduced density matrix with one subsystem traced out. If we want to determine the entanglement entropy in the particle partitioning, we have to trace out one of the hyperfine states (without loss of generality we choose the spin down state) and are left with the reduced density matrix

$$\rho_\uparrow = \begin{pmatrix} P_{LL} + P_{LR} & \rho_{1,3} + \rho_{2,4} \\ h.c. & P_{RL} + P_{RR} \end{pmatrix}. \tag{6.19}$$

We can directly extract all of the entries from the measured correlation functions as described above.
Instead of tracing out one spin state, we can also trace out one of the two wells (here, the right well) and thus assume a partitioning with respect to the spatial modes. In the basis $\{|\uparrow\downarrow\rangle, |\uparrow\rangle, |\downarrow\rangle, |0\rangle\}$ we arrive at

$$\rho_L = \begin{pmatrix} P_{LL} & & & \\ & P_{LR} & & \\ & & P_{RL} & \\ & & & P_{RR} \end{pmatrix}. \tag{6.20}$$

[5] While the formal concept of the entanglement entropy was only written down in the second half of the 1990s (see [37, 240–242]), it can actually be seen as a defining property of entanglement. Already Erwin Schrödinger wrote in his take on the EPR paradoxon in 1935: 'The best possible knowledge of a whole does not include the best possible knowledge of its parts.' [35].

As only populations and no coherences contribute in this case, we can also directly determine this density matrix. As a result, we can calculate the entanglement entropy $S_L = -\ln \mathrm{Tr}\,(\rho_L^2)$ in the mode partitioning and $S_\uparrow = -\ln \mathrm{Tr}\left(\rho_\uparrow^2\right)$ in the particle partitioning for all values of U/J. This is illustrated in figure 6.8.
Indeed, we observe that the entropy in the subsystem is finite and strongly dependents on the interaction strength. In the particle partitioning, we have a minimum for vanishing interactions and the entropy increases for increasing interactions $|U|/J$. Quite contrary, the entropy in the mode partitioning is largest for $U/J = 0$ as the system is maximally delocalized in this case. Interestingly, the mode entanglement entropy is always larger than the particle entropy (while approaching each other for $|U|/J \gg 1$). This is due to the fact that the coherent (single-particle) tunnelling dynamic always ensures that, without knowledge of the other spin state, the spatial mode of a single spin component is unknown.
We can also calculate the expected ground state entropy of the Hubbard dimer. In particular for positive interaction strength, we observe a reasonable agreement. However, in order to actually quantify the entanglement, we have to compare to the total entropy of the full system, as we do not want to assume that we have fully deterministically prepared the ground state. Crucially, for this, we either need the full density matrix, or, alternatively, additional collective measurements involving multiple copies of our system [114]. For larger systems, the more promising path is most likely to aim for collective measurements. For rather small systems, estimating the full density matrix is however still feasible and thus what we opt for here. Note that we have already determined 12 out of the 16 entries. In principle, we could also try to measure the remaining entries and thus perform a full quantum-state tomography. In order to access the single-particle coherences, we would have to either implement single spin rotations selectively on the individual wells and spins, specific gate operations involving one ore two wells [29, 243], or alternatively and more in line with the matter-wave optics framework, perform a time-of-flight expansion for $T/8$ to access the density in-between position and momentum space [244]. Here, we instead try to infer the most likely density matrix based on the measured entries (including their error bounds) based on a Bayesian estimate.
Our reconstruction scheme is based on [245], with additional details on our implementation given in [99]. In particular, in the reconstruction, we have to make sure to restrict ourselves to the space of physical density matrices, even though statistical and systematic measurement uncertainties can lead to unphysical properties, such as small eigenvalues becoming negative. We construct a likelihood function $\mathcal{L}(\rho) = p(M|\rho)/p(M)$ in terms of the measured data $M = \{M_j\}$ (pop-

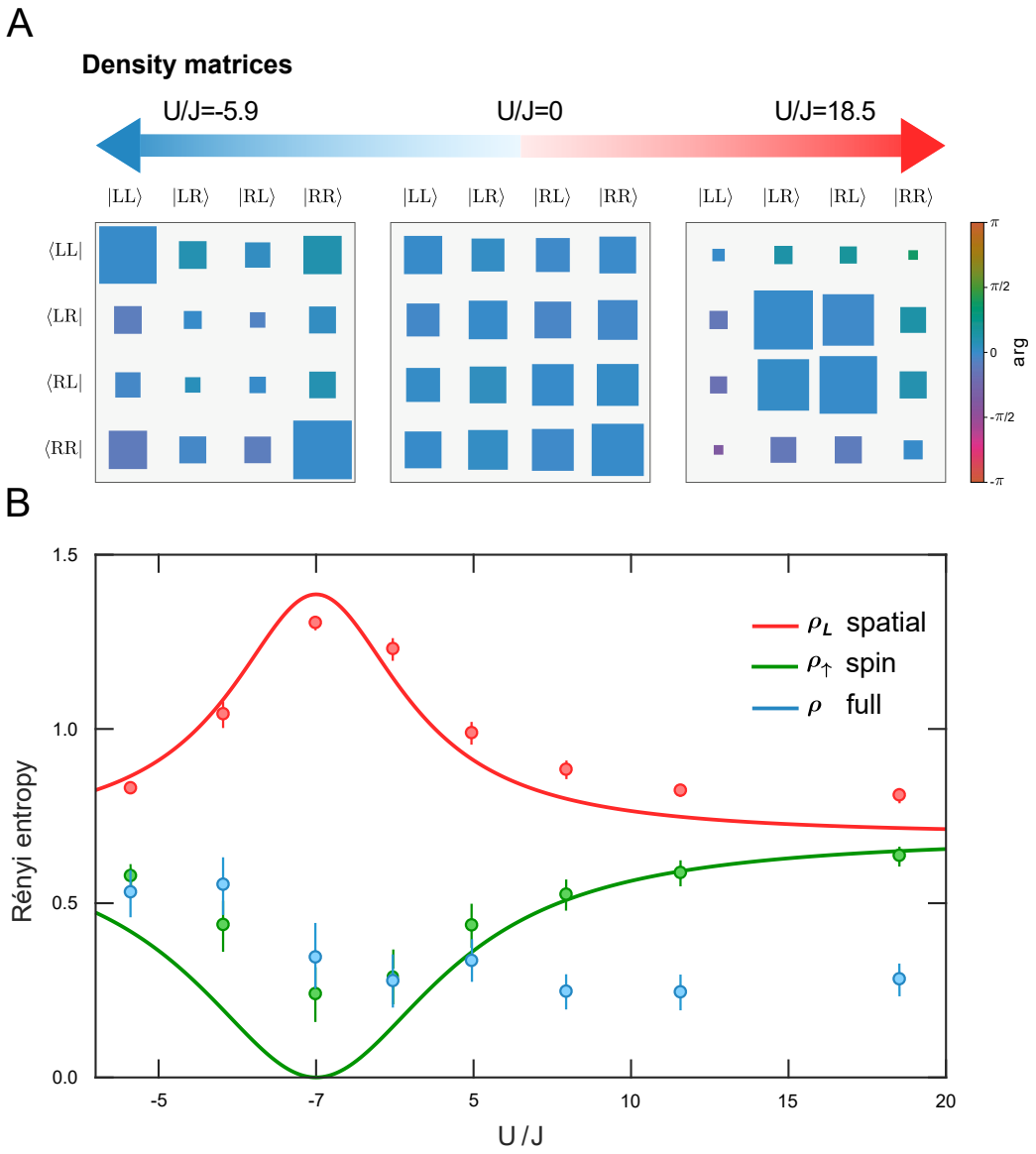

Figure 6.8.: **Reconstructed density matrices and measured Rényi entropy. A:** Reconstructed density matrices for three different values of U/J. The absolute value of the entry is represented by the size of the square, the phase is encoded in colour. This representation allows for an instructive qualitative interpretation: The block structure visible for strong interactions ($U/J = 18.5$ and $U/J = -5.9$) indicates particle entanglement as population and coherence of a subset of two-particle states are large and of similar magnitude, while the maximum delocalization over all entries visible for $U/J = 0$ suggests mode entanglement. **B:** Measured Rényi entropy in the mode partitioning tracing out the right mode (green), in the particle partitioning tracing out the spin down mode (red), and in the full system (blue). The Rényi entropy of the subsystems is calculated based only on the directly measured entries of the density matrix. The entropy of the full system is calculated based on the Bayesian estimate of the full density matrix. Adapted from [29].

ulations and coherences) and the conditional probability $p(M|\rho)$ with respect to the hypothesis density matrix ρ. Assuming the errors on M_j to be Gaussian distributed with a width σ_j, we arrive at

$$\mathcal{L}(\rho) = \prod_j \frac{1}{\sqrt{2\pi\sigma_j^2}} \exp\left(\frac{-\left(M_j - \mathrm{Tr}[\hat{M}_j\rho]\right)^2}{2\sigma_j^2}\right), \tag{6.21}$$

where $\hat{M}_j$ is the projector corresponding to the measurement M_j. Ultimately, we are interested in the posterior distribution $\pi_f(\rho)\,\mathrm{d}\rho$, which can be interpreted as the probability distribution of possible density matrices describing the measured data. As a consequence, it can be used to estimate the expectation value of any observable $\mathcal{O}$ via

$$\langle\mathcal{O}\rangle = \int \mathcal{O}(\rho)\pi_f(\rho)\,\mathrm{d}\rho. \tag{6.22}$$

Within this procedure, all the measurements and their uncertainties are fully reflected in the estimate. In a similar fashion, also the best estimate of the full density matrix is given by

$$\rho_{BME} = \int \rho\pi_f(\rho)\,\mathrm{d}\rho. \tag{6.23}$$

The posterior distribution is obtained, up to a proper normalization, from the likelihood function multiplied with a prior distribution $\pi_0(\rho)\,\mathrm{d}\rho$ which contains any prior information we have on the system,

$$\pi_f(\rho)\,\mathrm{d}\rho \propto \mathcal{L}(\rho)\pi_0(\rho)\,\mathrm{d}\rho. \tag{6.24}$$

We do not want to assume any specific prior knowledge on the states. However, via this step we can implement the restriction to physical density matrices, as the likelihood method itself is not formulated in a quantum mechanical framework. Therefore, the Hilbert-Schmidt prior is used here, which only requires positive definiteness and unity trace but is otherwise unbiased. In practice, we parametrize the density matrices as $\rho = \hat{T}^\dagger\hat{T}$ in terms of the random complex 4×4 matrix $\hat{T}$. This form ensures that ρ is always a positive semidefinite Hermitian matrix with trace 1. We now sample the posterior distribution using a Hamiltonian Monte Carlo algorithm. As we sample the space of physically allowed entries with the measurement errors on the individual entries taken into account, we can also directly extract credibility intervals of ρ_{BME} or any observable. I would like to stress the importance of this result. The credibility intervals directly translate to uncertainties on any observable calculated according to equation 6.22, thus allow-

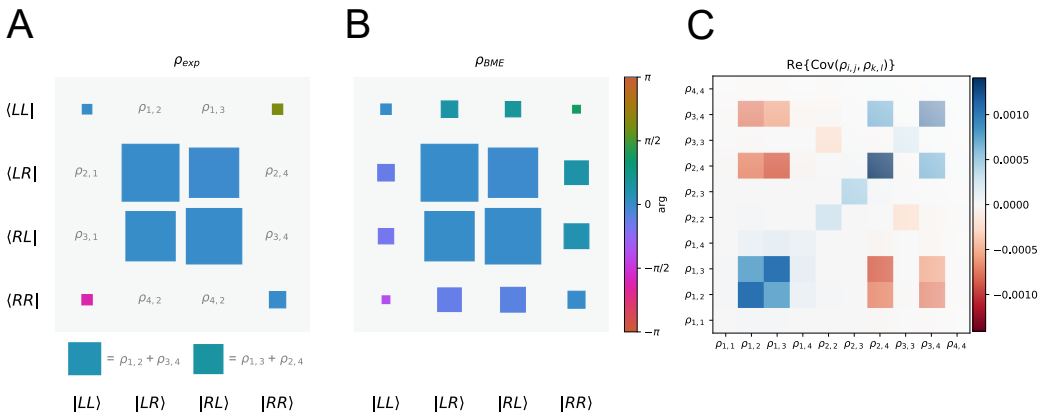

Figure 6.9.: **Bayesian reconstruction scheme. A:** We experimentally measure the real populations, as well as the complex two-particle coherences together with the sum of two respective single-particle coherences. **B:** The reconstructed density matrix based on the measurement results (and measured uncertainties) shown in A. In addition to the most likely matrix which is shown here, we also obtain the full posterior distribution of density matrices. **C:** Real values of the covariance matrix as a measure for the uncertainty of the individual entries. Note that the entries are partially correlated. For example, the diagonal entries are correlated by the requirements of $\mathrm{Tr}\rho = 1$, while $\rho_{1,2}$ and $\rho_{3,4}$ ($\rho_{1,3}$ and $\rho_{2,4}$) are anti-correlated due to the sum of the two entries being constrained. Adapted from [29].

ing for qualitative statements in addition to merely a best guess. The Bayesian reconstruction process is illustrated in figure 6.9.

With the density matrix reconstructed, we can now extract the entropy of the full system according to equation 6.18. Note again that the second order Rényi entropy is directly related to the purity of the system. The results are also presented in figure 6.8, together with a few relevant examples of reconstructed density matrices. Only now we can make a definite statement about the entanglement entropy in the system, as we now no longer have to assume a more or less pure state prepared based on other observations, but directly calculate the purity from the measurements taken. Indeed, we see that the particle entanglement surpasses the full state entropy for strong repulsive interactions. In addition, we observe that the purity of the system, as already anticipated above, is reduced for strong attractive interactions, such that here entanglement cannot be clearly certified. The entanglement entropy in the mode partitioning is always larger than the purity of the full system, indicating coherent delocalization.

Here we encounter the first example of a general question which will also become relevant in section 6.4: Which partitioning is actually relevant? The most com-

mon form of entanglement as a resource for computation or communication is the entanglement between the hyperfine states. Here, each party (typically referred to as Alice and Bob) take control over one spin sector. In this language, our first image of the spin up states would be Alice's measurement and the second image Bob's, with the entanglement between the two parties a possible resource. On the other hand, we measured also entanglement between modes. In this context, I should recall the observation made in the introduction that also the single-particle state $|\phi\rangle = \sqrt{\frac{1}{2}}\,|0,\uparrow\rangle \pm |\uparrow,0\rangle$ of a delocalized atom already features mode entanglement. Thus, typically this entanglement is rather interpreted as the computational cost of representing this state classically in terms of its particle number fluctuations. It has been realized, though, that also mode entanglement can be used as a resource for quantum teleportation [116]. We will come back to this question with the additional complication of indistinguishability introduced in section 6.4.
For now, let me summarize what was achieved in this section:

- I showed that the imaging scheme introduced can be indeed used to measure correlations in position and momentum space.

- Based on this, I presented a characterization of the correlation and entanglement properties of a Hubbard dimer for a broad range of interaction strengths. It was possible to certify and quantify both mode and particle entanglement.

- It was possible to fully reconstruct the density matrix though a Bayesian estimate.

- It became obvious that it can be a major advantage to use any *intuition* you already have on the state to be characterized in order to choose an appropriate measurement basis. This was rather straightforward in this case as I could assume with some confidence that the state is close to the ground state of the Hubbard dimer. For a true many-body state, this can in general be a hard task.

- Based on the methods introduced here, in line with the ultimate goal of a general toolbox, also specific measurements on larger systems now seem possible. For example, pairing in momentum space, as encountered for a BCS state, should also manifest itself as correlations at finite relative momenta, similar to the 'stripes' observed in this section.

6.3. Identical particle correlations

In the previous section 6.2, I discussed different manifestations of correlations and entanglement in a double-well of two atoms with different spin projections. As both particles were distinguishable by their hyperfine states, the fermionic nature of the particles did not play any role and all correlation features observed were induced by interactions between the atoms (and their delocalization). In a more general many-body scenario, we will however encounter a very complex interplay between correlation effects based on quantum statistics and interactions. This is one important reason to first study correlations arising from the many-body interference of indistinguishable fermions isolated from interaction effects. The many-body interference of massive fermionic fields is however also an important research topic on its own. The development of quantum optics has been one of the driving forces in our modern understanding of quantum mechanics [246, 247] and is rooted in correlation studies of massless bosonic fields, in particular facilitated by the advent of high purity single photon sources [248, 249]. Comparable fermionic sources and detection methods, on the other hand, are not yet readily available. In particular, as opposed to massless photons, fermionic fields are fundamentally massive and thus relevant also for questions involving quantum gravity [57, 250]. For an overview over the current status see [251].
Independent and thus non-interacting indistinguishable particles are completely unaware of each other except for the necessity to properly symmetrize the total wave function. In this section, I will discuss the setting where all internal degrees of freedom are identical. Therefore, the symmetrization has to be performed in the external degrees of freedom which are the position or momentum.[6] In second quantization, this is implicitly captured by the commutation relations of the field operators while in first quantization, the symmetrization is explicitly performed. Independently of the description, second (and higher) order correlations will be exclusively introduced by pairwise exchange operations. In general, the correlations arising are often times summarized by fermionic antibunching or bosonic bunching. The latter effect was famously used by Hanbury Brown and Twiss in the context of intensity interferometry of extended stellar objects [252, 253]. There are however also several experiments with ultracold atoms observing this effect [254–256]. In order to gain some intuition, in figure 6.10 a toy model is depicted and explained. An important distinction of the experiments I describe in this section is that we are preparing a deterministic number of fermions in a

[6] Note that we implicitly assume the validity of the lowest band approximation throughout this chapter.

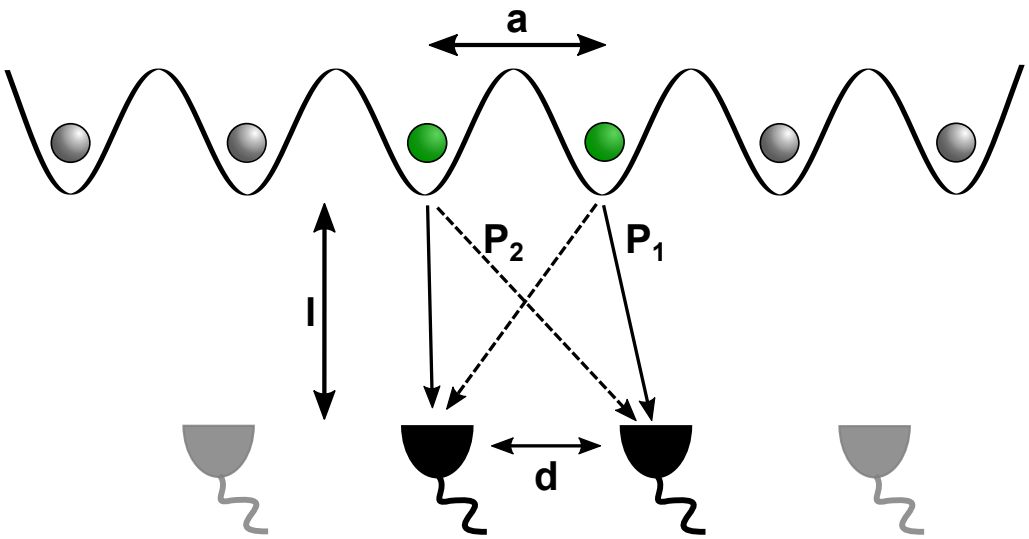

Figure 6.10.: **Toy model of the Hanbury Brown and Twiss effect.** In this toy model, two distinct emitters (single atoms, single photon sources etc.) depicted in green with a distance a from each other, and two distinct detectors in the far field (that is with $l \gg a$) and a distance d from each other are assumed. Coincident measurements of the signal from one emitter in one detector and the signal from the other emitter in the second detector are studied. There are two distinct two-particle paths P_1 and P_2 leading to a coincidence measurement. Interference based on the phase difference between the two paths is observed. Upon varying d, sinusoidal (cosinusoidal) oscillations in the coincidence rate are therefore expected for fermionic (bosonic) emitters, while for classical emitters (where a which-way information is provided), there is no interference between P_1 and P_2. If the number of emitters is increased (grey circles), the (Fourier) sum of all possible two-path interference terms has to be taken into account.

discrete set of modes. This can be seen as a direct implementation of the model depicted in figure 6.10. Thus, the experiments presented are specifically related to single photon quantum optics experiments, in particular the Hong-Ou-Mandel effect [249, 257]. In this section, I will focus on correlation measurements to study many-body interference, while in section 6.4 also the entanglement properties are discussed. The results presented in this section have been published in [30].

Two atoms in a double-well

In a first set of experiments we prepare, as described above, two identical and independent copies of a tweezer with exactly one atom in the ground state $a = 1.7\,\mu\text{m}$ apart from each other. In first quantization, we expect the wave function

to be given by

$$|A\rangle = \sqrt{\frac{1}{2}}\left(|LR\rangle - |RL\rangle\right). \tag{6.25}$$

This is exactly the situation depicted in figure 6.10. Note that in practice, we actually have one atom per spin state in each tweezer. However, we always make sure that the interactions are tuned to zero such that the spin sectors fully separate and we each time prepare two realizations of the same experiment. This effectively doubles our statistics and allows us to limit certain systematic errors. For each experimental run, we record the momenta of both particles. We repeat the experiment several thousand times, and postselect for exactly the right atom number detected. We achieve a postselection rate of around 80 %. As before, we visualize the correlation function through the conditional momentum distribution. The resulting histogram is shown in figure 6.11. Note that in the construction, we had to assign artificial labels to the atoms detected.
Comparing this correlation pattern with the pattern of two *distinguishable* particles in the *coupled* double-well shown in figure 6.6, we observe a qualitative similarity between the results shown here and and the correlations for strong repulsive interactions. This is not surprising, as the wave function of two identical fermions in first quantization $|A\rangle = \sqrt{\frac{1}{2}}\left(|LR\rangle - |RL\rangle\right)$ is identical to the ground state wave function of the Hubbard dimer for $U/J \to +\infty$ except for a relative phase factor of π. This phase also manifests itself in the correlation pattern as the oscillatory pattern is shifted by half a period. As done before, we can directly relate the measured histogram to a correlation function of second order in the momentum density $\langle :\, n_{k1} n_{k2} \,:\rangle$, where we have indicated normal ordering by $: \cdot :$. The normal ordering of the operators accounts for a very subtle difference between density correlations as obtained for example by noise correlations and single-particle based correlations. Here, we do not double count two atoms at the same momentum, as opposed to the case of continuous density or noise correlations, thereby avoiding the additional strong autocorrelation peak:

$$\begin{aligned}\langle n_{k1} n_{k2}\rangle &= \langle \hat{\Phi}^\dagger_{k1}\hat{\Phi}_{k1}\hat{\Phi}^\dagger_{k2}\hat{\Phi}_{k2}\rangle = -\langle \hat{\Phi}^\dagger_{k1}\hat{\Phi}^\dagger_{k2}\hat{\Phi}_{k1}\hat{\Phi}_{k2}\rangle + \langle \hat{\Phi}^\dagger_{k1}\hat{\Phi}_{k2}\delta_{k1,k2}\rangle \\ &= \langle :\, n_{k1} n_{k2} \,:\rangle + \langle n_{k1}\rangle\, \delta_{k1,k2},\end{aligned} \tag{6.26}$$

where $\hat{\Phi}$ is the fermionic field operator as defined before. Note that this subtlety did not show up for the distinguishable particles presented above as in this case (due to the creation and annihilation operators commuting) $\langle :\, n_{k1} n_{k2} \,:\rangle = \langle n_{k1} n_{k2}\rangle$. Very similar to before, we can define the normalized correlation function

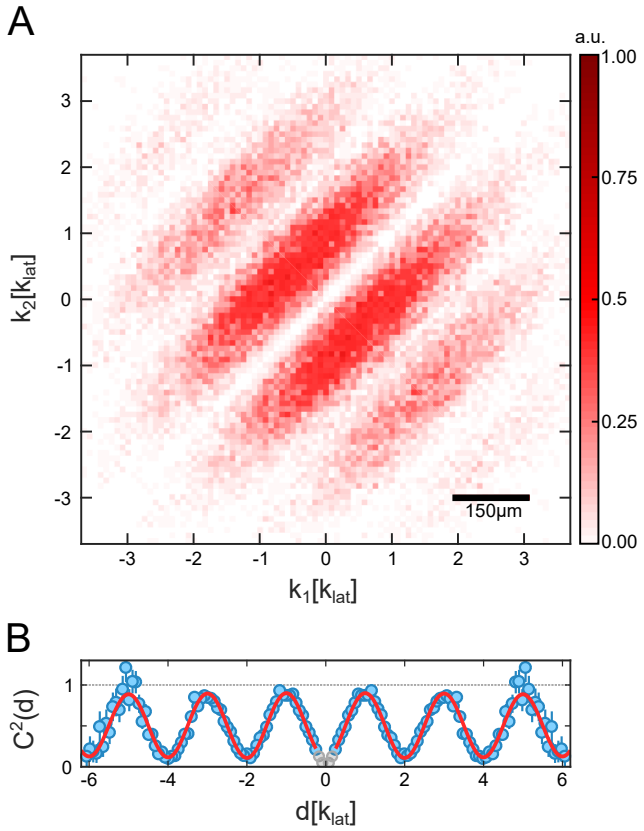

Figure 6.11.: **Second order momentum density correlations of two identical fermions. A:** Measured correlation map. In the construction arbitrary particle labels (1 and 2) had to be introduced. As a consequence, the correlation map is symmetrical around the antidiagonal as $\langle n_{k1} n_{k2} \rangle = \langle n_{k2} n_{k1} \rangle$. **B:** Normalized correlation function $C^2(d)$ extracted from the data shown in A. Indicated in red is a fit to the data according to equation 6.28. Greyed out is the detection hole where a reliable two-particle coincidence measurement is not possible. The correlation pattern has almost full visibility. Adapted from [30].

via

$$C^2(d) = \int \mathrm{d}k \frac{\langle : n_k n_{k+d} : \rangle}{\langle n_k \rangle \langle n_{k+d} \rangle}. \tag{6.27}$$

It is shown in figure 6.11 as well. In all of these correlation functions, we cannot distinguish the particles. Therefore, $k_1 = k_\alpha$, $k_2 = k_\beta$ corresponds to the same situation as $k_2 = k_\alpha$, $k_1 = k_\beta$. As a consequence, the two-dimensional correlation function is symmetric about the diagonal $k_1 = k_2$ by construction and similarly $C^2(d) = C^2(-d)$. In addition, we suffer from spurious correlations due to a higher probability to not detect particles if they are close to each other. We therefore exclude this detection hole from any further analysis.

The strong correlations shown in figure 6.11 indicate a strong non-separability of

the wave function. This is the discrete version of fermionic antibunching observed in continuum systems. In order to quantify this, we extract the modulation contrast by fitting a damped cosine function, with the detection hole taken into account, to the correlator C^2. The general cosine form can be calculated in close analogy to the calculations in 6.17, while a phenomenological decay model is added to account for the loss of contrast at larger distances. Therefore, we use the following function:

$$C^2(d) = \frac{1}{2}\left(1 + \mathrm{erf}\left(\frac{|d| - s}{w}\right)\right)\left(y_0 - c \cdot e^{-\frac{d^2}{2\chi^2}} \cos\left(\pi d / k_{lat}\right)\right). \tag{6.28}$$

Here, the error function (parametrized by s and w) accounts for the detection hole and the length scale χ for the decay of contrast for large separations. In addition, the lattice momentum is given by k_{lat}, the offset by y_0 and the contrast by c. We determine the contrast to be $79 \pm 2\,\%$. The contrast is a direct measure of the indistinguishability in our system. Very similar to the entanglement entropy determined above for the Hubbard dimer, also in this case the *strength* of the correlations (here measured by the contrast) determines how non-separable the system is. In the example shown here, this can be interpreted as the degree to which we have to take the antisymmetrization for indistinguishable particles into account. We therefore explicitly certify a high degree of indistinguishability in our system.

While the contrast is certainly large, it is in fact smaller than anticipated based on our preparation fidelity of 95 % and the corresponding expected purity. We attribute most of the difference to the slight misalignment angle between the double-well axis and the imaging axis mentioned already in the beginning of this chapter. This misalignment provides some degree of distinguishability to the wave functions as the spatial modes do not fully overlap any more when projected onto each other on the imaging axis defined by the waveguide potential. In fact, we can even tune the overlap and thus the distinguishability in a controlled way. To this end, we tune the distance between the individual wells. With a fixed misalignment angle, this is equivalent to the relative shift of the wells' position in the auxiliary dimension orthogonal to the double-well axis. In the language of quantum optics, we therefore introduce *which-way* information in a controlled way. Note that in photonic experiments (as in the original HBT experiments), such a which-way information is typically introduced by a time delay. The results of this measurement are shown in figure 6.12

It is instructive to note the differences between the correlations observed here and the case of (bosonic or fermionic) noise correlations in a lattice system [256].

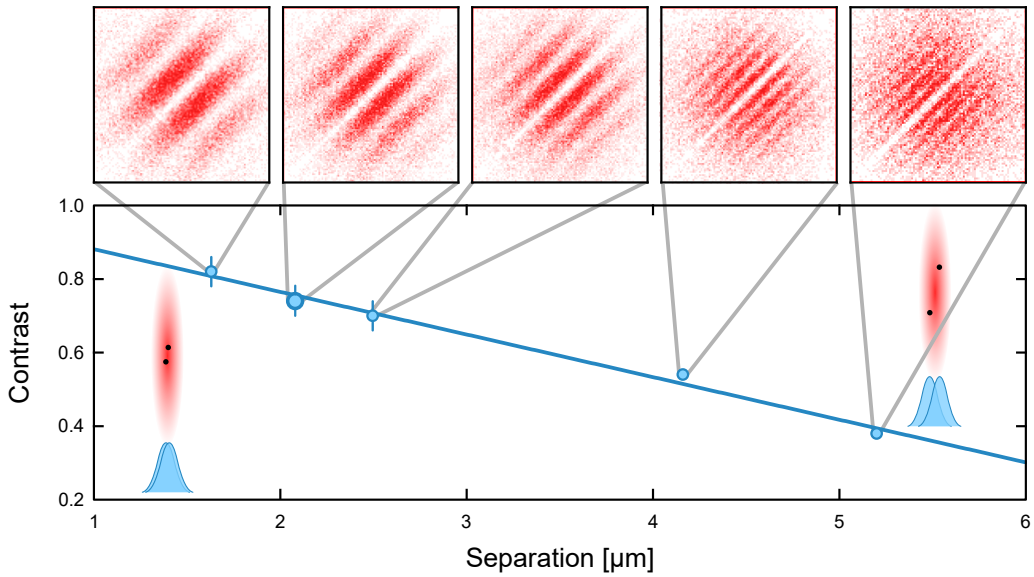

Figure 6.12.: **Which-way information.** Second order correlations are measured for different separations of the two wells (top panel) and the contrast of the interference pattern is extracted (bottom panel). The blue line is a guide to the eye. The observed drop of the contrast with the separation is consistent with an angle of around 1° between the double-well axis and the imaging axis. It allows us to introduce wich-way information in a controlled manner, but also limits the maximum contrast which can be observed based on the minimum separation possible. Adapted from [30].

For noise correlations, the signal given by the density fluctuations is partially masked by noise of the imaging light and other technical noise. Thus, the observed contrast is smaller by several orders of magnitude and does not allow for certifying a high degree of indistinguishability such as shown above. In addition, the noise correlations are typically performed in a lattice, where also multiples of the lattice spacing (or equivalently fractions of the lattice momentum) contribute. Each of the combination of lattices sites will contribute a correlation signal as presented above. It is straightforward (yet instructive; I have previously presented and illustrated the calculation in [183]) to show that the expected correlation signal in momentum space (assuming fully independent lattice sites) is thus proportional to the Fourier sum of the real space distribution. In an infinite lattice system (ignoring the finite resolution), thus delta peaks (or dips) at multiples of the fundamental lattice constant are expected. With our deterministic source of indistinguishable fermions at hand, we can directly observe the 'build-up' of the Fourier sum as a weighted sum of the individual spatial distances contributing. More precisely, for N localized sources of identical but independent fermions, we

expect a second-order correlation function of the form

$$C^2(d) = \frac{2}{N^2} \sum_{\langle i,j \rangle} \left(1 - \cos\left(d(x_i - x_j)\right)\right), \tag{6.29}$$

where $\langle i, j \rangle$ runs over all distinct pairs of emitters (atoms) at positions x_i and x_j. Experimentally, we can test this expectation as we can measure each contribution to the sum independent of the full correlation function. In addition, we have the freedom to use different, and in particular incommensurate, lattice spacings such that a more complex structure arises. Here, I present two datasets of a triple-well with $a_{12} = a_{23} = 2\,\mu\text{m}$ and $a_{12} = 1.6\,\mu\text{m}$, $a_{23} = 1.5a_{12}$, respectively. For each dataset, we prepared three identical fermions in these three different and uncoupled tweezers and measured the momenta of all particles. For each distinct setting, we repeated the experiment a few 10 000 times. The postselection rate is around 60 %. In addition, we measured the correlation function for each distinct combination of two atoms in two wells with a few thousand repetitions. The resulting second order correlation functions are shown in figure 6.13.

For the commensurate spacing, there are three contributions with two distinct frequencies contributing; two at the lattice momentum $k_{lat} = \pi/a$ from the neighbouring atom pairs and one contribution from the outermost atoms at twice the lattice momentum. Already with only two distinct frequency components, it can be observed that the antibunching minima become more narrow, while the maxima are starting to get flattened out. If we would add one tweezer (with one atom) after each other, we would thus build up the Fourier sum ultimately leading to delta dips; one Fourier order at a time. Importantly, we can exactly reproduce the measured second order correlation function for three atoms by a weighted sum over the correlations measured for each combination of two atoms, as shown in figure 6.13. By tuning the distance between the individual tweezers to be incommensurate, we effectively double the unit cell (defined with respect to the smallest spacing), as now all combinations of distances contribute with a distinct frequency. This is a prototype for correlation measurements in lattices with a more complex unit cell. Indeed, a more complex structure is observed in figure 6.13. Nevertheless, we can again reproduce the full correlator by a weighted sum over the individual contributions from two of the sites.

We can conclude from the measurements above that the second order correlation function of any configuration of tweezers is fully described by the contributions from the pairwise exchange correlations. This is not too surprising as the physical origin of the correlations is rooted in the pairwise anticommutation of fermionic operators (more precisely the creation and annihilation operators and

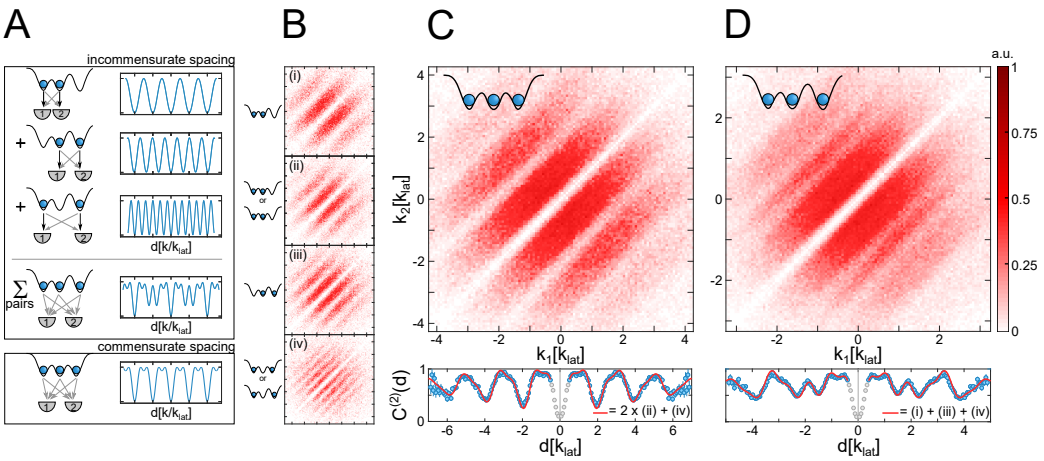

Figure 6.13.: **Interference of three fermions in three wells. A:** Schematic illustration of the different contributions to the full correlation function (compare to figure 6.10). **B:** Measurement of all possible individual correlation contributions of two atoms in two of the three wells for both a commensurate and an incommensurate triple-well. **C:** Second order momentum correlations of three atoms in a commensurate triple-well. In the bottom panel, the normalized correlation function is shown. The correlation pattern is fully explained by a sum over the individual two-particle contributions. This is indicated in red, where the weighted sum (without any free parameters) over the two distinct two-particle contributions, extracted by a fit to the data shown in B, is presented. **D:** Second order momentum correlations of three atoms in an incommensurate triple-well. The correlation pattern is explained by the sum over contributions from all three distinct two-particle contributions. Adapted from [30].

crucially not the density operator). Therefore, we might prematurely conclude that we have fully characterized the system by studying the second order correlation functions. This would imply that there is no structure left in third order density correlations. Since we have measured the momenta of all the atoms, we can directly construct the third order correlation function $\langle : \hat{n}_{k_1} \hat{n}_{k_2} \hat{n}_{k_3} : \rangle$. The correlation function is a three-dimensional object. In analogy to before, we can however also construct the - now two-dimensional - normalized correlation function

$$C^3(d_1, d_2) = \int \mathrm{d}k \frac{\langle : \hat{n}_k \hat{n}_{k+d_1} \hat{n}_{k+d_2} : \rangle}{\langle \hat{n}_k \rangle \langle \hat{n}_{k+d_1} \rangle \langle \hat{n}_{k+d_2} \rangle}. \tag{6.30}$$

For both the commensurate and the incommensurate spacing, the correlation function is displayed in figure 6.14. As can be clearly seen, there is a significant structure in the correlation function even at third order. Once again, we have to carefully evaluate the influence of spurious correlations. They show up if any two of the momenta are (almost) the same, that is for either $d_1 = 0$, $d_2 = 0$, or

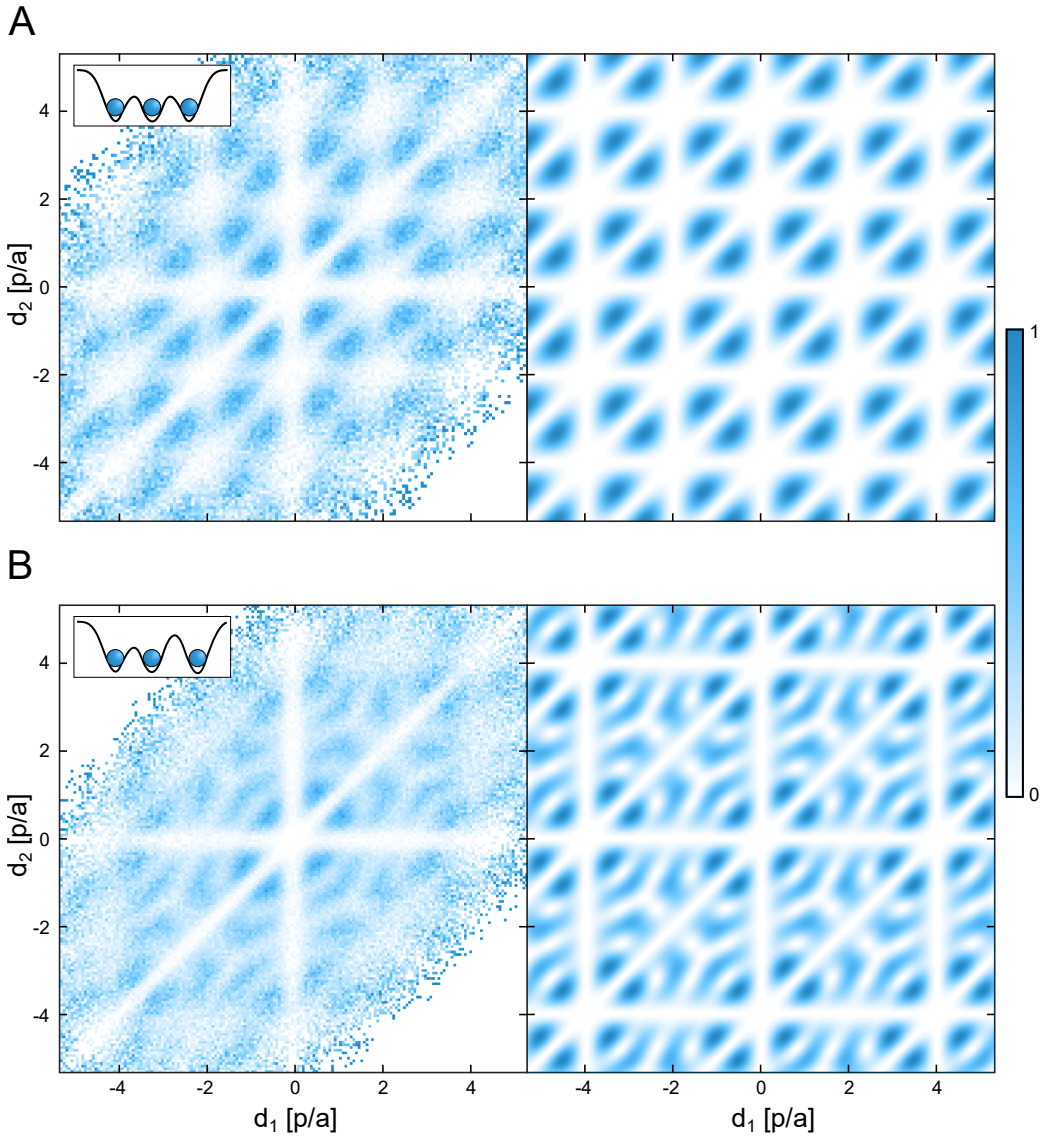

Figure 6.14.: **Third order correlation function of three fermions in three wells. A:** Measured (left) and calculated (right) third order correlation function for the commensurate triple-well. The full correlation function is three-dimensional, therefore the normalized correlation function in the two relative coordinates d_1 and d_2 is shown. There is a significant structure visible, with the essential features shared between the measurement and the theoretical calculation. **B:** Measured (left) and calculated (right) third order correlation function for the incommensurate triple-well. Again, a significant structure consistent with the theoretical expectation is visible. Adapted from [30].

$d_1 = d_2$. But even if we exclude these regions from further discussion, there is a significant structure left. At this point, we have to formally discuss the connected and disconnected parts of the correlation function, a concept we implicitly already used throughout this chapter.

Connected correlation function and Wick's theorem

Already when discussing the second order correlation function for either identical or distinguishable particles, we normalized the correlation function C^2 by removing the envelope on top of the correlation signal. The physical origin of the envelope was the (auto-)correlation of the single-particle momentum distribution (see equations 6.9, 6.10, 6.28). By dividing out these first order (that is, mean value) density correlations from the second order correlator, we removed any information which we already could have inferred based on lower order correlations. Similarly, I argued in the discussion of figure 6.6 that without interactions the correlation of second order can be reproduced taking into account only the outer product of the single-particle distributions. Also, in the definition of the third order correlation function in 6.30, the contributions from the first order correlations have already been removed. However, there are still contributions from second order correlations which are not yet taken care of. More formally, we can define the disconnected part of a correlation function as the sum of all contributions from lower orders and consequently the connected part - giving the intrinsic correlations at given order - as the remainder when the disconnected part is subtracted from the full correlation function. The exact form of the disconnected part can be explicitly calculated with the help of Wick's theorem, which formalizes the combinatorial problem of evaluating all the commutation relations in the normal ordering process [118]. For more complicated (and interacting) systems, there is a whole machinery of (diagrammatic) rules on how to disassemble the correlation functions. Here, we can still explicitly write down the different terms. In particular, we have

$$\langle : \hat{n}_{k_1} \hat{n}_{k_2} : \rangle = \langle \hat{n}_{k_1} \rangle \langle \hat{n}_{k_2} \rangle - G^1_{k_1,k_2} G^1_{k_2,k_1}, \tag{6.31}$$

where the expectation value is taken with respect to the prepared state and $G^1_{k_1,k_2} = \langle \hat{\psi}^\dagger(k_1) \hat{\psi}(k_2) \rangle$ is the propagator. Note that $\langle \hat{n} \rangle$ and G^1 are the population and the coherence of the one-body density matrix, respectively. We can further simplify this expression by using $G^1_{k_1,k_2} = (G^1_{k_2,k_1})^*$ such that $G^1_{k_1,k_2} G^1_{k_2,k_1} = \left| G^1_{k_1,k_2} \right|^2$. The result of 6.31 is already very important. By measuring second order density correlations, the absolute square of the first order coherence can be extracted. This is the mathematical basis of the original HBT method for stellar interferometry, but can also be used to study interacting systems such as heavy ions [258, 259] or Bose-Einstein condensates and coherent excitations on top of it [260, 261]. To this end, it is important to note that a Wick composition indeed also works in an interacting system.

Continuing with the decomposition, at third order we have

$$\begin{aligned}
\langle :\hat{n}_{k_1}\hat{n}_{k_2}\hat{n}_{k_3}: \rangle =& \langle \hat{n}_{k_1} \rangle \langle \hat{n}_{k_3} \rangle \langle \hat{n}_{k_3} \rangle - \langle \hat{n}_{k_1} \rangle G^1_{k_2,k_3} G^1_{k_3,k_2} - \langle \hat{n}_{k_2} \rangle G^1_{k_1,k_3} G^1_{k_3,k_1} \\
& - \langle \hat{n}_{k_3} \rangle G^1_{k_1,k_2} G^1_{k_2,k_1} + G^1_{k_1,k_2} G^1_{k_2,k_3} G^1_{k_3,k_1} + G^1_{k_1,k_3} G^1_{k_3,k_2} G^1_{k_2,k_1} \\
=& \langle \hat{n}_{k_1} \rangle \langle \hat{n}_{k_3} \rangle \langle \hat{n}_{k_3} \rangle - \langle \hat{n}_{k_1} \rangle \left| G^1_{k_2,k_3} \right|^2 - \langle \hat{n}_{k_2} \rangle \left| G^1_{k_1,k_3} \right|^2 \\
& - \langle \hat{n}_{k_3} \rangle \left| G^1_{k_1,k_2} \right|^2 + G^1_{k_1,k_2} G^1_{k_2,k_3} G^1_{k_3,k_1} + G^1_{k_1,k_3} G^1_{k_3,k_2} G^1_{k_2,k_1} \\
=& -2 \langle \hat{n}_{k_1} \rangle \langle \hat{n}_{k_3} \rangle \langle \hat{n}_{k_3} \rangle + \langle \hat{n}_{k_1} \rangle \langle :\hat{n}_{k_3}\hat{n}_{k_3}: \rangle + \langle \hat{n}_{k_2} \rangle \langle :\hat{n}_{k_1}\hat{n}_{k_3}: \rangle \\
& + \langle \hat{n}_{k_3} \rangle \langle :\hat{n}_{k_1}\hat{n}_{k_2}: \rangle + 2\mathcal{R}\left[G^1_{k_1,k_2} G^1_{k_2,k_3} G^1_{k_3,k_1} \right]
\end{aligned} \tag{6.32}$$

From 6.32, we can read off the disconnected correlator to be

$$\begin{aligned}
\langle \hat{n}_{k_1}\hat{n}_{k_2}\hat{n}_{k_3} \rangle_{dis} =& s_1(N) \left(\langle \hat{n}_{k_1} \rangle \langle :\hat{n}_{k_2}\hat{n}_{k_3}: \rangle + \langle \hat{n}_{k_2} \rangle \langle :\hat{n}_{k_1}\hat{n}_{k_3}: \rangle + \langle \hat{n}_{k_3} \rangle \langle :\hat{n}_{k_1}\hat{n}_{k_2}: \rangle \right) \\
& - 2 s_2(N) \langle \hat{n}_{k_1} \rangle \langle \hat{n}_{k_2} \rangle \langle \hat{n}_{k_3} \rangle ,
\end{aligned} \tag{6.33}$$

where the scaling factors $s_1(N)$ and $s_2(N)$ depending on the total particle number N were introduced for later convenience. For a fully fermionic theory as considered above, both factors are exactly equal to one for all N.
Before discussing the measured connected and disconnected correlation data, we have to take care of a quite intricate subtlety in the normalization of our correlation function. We have constructed the disconnected correlation function in a fully fermionic many-body theory. Thus, in addition to the measured correlations at lower order, also the fact that the Pauli principle holds has been used in its construction. As a consequence, a system of uncorrelated classical particles (or particles obeying any other statistics) would, within this framework, show a connected correlation contribution at third order due to it explicitly *not* following the antisymmetrization condition. This leaves us in a slightly uncomfortable situation, as our primary experimental imperfections result in a partial distinguishability of the atoms, such that they are in this effective model not fully fermionic any more. As a consequence, we would rather like to gauge our disconnected contribution such that the limit of fully distinguishable (and thus classical) particles corresponds to the limit of the connected correlation signal at third order exactly vanishing. We can achieve this by a suitable redefinition of $s_1(N)$ and $s_2(N)$. This can be motivated as follows: In a system of N classical particles, if one particle is detected at a specific location, this reduces the probability of detecting another particle at any other location by $\frac{1}{N}$ due to number

conservation. This is a very familiar concept and for example the mathematical basis of the well known Monty Hall problem (known as *Ziegenproblem* in German). In the *quantum Monty Hall* scenario, where the classical particles are replaced by bosonic or fermionic entities, this counting statistics changes due to (anti)bunching. For bosons, the factor is $1-\frac{2}{N}$ (as seen for example in [46]), while for fermions, as a consequence of Pauli exclusion the factor is exactly equal to 1. I should stress that all this is ultimately a consequence of explicitly imposing a fixed finite particle number. All the factors coincide in the many-body limit. As a consequence of the above discussion, we will use the following definitions from here on:

$$s_1(N) = \frac{N(N-1)(N-2)}{N^2(N-1)} \tag{6.34}$$

$$s_2(N) = \frac{N(N-1)(N-2)}{N^3}, \tag{6.35}$$

such that for any N the connected part is exactly zero for classical particles and that in the limit $N \to \infty$, the definition coincides with the full fermionic theory given in 6.32.

In figure 6.15, the measured data of the disconnected and the connected part of the correlation function are shown together with the theoretical expectation based on a fully fermionic theory.

We can observe that the main features expected from the theory calculation are well reflected in the measured data. In particular we indeed - and somewhat surprisingly - measure significant intrinsic third order momentum density correlations.[7] By comparison with 6.32, we can observe that the term

$$\langle \hat{n}_{k_1} \hat{n}_{k_2} \hat{n}_{k_3} \rangle_{con} = \mathcal{R}\left[G^1_{k_1,k_2} G^1_{k_2,k_3} G^1_{k_3,k_1} \right] \tag{6.36}$$

is responsible for the correlations. In other words: There are intrinsic third order correlations in the (momentum) density despite the mechanism responsible for the correlations being only of second order in the field operators. The reason is that we only measured the absolute value of the propagator, and crucially not its phase, in the second order correlation function. Therefore, the cyclic phase measured by $\langle \hat{n}_{k_1} \hat{n}_{k_2} \hat{n}_{k_3} \rangle_{con}$ known as Triad phase first shows up in third order of the density [262]. The equivalent of third order fermionic interference has already been studied with bosonic photons [262, 263], while this is the first measurement of intrinsic third order correlations in a non-interacting fermionic and massive field.

[7] Independent of the exact definition of $s_1(N)$ and $s_2(N)$ above.

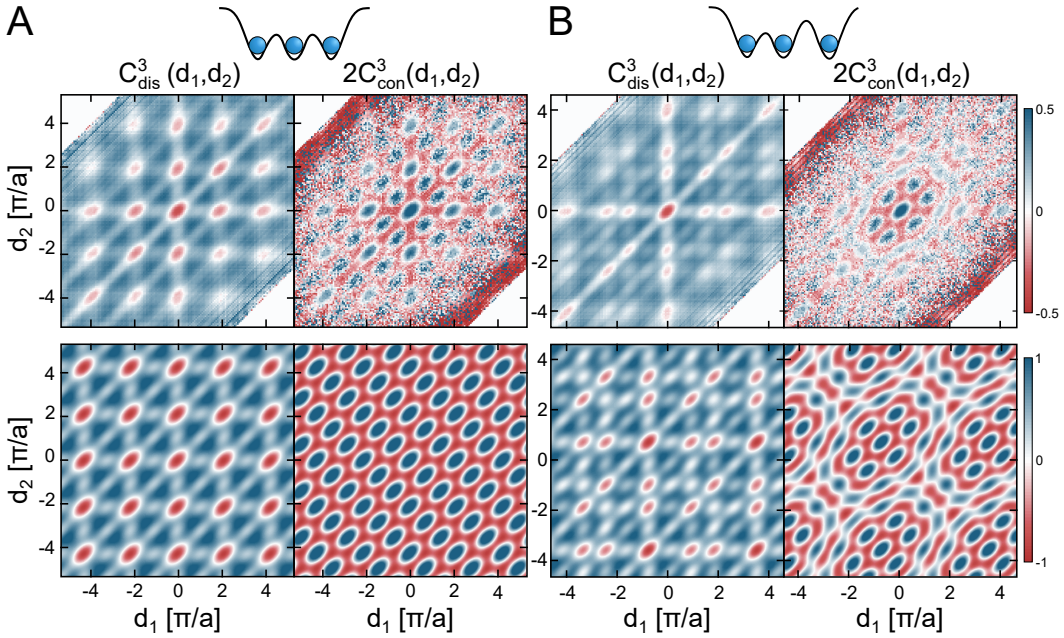

Figure 6.15.: **Third order connected and disconnected parts of the correlation function.** In **A** for the commensurate and in **B** for the incommensurate triple-well, the experimentally measured (top panel) and theoretically expected (bottom panel) connected and disconnected parts of the correlation function already presented in figure 6.14 are shown. Part of the correlation structure is due to contributions of lower (second) order which are captured by the disconnected part. Significant structure is left in the connected part of the correlation function, indicating intrinsic correlations at third order in the density. Adapted from [30].

I will conclude this section by again recapitulating what we achieved so far and which open questions are still left:

- I have shown that we are able both to prepare and characterize very pure sources of indistinguishable fermions.

- I have presented first experiments in the flavour of quantum optics, however with massive matter fields instead of massless bosonic fields (i.e. photons). In fact, while not discussed any further in the context of this thesis, this opens up a whole new research direction in the flavour of many-body interference [264]. Here, fermion sampling [265] and interference in the context of random unitarities [266] constitute two distinct examples.

- In a typical quantum many-body system, we will have both correlations induced by interactions and by quantum statistics. As an important first step, I have presented in this section how we have studied both effects

isolated from each other, such that each relevant contribution could be identified and classified independently.

- The topic of entanglement and indistinguishability has not been touched so far. When we study larger systems of mixed statistics, we therefore have to develop a consistent framework to describe entanglement in these systems.

6.4. Interactions vs Pauli principle

In section 6.2, I have discussed the correlations between interacting particles in a double-well, prepared for example in a state close to the Bell state $|\psi^+\rangle = \sqrt{\frac{1}{2}}\left(|L\rangle_1 |R\rangle_2 + |R\rangle_1 |L\rangle_2\right)$. I have furthermore discussed the entanglement properties of this state, in particular the particle entanglement, where the system is partitioned according to the particle labels $1 = \uparrow$ and $2 = \downarrow$, which in this case are given by the spin projection. In order to avoid confusion, I will in this section refer to this specific situation as *spin entanglement*. On the other hand, within the framework of first quantization, the state of two independent but indistinguishable particles two spatial modes could be written down in the particle basis as $|A\rangle = \sqrt{\frac{1}{2}}\left(|L\rangle_1 |R\rangle_2 - |R\rangle_1 |L\rangle_2\right)$. In this notation, it is obvious that the state, at least formally, features particle entanglement. As opposed to the spin entanglement, here the labels $1, 2$ are artificial however, in the sense that we fundamentally have no way of determining which of the atoms is the first subsystem and which the second. Therefore, also a standard Bell test where one party takes control over one subsystem and one party over the other is not possible. Thus the question arises if this should be considered *real* entanglement [100, 101]. I would argue that this is merely a matter of definition and the relevant question is rather if the identical particle entanglement is useful in any way, as has been argued recently [102–104]. Importantly, the identical particle entanglement definitely has physical consequences, as it results in measurable correlations very similar to correlations rooted in spin entanglement. Therefore, the focus of this section will be on a slightly rephrased question: Independent of the exact definition of entanglement and its usefulness, identical particle entanglement is fundamentally different from spin entanglement. However, in a strongly interacting system with multiple spin components, both concepts play a major role, sometimes contributing very similar correlations features. It is a very important open question how to measure and also distinguish identical particle entanglement. To this end, in this chapter, I will present a promising scheme based on a novel entanglement measure [31, 267, 268]. The results of this chapter have been published in [31].

Relevant states

Already above, I have presented measurements on correlations in identical fermion systems of two or three particles in two or three wells. These datasets will be used as examples with only identical particle entanglements. As an additional complication, we will also use a global $\pi/2$ rf rotation in order to rotate the global spin of these states into the equatorial plane. This is equivalent to the situation where we keep the state the same but measure in the x-basis instead of in the z-basis. Thus, the spin projection is not conserved any more and we can measure all three combinations, $\{\uparrow\uparrow, \uparrow\downarrow, \downarrow\downarrow\}$, of spin correlations. This will constitute the important test whether our method is capable of distinguishing apparent from inherent complexity. In addition, we will also use a hybrid state of a strongly repulsive Hubbard dimer $|_{+\infty}\rangle$ with an additional spectator spin-up particle independently prepared and placed next to the dimer without coupling the systems. This is an example of a state which features both spin and identical particle entanglement. Finally, we use the strongly interacting tunnel-coupled triple-well with two spin up and one spin down atoms introduced in section 6.1 as the prototype of an unknown state with potentially even tripartite entanglement. All the relevant classes of states have already been sketched in figure 6.2.

6.4.1. Antisymmetric negativity

In the seminal paper by Ghirardi, Marinatto and Weber [101], it was argued that any state of identical particles, which can be obtained by pure antisymmetrization of a (thus non-physical) product state, should be labeled as not entangled. This GMW criterion can be directly demonstrated for the familiar state of two atoms in a double-well. Here, $\mathcal{A}$ will refer to the operator performing the antisymmetrization. Starting from the product state $|L\rangle_1 |R\rangle_2$, we have

$$\mathcal{A}(|L\rangle_1 |R\rangle_2) = \sqrt{\frac{1}{2}} \left(|L\rangle_1 |R\rangle_2 - |R\rangle_1 |L\rangle_2\right), \tag{6.37}$$

such that according to the GMW criterion this state is not entangled. Building upon this criterion, and based on [31, 267, 268], we define the following functional acting on the physical fermionic two-particle density matrix $\rho_{\mathcal{A}}$

$$\mathcal{E}_{\mathcal{A}}(\rho_{\mathcal{A}}) = \min_{\sigma \geq 0} \left\{\mathcal{E}(\sigma) : P_{\mathcal{A}} \sigma P_{\mathcal{A}} = c\rho_{\mathcal{A}}\right\}, \tag{6.38}$$

where $P_{\mathcal{A}}$ is the projector on the antisymmetric subspace and $\mathcal{E}$ can be any entanglement measure. The factor $c = \max \mathrm{Tr}\left(P_{\mathcal{A}} \sigma_{ps}\right)$ is the maximum projection

possible for a fully separable state given by the density matrix σ_{ps}. In the bi- (tri-)partite case we obtain $c = 1/2$ ($c = 1/3$). The functional $\mathcal{E}_{\mathcal{A}}(\rho_{\mathcal{A}})$ searches over all positive semidefinite density matrices of trace 1, which are not yet restricted to any symmetry constraints but have a specific antisymmetric projection onto the target density matrix $\rho_{\mathcal{A}}$. We can explicitly perform this search for the above example. The density matrix of the state $\sqrt{\frac{1}{2}}\left(|L\rangle_1 |R\rangle_2 - |R\rangle_1 |L\rangle_2\right)$ in matrix representation in the (reduced) basis $\{|LR\rangle, |RL\rangle\}$ is given by

$$\rho_{\mathcal{A}} = \frac{1}{2}\begin{pmatrix} 1 & -1 \\ -1 & 1 \end{pmatrix} \tag{6.39}$$

If we *guess* the first density matrix σ to be used in the search to be $\sigma_g = |LR\rangle\langle LR|$, we get, using the explicit form of the projectors:

$$P_{\mathcal{A}}\sigma_g P_{\mathcal{A}} = \frac{1}{2}\begin{pmatrix} 1 & -1 \\ -1 & 1 \end{pmatrix} \cdot \begin{pmatrix} 1 & 0 \\ 0 & 0 \end{pmatrix} \cdot \frac{1}{2}\begin{pmatrix} 1 & -1 \\ -1 & 1 \end{pmatrix} = \frac{1}{4}\begin{pmatrix} 1 & -1 \\ -1 & 1 \end{pmatrix} = \frac{1}{2}\rho_{\mathcal{A}} \tag{6.40}$$

For any entanglement measure, $\mathcal{E}(\sigma_g) = 0$ such that we can stop the search immediately, and conclude that prior to antisymmetrization there was no entanglement. In this basic example, we could have come to this conclusion based on the GMW criterion alone straight away; however, the crucial step forward is that the functional $\mathcal{E}$ can be applied to any density matrix also of mixed states and states of mixed symmetry. Based on this, we define the antisymmetric negativity $\mathcal{N}_{\mathcal{A}}(\rho_{\mathcal{A}})$ ($\mathcal{AN}$) for the entanglement measure $\mathcal{E}$ given by the standard negativity $\mathcal{N}$ [269]. The advantage of the negativity is that equation 6.38, in this case, can be explicitly calculated when cast into a semidefinite programme. To this end, we adopt a first-quantized formalism by introducing particle labels $\{1, \ldots, N\}$. In this process, the 4×4 density matrices of the double-well system are mapped onto the 16-dimensional basis $\{|X\sigma\rangle |Y\tau\rangle\}$, with $X, Y \in \{L, R\}$ and $\sigma, \tau \in \{\uparrow, \downarrow\}$. The 9×9 density matrices of the triple-well system are correspondingly mapped onto the 216-dimensional basis $\{|X\sigma\rangle |Y\tau\rangle |Z\kappa\rangle\}$, with $X, Y, Z \in \{L, C, R\}$ and $\sigma, \tau, \kappa \in \{\uparrow, \downarrow\}$. This mapping is performed using the Slater determinant substitution rule, such that for example $|X\rangle_\uparrow |Y\rangle_\downarrow \rightarrow (|X\uparrow\rangle |Y\downarrow\rangle - |Y\downarrow\rangle |X\uparrow\rangle)$. For computational details on the $\mathcal{AN}$ and in particular the semidefinite programming, the reader is referred to [31, 99, 267, 268]. Here, we will focus on experimentally benchmarking the usefulness of this novel entanglement measure, in particular when facing experimental noise on the measured density matrices.

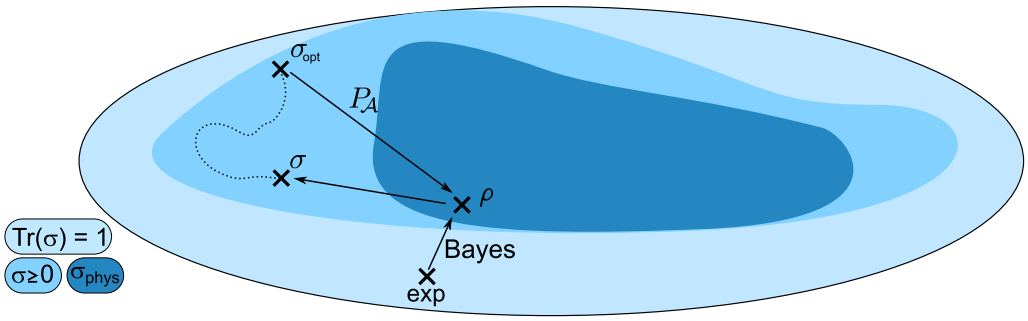

Figure 6.16.: **Scheme for determining the $\mathcal{AN}$.** An unknown state is prepared and the respective density matrix is partially reconstructed. The resulting density matrix is incomplete and not necessarily physical due to measurement uncertainties. The posterior distribution of the most likely physical density matrices ρ is determined by a Bayesian likelihood approach. For all density matrices in the posterior distribution, the space of positive definite (yet not symmetrized) density matrices σ is searched for the respective density matrix σ_{opt}, minimizing the negativity under the constraint of a specific (antisymmetric) projection $P_{\mathcal{A}}$ to ρ. The posterior distribution of the antisymmetric negativity is the distribution of minimized negativities obtained this way. Adapted from [31].

General scheme

I have presented above how we reconstruct the density matrices of an experimentally prepared Hubbard dimer. Here, we extend this method to indistinguishable fermions and also to three-particle systems in triple-wells. The general scheme we follow is thus, as also depicted in figure 6.16, given by:

- Measuring correlations in different conjugate basis sets.
- Extracting or restricting as many density matrix entries as possible.
- Determining the most likely physical density matrix $\rho_{\mathcal{A}}$ and in particular also extracting the full posterior distribution of the density matrices. These matrices are by construction fully symmetrized.
- Determining the $\mathcal{AN}$ for the matrices of the posterior distribution by searching the more general space of physical density matrices prior to symmetrization and comparing it to the standard negativity.

6.4.2. Experimental results

In this section, we will test and exemplify the usefulness of the $\mathcal{AN}$ by applying the general scheme presented above to a range of different experimentally

prepared states.

Identical particles

There are three different states prepared, with only identical particles involved (see figure 6.2):

- **State A:** two identical fermions in a double-well
- **State B:** three identical fermions in a triple-well
- **State C:** two identical fermions in a double-well with the total spin rotated into the equatorial plate

For both the states

$$|A\rangle = \sqrt{\frac{1}{2}} \left(|L\rangle_1 |R\rangle_2 - |R\rangle_1 |L\rangle_2 \right) \tag{6.41}$$

and

$$\begin{aligned} |B\rangle = & \sqrt{\frac{1}{6}} \left(|L\rangle_1 |C\rangle_2 |R\rangle_3 + |R\rangle_1 |L\rangle_2 |C\rangle_3 + |C\rangle_1 |R\rangle_2 |L\rangle_3 \right. \\ & \left. - |R\rangle_1 |C\rangle_2 |L\rangle_3 - |L\rangle_1 |R\rangle_2 |C\rangle_3 - |C\rangle_1 |L\rangle_2 |R\rangle_3 \right), \end{aligned} \tag{6.42}$$

where the number of spin up atoms is fixed, only one physical density matrix is possible within the one-dimensional Fermi Hubbard model, which is still assumed to be applicable here. This is due to the fact that there is only a single state of two (three) spin polarized particles without any double occupancies which is properly symmetrized. Therefore, we do not perform the Bayesian density matrix estimation for these states. The other way around, for the corresponding density matrix we would expect full contrast of the correlation features, which is as discussed above not the case. This discrepancy is explained by excitations in the physical system not captured by the in this case too simplistic model. In particular, as explained above, this is due to a mismatch between the double-well axis and the observation axis, but also the finite detection fidelity, other imaging defects, and in general any experimental imperfection. In all the situations considered above where distinguishable particles were involved, this was not directly apparent as this contribution resulted in an uncorrelated background in the correlations, and thus was absorbed in an incoherent contribution to the density matrix. In particular, this mechanism did not introduce any additional *spurious* entanglement. Without any incoherent contributions allowed, this is no longer possible for systems of only identical particles. In the specific case of states A

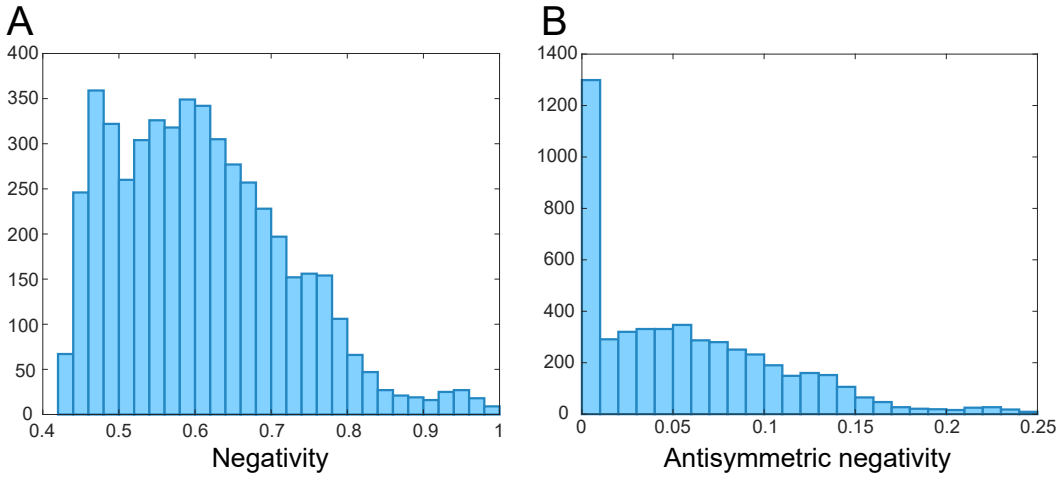

Figure 6.17.: **(Antisymmetric) negativity of the rotated spin triplet.** Posterior distribution of the extracted values of the negativity in **A** and the antisymmetric negativity in **B** based on the correlation measurements of the rotated spin triplet shown in figure 6.1. The data suggest a positive negativity while being consistent with an antisymmetric negativity of zero. Adapted from [31].

and B, we would have to introduce an artificial auxiliary dimension to absorb the partial distinguishability. Alternatively, we could only refer to an entanglement witness instead of a measure. To this end, it could be for example used that the visibility observed for the two particles in the two wells significantly exceeds the bound of $\sqrt{1/2}$, which is required for quantum locality tests employing these massive fermions [243, 270].

State C is identical to state A, except that we have chosen an unfavourable measurement axis rotated by 90° with respect to the natural quantization axis. Thus, we measure significant correlations between all combinations of spin projections, as shown already in the beginning of this chapter in figure 6.1. In this measurement campaign, we did not measure the in-situ populations independently as before, such that in addition to the two-particle coherences we can only extract the populations $P_{\uparrow\uparrow}$, $P_{\downarrow\downarrow}$ and the sum $P_{\uparrow\downarrow}+P_{\downarrow\uparrow}$. Nevertheless, we can perform the Bayesian state estimation. From the full posterior distribution, we can extract the best guess and the corresponding error bounds of the (antisymmetric) negativity. To this end, we evaluate the two measures on each entry of the posterior distribution, afterwards taking the mean value and the 68 % confidence bounds of the respective distribution obtained. This is shown in figure 6.17. We obtain for the negativity $\mathcal{N}(\rho_A) = 0.5$, $\mathcal{N}(\rho_B) = 1$ and $\mathcal{N}(\rho_C) = 0.66^{+0.13}_{-0.11}$, and for the antisymmetric negativity $\mathcal{AN}(\rho_A) = \mathcal{AN}(\rho_B) = 0$, and $\mathcal{AN}(\rho_C) = 0.048^{+0.064}_{-0.048}$. The standard negativity treats particle entanglement of distinguishable particles

and identical particles on equal footing and is thus blind to the fact that the labelling of the particles is artificial only. We therefore obtain a negativity consistent with the value of a Bell state for states A and C, and also for state B the negativity would suggest maximum entanglement. On the other hand, as already anticipated, for the states A and B the $\mathcal{AN}$ is exactly zero as the density matrix can be constructed by proper antisymmetrization of a product state. Importantly also for state C, that is in a setting where there is noise on the measured density matrix and correlations between all spin components are present, the result is consistent with zero. This is a first important indication that this scheme is indeed capable of removing any identical particle entanglement based on measured correlations.

Hubbard dimer

We have already reconstructed the density matrices for two interacting particles in a spin singlet in section 6.2. We can now use them to calculate the $\mathcal{AN}$ as a function of the interaction strength U/J and compare the results to the negativity. This is shown in figure 6.18.
We can observe that for both measures, the value is lowest for $U/J = 0$ and increases monotonously with increasing $|U|/J$. The fact that the baseline for the negativity is 0.5 rather than exactly 0 is due to the fact that in the full density matrix, the antisymmetrization of the spin degree is included, which is interpreted by the negativity as particle entanglement in analogy to the result of 0.5 obtained for the state A above. This contribution is reliably removed by the antisymmetric negativity such that it assumes a minimum of 0 at $U/J = 0$. This supports the claim that the $\mathcal{AN}$ is useful for extracting the entanglement caused by interactions alone, in particular as the $\mathcal{AN}$ is fully consistent with all other measures taking into account only the entanglement in the spin sector, as presented in section 6.2. We can compare the measured values to the theoretical expectations based on the two-site Hubbard model. Indeed, the general behaviour is well reflected in the data; however, as discussed before, due to the finite purity of the prepared state we measure a reduced (antisymmetric) negativity.

Three wells with three particles

Finally, we can take one further step and consider systems of three particles in three wells. Here, two additional ingredients are added. First of all, as these states will now include both interactions and indistinguishability, differentiating between the two contributions will be more challenging. Secondly, more intricate

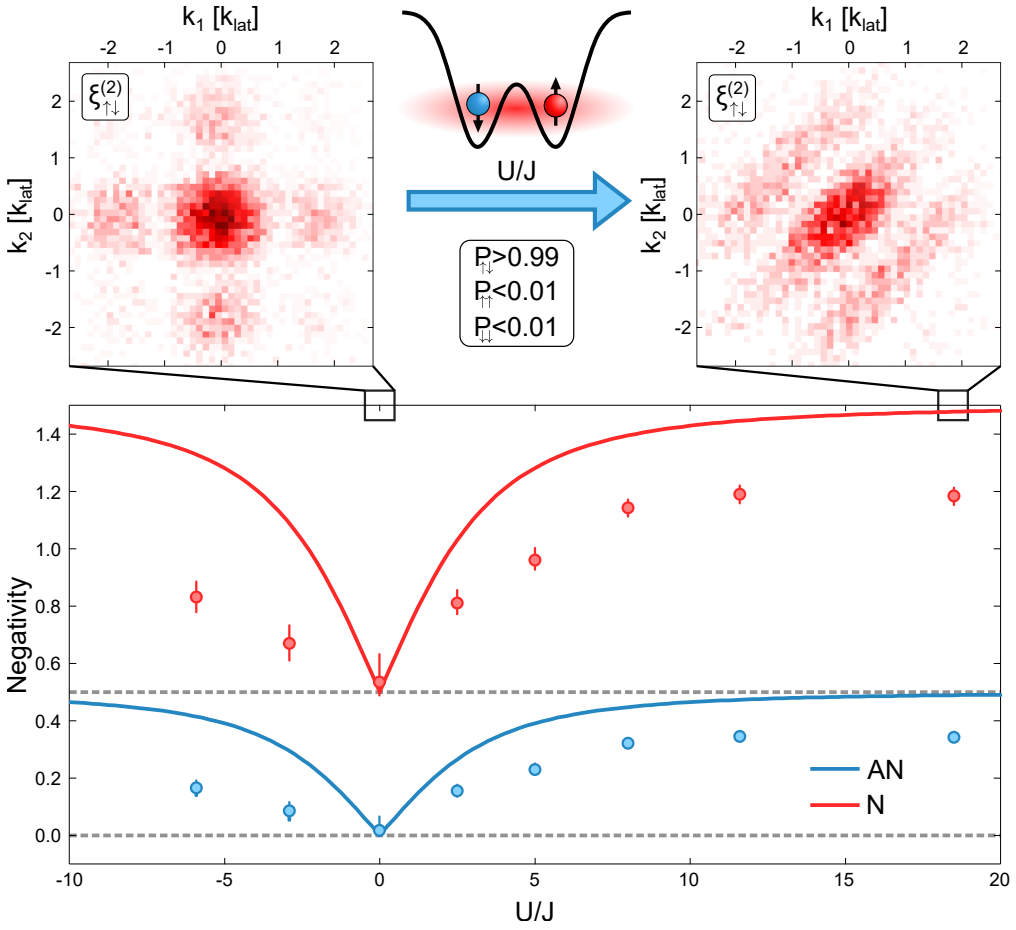

Figure 6.18.: **Negativity in the Hubbard dimer.** Based on the correlation measurements in the Hubbard dimer for a broad range of U/J already presented in section 6.2 (for reference the correlation functions for $U/J = 0$ ($U/J = 18.5$) are shown in the upper left (right) panel again), the negativity (red circles) and antisymmetric negativity (blue circles) are extracted. Both measures are smallest for vanishing interactions and increase upon increasing $|U|/J$, with the negativity offset by 0.5 but otherwise consistent to the antisymmetric negativity up to a linear rescaling. The experimentally extracted values are compared to the theoretical expectation based on the pure ground state of the Hubbard dimer (blue and red line). The measured negativities are smaller due to the finite purity. Adapted from [31].

multipartite entanglement, where the entanglement is shared between more than two parties, can show up and has to be tested for. Here, we use two different states as prototypes for these effects:

- **State 1:** a strongly repulsive Hubbard dimer with an auxiliary spectator spin up particle placed next to it
- **State 2:** two spin up and one spin down particle in a fully tunnel-coupled

triple-well

For both of the states, we measure the momentum density correlations up to third order as well as the in-situ populations, based on a sample size of around 20 000 images with a postselection rate of around 70 %. In analogy to the discussion around equation 6.17, also for the third order correlation function, we can extract a subset of the density matrix entries. The state space is spanned out by the nine basis vectors

$$\begin{aligned}\Big\{&|RC\rangle_\uparrow|L\rangle_\downarrow, |RL\rangle_\uparrow|C\rangle_\downarrow, |CL\rangle_\uparrow|R\rangle_\downarrow, |RC\rangle_\uparrow|R\rangle_\downarrow, |RC\rangle_\uparrow|C\rangle_\downarrow,\\ &|RL\rangle_\uparrow|L\rangle_\downarrow, |RL\rangle_\uparrow|R\rangle_\downarrow, |LC\rangle_\uparrow|L\rangle_\downarrow, |LC\rangle_\uparrow|C\rangle_\downarrow\Big\},\end{aligned} \tag{6.43}$$

where $|i,ii\rangle_\uparrow|iii\rangle_\downarrow$ denotes the state where the spin up particles i and ii and the spin down particle iii are in the left (L), central (C), or right (R) well, respectively. We can experimentally fix 69 out of the 81 real parameters of the density matrix. The full posterior distribution of physical density matrices is inferred based on a Bayesian estimate as before. Based on this, the bipartite negativity and $\mathcal{AN}$ is evaluated for the experimentally prepared states $|1\rangle$ (Hubbard dimer with a spectator atom) and $|2\rangle$ (approximation of the $|W\rangle$ state). This is shown in figure 6.19.

For both states the negativity is finite, as this measure cannot differentiate between interaction and symmetrization-based non-separability. In fact, the negativity is even slightly larger for state $|1\rangle$ due to the perfect symmetrization of the left well with the other two compared to the imperfect interaction-based entanglement of state $|2\rangle$. On the other hand, the antisymmetric negativity is compatible with zero for state $|1\rangle$ despite the fact that there is bipartite entanglement between the central and the right well. This is due to the fact that in each possible partitioning 1|23, 2|31, 3|12 (but of course not in all partitionings at the same time), the density matrix in the first quantized state space $\{|X\sigma\rangle|Y\tau\rangle|Z\kappa\rangle\}$ introduced above can be written in a form where a single atom is factorized out.[8] This is not expected to be the case any more for the W state. The fact that we nevertheless do not reconstruct a finite $\mathcal{AN}$ for the experimentally measured state $|2\rangle$ therefore indicates that we did not succeed in preparing the W state with a good fidelity.

The definition of the $\mathcal{AN}$ in equation 6.38 also allows for an evaluation of the tripartite antisymmetric negativity, based on a suitable definition of the tripartite negativity. Based on [271, 272], we infer a finite multipartite negativity if, and only if, the density matrix ρ cannot be expressed as a mixture of biseparable

[8] Note that the hyperfine state cannot be used as a label for the partitions any more.

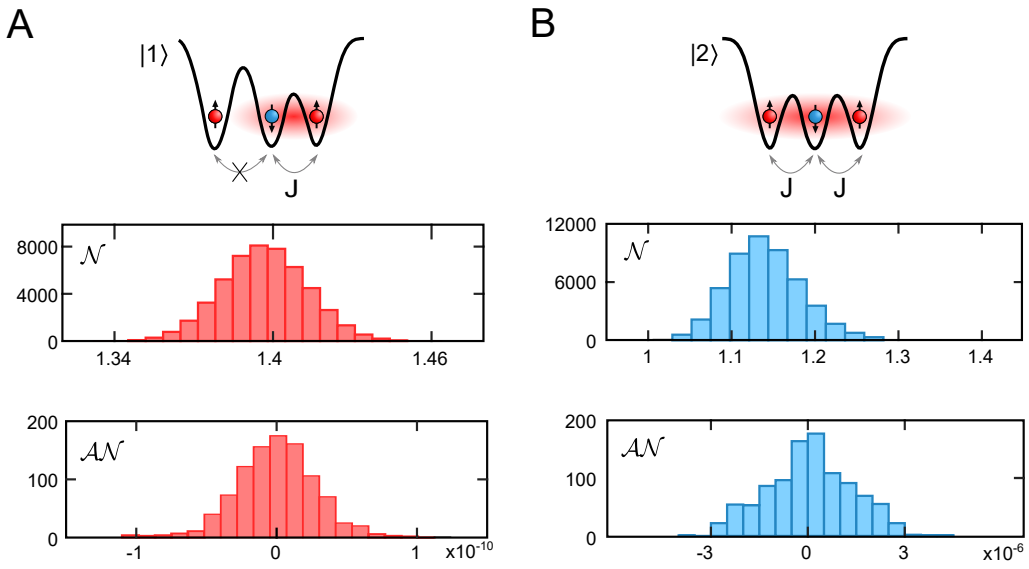

Figure 6.19.: **Bipartite (antisymmetric) negativity in a triple-well. A:** The sketched state $|1\rangle$ is experimentally prepared and characterized. Based on the measured correlation functions, the posterior distribution of possible physical density matrices is inferred as before. For each entry of the posterior distribution, the (antisymmetric) negativity is calculated. The resulting values are shown as a histogram in red. From the histogram, we extract a finite $\mathcal{N} = 1.39 \pm 0.02$ while the $\mathcal{AN}$ is compatible with zero. **B:** The sketched state $|2\rangle$ is experimentally prepared and characterized as before. From the histogram (in blue), we extract a finite $\mathcal{N} = 1.14^{+0.05}_{-0.04}$ while the $\mathcal{AN}$ is again compatible with zero.

states ρ^{sep} in the different possible bipartitions:

$$\rho \neq p_1 \rho^{sep}_{1|23} + p_2 \rho^{sep}_{2|31} + p_3 \rho^{sep}_{3|12} \tag{6.44}$$

Therefore, in order to quantify the tripartite (antisymmetric) negativity, the bipartite negativity is minimized over all possible bipartitions as well as for all possible convex combinations of biseparable density matrices. Due to computational limitations, these calculations are performed only on a (randomly sampled) subset of 1000 density matrices of the posterior distribution. In addition, also the theoretically expected density matrices for the Hubbard dimer with spectator atom and the fully tunnel-coupled triple-well are evaluated. The results are presented in figure 6.20.

I will first discuss the results obtained for the standard negativity. First of all, it should be noted that the calculations of the bi- and tripartite negativities actually result in the same value. As before, this is due to the fact that the negativity does not differentiate between non-separability due to the total antisymmetriza-

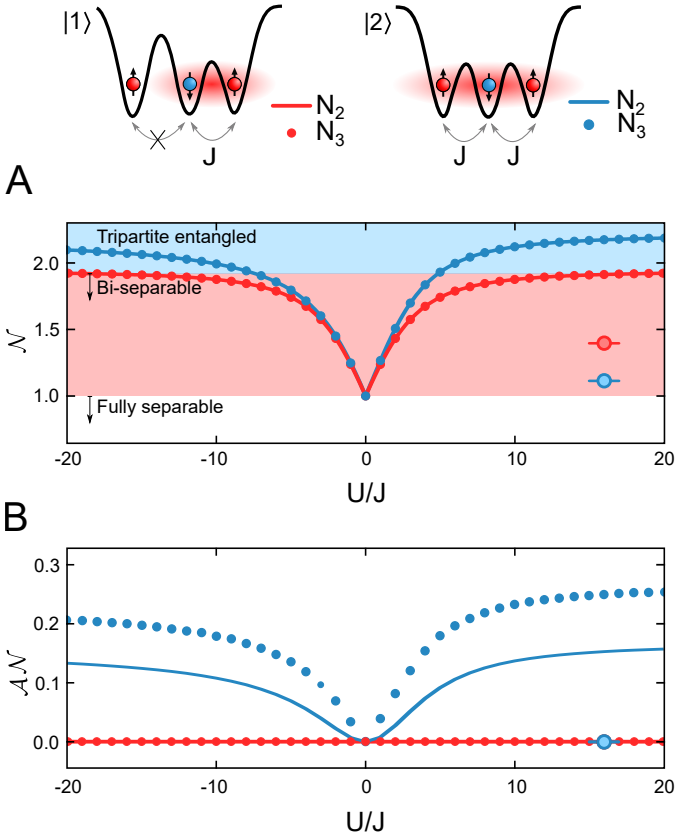

Figure 6.20.: **(Antisymmetric) negativity and multipartite entanglement. A:** For the two sketched states $|1\rangle$ (red) and $|2\rangle$ (blue), the theoretical bipartite (lines) and tripartite (dots) negativity is calculated. Due to the antisymmetric structure of the density matrix, the bi- and tripartite negativities are always identical. Indicated in shaded areas are values of the negativity witnessing bipartite (red) and tripartite (blue) entanglement. For both experimental realizations of the states, bipartite entanglement is witnessed with no statement about tripartite entanglement possible (red and blue data points). **B:** For the same states, the $\mathcal{AN}$ is calculated as well (colour scale as in A). For state $|1\rangle$ shown in red, both the theoretical and experimentally determined $\mathcal{AN}$ is zero, while for state $|2\rangle$ the theoretical tri- (bi-)partite $\mathcal{AN}$ shown as blue dots (blue line) takes a finite value, while the experimentally determined value (blue data point) is compatible with zero. Adapted from [31].

tion of the density matrices and the interaction effects. Nevertheless, it is still possible to construct a witness (instead of a measure) for bi- and tripartite entanglement. To this end, we use that the maximum negativity calculated for an antisymmetrized but otherwise separable three-particle state is one (see state B discussed above) and that the maximum negativity for an antisymmetrized biseparable state is 1.9428. Using this, it can be certified that the theoretic model of state 1 is indeed not fully separable for any finite interaction strength. In addi-

tion, it is also possible to certify tripartite entanglement for the theoretical model of state 2 for sufficiently large $|U|/J$, when it approaches the W state. In turn, it is not possible to identify the finite amount of tripartite entanglement already present for a smaller interaction strength. For this, we will need the $\mathcal{AN}$. For the experimental realization of state 1, we can certify based on the reconstructed negativity that the state is not fully separable, albeit the value of the negativity being reduced compared to the theoretical expectation due to the finite purity of the state. Also, the experimental state 2 is identified as not fully separable, while no tripartite entanglement is witnessed.

Turning towards the $\mathcal{AN}$, the first observation is that the result of the $\mathcal{AN}$ is indeed zero for all (experimental and theoretical) realizations of state 1; not only for the tripartite but also for the bipartite antisymmetric negativity as discussed above. The $\mathcal{AN}$ can therefore be used to explicitly certify that state 1 is not tripartite entangled, while with the negativity alone it is only possible to state that no tripartite entanglement is witnessed.

For the case of the (theoretical) second state, the $\mathcal{AN}$ indeed detects tripartite entanglement, for any finite interaction strength. This is reflected in two ways in figure 6.20. First of all, there is bipartite entanglement detected in all possible partitioning (see equation 6.44). In addition, also the tripartite $\mathcal{AN}$ takes a finite value for any finite $|U|/J$, allowing for a certification of genuine multipartite entanglement even in a regime where the witness based on standard negativity does not exceed the bound of 1.9428. Therefore, the $\mathcal{AN}$ can serve as a measure for genuine multipartite interaction-induced entanglement, while via the negativity only a witness could be constructed.

While for the measured state $|1\rangle$ - as engineered - indeed no tripartite entanglement is detected, this is also the case for state $|2\rangle$, finally assuring us that we did not succeed in preparing a state close to the W state. In order to nevertheless prove the usefulness of the tripartite $\mathcal{AN}$ in the presence of noise, we generate a set of density matrices based on the W state by adding white noise of the form

$$\rho_{noise} = p\mathbb{1} + (1-p)\,|W\rangle\langle W|\,, \tag{6.45}$$

with the noise amplitude $p \in [0,1]$. A finite tripartite entanglement is detected up to $p = 0.25$, corresponding to a purity of around 0.6. While we clearly were not able to reach such a purity with our state 2, it seems experimentally feasible to reach sufficiently pure states. To this end, note that for the two-particle case presented in section 6.2, we did in fact exceed this purity.

To summarize, in this section I introduced a conceptually and computationally

useful scheme to distinguish non-separability of a density matrix due to quantum statistics from 'real' entanglement due to interactions, based on [31, 267, 268]. We have used a set of experimentally prepared few-body states as well as theoretical density matrices to test several limiting cases and prove the usefulness. While this is first of all an important technical and previously unavailable achievement, an entanglement measure like the $\mathcal{AN}$ can also be a valuable contribution towards a better understanding of the fundamentals of entanglement, as it allows us to systematically classify different entanglement contributions. In the context of this thesis, the important conclusion is that we have gained both a new tool and new insight on how to study a general many-body state which will - quite in general - always feature an interplay between indistinguishability and interactions.

6.5. Concluding remarks

In this chapter, I have presented a novel toolbox to study correlations and entanglement in small systems driven by strong interactions, antisymmetrization, or even an interplay between both effects. The rather small systems allowed us to discuss the individual contributions independently and to prepare states prototypical of different effects. For these systems, we built up a complete toolbox to characterize them experimentally, based on density correlation measurements up to third order in conjugate basis sets, and to classify them according to different entanglement measures, including the novel antisymmetric negativity. Such a toolbox was not available before and constitutes the second major milestone outlined in section 4. It is clear that we will encounter a similar but much more involved interplay between indistinguishability and interactions also in larger systems. A prototypical (yet still comparably simple) example is a (3D) BCS superfluid. The BCS state is given by

$$|BCS\rangle = \prod_{\mathbf{k}} \left(u_{\mathbf{k}} + v_{\mathbf{k}} \hat{c}^{\dagger}_{\mathbf{k},\uparrow} \hat{c}^{\dagger}_{\mathbf{k},\downarrow} \right) |0\rangle \,, \tag{6.46}$$

in terms of the BCS coefficients $u_{\mathbf{k}}$ and $v_{\mathbf{k}}$. In other words, this is a state of coherent pair excitations on top of a Fermi sea. The pair correlations are of course mediated by interactions, while only due to the contribution from identical particle correlations the effective phase-space for the scattering is reduced to two dimensions, allowing for the pairs to even form. As a consequence, a BCS state could be characterized by measuring second order momentum correlations similar to what was shown above [27].
Another good example in the spirit of the BEC-BCS crossover is the regime of

strong interactions, where the Fermi surface is on the verge of breaking down. In such a system, the interplay between interactions and indistinguishability is much more intricate, and cannot be effectively 'separated out' as done for the BCS ground state. A relevant observable might nevertheless be correlations of momentum density, as they will be able to certify that we are facing pairing at a finite momentum in contrast to molecule formation centred at $k = 0$. However, it will be a necessity to measure correlations significantly beyond second order to characterize the system to a good degree. Finding a suitable basis where the smallest number of correlation orders has to be taken into account to capture the essential features of the system is thus an outstanding and unsolved question. For a system in the BEC-BCS crossover, correlations in real and momentum space are a reasonable first guess though, as real- and momentum-space pairing constitute the limiting BEC and BCS cases. It is therefore crucial to learn how to scale up the systems and methods introduced in this chapter. In the next chapter, I will present first results in this direction, where we study mesoscopic quantum systems and their correlations.

7. Correlations in mesoscopic systems

Arguably one of the most cited phrases in the field of many-body physics is 'more is different', based on the article by P. W. Anderson of the same name [273]. In simplified terms, the article states that while it is possible to reduce the fundamental physics to microscopic models, laws, and symmetries, when studying a many-body system, there is more to be expected than naively anticipated based on an extrapolation of microscopic phenomena. Only in large systems, collective behaviour such as collective excitations connected to broken symmetries and thus also phase transitions can emerge [134], in turn defining the many-body regime. Ultimately, this is a consequence of a separation of scales. While for example the ground state of a given Hamiltonian has to obey its fundamental symmetries, a non-equilibrium state may easily break this symmetry for a given time in terms of an oscillation around the symmetric value. If the oscillation is of a collective nature, it will depend on the particle number in the system. When approaching the thermodynamic limit, the timescale given by the oscillation period might even by shifted towards infinity. In this situation, the broken symmetry state becomes quasi-stationary, and depending on its energy even the effective ground state of the system, forming a symmetry-broken state.

The most instructive example for this, as used several times throughout this thesis (see section 2.3.3 for more details), is the BCS superfluid.[1] At the critical temperature T_C, the Fermi surface becomes unstable towards formation of Cooper pairs. Therefore, the many-body induced pairs can spontaneously form. Above T_C, it is of course also possible to excite a paired mode. However, this excitation is gapped in energy and in particular does not constitute the thermal ground state, reflecting the symmetry of the system. Below the critical temperature, the many-body gap is finite, as now the ground state is paired (see figure 2.6). Therefore, the thermal phase transition is accompanied by the opening of a many-body

[1] I will restrict the already simplified discussion to second order phase transitions. I will ignore any complications arising when going beyond this assumption as they are not relevant in this section.

gap, or equivalently by the fundamental correlation length and fluctuation decay time diverging. Similarly, also quantum phase transitions are of interest, where (at $T = 0$) the transition is driven by quantum fluctuations instead, with the temperature scale replaced by an intrinsic energy scale of the model. In any case, only in a macroscopic many-body system, a true divergence of time and length scales and therefore a full closing of the gap is possible according to the above discussion. Nevertheless, in a mesoscopic system we might be left with a *softening* of the fundamental mode, the correlation length scale becoming large (compared to the system size), and the fluctuation timescale becoming long (compared to the trap period).
Based on this, a few conclusions can be drawn:

- There is a fundamental step missing between preparing and studying microscopic systems as presented in chapter 6, and preparing and studying many-body systems as presented in chapter 3.
  - The toolbox of detecting correlations has to be extended to include collective effects. In this context, it should be stressed again that the 'charge density wave' and the 'antiferromagnetic order' discussed in the Hubbard dimer indeed serve only as toy models for their collective many-body equivalents. For example, there are only around 60 % singlet correlations in the antiferromagnetic ground state of a 3D Fermi-Hubbard model with $U/J \to \infty$.[2]
  - In a similar fashion, there is no adiabatic connection between the microscopic constituents of the system (such as the singlets) and the many-body ground state. Therefore, a naive approach of 'stitching' together individual microscopic systems to form the macroscopic ground state will not work (perfectly). There are methods to approximate the ground state, however. Most notably, this the resonating valence bond approach [202, 203], which is the most promising path when aiming at scaling up the lattice models presented in chapter 6 to a low entropy many-body Fermi-Hubbard system [195, 204].
  - In addition, adiabatically preparing the symmetry-broken ground state from a non-interacting ground state is not possible. This is due to the many-body gap opening up at the quantum critical point, such that the energy for the symmetry-breaking excitations becomes zero at this point. This fundamental diabatic nature can of course also be understood as a consequence of the diverging timescale of the symmetry-

[2] The so-called Heisenberg model.

breaking excitations as discussed above. This is formalized by the so-called Kibble-Zurek mechanism [198–201].

- Mesoscopic systems, defined here as being large enough to already feature collective behaviour, but still small enough such that deterministic preparation and control remain within reach, might constitute an important intermediate step. Apart from the possible (near) deterministic preparation of the non-interacting ground state, adiabatic ramping is still an option, as the gap closing is replaced by a softening with a finite gap persisting even at the precursor of the quantum critical point or temperature. It has been shown before that a many-body description can account for collective behaviour of nuclei or liquid helium droplets already for around 50 individual constituents [274–276], while the emergence of a Fermi sea [277] or the onset of coherent Josephson oscillations are possible for even smaller particle numbers.

- Studying mesoscopic systems is not only a compromise based on technical limitations. Due to the scale of the finite size introduced, mesoscopic systems can feature a very complex structure and can be extremely complicated to describe theoretically. On the other hand, mesoscopic systems are very relevant in physics in the form of the electronic structure of atoms, the nuclear structure of larger nuclei, liquid helium clusters, or small condensed matter systems [274–276]. An extensive review comparing nuclei and ultracold atomic gases is for example found in [278].

With all of these considerations in mind, I formulated in section 4 the milestones four and five, to identify, prepare and afterwards fully characterize mesoscopic systems as both an intermediate step towards a full characterization of many-body systems and an interesting research direction on its own. It should be clear that there are many different, equally interesting paths to proceed from this point on. Based on the experience built upon small lattice systems, a viable option could be to take an array of singlets as a starting point to study larger systems in the spirit of a resonating valence bond model. Alternatively, connections to the field quantum simulation (analogue or digital) could be explored, for example by a variational approach [279–282]. In this thesis, however, I would like to take the most direct route towards closing the circle to the many-body system discussed in the beginning by studying the interplay between pairing correlations and the Fermi surface.

7.1. Emergence of a quantum phase transition

I have argued above that studying mesoscopic systems as large as possible, but on the other hand still featuring deterministic control, provides a promising platform for studying the emergence of many-body physics. So where to begin? Based on the results of chapter 6, I might be tempted, while starting from the triple-well, to add one well after each other in a linear chain of tunnel-coupled tweezers. Apart from the technical limitations discussed already, this is also conceptually not the most direct way. What I am aiming for is the mesoscopic analogue of a many-body system which features both a mechanism of pairing and a Fermi surface. This is one of the defining features of a BCS superfluid and, as conjectured in chapter 3, also of a strongly correlated 2D system in the BEC-BCS crossover. Only the interplay between sufficient degeneracy at the Fermi surface (compare to the Fermi points in a 1D system) with interaction might be capable of reproducing an instability towards the formation of many-body pairing.[3]

The requirement for deterministic control of the system ultimately boils down to the necessity of introducing a finite (large) single-particle excitation energy. This is of course nothing else than the (non-interacting) energy levels we encountered for example in the microtrap, where the finite spacing between the energy levels allowed for a spilling process where certain levels were selectively allowed to tunnel out of the system. Therefore, we are now interested in a system where the single-particle levels at around the Fermi energy feature a significant degeneracy, such that they can be interpreted as a Fermi surface.

Such a situation is actually quite common in typical mesoscopic systems such as atoms and nuclei, where the degenerate single-particle energies are typically referred to as energy shells, a notion which I will adapt from here on. Interestingly, both in atoms and nuclei, interactions lead to a fascinating interplay between pairing correlations and the degeneracy due to the shell structure. In particular, this results in a sub-shell structure known as Hund's rule in this geometry [283, 284]. For very strong interactions, this competition of scales between the pairing energy and the single-particle energy will lead to even more additional structure. In particular, we will encounter a quantum phase transition not present in the homogeneous many-body system with a continuous density of state instead of discrete modes. Note to this end that while also the system in chapter 3 was of course trapped, the single-particle excitation energy was small and separated in

[3] As we are dealing with mesoscopic systems with a finite number of individual modes, it is of course also possible to engineer all the degeneracies and couplings in a 1D chain of tweezers in a smart way. Alternatively, a 2D lattice geometry is extremely interesting to study in this respect, too.

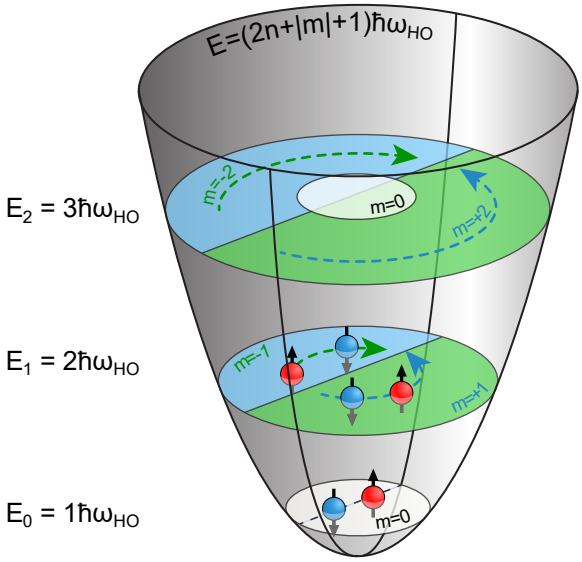

Figure 7.1.: **Two-dimensional harmonic oscillator.** Schematic illustration of the level structure in the angular momentum basis with the lowest two shells filled. The energy levels are given by $E_k = k \cdot \hbar\omega_{HO}$, with a degeneracy of $k+1$ (per spin state). Exciting one fundamental quantum of energy $\hbar\omega_{HO}$ is accompanied by an angular momentum change of $\Delta m = \pm 1$. The energy of the lowest monopole excitation is given by $\Delta E = 2\hbar\omega_{HO}$.

scale, reflected in the fact that it was possible to apply the local density approximation. As a consequence, while we are interested in the emergence of many-body physics in a mesoscopic system, taking the actual many-body limit is not necessarily straightforward.

I will argue that a trap geometry, which is approximately described by a 2D harmonic oscillator, is an ideal setting to study mesoscopic systems. The energy levels of an isotropic 2D harmonic oscillator are sketched in figure 7.1

In a 1D harmonic oscillator, the energy levels are equally spaced with $\Delta E = \hbar\omega_{HO}$, where each energy level can be occupied by one atom per spin state. In the two-dimensional analogue, there are two degenerate fundamental excitation frequencies $\omega_{HO} = \omega_x = \omega_y$. Therefore, the energy spacing is again $\Delta E = \hbar\omega_{HO}$, however with a degeneracy of each level E_k (starting from $E_0 = \hbar\omega_{HO}$) of $k+1$. This can easily by checked, as for example the first excited energy level can be reached by either exciting a single x or y energy quantum. Due to the rotational symmetry, it is instructive to write down the level structure in a relative angular momentum basis as done in figure 7.1 in terms of the principal quantum number $n = 0, 1, 2, 3, \ldots$ and the angular momentum projection $m = 0, \pm 1, \pm 2, \ldots,$

where

$$E_{n,m} = (2n + |m| + 1)\,\hbar\omega_{HO}. \tag{7.1}$$

Note that the total angular momentum is not limited or fixed based on the principle quantum number. Crucially, an excitation by $\Delta E = \hbar\omega_{HO}$ always changes the angular momentum projection m by one, and the lowest energy to excite a monopole mode (that is without changing m) is twice the fundamental frequency and achieved by either lifting one particle up two shells, or two particles of opposite angular momentum one shell.

Before discussing any preparation schemes and experimental observations, I should stress that choosing a 2D geometry (as opposed to 3D) is influenced far more by technical, than by conceptual reasoning. For a 2D system, we can use the axis which is integrated out in the model to gain access to the system for imaging and manipulation. This is in line with the geometry of the experiment, where the objective is aligned on the z-axis, singleing out the focal plane, but also with the magnetic field geometry which is designed to be axially symmetric. Of course, the connection to the system discussed in chapter 3 allows for an instructive narrative; however the subtleties of the reduced dimensions (i.e. the increased role of quantum fluctuations) are due to the respective density of states. In this chapter, I discuss systems with a finite number of discrete modes, such that these general statements, based on a universal structure of the density of states, are no longer possible. Nevertheless, the existence of a two-body dimer for each interaction strength in two dimensions will still provide us with the relevant scale for the interaction strength in the mesoscopic system as well.

Based on the considerations in this section, I will now discuss results on preparing and probing mesoscopic 2D systems. In particular, I will discuss the emergence of a zero temperature quantum phase transition in such a system. The following results have been published in [32]. Note that, even though working towards the study of mesoscopic systems - in particular including the development of the conceptual ideas and experimental strategies - has been a major part of my doctoral studies, I will keep this section rather short, as an extensive discussion has already been given in [285].

7.1.1. Preparation of deterministic 2D systems

In this chapter, I will briefly present the scheme used to prepare a deterministic two-dimensional system. This constitutes an important experimental milestone, allowing us for the first time to study the interplay between (pairing) interac-

tions and degeneracy in a controlled deterministic way. Nevertheless, the basic prerequisite is straightforward: We have to engineer a trap geometry where certain energy levels are bound, while all others are not. We will again use magnetic field gradients, trying to achieve a separation in scale between the tunnelling times of the energy levels below and above a fine-tuned energy scale. If the trap geometry is known, these timescales can be directly calculated or at least estimated. Therefore, also taking experimental imperfections into account, we can estimate based on the experience from the one-dimensional systems that a single-particle energy scale of a few hundred Hertz will be needed. In an (at most weakly interacting) 2D system, we have to take the degeneracies of the single-particle energy levels into account. Therefore, we will always prepare a filled or closed shell configuration, where the cut-off energy is tuned in-between two shells. Introducing strong interactions, it can be also interesting to use interaction-induced gaps in the energy spectrum in order to prepare other atom numbers.

The preparation scheme is based on the same standing wave trap already used in chapter 3. As discussed, typical axial trap frequencies are on the order of 7 kHz. Due to the very large aspect ratio, the effective radial trap frequency is only a few tens of Hertz at most. This was the perfect geometry for the preparation of low-temperature many-body 2D systems. On the other hand, there is at least one order of magnitude missing in the lowest single-particle excitation energy in radial direction to allow for deterministic control over individual levels. Therefore, we have to increase the radial trap frequency in a controlled way. This is achieved by superimposing an additional optical tweezer potential. If the laser frequency responsible for the tweezer potential is detuned by $\mathcal{O}(100\,\mathrm{MHz})$, there is no interference between the SWT and the tweezer, and the effective trap potential is given by the sum over the two individual potentials. We cannot use the same tweezer employed already in chapter 6, as this setup was designed with axial instead of radial excitations in mind. In particular, the ratio of the harmonic oscillator length to the waist of the potential is with $a_{HO}/w_0 \approx 1.3$ for a typical radial trap frequency of 1 kHz rather large. In other words, radial excitations will be sensitive to anharmonic contributions to the trap potential such that the harmonic oscillator assumption breaks down. The obvious solution is to increase the waist of the tweezer potential. It should be noted again, that this cannot be done without limit, as the optical power required for the same trap frequency increases upon increasing the waist. In addition, the potential becomes more prone to wavefront errors. Here, we use a tweezer beam with a focal waist of around 5 µm ($a_{HO}/w_0 \approx 0.26$). Note that the aspect ratio for this tweezer is already significantly larger ($\omega_{rad}/\omega_{ax} \approx 21$). Therefore, the radial and axial trap

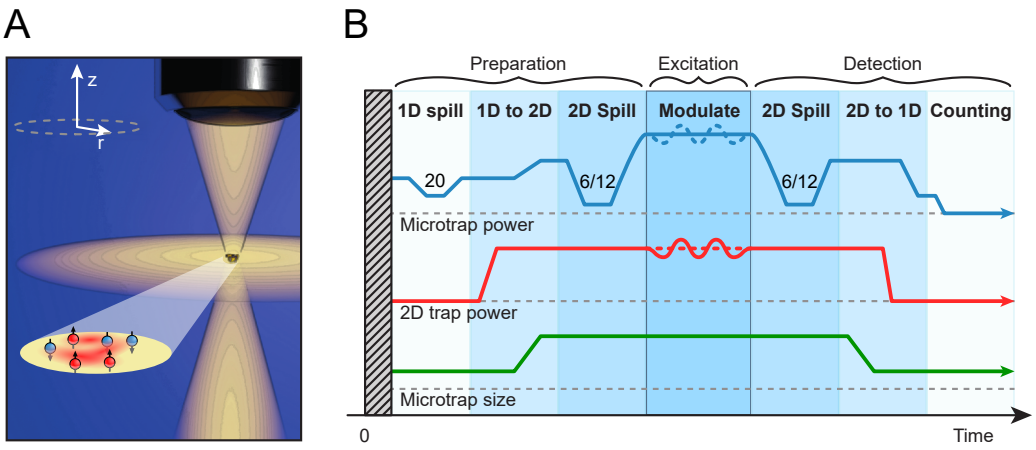

Figure 7.2.: **Preparation scheme. A:** The atoms are trapped in the hybrid trap formed by a single layer of the SWT and an additional tweezer potential. **B:** Preparation, excitation and detection scheme. First, in a quasi-1D geometry, around 20 atoms are prepared similar to before (microtrap power in blue, magnetic field gradient not shown). Then the microtrap power is ramped up in order to decrease the axial size of the wave function. Now, first the 2D trap is ramped on (SWT trap power in red) and subsequently the size of the tweezer (green) together with the power is increased in order to transfer the system from a quasi-1D to a quasi-2D geometry. Afterwards, two or three filled shells are prepared by a 2D spill. Pair (single-particle) excitations can be driven by modulating the SWT (microtrap) power. The excited particles can be removed by means of a second 2D spill. Subsequently, the atoms can be transferred back into a quasi-1D geometry and detected for example by recapturing them in a MOT. Adapted from [32].

frequencies of the combined trap can be almost independently set by the power in the tweezer and SWT, respectively. For the experiments described below, we set a typical radial trap frequency of 1 kHz, corresponding to an aspect ratio of $\omega_{ax}/\omega_{rad} \approx 7$ (see equation 2.4). As is expected, due to discretizing the radial excitations the *2D-ness* of the trap geometry decreases. Nevertheless, at least the lowest shells can still be considered to be quasi-2D, even if some excitations to higher shells are taken into account. In the setup for this set of experiments, we can tune the size of the Gaussian beam forming the tweezer potential in the Fourier plane by means of a spatial light modulator (for more details see [285]). As a consequence, we can continuously tune the size of the waist in the focus between almost the diffraction limit of around 1 µm up to the aforementioned 5 µm, significantly influencing the trap geometry. In figure 7.2, a schematic drawing of the effective trap geometry together with the preparation scheme explained below is shown.

The starting point for the preparation is a cigar-shaped potential formed by the tweezer alone, set to a waist of 1 µm with an aspect ratio of around $\omega_{rad}/\omega_{ax} = 5$. This geometry is very similar to the situation described in section 2.5.2. Therefore, the particle number can again be set by a loading and spilling procedure as described before. The only difference is that we do not spill to the ground state of one or two particles per spin state, but rather to around 20 atoms in the states $|1\rangle$ and $|3\rangle$. As a consequence, there are both radial and axial excitations present, and the spilling is not fully deterministic. Nevertheless, the final state has a very low entropy, with the lowest trap levels filled with almost unity fidelity. Afterwards, we change the effective geometry by adiabatically transferring the atoms from a geometry with $\omega_{rad}/\omega_{ax} = 5$ in the tweezer alone to the final setting in the combined trap discussed above with $\omega_{rad}/\omega_{ax} = 1/7$. To this end, first the SWT potential is ramped on. In this step it is ensured that the atoms are sufficiently compressed in axial direction, such that they are loaded into a single layer of the SWT. Subsequently, the size of the tweezer is ramped within 20 ms from 1 µm up to the final size of 5 µm with the help of the spatial light modulator. In this process, by controlling the optical power as well, the radial trap frequency is adiabatically tuned from 20 kHz to 1 kHz. The system is therefore slowly transferred from a mostly 1D geometry through a point where all the frequencies are of the same order to a mostly 2D geometry. It is important to take into account that ramping *slowly* does not guarantee adiabaticity. This is particularly true for a dimensional crossover. In a fully harmonic theory (without any other terms), there are several level crossings which are not avoided, as there is no coupling between the different fundamental excitations. Therefore, the initial state is adiabatically connected to a highly excited final state. Small anharmonicities and anisotropies couple the axes however. In the experiment, we have to engineer a situation where all avoided crossings are large enough to allow for an adiabatic dimensional transfer. We ensure this by performing the transfer additionally at a finite scattering length at a magnetic field of 750 G. The finite interaction strength increases the coupling while it is not strong enough to break the single-particle shell structure. In this way, we achieve the dimensional crossover. The state we have prepared at this point is quasi two-dimensional with a very low entropy. The lowest few shells are occupied with almost unity fidelity, while the residual entropy is reflected in fluctuations at the Fermi level. Similar to before, we can therefore try to set an energy threshold above the first, second or third shell, removing all atoms at higher energies by means of tunnelling. To this end (still at 750 G), a magnetic field gradient of 70 G/cm along the axial direction is applied. The gradient has also small contributions in the radial direction due to

the geometry of the magnetic field coils. The gradient is sufficiently strong such that all states in the SWT alone become unbound and tunnel out within a few ms. Therefore, only atoms within the trap volume of the tweezer remain bound. By setting an appropriate depth of the tweezer potential, while the gradient is on, a final atom number of two, six or twelve atoms corresponding to one, two or three filled shells can be chosen, before ramping off the gradient and ramping back the trap depth. This approach is, on a fundamental level, slightly different to the spill procedure in the 1D cigar-shaped trap. In the latter case, we have a rather deep trap with the atoms populating only the mostly harmonic potential region close to the minimum. The gradient cuts into this potential, such that only the lowest levels remain bound with the other levels shifted into the continuum. In the current situation, the total depth of the tweezer is reduced with only a few levels bound in the tweezer alone even without taking into account the gradient. Therefore, we have to rely on the fact that during the spilling the shell structure remains intact, even taking the strong anharmonicities into account. In figure 7.3, the success of this method is illustrated.
In this set of experiments, the trap depth of the tweezer is varied during the spilling, and the total atom number is recorded for each shot by recapture in the MOT as discussed in section 5.1. In the plot of the mean atom number, plateaus can be seen for approximately two, six, and twelve atoms, corresponding to a closed shell configuration. These plateaus correspond to the situation where the cut-off energy is tuned right in-between two shells. This interpretation and the near deterministic nature of the scheme are confirmed when studying the fluctuation of the atom number as a function of the trap depth. The standard deviation is minimized exactly when a closed shell configuration is prepared, while maximized when tuning the cut-off right to the energy of one of the shells. By carefully optimizing all the parameters of the preparation scheme, we achieve fidelities of $97 \pm 2\,\%$, $93 \pm 3\,\%$, and $76 \pm 2\,\%$ for two, six and twelve particles, respectively. This near deterministically prepared system is the ideal starting point for studying mesoscopic strongly interacting (quasi-) 2D systems. It therefore constitutes a further milestone outlined in section 4. Left to show is now, that this system indeed already features precursors of many-body physics. This is what I will discuss in the following section.

7.1.2. Measurement of a Higgs mode precursor

In this section, I will present experimental results on a collective mode in a system of six particles in a closed shell configuration. I will illustrate that this mode can

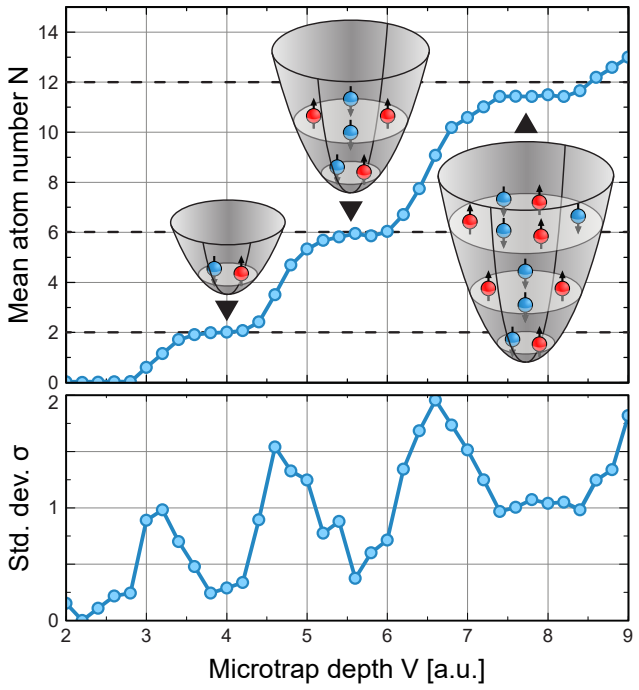

Figure 7.3.: **Deterministic preparation of closed shell configurations.** Measured mean atom number (upper panel) and the standard deviation of the recorded number (lower panel) as a function of the trap depth of the microtrap in arbitrary units. In the mean atom number, plateaus corresponding to closed shell configurations of two, six and twelve atoms are observed. These plateaus coincide with a local minimum in the atom number fluctuation, indicating the near-deterministic preparation. Adapted from [32].

be interpreted as the precursor of a Higgs mode, that is an amplitude oscillation of the order parameter. Afterwards, in the following section I will also discuss the emergence of the many-body aspect by also showing results on twelve-particle systems.

This experimental campaign is motivated by the theory proposal [286] to study the fate of the order parameter in small atomic Fermi systems. It is suggested that already in a rather small system, signatures of an order parameter corresponding to a broken symmetry might be present. Furthermore, it is proposed to study the emergence of a collective mode, corresponding to vibrations around the broken symmetry value of the order parameter, known as a Higgs mode [287, 288]. A Higgs mode has been observed in the many-body limit in cold atom experiments, but also in superconducting and ferromagnetic systems [22, 137–143]. Studying the emergence of the mode in our mesoscopic system with full single-particle control will constitute important progress in relating microscopic correlations to macroscopic (or thermodynamic) behaviour. Based on intuition (and the results

from [286]), we can expect that the collective mode will consist mostly of pair excitations of a time-reversed pair, that is two particles with opposite spin and momentum. To this end, compare this again to a BCS system, where the corresponding mode (in simplified terms) would correspond to lifting Cooper pairs across the Fermi surface. In the following section, I will therefore first introduce how we can couple to the pair excitation mode and afterwards present and interpret the results of the precursor of a Higgs mode in a mesoscopic system.

The most common method to excite specific modes in an energy-selective way is based on trap frequency modulation. For a non-interacting system of atoms in a harmonic trap, it is straightforward to show[4] that modulating the trap frequency at twice the harmonic oscillator frequency resonantly couples all equal parity states with $\Delta E = 2\hbar\omega_{HO}$. Therefore, in this scheme a single particle is excited two shells up. This is a very valuable method as it is easy to implement by modulating the optical power of the tweezer, which directly translates to a modulation of the radial trap frequency alone. In fact, similar methods were used throughout this thesis, whenever the trap frequency of an optical dipole trap had to be determined. Here, we are however interested in pair excitations, that is exciting two (time-reversed) particles one shell up. Without interactions, due to the parity of the wave functions and the drive, this excitation scheme does not allow for such pair excitations. This changes when interactions are introduced. Nevertheless, at least for weaker interactions the transition matrix element remains small. For this reason, we will use a different excitation scheme. It is intuitively clear (and explicitly calculated in [286]) that directly modulating the two-body binding energy strongly couples to pair excitations. The binding energy depends on the 3D scattering a, which in turn can be modulated by varying the magnetic offset field. Due to the large inductivity of the magnetic field coils implemented in the experiment, the bandwidth of this modulation method is rather small, however. Modulating the magnetic field with frequencies above around 1 kHz is therefore challenging. Here, we will use a different scheme. The binding energy is a function of the 2D scattering length, which in turn is renormalized by the trap frequency in axial direction. Therefore, by modulating the axial trap frequency, the (confinement-induced) 2D binding energy is modulated as well. It is important to ensure at all time that this modulation is off-resonant to axial excitations in order to avoid heating.[5] We choose to modulate the binding energy by around 2 % with a modulation time of 400 ms such that we are not

[4] Based on time-dependent pertubation theory, that is by calculating the transition matrix element.

[5] Note that this is equivalent to requiring $E_B < \hbar\omega_{ax}$ and therefore restricts us to the quasi-2D regime we are anyway interested in.

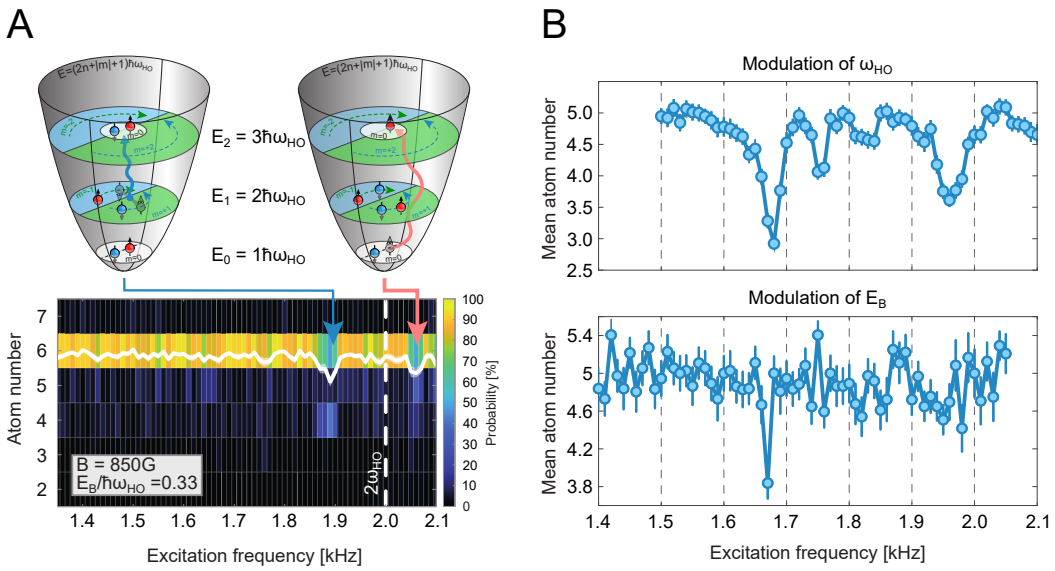

Figure 7.4.: **Measurement scheme. A:** Atom number distribution as a function of the frequency of the binding energy modulation. In the colour scale, the measured probability of different numbers of atoms remaining in the lowest two shells after the modulation sequence is shown. The mean atom number (white line) with the corresponding standard error (grey shaded area) is shown as well. There are two peaks visible. The lower peak below $2\hbar\omega_{HO}$ with mostly 4 atoms remaining corresponds to the excitation of time-reversed pairs as sketched in the upper panel. The peak above $2\hbar\omega_{HO}$ corresponds to single-particle excitations (also sketched above). **B:** Different excitation schemes at $E_B < \hbar\omega_{HO}$. Due to the finite interaction strength, both modulating the trap frequency (upper panel), and modulating the dimer binding energy (lower panel) couple to single-particle as well as pair excitations. The overlap with the pair excitation mode is however significantly larger in the latter case. The modulation strength in this figure is chosen such that the lower pair-breaking peak has a similar amplitude. Adapted from [32].

Fourier-limited. Excitation spectra are obtained by counting, as a function of the modulation frequency, the atoms which are not excited to higher shells. To this end, after the modulation step, an additional spilling stage is implemented (see figure 7.2). It is performed with identical parameters to the initial preparation stage, such that only particles remaining in the initially filled shells are kept. In figure 7.4, the two excitation methods are compared. In addition, a full excitation spectrum obtained by the latter method for a moderate interaction strength is shown.

Presented is the mean recorded atom number as a function of the modulation frequency, with the trap frequency set to $\omega_{rad} = 2\pi \cdot 1.001\,\mathrm{kHz}$. In addition, also the full number distribution is shown. There are two resonances visible. The upper

resonance at 2.06 kHz corresponds to a single-particle excitation by lifting one particle two shells up in energy. This is reflected in the atom number distribution where mostly a single atom is lost. The full atom number distribution is consistent with the assumption of an independent single-particle loss as given for example by Fermi's golden rule. With respect to the bare transition frequency $2\omega_{rad}$, the resonance is shifted up in frequency. This is explained by the attractive mean field interactions. In other words, the initial state lowers its interaction energy based on an increased wave function overlap (note the finite molecular binding energy). In the many-body language, this could be interpreted as an attractive mean field shift which could be taken into account by an effective *stiffening* of the trap. This excitation branch in theory should be three times degenerate ($(n = 0, m = 0) \rightarrow (n = 1, m = 0)$ and $(n = 0, m = \pm 1) \rightarrow (n = 1, m = \pm 1)$). In the experiment, this degeneracy is lifted by the anharmonicity and anisotropy of the trap (in addition also allowing transitions where m is changed), such that in figure 7.4 only the single transition from the lowest shell is visible.
In the spectrum, also a second resonance below the bare transition frequency can be seen. Importantly, this mode mostly consists of two-particle excitations as revealed by the atom number statistics. Therefore, we identify this resonance as the pair excitation mode, where two time-reversed atoms are lifted up in energy by one shell. Crucially, the excitation energy of this mode is reduced in energy compared to single-particle (bare) transitions. This can be intuitively understood by realizing that we transfer two particles from an filled into an initially empty shell. Therefore, there are more unoccupied states available in the final state, such that the system minimizes its energy by increasing the wave function overlap. Rephrased - again more in a many-body language - we lift a time-reversed pair of particles across the Fermi surface where the excited atoms use the available density of states, which is not Pauli-blocked, to reconfigure in an energetically more favourable way.
The next step is to vary the interaction strength and trace the modes identified above through different scattering regimes. In section 3.1, the interaction parameter $\ln(k_F a_{2D})$ was used in order to describe the scattering regime. This was adequate for the many-body system, with a locally defined density, varying as a function of temperature and spatial position. In this small system, where we keep the atom number and trap frequency constant between different runs, a slightly different description is favourable. We will use the two-body binding energy E_B as a measure for the interaction strength and compare it to the single-particle excitation energy $\hbar\omega_{rad}$. Note that the structure is exactly the same as in the many-body interaction parameter, which could be rewritten as the logarithm of

the ratio between the binding energy and the interparticle spacing (set by the trap frequency in addition to the particle number). In addition, this description also allows for a direct comparison to theory such as [32, 286], where the system is described by a Hamiltonian of the form

$$H = \sum_{i=1}^{N} \left(-\frac{\hbar^2}{2m} \nabla_i^2 + \frac{1}{2} m \omega_{HO}^2 r_i^2 \right) + g \sum_{k,l} \delta(r_k - r_l) \tag{7.2}$$

in terms of the spatial coordinates $r_i = (x_i, y_i)$ of particle i, with the sum k, l running over coordinates of opposite spin atoms. The interactions are included in the Hamiltonian by an attractive delta function with amplitude $g < 0$. When solving for the eigenstates of the system, the interactions have to be regularized and then renormalized, which is typically done by eliminating the coupling constant and the energy cut-off introduced in the regularization step by the binding energy as we had seen before [286]. Therefore, the eigenstates and energies obtained by exact diagonalization of equation 7.2 are also given in terms of E_B.
In the experiment, we change the binding energy with respect to the (fixed) trap frequency in a range $E_B/\hbar\omega_{rad} \in [0, 2]$. For a small interaction energy with $E_B/\hbar \ll 1$ we expect only small corrections to the single-particle shell structure (as seen in figure 7.4). This changes when $E_B \to \hbar\omega_{rad}$, as the interaction energy scale is large enough to significantly alter the shell structure. This can be interpreted as the strongly correlated regime. For $E_B/\hbar \gg 1$, the excitation structure becomes dominated by the interaction energy. In particular the ground state will at some point be formed by point-like (and three-dimensional) bosonic molecules in the motional ground state of the (two-dimensional) trap. Therefore, this regime can again be considered weakly interacting. In figure 7.5, a plot of the excitation spectrum upon varying $E_B/\hbar\omega_{rad}$ is presented.
It can be seen that by increasing the binding energy, the single-particle excitation branch is monotonously shifted up in energy. This is fully consistent with the picture of a mean field shift presented above. The pair excitation branch, on the other hand, shows a striking deviation from the naive expectation. Below $E_B/\hbar\omega_{rad} \lesssim 1$ the mode monotonously decreases in energy due to the increased pairing energy in the final state. However at around $E_B/\hbar\omega_{rad} \approx 1.2$, the excitation energy has a minimum and for larger binding energies increases again. In addition, there are two distinct pair excitation modes visible. We can attribute this splitting of the lowest mode to the anisotropy ($\approx 2\,\%$) and anharmonicity ($\omega_{1\to3}/\omega_{2\to4} \approx 1.1$) of the trap. As a consequence, we do not only drive the monopole mode $m = 0$, but also the $m = \pm 2$ mode.

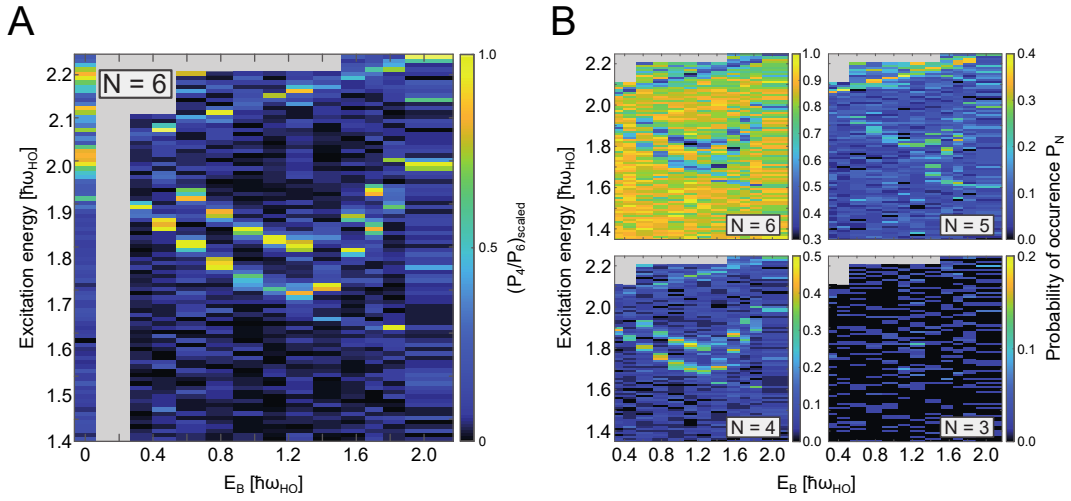

Figure 7.5.: **Excitation spectrum of the N = 6 system. A:** Probability of exciting a pair of particles (P_4) relative to the probability of retaining all particles (P_6), scaled such that for each interaction strength the maximum amplitude is unity. For reference, also the non-interacting excitation spectrum is shown, which is obtained by modulating the radial trap frequency (instead of E_B), and where the normalized excitation probability $1 - P_6$ is shown instead. The modulation strength is chosen for each interaction strength in a way to maximize the visibility of the relevant modes, and is not necessarily in the linear response regime. The two modes below $2\hbar\omega_{HO}$ are non-monotonous in E_B and show a minimum around $E_B^c \approx 1.2\hbar\omega_{HO}$, while all higher lying modes monotonously increase in energy. **B:** Probability of retaining $N = 3, 4, 5, 6$ particles ($N = 1, 2$ not shown due to the very low rate of occurrence). It can be seen that to the mode below $2\hbar\omega_{HO}$ predominantly pair excitations contribute, while the higher lying modes are driven by single-particle excitations. Adapted from [32].

Before interpreting this observed behaviour in terms of the emergence of many-body physics in the next section, it can be stated without any additional assumptions needed that the non-monotonous behaviour of the pair excitation mode signals a drastic (yet continuous) change in the nature of the ground state of the six-particle system around a specific value of $E_B/\hbar\omega_{rad}$. When the interaction energy approaches the single-particle excitation energy, admixtures of higher lying shells become relevant when writing down the interacting ground state in the non-interacting single-particle basis. Therefore, the ground state is allowed to reconfigure and minimizes its energy by forming pair correlations. The non-monotonous behaviour is therefore explained by a crossover from a Fermi sea of particles to a state with significant pairing correlations. For this reason, we will from here on refer to the position of the minimum as a 'critical' binding energy denoted by E_B^c. In [286], the amount of time-reversed pair correlations in the

ground state is calculated. The contribution of pairs is defined via

$$P = \sum_i |C_i|^2, \tag{7.3}$$

where C_i are the expansion coefficients corresponding to the time-reversed paired in the many-body basis used to diagonalize equation 7.2. In the regime experimentally studied above, P increases monotonously from zero to around 20 %. We have extended the methods used in [286] in [32] to calculate the eigenenergies of equation 7.2, such that the anharmonicity and the anisotropy of the trap is included as well, thus taking into account the Gaussian nature of the experimentally used trap beams.[6] In addition, we can weight the spectrum with the transition matrix element of the excitation scheme in order to recover only the modes excited. The matrix element from ground state $|G\rangle$ to excited state $|E\rangle$ for modulating the binding energy (to first order) is given by

$$\Gamma_{int} = \left| \langle G | \sum_{k,l} \delta(r_k - r_l) \, |E\rangle \right|^2 . \tag{7.4}$$

The resulting spectra are shown in figure 7.6.
All qualitative features, in particular the non-monotonicity of the pair excitation mode, are well recovered also in the numerical simulation. In addition, the lowest pair excitation mode is indeed identified as the monopole mode with $\Delta m = 0$. Due to the parity of the excitation scheme, we (mostly) excite modes with $\Delta m = 0, \pm 2$, such that modes with $\Delta m = \pm 1$ are neither observed in experiment nor visible in the numerical transition matrix element.

7.1.3. Approaching the many-body limit

In this section, I will discuss how the experimental results can be interpreted as the emergence of many-body physics in a mesoscopic system. As a first step in this direction, I can use that we can also prepare a system of twelve particles with three filled shells. Therefore, in figure 7.7 I present results obtained by repeating the same set of experiments with one additional shell filled and compare the resulting spectrum to the six-particle case.
First of all, it can be seen that there are already significantly more distinct single-particle excitations possible, which cannot be fully discerned any more. As a

[6] The model is regularized by a two-parameter cut-off scheme corresponding to the highest allowed single-particle energy and renormalized with respect to the molecular binding energy. The full diagonalization uses implicitly restarted Arnoldi routines for sparse matrices with a basis set of up to ten million states. See [32] and references therein.

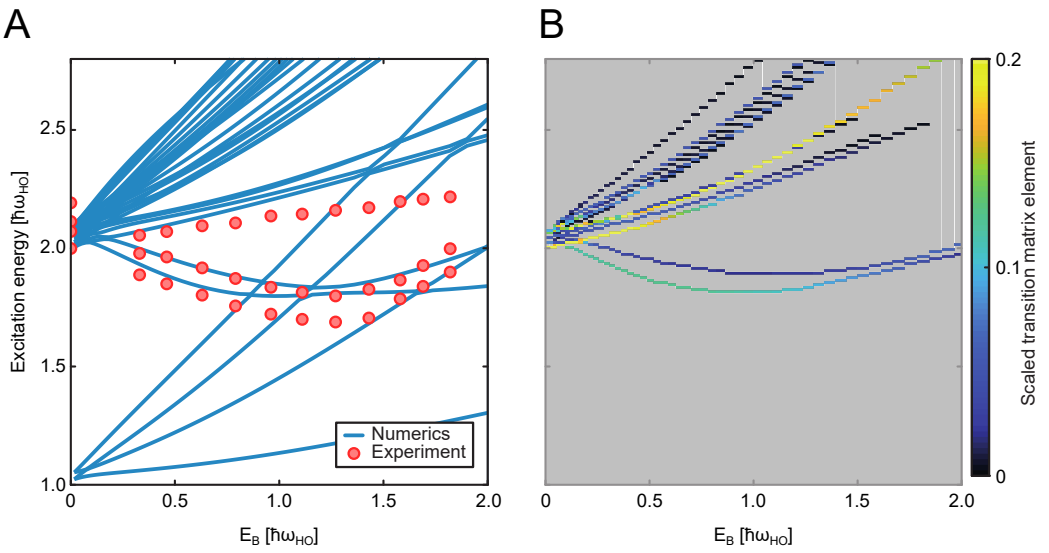

Figure 7.6.: **Numerical excitation spectrum of the N = 6 system. A:** Excitation energies calculated by exact diagonalization (blue lines) and the centre position of the experimentally measured excitation modes (red data points, obtained by a Gaussian fit to the data shown in figure 7.5). The two pair excitation modes corresponding to $\Delta m = 0$ and $\Delta m = \pm 2$, as well as the single-particle modes with $\Delta m = 0, \pm 2$ (with additional higher lying modes not studied in the experiment) are identified as well. They show an energy dependency compatible with the experimental results. In addition, single-particle modes with $\Delta m = \pm 1$ are identified, which are not observed in the experiment and weakly couple to the pair excitation modes due to the non-separability of the potential. **B:** Numerically calculated transition matrix element taking into account the excitation scheme. Consistent with the experimentally obtained spectrum, two non-monotonous pair excitation modes are recovered in addition to mean field shifted single-particle excitation modes. The modulation scheme does not (strongly) couple to the $\Delta m = \pm 1$ modes. Adapted from [32].

consequence, an effective description with a continuum of final states becomes favourable. Importantly, the energetically well-separated pair breaking mode is still present, however. By comparison to the six-particle results, we see that the minimum in the excitation energy is significantly lower, and in addition shifted to smaller interaction energies. We will interpret this as the emergence of a quantum phase transition by comparison to the many-body expectation. First of all, I have to specify how to take the many-body limit. The direct approach is to keep the trap frequency constant and increase the particle number and thus the density (while staying in the quasi-2D limit). In the thermodynamic limit, the ratio of the Fermi energy with respect to the trap frequency becomes very large, $E_F/\hbar\omega_{rad} \to \infty$, such that the finite single-particle energy spacings become negli-

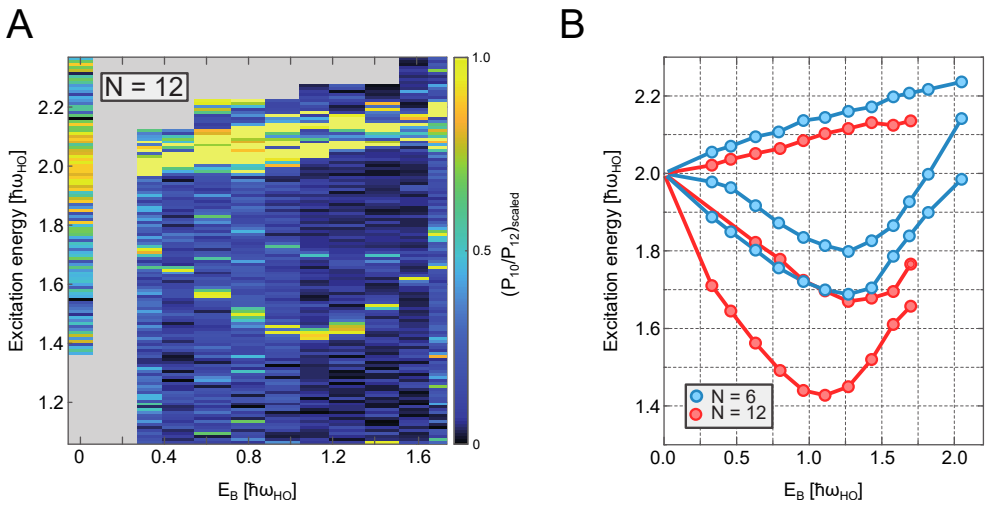

Figure 7.7.: **Excitation spectrum of the $N = 12$ system. A:** Probability of exciting a pair of particles (P_{10}) relative to the probability of retaining all particles (P_{12}), scaled such that for each interaction strength the maximum amplitude is unity. For reference, as before, the non-interacting excitation spectrum is given, where the normalized excitation probability $1 - P_{12}$ is shown instead. As for the six-particle system, two modes below $2\hbar\omega_{HO}$ which are non-monotonous in E_B are observed, while all higher lying modes monotonously increase in energy. We observe a weaker coupling to the $\Delta m = \pm 2$ mode compared to before. **B:** Comparison of the pair and lowest single-particle excitation modes of the six- with the twelve-particle system. The energy of the mode is determined by the peak position of a Gaussian fit to each experimentally identified mode. Upon increasing the particle number, the minimum of the pair excitation mode is shifted to smaller energies and weaker interactions. Adapted from [32].

gible. This is the situation encountered in section 3.1. Therefore, as also seen in a homogeneous BCS, already arbitrarily small attractive interactions lead (at T=0) to a superfluid state where the ground state features time-reversed (Cooper) pair correlations. We can see first indications of approaching this many-body limit based on the fact that the critical binding energy, where the pairing correlations are strong enough to allow for a back-bending of the corresponding mode, decreases upon increasing the particle number. This trend is numerically confirmed also for larger atom numbers [286].

If we want to retain the shell structure of the system, on the other hand, we have to rescale all energies by the critical binding energy E_B^c. In the above measurement, this would correspond to rescaling the x-axis such that the back-bending points coincide. It has been studied [286, 289–292] that a closed shell system in the thermodynamic limit features a quantum phase transition (at T=0) from a normal fluid to a superfluid upon increasing the interaction energy, enabled

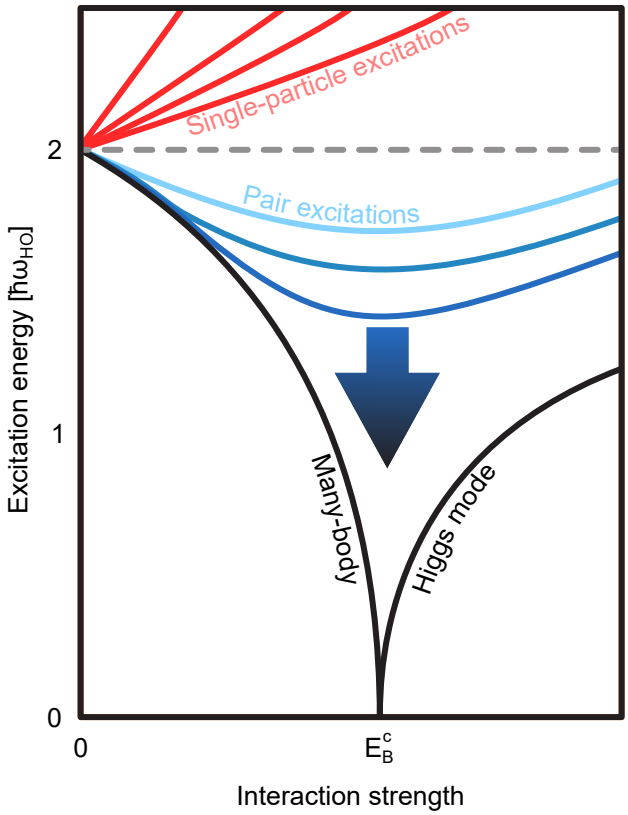

Figure 7.8.: **Many-body limit.** Schematic illustration of the Higgs mode emerging when approaching the many-body limit. Upon increasing the particle number, while at the same time rescaling the interaction strength to the minimum of the pair excitation mode E_B^c (blue and black lines, darker colour indicating larger atom number), the mode softens. Only in the thermodynamic limit, the minimum of the mode reaches zero energy, such that it signals the opening of a many-body gap at the critical interaction strength E_B^c for the normal to superfluid transition. In this limit, the mode is referred to as a Higgs mode.

by the competition between single-particle excitation energy and the interaction energy scale. Above a critical interaction strength E_B^c in a symmetry-breaking process (see section 2.3.3 and in particular equation 2.54), a many-body gap Δ opens up. As a consequence, the ground state changes nature by forming coherent pair correlations with a fixed (and spontaneously chosen) phase. On general grounds, it can be stated [134], that such a quantum phase transition gives rise to collective modes, with one of these modes softening (that is the excitation energy becoming zero) at the critical point.[7] In the case discussed here, and sketched in figure 7.8, this mode corresponds to vibrations in the amplitude of the order

[7] Not only the fact that the mode is going soft is generic, but also the asymptotic way the excitation energy approaches zero [134, 198–201, 291]. Neglecting deviations from the particle hole symmetry [286], the energy of the mode is given by $2|\Delta|$.

parameter. In other words it consists of coherent time-reversed pair excitations across the gap. This mode is usually referred to as the Higgs mode.
The fact that the energy of the Higgs mode becomes zero at the critical interaction strength can be intuitively understood. Below E_B^c, as in our mesoscopic system, the pairs have to be lifted across the single-particle excitation energy. Pairing correlations in the final state lead to a monotonously decreasing energy. This mode corresponds to vibrations around the normal phase expectation value of $\Delta = 0$. At the critical interaction strength, the Fermi surface becomes unstable towards pair formation, and pairing correlations can form without any energy cost associated to it (phrased differently, the spatial correlations, and the coherence time of spontaneously formed pairs diverge). Above the critical interaction strength, the pairs have to be lifted across the many-body gap $|\Delta| > 0$ to be broken up, such that the energy of the Higgs mode increases, again as in our mesoscopic system.
Based on our measurements, the above considerations, and the sketch in figure 7.8, we can interpret the observed pair excitation mode as the precursor of a Higgs mode signalling the emergence of a quantum phase transition from a normal to a superfluid in a mesoscopic system:

- We observe a non-monotonous mode of predominantly pair excitations with a minimum at a 'critical' binding energy E_B^c reminiscent of a Higgs mode.
  - The few-body aspect of this mode is reflected in the fact that the minimum excitation energy remains finite and that the asymptotic behaviour of the excitation energy in the vicinity of the critical binding energy is not yet recovered.
  - A trend of the critical binding energy reducing, and the mode softening further upon increasing the particle number, is observed in the experiment consistent with numerical modelling.

- The nature of the ground state changes character in terms of its pair correlations when crossing the critical binding energy. Below E_B^c, pairing correlations in the final state lead to a mode which is decreasing in energy. At around E_B^c, the interaction strength is strong enough to allow for pairing correlations (by admixtures of higher shells) in the initial state. Therefore, the initial state develops increasing pairing correlations, leading to an increase in the mode energy.
  - The few-body aspect is reflected in the fact that the discrete phase transition at E_B^c has to be replaced by a continuous crossover.

7.1.4. Concluding remarks

There are a few interesting additional considerations to be made:
I have discussed above that the Higgs mode constitutes coherent oscillations on the magnitude of the order parameter. While a Higgs mode has already been observed in a many-body scenario [22, 137–143], the mode is usually not long lived (i.e. coherent), due to the decay into continuum modes [291] (if not stabilized by additional symmetries, in particular particle hole symmetry, see also section 2.3.3). In the experiments presented above, we are working with discrete available energy levels. Therefore, it is indeed possible to coherently drive the Higgs mode. This is illustrated in figure 7.9.
Up to now I have only discussed the Higgs mode, that is oscillations in the amplitude of the order parameter. Equally important and interesting are however also oscillations in its phase, as given by the Goldstone mode. In our system, it was not possible to identify a precursors of a Goldstone mode. This is due to the fact that in order to have oscillations on top of it, the phase has to be defined on length scales much smaller than the system size [292]. In other words, the (superfluid) gap has to be much larger than the single-particle energy spacing. This regime is not (yet) accessible in the experiment.
Finally, I would like to relate the regime studied in this chapter back to the macroscopic BEC-BCS crossover. By introducing the single-particle excitation energy, we have shifted the critical binding energy for condensation from zero to a finite energy. As a consequence, we cannot tune across the superfluid BEC-BCS crossover by changing the binding energy (or experimentally the magnetic offset field) without limits. Therefore, it is instructive to ask which regime we actually accessed with our six and twelve-particle systems. In the continuous case, we have compared the two-body binding energy to the the typical interparticle spacing (as quantified by $\ln(k_F a_{2D})$) in order to estimate the regime. Here, we should instead compare the magnitude of the gap to the single-particle excitation energy. In the limit $|\Delta| \ll \hbar\omega_{rad}$, the pairing is predominantly intrashell [291]. This is analogous to a BCS limit, where we have pairing at around the Fermi surface. In our mesoscopic system, this translates to the condition that $E_B^c \ll \hbar\omega_{rad}$, as only in this limit also the minimum of the Higgs-precursor excitation energy is significantly smaller than (twice) the single-particle shell spacing. To this end, note that in the many-body limit, the asymptotic excitation energy (assuming particle hole symmetry) is given by $2|\Delta|$. On the other hand, we can always enter the BEC regime by tuning the two-body binding energy larger than all other energy scales such that intershell pairing becomes predominant. These considerations

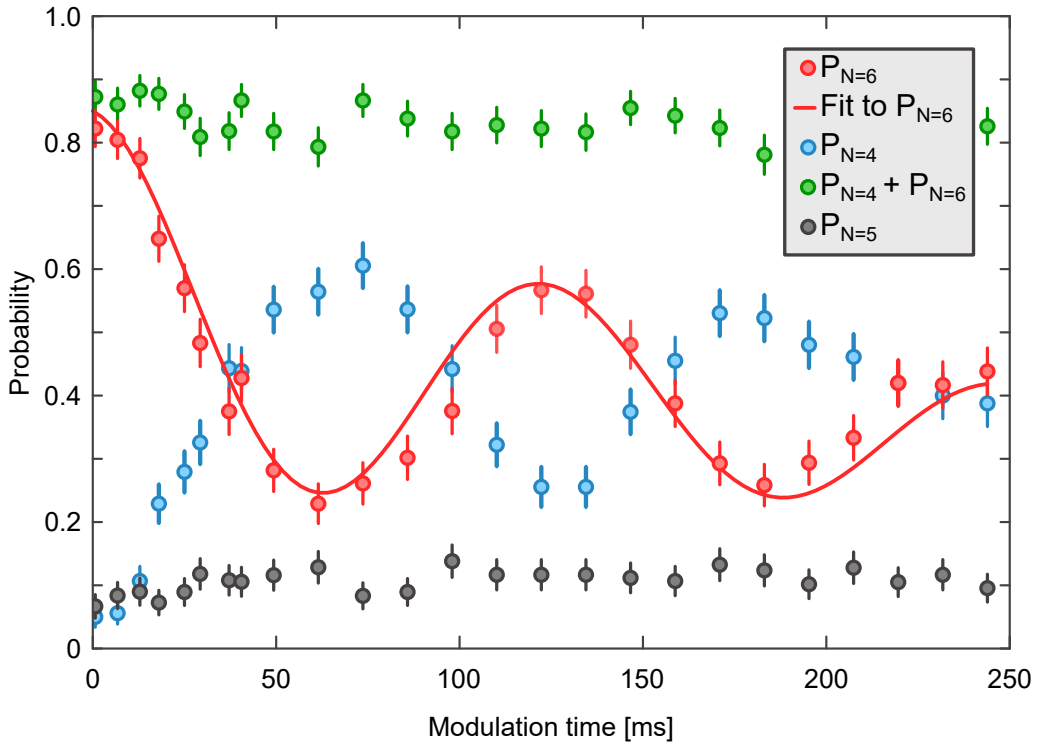

Figure 7.9.: **Coherent excitation of the Higgs mode.** We set the modulation frequency to the centre position of the lowest pair excitation mode for $E_B = 0.57\hbar\omega_{HO}$ in the six-particle system. We record the probability of different atom numbers retained in the lowest two shells as a function of the modulation time. Shown is the mean value and the standard error of the mean based on around 180 measurements per data point. The $P_{N=4}$ (blue data points), and $P_{N=6}$ (red data points) probabilities coherently oscillate out of phase, with the combined probability (green data points) remaining almost constant. All other probabilities are small and constant (shown is $P_{N=5}$, grey data points). Together, this indicates that the mode can be described as a coherently driven two-level system. Therefore, the $P_{N=6}$ contribution is consistent with an exponentially damped (due to dephasing) Rabi oscillation. Based on a fit to $P_{N=6}$ (red line), we extract a Rabi rate of 8.0 ± 0.1 Hz, with a $1/e$ decay rate of 4.5 ± 0.5 Hz. Adapted from [32].

are in line with my previous, naive, interpretation of $E_B \approx \hbar\omega_{rad}$ as the crossover regime. As a consequence, in the mesoscopic system of six or twelve particles, the system becomes 'superfluid' right in the crossover regime between BCS (that is intrashell) and BEC (that is intershell) pairing.

This result closes the circle to the very first results shown in chapter 3 on a macroscopic system showing intricate pairing correlations in the crossover regime. Due to the progress presented in this chapter, we now have also a mesoscopic system in a similar regime at hand. The crucial advantage we have gained in the process

is that we now have a full toolbox at our disposal to measure and classify the correlations present. In particular, all ingredients are there to study single-particle resolved correlation measurements in real and/or momentum space. This will be a very exciting next step on the quest outlined in this thesis.

8. Conclusion and outlook

The results presented in this thesis open up new ways to study correlations influenced by interactions and indistinguishability. I have presented a toolbox capable of measuring correlations in position and momentum space independent of any specific trapping potential. This approach can possibly be combined with more complicated matterwave manipulations to access further observables. Together with the capabilities of preparing low entropy or even deterministic systems from very small *toy-models* to full scale, extremely complicated, many-body systems, I have presented several different but related studies on strong correlations and entanglement. Nevertheless, all these results rather mark the beginning than the end of studying correlations in microscopic, mesoscopic and ultimately also macroscopic systems. Therefore, before concluding this thesis, I would like to point out a few specific possible next steps.

8.1. Single-particle resolved correlation measurements in mesoscopic systems

Based on the discussions in this thesis, the immediate next steps to take can be readily formulated: With the deterministically prepared mesoscopic 2D systems, an exciting prospect is to study momentum correlations within this setting. Numerical calculations based on the exact diagonalization assure us that signatures of pairing at a finite momentum can be observed when crossing the 'phase transition' identified in the previous section [286]. It is important to point out that the techniques established in this thesis are directly and fully applicable to measuring correlations also in theses systems, as preliminary measurements have confirmed. Therefore, this will be next major step.
In addition, the capabilities of preparing deterministic 2D systems can be explored further. First of all, further increasing the particle number is a major goal. There are indications that the deterministic initialization of systems with one or two additional shells is within reach. Furthermore, the level structure of partially filled shells can be explored in order to study the emergence of sub-shells

due to interactions similar to a Hund's rule in atomic or nuclear physics [283]. Finally, spin-imbalanced systems are of particular interest, where either minimum instances of polaronic models could be probed, or the intricate phenomena of pairing at finite centre of mass momentum studied [293].

8.1.1. Real space pairing correlations

It is important to ask whether it is already possible to directly apply the imaging and correlation measurement scheme to even larger systems. Therefore, in a preliminary study, we have prepared a system of around 60 particles per spin state in the single layer of a very shallow 2D trap with a radial trap frequency of around $\omega_{rad} = 2\pi \cdot 13.5\,\mathrm{Hz}$ (with the axial trap frequency of around $\omega_{ax} = 2\pi \cdot 650\,\mathrm{Hz}$). For these settings, we have a typical radial cloud size of around $2\sigma_{rad} = 35\,\mu\mathrm{m}$ and a typical interparticle distance in the centre of the cloud of around $6\,\mu\mathrm{m}$ (compared to a typical value of $1\,\mu\mathrm{m}$ in other experiments on 2D quantum systems). Due to the very small energy scale of the confinement, deterministic control is not possible in this regime. Nevertheless, the prepared states are at a rather low temperature of around $T/T_F \approx 0.2$. This system can serve as a first test to study in-situ correlations. Based on several hundred individual realizations per setting, we study the second order density correlation function $g_2(r_\uparrow, r_\downarrow)$ as presented in figure 8.1.

Indeed, in the correlation map in the bosonic and the crossover regime, a single peak is visible in the correlation function between different spin components. It is centred around zero relative distance. This correlation peak directly indicates pairing between spin up and spin down atoms, consistent with the simulations presented in section 5.4.5. In particular, based on the weight of the peak, we can make statements about the paired fraction at different magnetic fields, as illustrated in figure 8.2. Less obvious is the interpretation of the shape of the pairing peak. In fact, we have observed that the spatial extent of the correlation peak is not significantly larger than the size obtained when correlating two particles confined in a tight microtrap, and thus our effective resolution. In the crossover regime, we expect the typical size of the pairs to be on the order of the interparticle spacing. This is similar in scale to the resolution of the imaging scheme, even though in this measurement campaign the imaging was adapted such that significantly fewer photons are scattered per atom (with an exposure time of $5\,\mu\mathrm{s}$ to $10\,\mu\mathrm{s}$). Furthermore, also the system size is not fully separated from the scale set by the pairing correlations. First of all, this means that we average over significantly different densities, even when we study the correlations

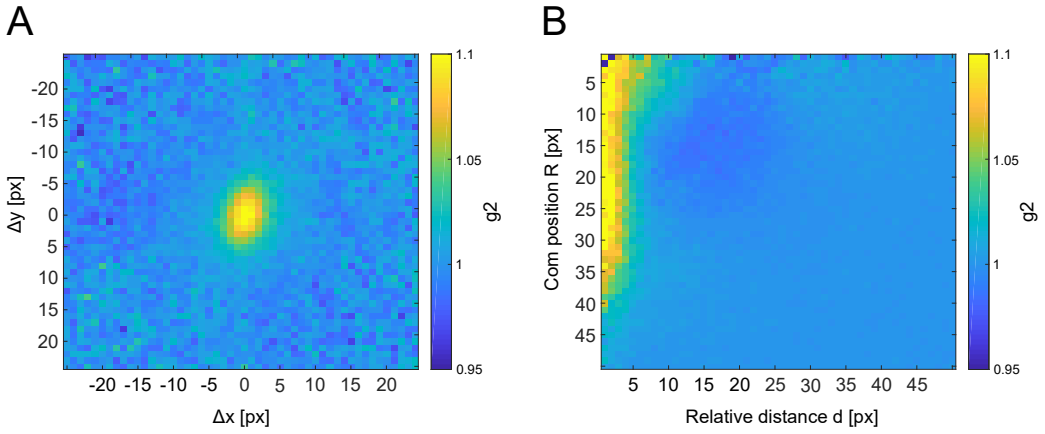

Figure 8.1.: **In-situ correlations in a mesoscopic quantum system.** Normalized second order density correlation function $g_2(r_\uparrow, r_\downarrow)$, for a system of 60 particles per spin state and a central interaction parameter of $\ln(k_F a_{2D}) = -1.3$. The full correlation function is four-dimensional. **A:** Map of $g_2(d_{\uparrow\downarrow})$ in the relative coordinates $d_{\uparrow\downarrow} = r_\uparrow - r_\downarrow$ (see equation 6.9) with the centre of mass integrated out. A single strong peak on top of an uncorrelated background is seen, indicating pairing between the different spin components. This is the most intuitive representation of the correlation function, however the radial symmetry of the trap is not used, and in addition the correlation function is averaged over different density regimes **B:** The same correlation function as a function of the centre of mass position R relative to the centre of the cloud and the relative coordinate d. In this representation, the radial symmetry of the potential is used and different density regimes can be discerned based on the centre of mass coordinate. This is the most useful representation for studying in-situ density-dependent pairing. In this plot, spurious correlations due to the finite size of the cloud (see also [183]) become most visible, for example by anti-correlations on the scale of the cloud size (darker blue region).

in the relative coordinate only for a fixed value of the centre of mass position. In addition, correlations on the scale of the cloud (caused for example by technical fluctuations in the cloud size or atom number between different realisations), can mask the correlations due to pairing. Finally, any direct indications of pairing at the Fermi surface, which would manifest itself as oscillations in the pairing correlations on the scale of the Fermi wave vector, are well below our resolution limit.

While in this preliminary study it was not possible to study the nature of the pairing mechanism in detail, this is nevertheless a promising path for future studies. In particular, shifting the measurements to momentum space can be quite beneficial, as the relevant scale of the correlation feature is shifted to larger distances given by the scale of the Fermi momentum. While in a mesoscopic system,

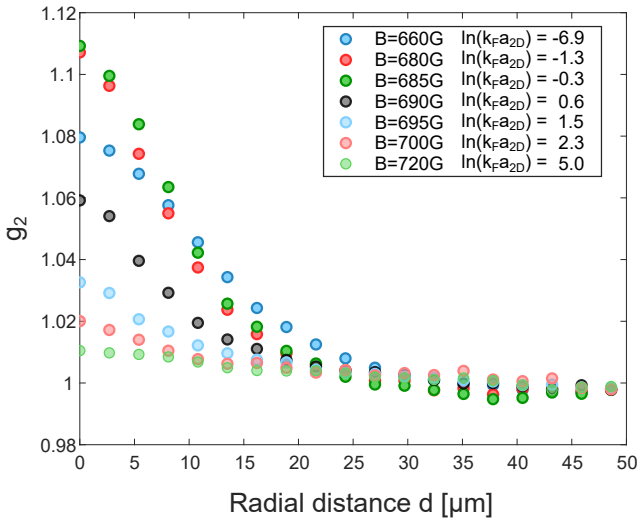

Figure 8.2.: **In-situ correlations across the BEC-BCS crossover.** Radial average of $g_2(d)$ as a function of the radial (relative) distance d. The data points in different colours result from samples prepared at different magnetic offset fields and thus different interaction parameters. The number of particles and the temperature were kept mostly constant. Note however that the cloud size changes as a function of the interaction strength. The interaction parameter $\ln(k_F a_{2D})$ is calculated based on the central density. The weight in the pairing peak is strongly dependent on the magnetic offset field, while the shape is dominated by the imaging point spread function. The integrated weight of the peak is proportional to the paired fraction and the peak height far on the BEC side is consistent with a fully paired system.

by definition, it will never by possible to separate all involved scales (resolution, correlation feature, system size), implementing the improvements presented in section 5.4 indeed holds the promise to be sufficient to enable detailed correlation measurements on pairing in similar systems of around 100 particles per spin state. This approach is very well suited to complement the correlation measurements on deterministically prepared systems outlined above. It will constitute the very exciting step of bridging the gap between deterministic mesoscopic and thermal macroscopic quantum systems.

8.2. Concluding remarks

To conclude, I would like to briefly recapitulate the main results of this thesis. Based on very intriguing measurements of high temperature pairing in the crossover regime of a 2D BEC-BCS crossover, I formulated an agenda with the goal to study microscopic correlations in such a system. The agenda consisted of

the following six milestones:

- **MILESTONE 1:** Develop an imaging scheme suited for correlation measurements.
- **MILESTONE 2:** Identify the most basic systems which feature prototypical correlations or pose typical challenges of interpreting the results.
- **MILESTONE 3:** Develop a toolbox for correlation functions and benchmark the measurement scheme.
- **MILESTONE 4:** Scale up the system size to the mesoscopic regime.
- **MILESTONE 5:** Characterize a mesoscopic system which features first signatures of many-body effects.
- **MILESTONE 6:** Characterize an unknown strongly correlated many-body state based on suitable correlation measurements.

Along these lines, I have presented a versatile imaging scheme. It proved suitable for the many challenges involved in measuring correlation functions in two-component Fermi gases, thus achieving the first milestone. Afterwards, I discussed correlation measurements in few-body systems. Indeed, it was possible to identify systems which are prototypical of certain phenomena and posed challenges in interpreting them. In particular, when both indistinguishability and the notion of entanglement were involved, even these small systems offered fundamentally new insights. Therefore, it was crucial to include the second and third milestone, which were achieved this way, in this agenda. Afterwards, I identified a small 2D system with a single-particle shell structure as the ideal intermediate step towards scaling up the system size. I presented measurements on a collective excitation indicating first signatures of many-body behaviour in this system. There is still great prospect in further work towards the fourth and fifth milestone, for example by performing momentum density correlations and investigating thermal systems. Finally, I have discussed in this outlook that there is still some work to be done until the final milestone can be ticked of the list. Importantly however, by combining all the results in this thesis, this ultimate goal, which initially seemed completely out of reach, is now tamed to be a number of challenging, yet realistic, additional steps. Only by tackling all these intermediate, but by themself already major, milestones, I have explored many intricate phenomena of quantum mechanics, where correlations lead to surprising collective and entangled behaviour of very exotic and highly *non-classical* states of matter!

Bibliography

[1] M. H. Anderson, J. R. Ensher, M. R. Matthews, C. E. Wieman, and E. A. Cornell. Observation of Bose-Einstein Condensation in a Dilute Atomic Vapor. *Science* **269**.5221 (1995), pp. 198–201.

[2] K. B. Davis, M. O. Mewes, M. R. Andrews, N. J. van Druten, D. S. Durfee, D. M. Kurn, and W. Ketterle. Bose-Einstein Condensation in a Gas of Sodium Atoms. *Physical Review Letters* **75**.22 (1995), pp. 3969–3973.

[3] J. J. Sakurai and J. Napolitano. *Modern Quantum Mechanics*. 3. Edition. Cambridge University Press, 2020.

[4] J. Bardeen, L. N. Cooper, and J. R. Schrieffer. Microscopic Theory of Superconductivity. *Physical Review* **106**.1 (1957), pp. 162–164.

[5] L. N. Cooper. Bound Electron Pairs in a Degenerate Fermi Gas. *Physical Review* **104**.4 (1956), pp. 1189–1190.

[6] *DFG Sonderforschungsbereich 1225: Isolierte Quantensysteme und Universalität unter extremen Bedingungen (ISOQUANT)*. URL: https://www.isoquant-heidelberg.de/.

[7] J. G. Bednorz and K. A. Müller. Possible high Tc superconductivity in the Ba-La-Cu-O system. *Zeitschrift für Physik B Condensed Matter* **64**.2 (1986), pp. 189–193.

[8] B. Mueller. *The Physics of the Quark-Gluon Plasma*. Springer Berlin Heidelberg, 1985.

[9] D Rischke. The quark–gluon plasma in equilibrium. *Progress in Particle and Nuclear Physics* **52**.1 (2004), pp. 197–296.

[10] P. Koch, B. Müller, and J. Rafelski. From strangeness enhancement to quark–gluon plasma discovery. *International Journal of Modern Physics A* **32**.31 (2017), 1730024.

[11] W. Ketterle and M. W. Zwierlein. Making, probing and understanding ultracold Fermi gases. *La Rivista del Nuovo Cimento* **31** (2008), pp. 247–422.

[12] I. Georgescu, S. Ashhab, and F. Nori. Quantum simulation. *Reviews of Modern Physics* **86**.1 (2014), pp. 153–185.

[13] I. Bloch, J. Dalibard, and W. Zwerger. Many-body physics with ultracold gases. *Reviews of Modern Physics* **80**.3 (2008), pp. 885–964.

[14] I. Bloch, J. Dalibard, and S. Nascimbène. Quantum simulations with ultracold quantum gases. *Nature Physics* **8**.4 (2012), pp. 267–276.

[15] M. G. Ries, A. N. Wenz, G. Zürn, L. Bayha, I. Boettcher, D. Kedar, P. A. Murthy, M. Neidig, T. Lompe, and S. Jochim. Observation of Pair Condensation in the Quasi-2D BEC-BCS Crossover. *Physical Review Letters* **114**.23 (2015), 230401.

[16] P. Murthy, I. Boettcher, L. Bayha, M. Holzmann, D. Kedar, M. Neidig, M. Ries, A. Wenz, G. Zürn, and S. Jochim. Observation of the Berezinskii-Kosterlitz-Thouless Phase Transition in an Ultracold Fermi Gas. *Physical Review Letters* **115**.1 (2015), 010401.

[17] I. Boettcher, L. Bayha, D. Kedar, P. Murthy, M. Neidig, M. Ries, A. Wenz, G. Zürn, S. Jochim, and T. Enss. Equation of State of Ultracold Fermions in the 2D BEC-BCS Crossover Region. *Physical Review Letters* **116**.4 (2016), 045303.

[18] P. A. Murthy, M. Neidig, R. Klemt, L. Bayha, I. Boettcher, T. Enss, M. Holten, G. Zürn, P. M. Preiss, and S. Jochim. High-temperature pairing in a strongly interacting two-dimensional Fermi gas. *Science* **359**.6374 (2017), pp. 452–455.

[19] M.-O. Mewes, M. R. Andrews, N. J. van Druten, D. M. Kurn, D. S. Durfee, C. G. Townsend, and W. Ketterle. Collective Excitations of a Bose-Einstein Condensate in a Magnetic Trap. *Physical Review Letters* **77**.6 (1996), pp. 988–991.

[20] D. S. Jin, J. R. Ensher, M. R. Matthews, C. E. Wieman, and E. A. Cornell. Collective Excitations of a Bose-Einstein Condensate in a Dilute Gas. *Physical Review Letters* **77**.3 (1996), pp. 420–423.

[21] L. A. Sidorenkov, M. K. Tey, R. Grimm, Y.-H. Hou, L. Pitaevskii, and S. Stringari. Second sound and the superfluid fraction in a Fermi gas with resonant interactions. *Nature* **498**.7452 (2013), pp. 78–81.

[22] A. Behrle, T. Harrison, J. Kombe, K. Gao, M. Link, J.-S. Bernier, C. Kollath, and M. Köhl. Higgs mode in a strongly interacting fermionic superfluid. *Nature Physics* **14**.8 (2018), pp. 781–785.

[23] S. Fölling, F. Gerbier, A. Widera, O. Mandel, T. Gericke, and I. Bloch. Spatial quantum noise interferometry in expanding ultracold atom clouds. *Nature* **434**.7032 (2005), pp. 481–484.

[24] P. Kunkel, M. Prüfer, H. Strobel, D. Linnemann, A. Frölian, T. Gasenzer, M. Gärttner, and M. K. Oberthaler. Spatially distributed multipartite entanglement enables EPR steering of atomic clouds. *Science* **360**.6387 (2018), pp. 413–416.

[25] M. Fadel, T. Zibold, B. Décamps, and P. Treutlein. Spatial entanglement patterns and Einstein-Podolsky-Rosen steering in Bose-Einstein condensates. *Science* **360**.6387 (2018), pp. 409–413.

[26] K. Lange, J. Peise, B. Lücke, I. Kruse, G. Vitagliano, I. Apellaniz, M. Kleinmann, G. Tóth, and C. Klempt. Entanglement between two spatially separated atomic modes. *Science* **360**.6387 (2018), pp. 416–418.

[27] E. Altman, E. Demler, and M. D. Lukin. Probing many-body states of ultracold atoms via noise correlations. *Physical Review A* **70**.1 (2004), 013603.

[28] A. Bergschneider, V. M. Klinkhamer, J. H. Becher, R. Klemt, G. Zürn, P. M. Preiss, and S. Jochim. Spin-resolved single-atom imaging of ^{6}Li in free space. *Physical Review A* **97**.6 (2018), 063613.

[29] A. Bergschneider, V. M. Klinkhamer, J. H. Becher, R. Klemt, L. Palm, G. Zürn, S. Jochim, and P. M. Preiss. Experimental characterization of two-particle entanglement through position and momentum correlations. *Nature Physics* **15**.7 (2019), pp. 640–644.

[30] P. M. Preiss, J. H. Becher, R. Klemt, V. Klinkhamer, A. Bergschneider, N. Defenu, and S. Jochim. High-Contrast Interference of Ultracold Fermions. *Physical Review Letters* **122**.14 (2019), 143602.

[31] J. Becher, E. Sindici, R. Klemt, S. Jochim, A. Daley, and P. Preiss. Measurement of Identical Particle Entanglement and the Influence of Antisymmetrization. *Physical Review Letters* **125**.18 (2020), 180402.

[32] L. Bayha, M. Holten, R. Klemt, K. Subramanian, J. Bjerlin, S. M. Reimann, G. M. Bruun, P. M. Preiss, and S. Jochim. Observing the emergence of a quantum phase transition shell by shell. *Nature* **587**.7835 (2020), pp. 583–587.

[33] Q. Guan, V. Klinkhamer, R. Klemt, J. Becher, A. Bergschneider, P. Preiss, S. Jochim, and D. Blume. Density Oscillations Induced by Individual Ultracold Two-Body Collisions. *Physical Review Letters* **122**.8 (2019), 083401.

[34] A. Altland and B. D. Simons. *Condensed matter field theory*. Cambridge university press, 2010.

[35] E. Schrödinger. Die gegenwärtige Situation in der Quantenmechanik. *Naturwissenschaften* **23**.49 (1935), pp. 823–828.

[36] A. Einstein, B. Podolsky, and N. Rosen. Can Quantum-Mechanical Description of Physical Reality Be Considered Complete? *Physical Review* **47**.10 (1935), pp. 777–780.

[37] R. Horodecki, P. Horodecki, M. Horodecki, and K. Horodecki. Quantum entanglement. *Reviews of Modern Physics* **81**.2 (2009), pp. 865–942.

[38] M. B. Plenio and S. S. Virmani. "An Introduction to Entanglement Theory". In: *Quantum Information and Coherence*. Springer International Publishing, 2014, pp. 173–209.

[39] M. A. Nielsen and I. L. Chuang. *Quantum Computation and Quantum Information*. Cambridge University Press, 2010.

[40] L. Amico, R. Fazio, A. Osterloh, and V. Vedral. Entanglement in many-body systems. *Reviews of Modern Physics* **80**.2 (2008), pp. 517–576.

[41] A. M. Kaufman, M. E. Tai, A. Lukin, M. Rispoli, R. Schittko, P. M. Preiss, and M. Greiner. Quantum thermalization through entanglement in an isolated many-body system. *Science* **353**.6301 (2016), pp. 794–800.

[42] M. Gärttner, J. G. Bohnet, A. Safavi-Naini, M. L. Wall, J. J. Bollinger, and A. M. Rey. Measuring out-of-time-order correlations and multiple quantum spectra in a trapped-ion quantum magnet. *Nature Physics* **13**.8 (2017), pp. 781–786.

[43] M. Knap. Entanglement production and information scrambling in a noisy spin system. *Physical Review B* **98**.18 (2018), 184416.

[44] M. McGinley, A. Nunnenkamp, and J. Knolle. Slow Growth of Out-of-Time-Order Correlators and Entanglement Entropy in Integrable Disordered Systems. *Physical Review Letters* **122**.2 (2019), 020603.

[45] A. Lukin, M. Rispoli, R. Schittko, M. E. Tai, A. M. Kaufman, S. Choi, V. Khemani, J. Léonard, and M. Greiner. Probing entanglement in a many-body–localized system. *Science* **364**.6437 (2019), pp. 256–260.

[46] M. Rispoli, A. Lukin, R. Schittko, S. Kim, M. E. Tai, J. Léonard, and M. Greiner. Quantum critical behaviour at the many-body localization transition. *Nature* **573**.7774 (2019), pp. 385–389.

[47] S. Popescu and D. Rohrlich. Quantum nonlocality as an axiom. *Foundations of Physics* **24**.3 (1994), pp. 379–385.

[48] J. S. Bell. On the Einstein Podolsky Rosen Paradox. *Physics Physique Fizika* **1**.3 (1964), pp. 195–200.

[49] J. F. Clauser, M. A. Horne, A. Shimony, and R. A. Holt. Proposed Experiment to Test Local Hidden-Variable Theories. *Physical Review Letters* **23**.15 (1969), pp. 880–884.

[50] A. Aspect, P. Grangier, and G. Roger. Experimental Tests of Realistic Local Theories via Bell's Theorem. *Physical Review Letters* **47**.7 (1981), pp. 460–463.

[51] B. Hensen et al. Loophole-free Bell inequality violation using electron spins separated by 1.3 kilometres. *Nature* **526**.7575 (2015), pp. 682–686.

[52] M. Giustina et al. Significant-Loophole-Free Test of Bell's Theorem with Entangled Photons. *Physical Review Letters* **115**.25 (2015), 250401.

[53] L. K. Shalm et al. Strong Loophole-Free Test of Local Realism. *Physical Review Letters* **115**.25 (2015), 250402.

[54] W. Rosenfeld, D. Burchardt, R. Garthoff, K. Redeker, N. Ortegel, M. Rau, and H. Weinfurter. Event-Ready Bell Test Using Entangled Atoms Simultaneously Closing Detection and Locality Loopholes. *Physical Review Letters* **119**.1 (2017), 010402.

[55] D. Rauch et al. Cosmic Bell Test Using Random Measurement Settings from High-Redshift Quasars. *Physical Review Letters* **121**.8 (2018), 080403.

[56] Z. Y. Ou and L. Mandel. Violation of Bell's Inequality and Classical Probability in a Two-Photon Correlation Experiment. *Physical Review Letters* **61**.1 (1988), pp. 50–53.

[57] T. A. Palomaki, J. D. Teufel, R. W. Simmonds, and K. W. Lehnert. Entangling Mechanical Motion with Microwave Fields. *Science* **342**.6159 (2013), pp. 710–713.

[58] R. A. Thomas, M. Parniak, C. Østfeldt, C. B. Møller, C. Bærentsen, Y. Tsaturyan, A. Schliesser, J. Appel, E. Zeuthen, and E. S. Polzik. Entanglement between distant macroscopic mechanical and spin systems. *Nature Physics* (2020).

[59] W. K. Wootters and W. H. Zurek. A single quantum cannot be cloned. *Nature* **299**.5886 (1982), pp. 802–803.

[60] C. H. Bennett, G. Brassard, C. Crépeau, R. Jozsa, A. Peres, and W. K. Wootters. Teleporting an unknown quantum state via dual classical and Einstein-Podolsky-Rosen channels. *Physical Review Letters* **70**.13 (1993), pp. 1895–1899.

[61] D. Bouwmeester, J.-W. Pan, K. Mattle, M. Eibl, H. Weinfurter, and A. Zeilinger. Experimental quantum teleportation. *Nature* **390**.6660 (1997), pp. 575–579.

[62] A. K. Ekert. Quantum cryptography based on Bell's theorem. *Physical Review Letters* **67**.6 (1991), pp. 661–663.

[63] S.-K. Liao et al. Satellite-to-ground quantum key distribution. *Nature* **549**.7670 (2017), pp. 43–47.

[64] C. H. Bennett and S. J. Wiesner. Communication via one- and two-particle operators on Einstein-Podolsky-Rosen states. *Physical Review Letters* **69**.20 (1992), pp. 2881–2884.

[65] K. Mattle, H. Weinfurter, P. G. Kwiat, and A. Zeilinger. Dense Coding in Experimental Quantum Communication. *Physical Review Letters* **76**.25 (1996), pp. 4656–4659.

[66] R. P. Feynman. Simulating physics with computers. *International Journal of Theoretical Physics* **21**.6-7 (1982), pp. 467–488.

[67] P. W. Shor. Scheme for reducing decoherence in quantum computer memory. *Physical Review A* **52**.4 (1995), R2493.

[68] N. Ofek et al. Extending the lifetime of a quantum bit with error correction in superconducting circuits. *Nature* **536**.7617 (2016), pp. 441–445.

[69] F. Arute et al. Quantum supremacy using a programmable superconducting processor. *Nature* **574**.7779 (2019), pp. 505–510.

[70] J. Eisert, M. Cramer, and M. B. Plenio. Colloquium: Area laws for the entanglement entropy. *Reviews of Modern Physics* **82**.1 (2010), pp. 277–306.

[71] A. Kitaev and J. Preskill. Topological Entanglement Entropy. *Physical Review Letters* **96**.11 (2006), 110404.

[72] H. Li and F. D. M. Haldane. Entanglement Spectrum as a Generalization of Entanglement Entropy: Identification of Topological Order in Non-Abelian Fractional Quantum Hall Effect States. *Physical Review Letters* **101**.1 (2008), 010504.

[73] B. Zeng, X. Chen, D.-L. Zhou, and X.-G. Wen. *Quantum Information Meets Quantum Matter*. Springer New York, 2019.

[74] P. Fromholz, G. Magnifico, V. Vitale, T. Mendes-Santos, and M. Dalmonte. Entanglement topological invariants for one-dimensional topological superconductors. *Physical Review B* **101**.8 (2020), 085136.

[75] E. S. Polzik and J. Ye. Entanglement and spin squeezing in a network of distant optical lattice clocks. *Physical Review A* **93**.2 (2016), 021404.

[76] E. Pedrozo-Peñafiel et al. Entanglement on an optical atomic-clock transition. *Nature* **588**.7838 (2020), pp. 414–418.

[77] A. Chefles, C. R. Gilson, and S. M. Barnett. Entanglement and collective quantum operations. *Physics Letters A* **273**.1-2 (2000), pp. 10–14.

[78] D. Collins, N. Linden, and S. Popescu. Nonlocal content of quantum operations. *Physical Review A* **64**.3 (2001), 032302.

[79] C. H. Bennett, G. Brassard, S. Popescu, B. Schumacher, J. A. Smolin, and W. K. Wootters. Purification of Noisy Entanglement and Faithful Teleportation via Noisy Channels. *Physical Review Letters* **76**.5 (1996), pp. 722–725.

[80] A. Miyake and H. J. Briegel. Distillation of Multipartite Entanglement by Complementary Stabilizer Measurements. *Physical Review Letters* **95**.22 (2005), 220501.

[81] L. Masanes. Useful entanglement can be extracted from all nonseparable states. *Journal of Mathematical Physics* **49**.2 (2008), 022102.

[82] C. H. Bennett, D. P. DiVincenzo, J. A. Smolin, and W. K. Wootters. Mixed-state entanglement and quantum error correction. *Physical Review A* **54**.5 (1996), pp. 3824–3851.

[83] V. Vedral, M. B. Plenio, M. A. Rippin, and P. L. Knight. Quantifying Entanglement. *Physical Review Letters* **78**.12 (1997), pp. 2275–2279.

[84] V. Vedral and M. B. Plenio. Entanglement measures and purification procedures. *Physical Review A* **57**.3 (1998), pp. 1619–1633.

[85] M. B. Plenio and V. Vedral. Teleportation, entanglement and thermodynamics in the quantum world. *Contemporary Physics* **39**.6 (1998), pp. 431–446.

[86] F. Mintert and A. Buchleitner. Observable Entanglement Measure for Mixed Quantum States. *Physical Review Letters* **98**.14 (2007), 140505.

[87] A. Z. D. M. Greenberger M.A. Horne. "Bell's Theorem, Quantum Theory and Conceptions of the Universe". In: ed. by M. Kafatos. Springer Netherlands, 1989. Chap. Going Beyond Bell's Theorem, pp. 69–72.

[88] W. Dür, G. Vidal, and J. I. Cirac. Three qubits can be entangled in two inequivalent ways. *Physical Review A* **62**.6 (2000), 062314.

[89] W. Dür and J. I. Cirac. Classification of multiqubit mixed states: Separability and distillability properties. *Physical Review A* **61**.4 (2000), 042314.

[90] C. H. Bennett, H. J. Bernstein, S. Popescu, and B. Schumacher. Concentrating partial entanglement by local operations. *Physical Review A* **53**.4 (1996), pp. 2046–2052.

[91] M. B. Plenio, S Virmani, and P Papadopoulos. Operator monotones, the reduction criterion and the relative entropy. *Journal of Physics A: Mathematical and General* **33**.22 (2000), pp. L193–L197.

[92] M. Horodecki, P. Horodecki, and R. Horodecki. Separability of mixed states: necessary and sufficient conditions. *Physics Letters A* **223**.1-2 (1996), pp. 1–8.

[93] A. Peres. Separability Criterion for Density Matrices. *Physical Review Letters* **77**.8 (1996), pp. 1413–1415.

[94] S. Hill and W. K. Wootters. Entanglement of a Pair of Quantum Bits. *Physical Review Letters* **78**.26 (1997), pp. 5022–5025.

[95] W. K. Wootters. Entanglement of Formation of an Arbitrary State of Two Qubits. *Physical Review Letters* **80**.10 (1998), pp. 2245–2248.

[96] W. K. Wootters. Entanglement of Formation and Concurrence. *Quantum Info. Comput.* **1**.1 (2001), pp. 27–44.

[97] T. Wellens and M. Kuś. Separable approximation for mixed states of composite quantum systems. *Physical Review A* **64**.5 (2001), 052302.

[98] B. M. Terhal. Bell inequalities and the separability criterion. *Physics Letters A* **271**.5-6 (2000), pp. 319–326.

[99] J. H. Becher. Characterizing Few-Fermion Systems with Momentum Correlations. PhD thesis. Heidelberg University, 2020.

[100] M. C. Tichy, F. Mintert, and A. Buchleitner. Essential entanglement for atomic and molecular physics. *Journal of Physics B: Atomic, Molecular and Optical Physics* **44**.19 (2011), 192001.

[101] G. Ghirardi, L. Marinatto, and T. Weber. Entenglement and Properties of Composite Quantum Systems: A Conceptual and Mathematical Analysis. *Journal of Statistical Physics* **108**.1/2 (2002), pp. 49–122.

[102] B. Morris, B. Yadin, M. Fadel, T. Zibold, P. Treutlein, and G. Adesso. Entanglement between Identical Particles Is a Useful and Consistent Resource. *Physical Review X* **10**.4 (2020), 041012.

[103] P. Zanardi. Quantum entanglement in fermionic lattices. *Physical Review A* **65**.4 (2002), 042101.

[104] M. R. Dowling, A. C. Doherty, and H. M. Wiseman. Entanglement of indistinguishable particles in condensed-matter physics. *Physical Review A* **73**.5 (2006), 052323.

[105] J. Schliemann, J. I. Cirac, M. Kuś, M. Lewenstein, and D. Loss. Quantum correlations in two-fermion systems. *Physical Review A* **64**.2 (2001), 022303.

[106] K. Eckert, J. Schliemann, D. Bruß, and M. Lewenstein. Quantum Correlations in Systems of Indistinguishable Particles. *Annals of Physics* **299**.1 (2002), pp. 88–127.

[107] H. M. Wiseman and J. A. Vaccaro. Entanglement of Indistinguishable Particles Shared between Two Parties. *Physical Review Letters* **91**.9 (2003), 097902.

[108] G. Ghirardi and L. Marinatto. General criterion for the entanglement of two indistinguishable particles. *Physical Review A* **70**.1 (2004), 012109.

[109] A. P. Balachandran, T. R. Govindarajan, A. R. de Queiroz, and A. F. Reyes-Lega. Entanglement and Particle Identity: A Unifying Approach. *Physical Review Letters* **110**.8 (2013), 080503.

[110] Y. Shi. Quantum entanglement of identical particles. *Physical Review A* **67**.2 (2003), 024301.

[111] Y. S. Li, B. Zeng, X. S. Liu, and G. L. Long. Entanglement in a two-identical-particle system. *Physical Review A* **64**.5 (2001), 054302.

[112] N. Killoran, M. Cramer, and M. Plenio. Extracting Entanglement from Identical Particles. *Physical Review Letters* **112**.15 (2014), 150501.

[113] S. Sciara, R. L. Franco, and G. Compagno. Universality of Schmidt decomposition and particle identity. *Scientific Reports* **7**.1 (2017).

[114] R. Islam, R. Ma, P. M. Preiss, M. E. Tai, A. Lukin, M. Rispoli, and M. Greiner. Measuring entanglement entropy in a quantum many-body system. *Nature* **528**.7580 (2015), pp. 77–83.

[115] M. Cramer, A. Bernard, N. Fabbri, L. Fallani, C. Fort, S. Rosi, F. Caruso, M. Inguscio, and M. Plenio. Spatial entanglement of bosons in optical lattices. *Nature Communications* **4**.1 (2013).

[116] H.-W. Lee and J. Kim. Quantum teleportation and Bell's inequality using single-particle entanglement. *Physical Review A* **63**.1 (2000), 012305.

[117] S. Azzini, S. Mazzucchi, V. Moretti, D. Pastorello, and L. Pavesi. Single-Particle Entanglement. *Advanced Quantum Technologies* **3**.10 (2020), 2000014.

[118] M. E. Peskin and D. V. Schroeder. *An Introduction To Quantum Field Theory*. Westview Press, 1995.

[119] S. Giorgini, L. P. Pitaevskii, and S. Stringari. Theory of ultracold atomic Fermi gases. *Reviews of Modern Physics* **80**.4 (2008), pp. 1215–1274.

[120] D. S. Petrov, C. Salomon, and G. V. Shlyapnikov. Weakly Bound Dimers of Fermionic Atoms. *Physical Review Letters* **93**.9 (2004), 090404.

[121] T. Busch, B.-G. Englert, K. Rzażewski, and M. Wilkens. *Foundations of Physics* **28**.4 (1998), pp. 549–559.

[122] M. Olshanii. Atomic Scattering in the Presence of an External Confinement and a Gas of Impenetrable Bosons. *Physical Review Letters* **81**.5 (1998), pp. 938–941.

[123] T. Bergeman, M. G. Moore, and M. Olshanii. Atom-Atom Scattering under Cylindrical Harmonic Confinement: Numerical and Analytic Studies of the Confinement Induced Resonance. *Physical Review Letters* **91**.16 (2003), 163201.

[124] Z. Idziaszek and T. Calarco. Analytical solutions for the dynamics of two trapped interacting ultracold atoms. *Physical Review A* **74**.2 (2006), 022712.

[125] Y. Chen, D.-W. Xiao, R. Zhang, and P. Zhang. Analytical solution for the spectrum of two ultracold atoms in a completely anisotropic confinement. *Physical Review A* **101**.5 (2020), 053624.

[126] J. Levinsen and M. M. Parish. "Strongly Interacting Two-Dimensional Fermi Gases". In: *Annual Review of Cold Atoms and Molecules*. World Scientific, 2015, pp. 1–75.

[127] A. V. Turlapov and M. Y. Kagan. Fermi-to-Bose crossover in a trapped quasi-2D gas of fermionic atoms. *Journal of Physics: Condensed Matter* **29**.38 (2017), 383004.

[128] N. D. Mermin and H. Wagner. Absence of Ferromagnetism or Antiferromagnetism in One- or Two-Dimensional Isotropic Heisenberg Models. *Physical Review Letters* **17**.22 (1966), pp. 1133–1136.

[129] Z. Hadzibabic and J. Dalibard. "Two-dimensional Bose fluids: An atomic physics perspective". In: *Nano Optics and Atomics: Transport of Light and Matter Waves*. Ed. by R Kaiser and D Wiersma. Enrico Fermi summer school. IOP Press, 2009.

[130] V. L. Berezinskii. Destruction of long-range order in one-dimensional and two-dimensional systems having a continuous symmetry group I. Classical systems. *Sov. Phys. JETP* **32**.3 (1971), pp. 493–500.

[131] J. M. Kosterlitz and D. J. Thouless. Ordering, metastability and phase transitions in two-dimensional systems. *Journal of Physics C: Solid State Physics* **6**.7 (1973), pp. 1181–1203.

[132] P. W. Anderson. *Basic Notions of Condensed Matter Physics*. Ed. by P. W. Anderson. CRC Press, 2018.

[133] F. Schwabl. *Statistical Mechanics*. Springer, 2006.

[134] S. Sachdev. *Quantum Phase Transitions*. Cambridge University Press, 2009.

[135] L. Landau. The Theory of Phase Transitions. *Nature* **138**.3498 (1936), pp. 840–841.

[136] C. J. Pethick and H. Smith. *Bose-Einstein Condensation in Dilute Gases*. Cambridge University Press, 2001.

[137] R. Sooryakumar and M. V. Klein. Raman Scattering by Superconducting-Gap Excitations and Their Coupling to Charge-Density Waves. *Physical Review Letters* **45**.8 (1980), pp. 660–662.

[138] C. Rüegg, B. Normand, M. Matsumoto, A. Furrer, D. F. McMorrow, K. W. Krämer, H. U. Güdel, S. N. Gvasaliya, H. Mutka, and M. Boehm. Quantum Magnets under Pressure: Controlling Elementary Excitations in $TlCuCl_3$. *Physical Review Letters* **100**.20 (2008), 205701.

[139] U. Bissbort, S. Götze, Y. Li, J. Heinze, J. S. Krauser, M. Weinberg, C. Becker, K. Sengstock, and W. Hofstetter. Detecting the Amplitude Mode of Strongly Interacting Lattice Bosons by Bragg Scattering. *Physical Review Letters* **106**.20 (2011), 205303.

[140] M. Endres, T. Fukuhara, D. Pekker, M. Cheneau, P. Schauß, C. Gross, E. Demler, S. Kuhr, and I. Bloch. The 'Higgs' amplitude mode at the two-dimensional superfluid/Mott insulator transition. *Nature* **487**.7408 (2012), pp. 454–458.

[141] R. Matsunaga, Y. I. Hamada, K. Makise, Y. Uzawa, H. Terai, Z. Wang, and R. Shimano. Higgs Amplitude Mode in the BCS Superconductors $Nb_{1-x}Ti_xN$ Induced by Terahertz Pulse Excitation. *Physical Review Letters* **111**.5 (2013), 057002.

[142] J. Léonard, A. Morales, P. Zupancic, T. Donner, and T. Esslinger. Monitoring and manipulating Higgs and Goldstone modes in a supersolid quantum gas. *Science* **358**.6369 (2017), pp. 1415–1418.

[143] K. Katsumi, N. Tsuji, Y. I. Hamada, R. Matsunaga, J. Schneeloch, R. D. Zhong, G. D. Gu, H. Aoki, Y. Gallais, and R. Shimano. Higgs Mode in the d -Wave Superconductor $Bi_2Sr_2CaCu_2O_{8+x}$ Driven by an Intense Terahertz Pulse. *Physical Review Letters* **120**.11 (2018), 117001.

[144] D. M. Eagles. Possible Pairing without Superconductivity at Low Carrier Concentrations in Bulk and Thin-Film Superconducting Semiconductors. *Physical Review* **186**.2 (1969), pp. 456–463.

[145] A. J. Leggett. "Diatomic molecules and cooper pairs". In: *Modern Trends in the Theory of Condensed Matter*. Springer Berlin Heidelberg, 1980, pp. 13–27.

[146] A. J. Leggett and S. Zhang. "The BEC–BCS Crossover: Some History and Some General Observations". In: *The BCS-BEC Crossover and the Unitary Fermi Gas*. Springer Berlin Heidelberg, 2011, pp. 33–47.

[147] C. A. Regal, M. Greiner, and D. S. Jin. Observation of Resonance Condensation of Fermionic Atom Pairs. *Physical Review Letters* **92**.4 (2004), 040403.

[148] M. W. Zwierlein, C. A. Stan, C. H. Schunck, S. M. F. Raupach, A. J. Kerman, and W. Ketterle. Condensation of Pairs of Fermionic Atoms near a Feshbach Resonance. *Physical Review Letters* **92**.12 (2004), 120403.

[149] S. Kasahara et al. Giant superconducting fluctuations in the compensated semimetal FeSe at the BCS–BEC crossover. *Nature Communications* **7**.1 (2016).

[150] M. Greiner, C. A. Regal, and D. S. Jin. Emergence of a molecular Bose–Einstein condensate from a Fermi gas. *Nature* **426**.6966 (2003), pp. 537–540.

[151] S. Jochim. Bose-Einstein Condensation of Molecules. *Science* **302**.5653 (2003), pp. 2101–2103.

[152] M. W. Zwierlein, C. A. Stan, C. H. Schunck, S. M. F. Raupach, S. Gupta, Z. Hadzibabic, and W. Ketterle. Observation of Bose-Einstein Condensation of Molecules. *Physical Review Letters* **91**.25 (2003), 250401.

[153] J. R. Schrieffer and J. S. Brooks, eds. *Handbook of High-Temperature Superconductivity*. Springer New York, 2007.

[154] M. E. Gehm. Preparation of an optically-trapped degenerate Fermi gas of 6Li: Finding the route to degeneracy. PhD thesis. Department of physics, Duke University, 2003.

[155] G. Zürn, T. Lompe, A. N. Wenz, S. Jochim, P. S. Julienne, and J. M. Hutson. Precise Characterization ofLi6Feshbach Resonances Using Trap-Sideband-Resolved RF Spectroscopy of Weakly Bound Molecules. *Physical Review Letters* **110**.13 (2013), 135301.

[156] M. G. Ries. A Two-Dimensional Fermi Gas in the BEC-BCS Crossover. PhD thesis. Heidelberg University, 2015.

[157] M. Neidig. Many-Body Pairing in a Two-Dimensional Fermi Gas. PhD thesis. Heidelberg University, 2017.

[158] A. Bergschneider. Strong correlations in few-fermion systems. PhD thesis. Heidelberg University, 2017.

[159] V. M. Klinkhamer. Few-fermion systems under a matterwace microscope. PhD thesis. Heidelberg University, 2018.

[160] F. Serwane, G. Zurn, T. Lompe, T. B. Ottenstein, A. N. Wenz, and S. Jochim. Deterministic Preparation of a Tunable Few-Fermion System. *Science* **332**.6027 (2011), pp. 336–338.

[161] D. M. Stamper-Kurn, H.-J. Miesner, A. P. Chikkatur, S. Inouye, J. Stenger, and W. Ketterle. Reversible Formation of a Bose-Einstein Condensate. *Physical Review Letters* **81**.11 (1998), pp. 2194–2197.

[162] M. Dehabe. Creating an optical microtrap with tunable aspect ratio for ultracold fermions. Master thesis. Heidelberg University, 2016.

[163] S. Murmann, A. Bergschneider, V. M. Klinkhamer, G. Zürn, T. Lompe, and S. Jochim. Two Fermions in a Double Well: Exploring a Fundamental Building Block of the Hubbard Model. *Physical Review Letters* **114**.8 (2015), 080402.

[164] M. Bauer, M. M. Parish, and T. Enss. Universal Equation of State and Pseudogap in the Two-Dimensional Fermi Gas. *Physical Review Letters* **112**.13 (2014), 135302.

[165] E. J. Mueller. Review of pseudogaps in strongly interacting Fermi gases. *Reports on Progress in Physics* **80**.10 (2017), 104401.

[166] Q. Chen, Y. He, C.-C. Chien, and K Levin. Theory of radio frequency spectroscopy experiments in ultracold Fermi gases and their relation to photoemission in the cuprates. *Reports on Progress in Physics* **72**.12 (2009), 122501.

[167] J. J. Lee et al. Interfacial mode coupling as the origin of the enhancement of Tc in FeSe films on SrTiO3. *Nature* **515**.7526 (2014), pp. 245–248.

[168] H. Ding, T. Yokoya, J. C. Campuzano, T. Takahashi, M. Randeria, M. R. Norman, T. Mochiku, K. Kadowaki, and J. Giapintzakis. Spectroscopic evidence for a pseudogap in the normal state of underdoped high-Tc superconductors. *Nature* **382**.6586 (1996), pp. 51–54.

[169] M. Feld, B. Fröhlich, E. Vogt, M. Koschorreck, and M. Köhl. Observation of a pairing pseudogap in a two-dimensional Fermi gas. *Nature* **480**.7375 (2011), pp. 75–78.

[170] A. T. Sommer, L. W. Cheuk, M. J. H. Ku, W. S. Bakr, and M. W. Zwierlein. Evolution of Fermion Pairing from Three to Two Dimensions. *Physical Review Letters* **108**.4 (2012), 045302.

[171] S. Nascimbène, N. Navon, S. Pilati, F. Chevy, S. Giorgini, A. Georges, and C. Salomon. Fermi-Liquid Behavior of the Normal Phase of a Strongly Interacting Gas of Cold Atoms. *Physical Review Letters* **106**.21 (2011), 215303.

[172] J. P. Gaebler, J. T. Stewart, T. E. Drake, D. S. Jin, A. Perali, P. Pieri, and G. C. Strinati. Observation of pseudogap behaviour in a strongly interacting Fermi gas. *Nature Physics* **6**.8 (2010), pp. 569–573.

[173] A. Perali, F. Palestini, P. Pieri, G. C. Strinati, J. T. Stewart, J. P. Gaebler, T. E. Drake, and D. S. Jin. Evolution of the Normal State of a Strongly Interacting Fermi Gas from a Pseudogap Phase to a Molecular Bose Gas. *Physical Review Letters* **106**.6 (2011), 060402.

[174] Y. Sagi, T. E. Drake, R. Paudel, R. Chapurin, and D. S. Jin. Breakdown of the Fermi Liquid Description for Strongly Interacting Fermions. *Physical Review Letters* **114**.7 (2015), 075301.

[175] C. H. Schunck, Y. Shin, A. Schirotzek, M. W. Zwierlein, and W. Ketterle. Pairing Without Superfluidity: The Ground State of an Imbalanced Fermi Mixture. *Science* **316**.5826 (2007), pp. 867–870.

[176] P. Törmä. Physics of ultracold Fermi gases revealed by spectroscopies. *Physica Scripta* **91**.4 (2016), 043006.

[177] M. Barth and J. Hofmann. Pairing effects in the nondegenerate limit of the two-dimensional Fermi gas. *Physical Review A* **89**.1 (2014), 013614.

[178] V. Ngampruetikorn, J. Levinsen, and M. M. Parish. Pair Correlations in the Two-Dimensional Fermi Gas. *Physical Review Letters* **111**.26 (2013), 265301.

[179] F. Marsiglio, P. Pieri, A. Perali, F. Palestini, and G. C. Strinati. Pairing effects in the normal phase of a two-dimensional Fermi gas. *Physical Review B* **91**.5 (2015), 054509.

[180] P. A. Murthy, D. Kedar, T. Lompe, M. Neidig, M. G. Ries, A. N. Wenz, G. Zürn, and S. Jochim. Matter-wave Fourier optics with a strongly interacting two-dimensional Fermi gas. *Physical Review A* **90**.4 (2014), 043611.

[181] K. Hueck, N. Luick, L. Sobirey, J. Siegl, T. Lompe, and H. Moritz. Two-Dimensional Homogeneous Fermi Gases. *Physical Review Letters* **120**.6 (2018), 060402.

[182] P. Dyke, E. D. Kuhnle, S. Whitlock, H. Hu, M. Mark, S. Hoinka, M. Lingham, P. Hannaford, and C. J. Vale. Crossover from 2D to 3D in a Weakly Interacting Fermi Gas. *Physical Review Letters* **106**.10 (2011), 105304.

[183] R. Klemt. Many-body correlations in a quasi-two-dimensional, ultracold atomic Fermi gas. Master thesis. Heidelberg University, 2016.

[184] S. Gupta. Radio-Frequency Spectroscopy of Ultracold Fermions. *Science* **300**.5626 (2003), pp. 1723–1726.

[185] Y. Zhang, W. Ong, I. Arakelyan, and J. E. Thomas. Polaron-to-Polaron Transitions in the Radio-Frequency Spectrum of a Quasi-Two-Dimensional Fermi Gas. *Physical Review Letters* **108**.23 (2012), 235302.

[186] R. Schmidt, T. Enss, V. Pietilä, and E. Demler. Fermi polarons in two dimensions. *Physical Review A* **85**.2 (2012), 021602.

[187] V. Ngampruetikorn, J. Levinsen, and M. M. Parish. Repulsive polarons in two-dimensional Fermi gases. *Europhysics Letters* **98**.3 (2012), 30005.

[188] C. Langmack, M. Barth, W. Zwerger, and E. Braaten. Clock Shift in a Strongly Interacting Two-Dimensional Fermi Gas. *Physical Review Letters* **108**.6 (2012), 060402.

[189] A. Schirotzek, Y. il Shin, C. H. Schunck, and W. Ketterle. Determination of the Superfluid Gap in Atomic Fermi Gases by Quasiparticle Spectroscopy. *Physical Review Letters* **101**.14 (2008), 140403.

[190] D. Mitra, P. T. Brown, P. Schauß, S. S. Kondov, and W. S. Bakr. Phase Separation and Pair Condensation in a Spin-Imbalanced 2D Fermi Gas. *Physical Review Letters* **117**.9 (2016), 093601.

[191] B. Fröhlich, M. Feld, E. Vogt, M. Koschorreck, M. Köhl, C. Berthod, and T. Giamarchi. Two-Dimensional Fermi Liquid with Attractive Interactions. *Physical Review Letters* **109**.13 (2012), 130403.

[192] L. Sobirey, N. Luick, M. Bohlen, H. Biss, H. Moritz, and T. Lompe. Observation of superfluidity in a strongly correlated two-dimensional Fermi gas (2020). arXiv: 2005.07607 [cond-mat.quant-gas].

[193] A. Damascelli, Z. Hussain, and Z.-X. Shen. Angle-resolved photoemission studies of the cuprate superconductors. *Reviews of Modern Physics* **75**.2 (2003), pp. 473–541.

[194] P. T. Brown, E. Guardado-Sanchez, B. M. Spar, E. W. Huang, T. P. Devereaux, and W. S. Bakr. Angle-resolved photoemission spectroscopy of a Fermi–Hubbard system. *Nature Physics* **16**.1 (2019), pp. 26–31.

[195] S. Nascimbène, Y.-A. Chen, M. Atala, M. Aidelsburger, S. Trotzky, B. Paredes, and I. Bloch. Experimental Realization of Plaquette Resonating Valence-Bond States with Ultracold Atoms in Optical Superlattices. *Physical Review Letters* **108**.20 (2012), 205301.

[196] M. F. Parsons, A. Mazurenko, C. S. Chiu, G. Ji, D. Greif, and M. Greiner. Site-resolved measurement of the spin-correlation function in the Fermi-Hubbard model. *Science* **353**.6305 (2016), pp. 1253–1256.

[197] L. W. Cheuk, M. A. Nichols, K. R. Lawrence, M. Okan, H. Zhang, E. Khatami, N. Trivedi, T. Paiva, M. Rigol, and M. W. Zwierlein. Observation of spatial charge and spin correlations in the 2D Fermi-Hubbard model. *Science* **353**.6305 (2016), pp. 1260–1264.

[198] T. W. B. Kibble. Topology of cosmic domains and strings. *Journal of Physics A: Mathematical and General* **9**.8 (1976), pp. 1387–1398.

[199] T. Kibble. Some implications of a cosmological phase transition. *Physics Reports* **67**.1 (1980), pp. 183–199.

[200] W. H. Zurek. Cosmological experiments in superfluid helium? *Nature* **317**.6037 (1985), pp. 505–508.

[201] W. Zurek. Cosmological experiments in condensed matter systems. *Physics Reports* **276**.4 (1996), pp. 177–221.

[202] P. W. Anderson. The Resonating Valence Bond State in La2CuO4 and Superconductivity. *Science* **235**.4793 (1987), pp. 1196–1198.

[203] G. Baskaran, Z. Zou, and P. Anderson. The resonating valence bond state and high-Tc superconductivity — A mean field theory. *Solid State Communications* **63**.11 (1987), pp. 973–976.

[204] S. Trebst, U. Schollwöck, M. Troyer, and P. Zoller. d-Wave Resonating Valence Bond States of Fermionic Atoms in Optical Lattices. *Physical Review Letters* **96**.25 (2006), 250402.

[205] R. B. Laughlin. Anomalous Quantum Hall Effect: An Incompressible Quantum Fluid with Fractionally Charged Excitations. *Physical Review Letters* **50**.18 (1983), pp. 1395–1398.

[206] S. Kuhr. Quantum-gas microscopes: a new tool for cold-atom quantum simulators. *National Science Review* **3**.2 (2016), pp. 170–172.

[207] C. Veit, N. Zuber, O. A. Herrera-Sancho, V. S. V. Anasuri, T. Schmid, F. Meinert, R. Löw, and T. Pfau. A pulsed ion microscope to probe quantum gases (2020). arXiv: 2008.08512 [physics.atom-ph].

[208] D. K. Shin, B. M. Henson, S. S. Hodgman, T. Wasak, J. Chwedeńczuk, and A. G. Truscott. Bell correlations between spatially separated pairs of atoms. *Nature Communications* **10**.1 (2019).

[209] M. Gajdacz, P. L. Pedersen, T. Mørch, A. J. Hilliard, J. Arlt, and J. F. Sherson. Non-destructive Faraday imaging of dynamically controlled ultracold atoms. *Review of Scientific Instruments* **84**.8 (2013), 083105.

[210] D. B. Hume, I. Stroescu, M. Joos, W. Muessel, H. Strobel, and M. K. Oberthaler. Accurate Atom Counting in Mesoscopic Ensembles. *Physical Review Letters* **111**.25 (2013), 253001.

[211] A. Fuhrmanek, Y. R. P. Sortais, P. Grangier, and A. Browaeys. Measurement of the atom number distribution in an optical tweezer using single-photon counting. *Physical Review A* **82**.2 (2010), 023623.

[212] R Bücker, A Perrin, S Manz, T Betz, C. Koller, T Plisson, J Rottmann, T Schumm, and J Schmiedmayer. Single-particle-sensitive imaging of freely propagating ultracold atoms. *New Journal of Physics* **11**.10 (2009), 103039.

[213] C. J. Picken, R. Legaie, and J. D. Pritchard. Single atom imaging with an sCMOS camera. *Applied Physics Letters* **111**.16 (2017), 164102.

[214] M. A. Joffe, W. Ketterle, A. Martin, and D. E. Pritchard. Transverse cooling and deflection of an atomic beam inside a Zeeman slower. *Journal of the Optical Society of America B* **10**.12 (1993), 2257.

[215] E. Lantz, J.-L. Blanchet, L. Furfaro, and F. Devaux. Multi-imaging and Bayesian estimation for photon counting with EMCCDs. *Monthly Notices of the Royal Astronomical Society* **386**.4 (2008), pp. 2262–2270.

[216] A. G. Basden, C. A. Haniff, and C. D. Mackay. Photon counting strategies with low-light-level CCDs. *Monthly Notices of the Royal Astronomical Society* **345**.3 (2003), pp. 985–991.

[217] M. Hirsch, R. J. Wareham, M. L. Martin-Fernandez, M. P. Hobson, and D. J. Rolfe. A Stochastic Model for Electron Multiplication Charge-Coupled Devices – From Theory to Practice. *PLoS ONE* **8**.1 (2013). Ed. by C.-T. Chen, e53671.

[218] T. B. Ottenstein, T. Lompe, M. Kohnen, A. N. Wenz, and S. Jochim. Collisional Stability of a Three-Component Degenerate Fermi Gas. *Physical Review Letters* **101**.20 (2008), 203202.

[219] S. Tung, G. Lamporesi, D. Lobser, L. Xia, and E. A. Cornell. Observation of the Presuperfluid Regime in a Two-Dimensional Bose Gas. *Physical Review Letters* **105**.23 (2010), 230408.

[220] R. Blatt and C. F. Roos. Quantum simulations with trapped ions. *Nature Physics* **8**.4 (2012), pp. 277–284.

[221] J. Turcotte, É. Artigau, O. Daigle, and R. Doyon. "Preliminary characterization results of a large format 4k x 4k EMCCD". In: *High Energy, Optical, and Infrared Detectors for Astronomy VIII*. Ed. by A. D. Holland and J. Beletic. SPIE, 2018.

[222] M. Masias, J. Freixenet, X. Lladó, and M. Peracaula. A review of source detection approaches in astronomical images. *Monthly Notices of the Royal Astronomical Society* **422**.2 (2012), pp. 1674–1689.

[223] M. Masias, M. Peracaula, J. Freixenet, and X. Lladó. A quantitative analysis of source detection approaches in optical, infrared, and radio astronomical images. *Experimental Astronomy* **36**.3 (2013), pp. 591–629.

[224] Ž. Ivezić, A. J. Connolly, J. T. VanderPlas, and A. Gray. *Statistics, Data Mining, and Machine Learning in Astronomy: A Practical Python Guide for the Analysis of Survey Data*. Princeton University Press, 2019.

[225] URL: https://www.sony.net/SonyInfo/News/Press/201802/18-018E/.

[226] S. Blänsdorf. Light-induced nuuclear spin-flips in ^{6}Li ground states through Raman-transitions. Bachelor thesis. Heidelberg University, 2018.

[227] L. W. Cheuk, A. T. Sommer, Z. Hadzibabic, T. Yefsah, W. S. Bakr, and M. W. Zwierlein. Spin-Injection Spectroscopy of a Spin-Orbit Coupled Fermi Gas. *Physical Review Letters* **109**.9 (2012), 095302.

[228] T. Schweigler, V. Kasper, S. Erne, I. Mazets, B. Rauer, F. Cataldini, T. Langen, T. Gasenzer, J. Berges, and J. Schmiedmayer. Experimental characterization of a quantum many-body system via higher-order correlations. *Nature* **545**.7654 (2017), pp. 323–326.

[229] M. Kjaergaard, M. E. Schwartz, J. Braumüller, P. Krantz, J. I.-J. Wang, S. Gustavsson, and W. D. Oliver. Superconducting Qubits: Current State of Play. *Annual Review of Condensed Matter Physics* **11**.1 (2020), pp. 369–395.

[230] C. Gross and I. Bloch. Quantum simulations with ultracold atoms in optical lattices. *Science* **357**.6355 (2017), pp. 995–1001.

[231] M. Boll, T. A. Hilker, G. Salomon, A. Omran, J. Nespolo, L. Pollet, I. Bloch, and C. Gross. Spin- and density-resolved microscopy of antiferromagnetic correlations in Fermi-Hubbard chains. *Science* **353**.6305 (2016), pp. 1257–1260.

[232] A. Mazurenko, C. S. Chiu, G. Ji, M. F. Parsons, M. Kanász-Nagy, R. Schmidt, F. Grusdt, E. Demler, D. Greif, and M. Greiner. A cold-atom Fermi–Hubbard antiferromagnet. *Nature* **545**.7655 (2017), pp. 462–466.

[233] P. Weinberg and M. Bukov. QuSpin: a Python package for dynamics and exact diagonalisation of quantum many body systems part I: spin chains. *SciPost Physics* **2**.1 (2017).

[234] P. Weinberg and M. Bukov. QuSpin: a Python package for dynamics and exact diagonalisation of quantum many body systems. Part II: bosons, fermions and higher spins. *SciPost Physics* **7**.2 (2019).

[235] S. Murmann. Few-particle quantum magnetism with ultracold atoms. PhD thesis. Heidelberg University, 2015.

[236] S. Trotzky, P. Cheinet, S. Folling, M. Feld, U. Schnorrberger, A. M. Rey, A. Polkovnikov, E. A. Demler, M. D. Lukin, and I. Bloch. Time-Resolved Observation and Control of Superexchange Interactions with Ultracold Atoms in Optical Lattices. *Science* **319**.5861 (2008), pp. 295–299.

[237] C. Yannouleas and U. Landman. Third-order momentum correlation interferometry maps for entangled quantal states of three singly trapped massive ultracold fermions. *Physical Review A* **100**.2 (2019), 023618.

[238] A. Aspect, P. Grangier, and G. Roger. Experimental Realization of Einstein-Podolsky-Rosen-Bohm Gedankenexperiment: A New Violation of Bell's Inequalities. *Physical Review Letters* **49**.2 (1982), pp. 91–94.

[239] A. M. Kaufman, B. J. Lester, M. Foss-Feig, M. L. Wall, A. M. Rey, and C. A. Regal. Entangling two transportable neutral atoms via local spin exchange. *Nature* **527**.7577 (2015), pp. 208–211.

[240] R. Horodecki and P. Horodecki. Quantum redundancies and local realism. *Physics Letters A* **194**.3 (1994), pp. 147–152.

[241] R. Horodecki, P. Horodecki, and M. Horodecki. Quantum alpha-entropy inequalities: independent condition for local realism? *Physics Letters A* **210**.6 (1996), pp. 377–381.

[242] N. J. Cerf and C. Adami. Negative Entropy and Information in Quantum Mechanics. *Physical Review Letters* **79**.26 (1997), pp. 5194–5197.

[243] M. Bonneau, W. J. Munro, K. Nemoto, and J. Schmiedmayer. Characterizing twin-particle entanglement in double-well potentials. *Physical Review A* **98**.3 (2018), 033608.

[244] G. Taguchi, T. Dougakiuchi, N. Yoshimoto, K. Kasai, M. Iinuma, H. F. Hofmann, and Y. Kadoya. Measurement and control of spatial qubits generated by passing photons through double slits. *Physical Review A* **78**.1 (2008), 012307.

[245] R. Blume-Kohout. Optimal, reliable estimation of quantum states. *New Journal of Physics* **12**.4 (2010), 043034.

[246] R. J. Glauber. The Quantum Theory of Optical Coherence. *Physical Review* **130**.6 (1963), pp. 2529–2539.

[247] M. O. Scully and M. S. Zubairy. *Quantum Optics*. England, U.K.: Cambridge University Press, 1997.

[248] R. Ghosh and L. Mandel. Observation of nonclassical effects in the interference of two photons. *Physical Review Letters* **59**.17 (1987), pp. 1903–1905.

[249] C. K. Hong, Z. Y. Ou, and L. Mandel. Measurement of subpicosecond time intervals between two photons by interference. *Physical Review Letters* **59**.18 (1987), pp. 2044–2046.

[250] C. Pfister, J. Kaniewski, M. Tomamichel, A. Mantri, R. Schmucker, N. McMahon, G. Milburn, and S. Wehner. A universal test for gravitational decoherence. *Nature Communications* **7**.1 (2016).

[251] M. C. Tichy. Interference of identical particles from entanglement to boson-sampling. *Journal of Physics B: Atomic, Molecular and Optical Physics* **47**.10 (2014), 103001.

[252] R Hanbury Brown and R. Q. Twiss. Correlation between photons in two coherent beams of light. *Nature* **177**.27 (1956).

[253] R. Hanbury Brown and R. Q. Twiss. A test of a new type ofstellar interferometer on Sirius. *Nature* **178**.1046 (1956).

[254] M. Yasuda and F. Shimizu. Observation of Two-Atom Correlation of an Ultracold Neon Atomic Beam. *Physical Review Letters* **77**.15 (1996), pp. 3090–3093.

[255] M. Schellekens. Hanbury Brown Twiss Effect for Ultracold Quantum Gases. *Science* **310**.5748 (2005), pp. 648–651.

[256] S. Fölling. "Quantum Noise Correlation Experiments with Ultracold Atoms". In: *Cold Atoms*. Imperial College Press, 2014, pp. 145–177.

[257] R. Lopes, A. Imanaliev, A. Aspect, M. Cheneau, D. Boiron, and C. I. Westbrook. Atomic Hong–Ou–Mandel experiment. *Nature* **520**.7545 (2015), pp. 66–68.

[258] G. Baym. "The quantum-mechanics of Hanbury-Brown Twiss interferometry in ultrarelativistic heavy-ion collisions". In: *Relativistic Aspects of Nuclear Physics*. World Scientific, 1998, pp. 2–17.

[259] T Csörgö. Review of HBT or Bose-Einstein correlations in high energy heavy ion collisions. *Journal of Physics: Conference Series* **50** (2006), pp. 259–270.

[260] H. Cayla, S. Butera, C. Carcy, A. Tenart, G. Hercé, M. Mancini, A. Aspect, I. Carusotto, and D. Clément. Hanbury Brown and Twiss Bunching of Phonons and of the Quantum Depletion in an Interacting Bose Gas. *Physical Review Letters* **125**.16 (2020), 165301.

[261] S. Butera, D. Clément, and I. Carusotto. Position- and momentum-space two-body correlations in a weakly interacting trapped condensate (2020). arXiv: 2008.13039 [cond-mat.quant-gas].

[262] A. J. Menssen, A. E. Jones, B. J. Metcalf, M. C. Tichy, S. Barz, W. S. Kolthammer, and I. A. Walmsley. Distinguishability and Many-Particle Interference. *Physical Review Letters* **118**.15 (2017), 153603.

[263] S. Agne, T. Kauten, J. Jin, E. Meyer-Scott, J. Z. Salvail, D. R. Hamel, K. J. Resch, G. Weihs, and T. Jennewein. Observation of Genuine Three-Photon Interference. *Physical Review Letters* **118**.15 (2017), 153602.

[264] T. Giordani et al. Experimental statistical signature of many-body quantum interference. *Nature Photonics* **12**.3 (2018), pp. 173–178.

[265] V. Shchesnovich. Universality of Generalized Bunching and Efficient Assessment of Boson Sampling. *Physical Review Letters* **116**.12 (2016), 123601.

[266] M. Walschaers, J. Kuipers, and A. Buchleitner. From many-particle interference to correlation spectroscopy. *Physical Review A* **94**.2 (2016), 020104.

[267] E. Sindici and M. Piani. Simple class of bound entangled states based on the properties of the antisymmetric subspace. *Physical Review A* **97**.3 (2018), 032319.

[268] E. Sindici. Quantum Correlations and Exchange Symmetry. PhD thesis. Strathclyde University, 2019.

[269] G. Vidal and R. F. Werner. Computable measure of entanglement. *Physical Review A* **65**.3 (2002), 032314.

[270] P. Samuelsson, E. V. Sukhorukov, and M. Büttiker. Two-Particle Aharonov-Bohm Effect and Entanglement in the Electronic Hanbury Brown–Twiss Setup. *Physical Review Letters* **92**.2 (2004), 026805.

[271] B. Jungnitsch, T. Moroder, and O. Gühne. Taming Multiparticle Entanglement. *Physical Review Letters* **106**.19 (2011), 190502.

[272] M. Hofmann, T. Moroder, and O. Gühne. Analytical characterization of the genuine multiparticle negativity. *Journal of Physics A: Mathematical and Theoretical* **47**.15 (2014), 155301.

[273] P. W. Anderson. More Is Different. *Science* **177**.4047 (1972), pp. 393–396.

[274] A. Bohr, B. R. Mottelson, G. Breit, and G. E. Brown. Nuclear Structure, Vol. 2: Nuclear Deformations. *Physics Today* **30**.3 (1977), pp. 59–62.

[275] K. D. Launey. *Emergent Phenomena in Atomic Nuclei from Large-Scale Modeling*. World Scientific, 2017.

[276] A. V. S. Grebenev J.P. Toennies. Superfluidity Within a Small Helium-4 Cluster: The Microscopic Andronikashvili Experiment. *Science* **279**.5359 (1998), pp. 2083–2086.

[277] A. N. Wenz, G. Zurn, S. Murmann, I. Brouzos, T. Lompe, and S. Jochim. From Few to Many: Observing the Formation of a Fermi Sea One Atom at a Time. *Science* **342**.6157 (2013), pp. 457–460.

[278] N. T. Zinner and A. S. Jensen. Comparing and contrasting nuclei and cold atomic gases. *Journal of Physics G: Nuclear and Particle Physics* **40**.5 (2013), 053101.

[279] J. R. McClean, J. Romero, R. Babbush, and A. Aspuru-Guzik. The theory of variational hybrid quantum-classical algorithms. *New Journal of Physics* **18**.2 (2016), 023023.

[280] P. J. O'Malley et al. Scalable Quantum Simulation of Molecular Energies. *Physical Review X* **6**.3 (2016), 031007.

[281] J. Argüello-Luengo, A. González-Tudela, T. Shi, P. Zoller, and J. I. Cirac. Analogue quantum chemistry simulation. *Nature* **574**.7777 (2019), pp. 215–218.

[282] R. Sweke, F. Wilde, J. Meyer, M. Schuld, P. K. Faehrmann, B. Meynard-Piganeau, and J. Eisert. Stochastic gradient descent for hybrid quantum-classical optimization. *Quantum* **4** (2020), 314.

[283] M. Rontani, J. R. Armstrong, Y. Yu, S. Åberg, and S. M. Reimann. Cold Fermionic Atoms in Two-Dimensional Traps: Pairing versus Hund's Rule. *Physical Review Letters* **102**.6 (2009), 060401.

[284] H. Heiselberg and B. Mottelson. Shell Structure and Pairing for Interacting Fermions in a Trap. *Physical Review Letters* **88**.19 (2002), 190401.

[285] L. Bayha. Emergence of Many-Body Physics in Two-Dimensional Few-Fermion Systems. PhD thesis. Heidelberg University, 2020.

[286] J. Bjerlin, S. Reimann, and G. Bruun. Few-Body Precursor of the Higgs Mode in a Fermi Gas. *Physical Review Letters* **116**.15 (2016), 155302.

[287] J. Goldstone. Field theories with Superconductor solutions. *Il Nuovo Cimento* **19**.1 (1961), pp. 154–164.

[288] P. W. Higgs. Broken Symmetries and the Masses of Gauge Bosons. *Physical Review Letters* **13**.16 (1964), pp. 508–509.

[289] M. Kohmoto and Y. Takada. Superconductivity from an Insulator. *Journal of the Physical Society of Japan* **59**.5 (1990), pp. 1541–1544.

[290] P. Nozières and F. Pistolesi. From semiconductors to superconductors: a simple model for pseudogaps. *The European Physical Journal B* **10**.4 (1999), pp. 649–662.

[291] G. M. Bruun. Long-lived Higgs mode in a two-dimensional confined Fermi system. *Physical Review A* **90**.2 (2014), 023621.

[292] G. M. Bruun and B. R. Mottelson. Low Energy Collective Modes of a Superfluid Trapped Atomic Fermi Gas. *Physical Review Letters* **87**.27 (2001), 270403.

[293] D. Pęcak and T. Sowiński. Signatures of unconventional pairing in spin-imbalanced one-dimensional few-fermion systems. *Physical Review Research* **2**.1 (2020), 012077.

List of Publications

- **High temperature pairing in a strongly interacting two-dimensional Fermi gas**†
  P. A. Murthy*, M. Neidig*, R. Klemt*, L. Bayha, I. Boettcher, T. Enss, M. Holten, G. Zürn, P. M. Preiss, S. Jochim
  Science **359**, 452-455 (2018)

- **Spin-resolved single-atom imaging of ^{6}Li in free space**†
  A. Bergschneider*, V. M. Klinkhamer*, J. H. Becher, R. Klemt, G. Zürn, P. M. Preiss, S. Jochim
  Physical Review A **97**.6 (2018)

- **Experimental characterization of two-particle entanglement through position and momentum correlations**†
  A. Bergschneider*, V. M. Klinkhamer*, J. H. Becher, R. Klemt, L. Palm, G. Zürn, S. Jochim, P. M. Preiss
  Nature Physics **15**.7 (2019)

- **Density Oscillations Induced by Individual Ultracold Two-Body Collisions**
  Q. Guan, V. M. Klinkhamer, R. Klemt, J. H. Becher, A. Bergschneider, P. M. Preiss, S. Jochim, D. Blume
  Physical Review Letters **122**.8 (2019)

- **High-Contrast Interference of Ultracold Fermions**†
  P. M. Preiss, J. H. Becher, R. Klemt, V. M. Klinkhamer, A. Bergschneider, N. Defenu, S. Jochim
  Physical Review Letters **122**.14, (2019)

- **Measurement of Identical Particle Entanglement and the Influence of Antisymmetrization**†
  J. H. Becher, E. Sindici, R. Klemt, S. Jochim, A. Daley, P. Preiss
  Physical Review Letters **125**.18, (2020)

- **Observing the emergence of a quantum phase transition – shell by shell**†
  L. Bayha*, M. Holten*, R. Klemt, K. Subramanian, J. Bjerlin, S. M. Reimann, G. M. Bruun, P. M. Preiss, S. Jochim
  Nature **587**, 583-587 (2020)

The authors marked with * contributed equally to the respective publication.
Publications marked with † have been explicitly discussed in this thesis.

Danksagung:

Ich möchte mich bei allen, die zum Gelingen dieser Arbeit beigetragen haben, bedanken.
Ein besonderer Dank gilt Selim für die Betreuung meiner Promotion und die vielen Jahre, in denen er mir mit Rat und Tat zur Seite gestanden hat.
Ebenso möchte ich mich bei Priv.-Doz. Dr. Martin Gärttner für die Übernahme der Zweitkorrektur sowie bei Prof. Dr. Peter Bachert und Prof. Dr. Thomas Pfeifer für die Bereitschaft, Teil meines Prüfungskommitees zu werden, bedanken.
Ein großer Dank gilt natürlich auch meinen Kollegen, mit denen ich über die Jahre zusammenarbeiten durfte: Mathias, Luca, Puneet, Marvin und Keerthan am neuen Experiment, Andrea, Vincent, Michael, Lukas, Ram-Janik, Laurin und insbesondere auch Jan Hendrik und Philipp L. am alten Experiment, sowie an beiden Experimenten Gerhard und Philipp P. Im Besonderen möchte ich mich noch explizit bei Luca, Marvin und den beiden Philipps für das Lesen meiner Arbeit und die vielen hilfreichen Korrekturvorschlägen bedanken.
Außerdem hatte ich über die Jahre auch die Möglichkeit mit vielen Theoretikern zusammenzuarbeiten. Für die fruchtbare Zusammenarbeit möchte ich mich daher bei Tilman Enss, Nicolò Defenu, Igor Boettcher, Quingze Guan, Dörte Blume, Johannes Bjerlin, Steffi Reimann, Georg Bruun, Enrico Sindici sowie Andrew Daley bedanken.
Größter Dank gebührt meinen Freunden und meiner Familie für die großartige Unterstützung und auch den Rückhalt in den letzten Jahren. Zu guter Letzt möchte ich mich bei meiner Frau bedanken: Für 2369 in dieser Arbeit gefundene Rechtschreibfehler und insbesondere einfach dafür, dass du da bist.